The Structure and Dynamics of the Near-Sun Solar Wind

Thomas Woolley

Submitted in part fulfilment of the

requirements for the degree of

Doctor of Philosophy

Department of Physics

Imperial College London

January 21, 2023

I confirm that the research presented throughout this thesis has been completed by me. I have appropriately referenced any work and/or ideas from other sources.

The copyright of this thesis rests with the author. Unless otherwise indicated, its contents are licensed under a Creative Commons Attribution-Non Commercial 4.0 International Licence (CC BY-NC). Under this licence, you may copy and redistribute the material in any medium or format. You may also create and distribute modified versions of the work. This is on the condition that: you credit the author and do not use it, or any derivative works, for a commercial purpose. When reusing or sharing this work, ensure you make the licence terms clear to others by naming the licence and linking to the licence text. Where a work has been adapted, you should indicate that the work has been changed and describe those changes. Please seek permission from the copyright holder for uses of this work that are not included in this licence or permitted under UK Copyright Law.

Thomas Woolley, October 2022

Abstract

The solar wind is a collisionless plasma that flows at hundreds of km/s away from the Sun into interplanetary space. Despite over half a century of solar wind research many questions remain unanswered. To address these questions, in situ data from small heliocentric distances is required. To date, Parker Solar Probe (PSP) is the only spacecraft to measure data within 0.29 au. Therefore, the PSP data set offers a unique opportunity to study the near-Sun solar wind.

The data from the Solar Probe Cup instrument are fitted to extract bulk solar wind parameters. These parameters are used in conjunction with data from the SPAN and MAG instruments to analyse three structures found in the solar wind: switchbacks, patches and quiet periods.

The ion velocity distribution functions within full-reversal switchbacks are shown to be consistent with a velocity-space rotation of the background plasma. This suggests that the proton core parallel temperature is the same inside and outside of full-reversal switchbacks despite the enhanced plasma velocity above the background.

The solar wind associated with two switchback patches is found to be consistent with slow Alfvénic solar wind from near the boundary of the southern polar coronal hole. A patch is also found to have a particularly low $\alpha-$particle abundance which is in contrast to a subsequent study, suggesting that $\alpha-$particle abundance within patches is variable.

Quiet periods are found to be consistent with longitudinal solar wind streams in close proximity to the heliospheric current sheet (HCS). The typical longitudinal scale size of these quiet periods is $\sim 2^{\circ}$. However, most quiet period durations are not consistent with this scale, as they are modulated by PSP's orbital trajectory and the HCS dynamics.

Acknowledgements

I would like to thank all the people who have helped me reach this stage, I could not have done it without you.

To Lorenzo, thank you so much for the last three years. You have helped me so much! I will always appreciate our many talks about physics and our many talks about Italy!

To Tim, thanks for always pushing me to publish and present my work. You really helped to motivate me, particularly in the depths of lockdown!

To Chadi, I am so grateful that you hosted me at UC Berkeley. I had a fantastic experience throughout the whole trip, thank you.

To Stuart, Julia and Lloyd, thank you for all the insightful discussions and your patience when describing turbulence to me!

Thanks to Ronan, Adrian, Sophia, Earn and Ozzy for sharing an office and many adventures with me.

Thank you to everyone else in the Space and Atmospheric Physics group that I met along the way.

Thanks to Robert Wicks and Robert Forsyth for taking the time to assess me throughout my viva. I really enjoyed answering your insightful questions and engaging in interesting discussions.

Thank you to Mum, Dad, Meg and the rest of my family. In particular I want to thank Granny who took the time to read through this whole thesis!

To Phil, Griffin and Ewa, thanks for entertaining me during lockdown and making lunch times a lot more fun!

And finally thanks to Silvia for putting up with me for the last five and a half years.

Contents

1 Introduction **13**

2 Background **14**

2.1 Plasma Theory . . . 14

2.1.1 Kinetic Regime . . . 15

2.1.2 Fluid Regime . . . 16

2.2 The Sun . . . 18

2.2.1 The Solar Cycle and Magnetic Field . . . 19

2.2.2 Solar Features . . . 21

2.3 Solar Wind Theory . . . 23

2.3.1 Parker's Solar Wind . . . 23

2.3.2 The Parker Spiral . . . 25

2.3.3 Chew-Goldberger-Low Invariants . . . 26

2.4 Solar Wind Observations . . . 28

2.4.1 Velocity Distribution Functions . . . 28

2.4.2 Composition . . . 32

2.4.3 Alfvén Waves in the Solar Wind . . . 33

2.4.4 Categorisation . . . 35

2.4.5 Slow Alfvénic Solar Wind . . . 38

2.4.6 Proton Temperature-Velocity Relationships . . . 40

2.4.7 Radial Plasma Evolution . . . 41

2.5 Instrumentation . . . 42

2.5.1 Electrostatic Analysers . . . 42

2.5.2 Fluxgate Magnetometers . . . 43

2.6 Current Space Missions . . . 44

2.6.1 Parker Solar Probe . . . 45
2.6.2 Solar Orbiter . . . 48

3 Fitting Solar Probe Cup Data **49**
3.1 Introduction . . . 49
3.2 The SWEAP Instrument Suite . . . 50
3.3 Solar Probe Cup: Design and Operation . . . 51
3.4 Processing Reduced Distribution Functions . . . 53
3.5 Radial Cuts through Ion Distribution Functions . . . 56
3.6 Fitting the Reduced Distribution Functions . . . 59
3.7 Instrument Limitations . . . 63
3.8 Comparing Moments and Fits of the Proton Core . . . 64
3.9 PSP Encounter 1 Overview . . . 67
3.10 Conclusions . . . 70

4 The Proton Core Population Inside Slow Solar Wind Switchbacks **71**
4.1 Introduction . . . 71
4.2 Switchback Background . . . 72
4.3 Case Study Switchback . . . 75
4.3.1 Selecting the Case Study . . . 75
4.3.2 Proton Core Temperature . . . 77
4.3.3 Reduced Distribution Functions . . . 78
4.3.4 Poynting Flux and Kinetic Energy Flux . . . 81
4.4 Other Switchbacks in Parker Solar Probe Data . . . 84
4.5 Switchback Origins . . . 85
4.6 Temperature Profiles for Switchbacks . . . 87
4.7 Conclusions . . . 88

5 Characterising Slow Alfvénic Solar Wind inside Patches at 0.13au **91**
5.1 Introduction . . . 91
5.2 Patch Background . . . 92
5.3 Data . . . 93
5.4 Encounter 4 and 5 Overview . . . 95
5.5 Identification of Patches . . . 98

5.6 Plasma Properties of the Patches . . . 99
5.7 Determining the Source Region . . . 102
5.7.1 Electron Strahl Parallel Temperature . . . 102
5.7.2 Potential Field Source Surface Mapping . . . 103
5.7.3 Magnetic Field Power Spectral Density . . . 105
5.7.4 Similarity to Fast Solar Wind . . . 105
5.7.5 Summary of Possible Source Regions . . . 107
5.8 Switchback Statistics in Patches . . . 107
5.9 Low $\alpha-$particle Abundance in E5 Patch . . . 109
5.10 Evolution of Slow Alfvénic Solar Wind . . . 112
5.11 Conclusions . . . 115

6 Quiet Periods in Low Latitude Solar Wind 117
6.1 Introduction . . . 117
6.2 Structures in the Low Latitude Solar Wind . . . 118
6.3 Data . . . 120
6.4 Identifying Quiet Periods . . . 120
6.5 Does θ_{BV} Control the Quietness? . . . 122
6.6 Quiet Period Properties . . . 125
6.7 Comparing Quiet Periods to Surrounding Wind . . . 128
6.8 Do Quiet Periods Have a Characteristic Scale? . . . 131
6.9 Occurrence of Quiet Periods in each Encounter . . . 134
6.10 Discussion . . . 135
6.11 Conclusions . . . 137

7 Conclusions 139

Bibliography 143

A Papers 165

B Symbols 166

C Acronyms 168

D Software 169

E Data **170**

F Permissions **171**

List of Figures

2.1 Solar Granulation Pattern 19
2.2 Solar Atmosphere Density and Temperature Profiles 20
2.3 Sunspots at Solar Minimum and Maximum 21
2.4 19.3nm AIA image of the Sun 23
2.5 Solutions to Parker's Solar Wind Equation 25
2.6 Schematic of the Parker Spiral 27
2.7 Proton Velocity Distribution Functions Measured by Helios 30
2.8 Electron Velocity Distribution Functions Measured by Parker Solar Probe . 31
2.9 Power Spectral Density of Magnetic Field Fluctuations in the Solar Wind . 34
2.10 In Situ Data Showing Ion Species Motion Under Alfvénic Fluctuations . . 36
2.11 Schematic of Ion Species Motion Under Alfvénic Fluctuations 37
2.12 Latitudinal Solar Wind Distribution Measured by Ulysses 38
2.13 Helios Slow Alfvénic Solar Wind Stream 39
2.14 Cross Section of a Top Hat Electrostatic Analyser 43
2.15 Fluxgate Magnetometer Design 44
2.16 Parker Solar Probe and Solar Orbiter Before Launch 46
2.17 Parker Solar Probe Orbit Trajectory 47

3.1 SWEAP Instruments on Parker Solar Probe 51
3.2 Cross Sectional Diagram of Solar Probe Cup 52
3.3 Reduced Distribution Function from Solar Probe Cup 55
3.4 Expected Solar Probe Cup Measurements for Various Magnetic Field Orientations 57
3.5 Proton Core Fits to Reduced Distribution Functions 61
3.6 Reduced Distribution Function with Proton Core, Proton Beam and $\alpha-$particle Fits 62

3.7 Time Series Comparing Proton Core Fits and Moments 65
3.8 Model Reduced Distribution Functions Comparing Moments and Fits . . . 66
3.9 Time Series of Parker Solar Probe's First Solar Encounter 68
3.10 Scatter Plots Showing the Behaviour of the Magnetic Field and Proton Core Velocity in the T-R Plane under Alfvénic Fluctuations 69

4.1 Time Series of Magnetic Field Switchbacks Measured by Parker Solar Probe 74
4.2 Time Series of Switchback Patches Measured by Parker Solar Probe 75
4.3 Time Series of a Case Study Switchback Measured During Parker Solar Probe's First Solar Encounter 76
4.4 Scatter Plot Showing the Dependence of SPC-measured Temperature on Magnetic Field Cone Angle 79
4.5 Reduced Distribution Functions Throughout a Case Study Switchback . . 82
4.6 Scatter Plot of Normal Velocity and Normalised Magnetic Field Fluctuations 83
4.7 Comparison of Switchback Temperatures Measured with the SPAN and SPC Instruments 87

5.1 Example Ion and Electron Velocity Distribution Functions Measured by SPAN 94
5.2 Time Series of Parker Solar Probe's Fourth and Fifth Solar Encounters . . 96
5.3 Time Series of Two Patches and a Quiet Period During Encounter 4 and 5 97
5.4 Histograms of Proton Core Plasma Parameters for Two Patches and a Quiet Period 99
5.5 Histograms of $\alpha-$particle Plasma Parameters for a Patch 101
5.6 Histograms of the Electron Strahl Parallel Temperature for Two Patches and a Quiet Period 104
5.7 Potential Field Source Surface Mapping for Two Patches 106
5.8 Power Spectral Density of Magnetic Field Fluctuations within Two Patches 108
5.9 Schematic Explaining How Interchange Reconnection Could Work 112
5.10 Temperature Profiles for Slow Alfvénic Solar Wind Measured by the Helios Spacecraft 113

6.1 Time Series of Structures in the Low Latitude Solar Wind 118
6.2 Scatter Plot of Magnetic Field Variance Against θ_{BV} 123
6.3 Time Series of Quiet Period and non-Quiet Period 124

6.4 Time Series of a Quiet Period Close to the Heliospheric Current Sheet in Encounter 7 126
6.5 Electron Strahl Schematic 127
6.6 Magnetic Field Orientations Within Quiet Periods 129
6.7 Histograms and Correlations of Solar Wind Parameters Inside and Outside Quiet Periods 132
6.8 Scatter Plots of Duration against Relative Spacecraft-Solar Wind Speed . . 134
6.9 Quiet Periods Surrounding HCS Crossings 136

List of Tables

3.1 Parameters Used for Fig. 3.4 58

4.1 Proton Core Parallel Temperatures Inside and Outside Switchbacks 86

5.1 Statistics of Switchbacks Identified in the E4 and E5 Patches 109

6.1 Number of Quiet Periods Identified in each PSP Solar Encounter 122

Chapter 1

Introduction

The solar wind is a collisionless plasma that expands into the heliosphere at very high velocities ($\sim$ 200-800 km/s). Its most abundant constituents are protons and electrons, but it also contains ionised helium (a few % by number density) and traces of heavier ions. The solar wind has a direct influence on the Earth, making it an important phenomenon to study. Over the last 60 years, many spacecraft have measured the solar wind in situ and measured the Sun using remote instruments. However, it is still extremely difficult to connect remote sensing observations with in situ data, particularly as the solar wind evolves significantly as it travels away from the Sun. In order to connect remote and in situ data, a better understanding of the near-Sun solar wind is needed. This is where the Parker Solar Probe mission comes in.

The Parker Solar Probe (PSP; Fox et al., 2016) mission was launched in August 2018 and since then has continued to take in situ measurements down to closer heliocentric distances. The early PSP observations indicate a highly-structured near-Sun solar wind that is very different from the solar wind measured at Earth. The high cadence of PSP data provides a fantastic opportunity to investigate these structures and to gain an understanding of the state of the solar wind as it leaves the Sun.

In this thesis, the PSP data set is exploited to develop knowledge about various solar wind structures. In Chapter 2, the relevant plasma and solar wind physics is outlined. Chapter 3 outlines a method for fitting the data from the Faraday cup on board PSP, and Chapters 4, 5, and 6 contain studies on three different structures in the near-Sun solar wind. Chapter 7 presents the conclusions of this thesis and possibilities for future work.

Chapter 2

Background

In this chapter, the relevant background information is outlined. The chapter begins with a discussion of plasma theory, focusing on the kinetic and fluid approaches. The concepts discussed here are based on two textbooks: Baumjohann and Treumann (1997) and Meyer-Vernet (2012). Key features of the Sun's atmosphere are then given before both solar wind theory and observational results are discussed. The chapter ends with an outline of common instrumentation and the current space missions providing vital data for solar wind studies.

2.1 Plasma Theory

A plasma is typically a hot, ionised gas in which particles exhibit collective behaviour due to coupled magnetic (**B**) and electric (**E**) fields. The treatment of plasmas differs from that of gases in statistical mechanics and thermodynamics due to the coupling of **B** and **E**, and because certain plasmas (e.g. space plasmas) cannot reach an equilibrium state through collisions alone. Plasmas which have a low rate of collisions are often called collisionless plasmas. The solar wind, for example, is a collisionless plasma.

There is a variety of different methods one can use when addressing plasma physics. The simplest approach, called particle orbit theory, relies on calculating the Lorentz force on a particle of mass m, charge q, and velocity **v** for given magnetic and electric fields:

$$\mathbf{F} = q(\mathbf{E} + \mathbf{v} \times \mathbf{B}). \tag{2.1}$$

This method works well when the electric and magnetic field are not significantly influ-

enced by the particle motion. However, this method is not appropriate in a plasma as **E** and **B** need to be updated as the particles move. For plasma physics, there are two commonly used self consistent approaches: the kinetic approach which focuses on particle distribution functions and the fluid approach which considers the bulk plasma properties.

2.1.1 Kinetic Regime

The kinetic approach to plasma physics considers the plasma in a statistical sense rather than tracking individual particles. This is done by considering the distribution of each particle species in 6-dimensional phase space (i.e. 3 velocity and 3 spatial dimensions). The distribution function, $f(\mathbf{r}, \mathbf{v}, t)$, of a particle species is defined as the probability of finding a given particle in a given phase space volume element.

In general, the evolution of distribution functions is given by the Boltzmann equation:

$$\frac{\partial f(\mathbf{r}, \mathbf{v}, t)}{\partial t} + \mathbf{v} \cdot \nabla_X f(\mathbf{r}, \mathbf{v}, t) + \frac{q}{m}(\mathbf{E} + \mathbf{v} \times \mathbf{B}) \cdot \nabla_v f(\mathbf{r}, \mathbf{v}, t) = \left(\frac{\partial f(\mathbf{r}, \mathbf{v}, t)}{\partial t}\right)_c, \quad (2.2)$$

where ∇_X and ∇_v are spatial and velocity derivatives, respectively. The Boltzmann equation applies to non-plasmas too, but here the Lorentz force (Eq. 2.1) is included to make it applicable to plasmas. The term on the right hand side of Eq. 2.2 contains all the changes of $f(\mathbf{r}, \mathbf{v}, t)$ due to collisions. In order to solve the Boltzmann equation, the form of this collisional term is required. However, because space plasmas are collisionless, it is possible to drop this term and get the Vlasov equation:

$$\frac{\partial f(\mathbf{r}, \mathbf{v}, t)}{\partial t} + \mathbf{v} \cdot \nabla_X f(\mathbf{r}, \mathbf{v}, t) + \frac{q}{m}(\mathbf{E} + \mathbf{v} \times \mathbf{B}) \cdot \nabla_v f(\mathbf{r}, \mathbf{v}, t) = 0. \quad (2.3)$$

The Vlasov equation describes the evolution of particle distribution functions in a collisionless plasma such as the solar wind. The electric and magnetic fields within the Vlasov equation are governed by Maxwell's equations:

$$\nabla \cdot \mathbf{B} = 0 \quad (2.4)$$

$$\nabla \cdot \mathbf{E} = \frac{\rho_c}{\epsilon_0} \quad (2.5)$$

$$\nabla \times \mathbf{B} = \mu_0 \mathbf{j} + \epsilon_0 \mu_0 \frac{\partial \mathbf{E}}{\partial t} \tag{2.6}$$

$$\nabla \times \mathbf{E} = -\frac{\partial \mathbf{B}}{\partial t}, \tag{2.7}$$

where ρ_c is the charge density and $\mathbf{j}$ is the current density.

2.1.2 Fluid Regime

The fluid regime for studying plasma physics focuses on understanding the evolution of bulk parameters. Fluid descriptions are governed by a set of equations that can be derived by taking higher order velocity moments of the Vlasov equation and by making suitable assumptions and simplifications. Here single fluid ideal magnetohydrodynamics (MHD), which is one of the most commonly used fluid plasma descriptions, is considered.

2.1.2.1 Ideal Magnetohydrodynamics

In ideal MHD, it is assumed that the plasma is a perfectly conducting fluid with no viscosity and non-relativistic velocities. Under these assumptions an ideal MHD plasma is described by the following equations (in the absence of gravity):

$$\frac{\partial \rho}{\partial t} + \nabla \cdot (\rho \mathbf{u}) = 0 \tag{2.8}$$

$$\rho \left(\frac{\partial}{\partial t} + \mathbf{u} \cdot \nabla \right) \mathbf{u} = -\nabla P + \frac{(\mathbf{B} \cdot \nabla)\mathbf{B}}{\mu_0} - \nabla \left(\frac{B^2}{2\mu_0} \right) \tag{2.9}$$

$$\frac{\partial \mathbf{B}}{\partial t} = \nabla \times (\mathbf{u} \times \mathbf{B}), \tag{2.10}$$

where $\mathbf{u}$ is the bulk plasma velocity of the single fluid, ρ is the the mass density and P is the scalar pressure. This set of 7 equations (Eq. 2.8 - 2.10) has 8 unknowns and therefore requires a closure equation. A common assumption when applying ideal MHD to the solar wind is that the plasma behaves as an adiabatic monatomic ideal gas. The ideal MHD equations can then be closed with the adiabatic energy equation:

$$\frac{d}{dt} \left(\frac{P}{\rho^\gamma} \right) = 0, \tag{2.11}$$

where $\gamma = 5/3$ for a monatomic gas.

2.1.2.2 Plasma β

The final term on the right hand side of Eq. 2.9 is the gradient of the magnetic pressure ($P_B = B^2/2\mu_0$). This means that there is both a thermal pressure (∇P) and a magnetic pressure (∇P_B) term in the momentum equation. The relative sizes of these two pressure terms vary. Therefore, the ratio of them is used to determine whether thermal or magnetic pressure controls the plasma dynamics. This ratio, called the plasma β, is defined as:

$$\beta = \frac{P}{P_B} = \frac{2\mu_0 n k_B T}{B^2}. \tag{2.12}$$

When $\beta << 1$ then the magnetic pressure dominates over the thermal pressure. However, if $\beta >> 1$, the thermal pressure dominates over the magnetic pressure.

2.1.2.3 Frozen-in Flux

An interesting result that is worth discussing with the ideal MHD assumptions is the frozen-in flux theory. In the MHD picture, a plasma with some resistivity obeys the following form of Ohm's law:

$$\mathbf{E} + \mathbf{u} \times \mathbf{B} = \eta \mathbf{j}, \tag{2.13}$$

where η is the electrical resistivity. The term on the right hand side, therefore, corresponds to the resistivity of the plasma. When this term is non-zero, it is possible for magnetic field lines to diffuse through the plasma. However, under the ideal MHD assumptions this resistivity term is zero, which means that the magnetic field can no longer diffuse. Instead the magnetic field lines are 'frozen-in' to the plasma and can be dragged around by the plasma motion (Alfvén's theorem; Alfvén, 1942). Equally, plasma from different magnetic field lines cannot mix and remains confined to its original field. The frozen-in theory forms the basis of the Parker spiral model for the interplanetary magnetic field which is discussed in Sect. 2.3.2.

2.1.2.4 Alfvén Waves

Plasmas often play host to a variety of fluctuations and waves at many scales. Within the MHD picture, a plasma can only maintain 3 distinct types of wave. These are the slow

magnetosonic, fast magnetosonic and Alfvén wave (Alfvén, 1942) modes. In this thesis, the latter are the main focus as the solar wind is full of fluctuations consistent with Alfvén waves (Belcher and Davis, 1971).

Alfvén waves are fluctuations that travel along the magnetic field (at the Alfvén speed, v_A) and are supported by the magnetic field tension, which provides the restoring force. Individual Alfvén waves are incompressible, meaning that both plasma density and $|\mathbf{B}|$ remain constant. The highly correlated fluctuations in the magnetic field and plasma velocity caused by Alfvén waves are related by:

$$\frac{\delta \mathbf{v}}{v_A} \propto \pm \frac{|\delta \mathbf{B}|}{|\mathbf{B}|}, \tag{2.14}$$

where v_A is given by (Alfvén, 1942):

$$v_A = \frac{|\mathbf{B}|}{\sqrt{\mu_0 \rho}}. \tag{2.15}$$

2.2 The Sun

The Sun is a 4.6 billion-year-old main sequence star at the centre of the solar system. It has a radius of ~695,700 km and is, on average, 1.496×10^8 km (1 astronomical unit) from the Earth. Despite this seemingly large separation, the Sun heavily influences the Earth, causing space weather events (e.g. Carrington 1859) that have the potential to damage satellite and communication systems (see e.g. Morley, 2020). Therefore, it is important to study the Sun not only from a science understanding perspective but also to aid with space weather prediction and mitigation.

The Sun, like many bodies in the solar system, consists of layers which are dominated by different processes. At the centre of the Sun is the core where hydrogen fuses to form helium, releasing an abundance of energy. The core is the densest and hottest region of the Sun and extends out to approximately $0.25 R_S$. Surrounding the core is the radiative zone where radiation dominates the transport of energy towards the surface. At 0.7-1.0R_S, bulk convective motion supersedes radiation as the dominant form of energy transfer (this is called the convective zone). This convective motion brings plasma to the photosphere (which is considered to be the Sun's surface) forming a granulation pattern that is observable with remote measurements (see Fig. 2.1). The photosphere is the deep-

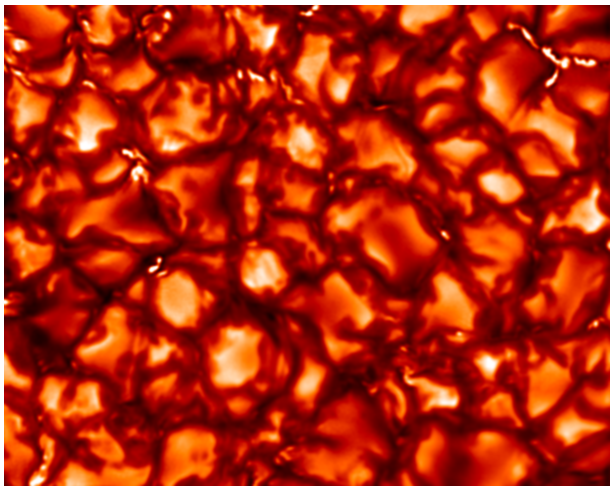


Figure 2.1: Solar granulation pattern observed by the Swedish Vacuum Solar Telescope. The brighter regions show hotter, rising plasma and the darker regions show colder, falling plasma. *Figure credit: Vasco Henriques, Henriques (2010).*

---

est layer of the Sun that is optically thin to visible light and the plasma in the photosphere has a temperature of $\sim$ 5,800 K. Above the photosphere is the solar atmosphere which consists of the chromosphere, transition region and the corona. The temperature of the solar atmosphere increases from the chromosphere to the corona, with an extremely sharp increase within the transition region (see Fig. 2.2). The temperature of the solar corona is $\sim 10^6$ K. It is currently unclear how the corona is heated to these high temperatures given its large distance from the Sun's energy source. This is often referred to as the coronal heating problem (Klimchuk, 2006).

2.2.1 The Solar Cycle and Magnetic Field

The conditions of the Sun periodically change over the course of the solar cycle which is driven by the Sun's internal dynamo. The behaviour of this cycle is closely related to the number of sunspots.

Sunspots are dark features on the photosphere (see Fig. 2.3) that have been recorded for hundreds of years (Solanki, 2003). These features can last from hours to months with the largest sunspots typically having the longest durations (Petrovay and van Driel-Gesztelyi, 1997). Sunspots are known to be associated with strong magnetic fields (e.g. Hale, 1908), and it is thought that they appear darker because these strong fields inhibit the energy transfer from convective motion at the photosphere. The number of sunspots

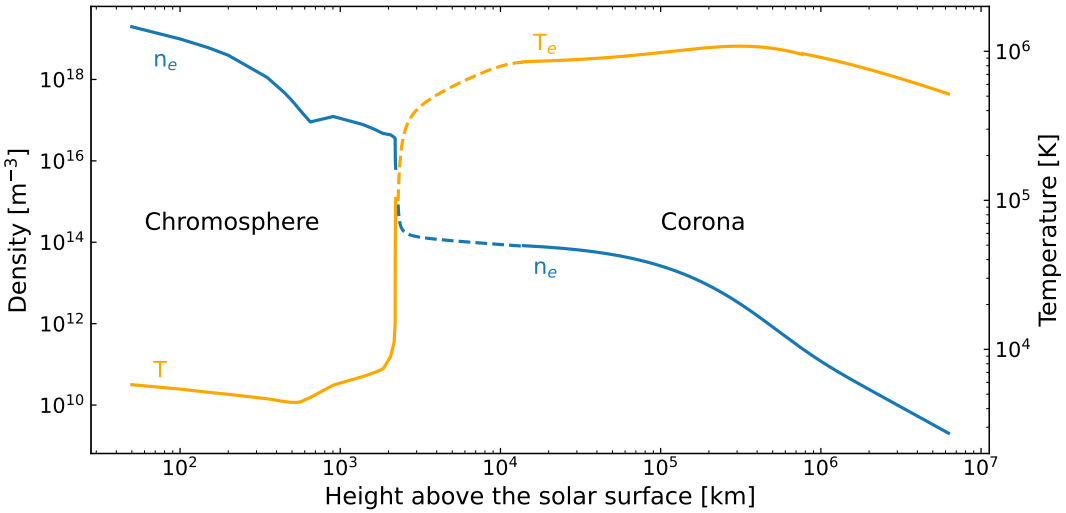


Figure 2.2: Temperature and electron density profiles in the solar atmosphere. These profiles have been constructed using various solar models following the procedure outlined in Meyer-Vernet (2012). The dashed lines are interpolations between models. *Figure credit: Meyer-Vernet (2012). Reproduced (with minor edits) with permission of Cambridge University Press through PLSclear.*

---

varies with a periodicity of approximately 11 years (Schove, 1955) and is closely related to the magnetic field of the Sun. More sunspots coincide with a greater level of solar magnetic activity (Harvey, 1992).

At solar minimum (see left panel in Fig. 2.3), the number of sunspots is very small (and often zero) and the magnetic field of the Sun is dipole-like. The magnetic field is well organised into regions of open magnetic field - field lines with one end connected to the Sun and one end extended out into interplanetary space, and closed magnetic field - field lines with both ends connected to the Sun. The open magnetic field is found at either pole and the closed field lines occupy the equatorial regions of the Sun. In this ordered configuration, the opposite polarity open field from each pole extends towards the equatorial plane where they are separated by a flat current sheet, as required by Maxwell's equations. This current sheet is referred to as the heliospheric current sheet (HCS).

As the solar activity (and sunspot number) increases, the magnetic field of the Sun becomes less ordered. At solar maximum (maximum number of sunspots, see right panel in Fig. 2.3), it is no longer well approximated by a dipole, and open and closed field lines can be found at all latitudes. The HCS no longer remains flat and close to the

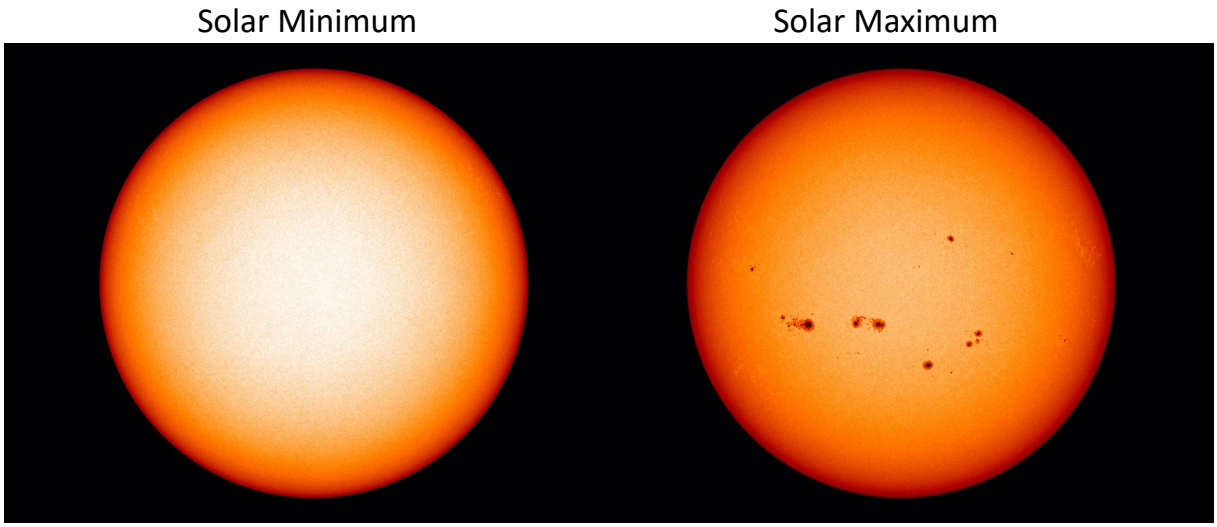


Figure 2.3: Image showing the occurrence of sunspots at solar minimum (left) and maximum (right). *Figure credit: NASA's Goddard Space Flight Center / Joy Ng, Ng (2020).*

---

equatorial plane as it has to separate a much more complex magnetic field configuration. This leads to a highly warped and structured HCS. Every 11 years during solar maximum, the polarity of the Sun reverses, leading to a 22 year magnetic field cycle. After solar maximum the solar activity decreases again. The Sun returns to solar minimum but with an opposite polarity magnetic field to the previous solar minimum.

2.2.2 Solar Features

There are many solar features that are distinguishable using remote observations. These features change and evolve as the solar cycle progresses, with some completely disappearing at solar minimum. An outline of the key features is given below.

2.2.2.1 Solar Granulation

Solar granulation is the visible component of the convective motion that brings plasma from the solar interior to the photosphere. This motion appears as irregular cells with contrasting brightness (see Fig. 2.1). The observed brightness differences are due to temperature variations between the hot, rising plasma and cold, falling plasma. Typically, these granules have a length scale of $\sim$ 1Mm and increase in size slightly during periods of higher solar activity (Ballot et al., 2021).

2.2.2.2 Coronal Holes

Coronal holes appear as darker regions in ultraviolet and X-ray images due to the reduced plasma density inside them (see Fig. 2.4). These features are associated with regions of open magnetic field and are predominantly confined to the poles during solar minimum. During solar maximum, they are found at various latitudes as the Sun's magnetic field becomes more disordered. The boundaries of coronal holes continuously change and evolve on a daily basis, and individual coronal holes can spontaneously appear or disappear throughout the solar cycle.

2.2.2.3 Active Regions

Active regions, in contrast to coronal holes, appear as very bright regions in solar images. This is a direct result of the high density within these structures. Active regions are particularly complex as they contain both open and closed magnetic field which can interact with each other and evolve. The solar cycle heavily modulates the presence of active regions, with very few occurring during solar minimum. Fig. 2.4 shows an image of the Sun with an active region shown by the white box.

2.2.2.4 Streamers

Streamers are magnetic field structures that form when open magnetic field lines rooted in different locations on the Sun converge towards each other. If these open field lines have opposite polarities then the structure is referred to as a helmet streamer, and if the open field lines have the same polarity then it is called a pseudo streamer. One of the big differences between these two types of structures is that helmet streamers, according to Maxwell's equations, must contain a current sheet that separates the opposite polarity magnetic field. This is not necessary for pseudo streamers.

During solar minimum when the solar magnetic field is well-organised and dipole-like, helmet streamers typically form from field lines rooted in opposite hemispheres. In this case, the converging open field is separated by the heliospheric current sheet and the region surrounding the HCS is commonly referred to as the streamer belt. At solar maximum, helmet streamers can form in a single hemisphere due to more complicated solar magnetic field structure. Pseudo streamers can also form during all stages of the solar cycle.

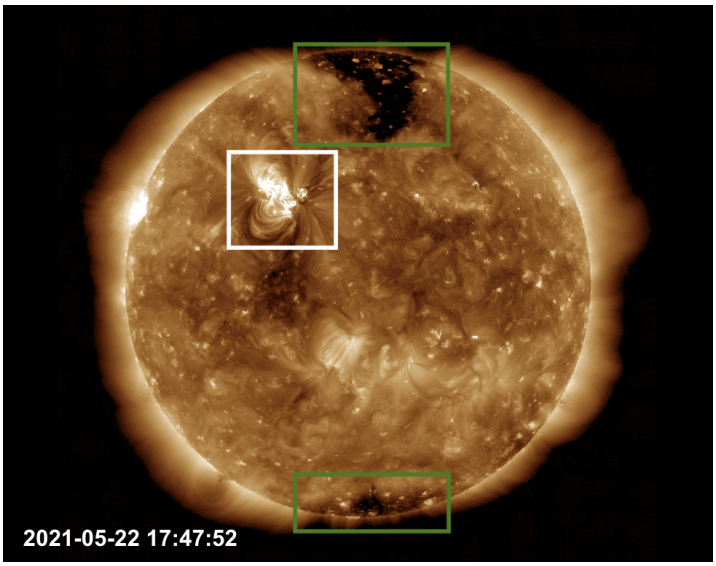


Figure 2.4: 19.3nm AIA image of the solar corona taken on May 22, 2021 at 17:47:52. The dark regions at each pole (green boxes) are coronal holes and the bright feature in the centre of the Sun (white box) is an active region. *Figure credit: NASA SDO and the AIA team.*

2.3 Solar Wind Theory

The solar wind is a collisionless plasma that expands into the heliosphere at speeds $\sim$ 400 km/s. It is an extension of the Sun's corona that fills interplanetary space. In this section, an outline of the key solar wind theory is provided before Sect. 2.4 describes solar wind observations to date.

2.3.1 Parker's Solar Wind

Early observations of the inner heliosphere revealed that comet tails were always located on the anti-sunward side of the comet (Biermann, 1957). These findings were consistent with a continual flow of material outward from the Sun (Parker, 1958). In 1958, Eugene Parker suggested that such a flow could be driven by pressure gradients using a purely hydrodynamic argument (Parker, 1958). This flow is now known as the solar wind. The key results of Parker (1958) are detailed below.

Under the assumption of a radial, spherically symmetric fully-ionised fluid it is possible to show that the two governing hydrodynamic equations are:

$$u\frac{du}{dr} = -\frac{1}{\rho}\frac{dP}{dr} - \frac{GM_S}{r^2} \tag{2.16}$$

$$\rho u r^2 = constant, \tag{2.17}$$

where u is the fluid bulk speed, ρ is the mass density, M_S is the solar mass, and $P(= 2nk_BT)$ is the total pressure. By assuming that the fluid, with average particle mass m, is isothermal (as Parker (1958) did) the bulk speed of the fluid is governed by:

$$\frac{1}{u}\frac{du}{dr}\left(\frac{u^2}{\omega^2} - 1\right) = \frac{2}{r^2}\left(r - r_c\right), \tag{2.18}$$

where:

$$r_c = \frac{GM_S}{2\omega^2} \qquad \text{critical radius} \tag{2.19}$$

and

$$\omega^2 = \frac{2k_BT}{m} \qquad \text{thermal speed.} \tag{2.20}$$

Eq. 2.18 can then be used to understand how the solar wind evolves with distance.

Eq. 2.18 is not analytically solvable, but an idea of the resulting solar wind can be obtained by considering various cases. The final conditions of the solar wind depend on the solar wind speed when it reaches the critical radius. There are two important situations to consider.

1. If, when the solar wind reaches r_c, it has a speed smaller than the thermal speed (i.e. $u < \omega$) then the maximum wind speed is limited to the wind speed at r_c. At distances larger than r_c, the wind decelerates and the bulk speed approaches 0 as $r \to \infty$. This behaviour is evident as $\frac{du}{dr} < 0$ for $r > r_c$. This solution involves a solar wind speed that initially increases with heliocentric distance, but then decreases after the critical radius. This is often referred to as a solar breeze due to its subsonic flow speed.

2. Alternatively, if the solar wind speed matches the thermal speed (i.e. $u = \omega$) as the solar wind reaches r_c, the solar wind will continue to accelerate for all heliocentric distances. In this case, $\frac{du}{dr} > 0$ for all r. The acceleration of this wind falls with heliocentric distance but never becomes negative as in scenario 1. At large heliocentric distances this solar wind has a supersonic flow speed.

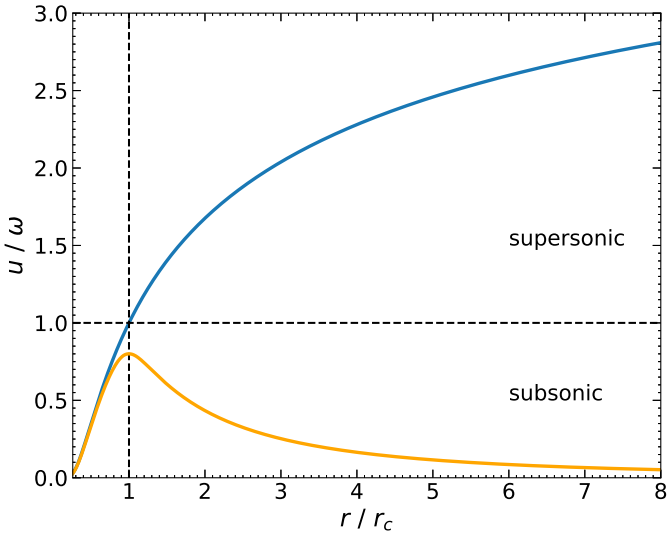


Figure 2.5: Two solutions to the solar wind equation (Eq. 2.18). The blue line shows the case of a supersonic solar wind and the orange line shows a subsonic solar breeze.

Fig. 2.5 shows the bulk velocity profile for the scenarios outlined above. These are the only two physically reasonable solutions of an escaping solar wind (i.e. no infinite acceleration and no infinite speed as $r \rightarrow 0$). Scenario 2 is directly applicable to the Sun and is consistent with the supersonic solar wind observed in the heliosphere. In fact, it was shortly after Parker's original paper that in situ measurements (e.g. Gringauz et al., 1960; Neugebauer and Snyder, 1962) confirmed Parker's theoretical predictions. The solar wind speeds that result from scenario 2 are also consistent with Biermann's cometary observations (Biermann, 1957).

It is worth noting that while the Parker model makes many simplified assumptions, such as not considering plasma waves, qualitatively it is still applicable to aspects of the solar wind. For example, work with Parker Solar Probe (see Sect. 2.6) showed that a thermally driven wind could explain the slowest solar wind speeds, but that extra acceleration is needed for faster wind (Halekas et al., 2022).

2.3.2 The Parker Spiral

Due to the frozen-in theory (see Sect. 2.1.2.3), as the solar wind expands into the heliosphere it drags the magnetic field with it. This forms an interplanetary magnetic field. By assuming a purely radial solar wind flow with speed (v_{SW}), Parker (1958) derived a

general equation for this interplanetary magnetic field. This general equation describes two parcels of plasma released from the same source at different times. Under the assumption of frozen-in magnetic field these two plasma parcels are connected by a single magnetic field line. The ratio of the azimuthal and radial magnetic field components that threads these two parcels is given by:

$$\frac{B_\phi}{B_R} = \frac{-v_{SW}}{\Omega r \cos\theta}. \tag{2.21}$$

where Ω is the rotation rate of the Sun, r is heliocentric distance and θ is the latitude. Using the conservation of magnetic flux (i.e. $B_R \propto r^{-2}$) leads to the general form of the interplanetary magnetic field:

$$B_R = B_{R,0}\left(\frac{r_0}{r}\right)^2 \tag{2.22}$$

$$B_\phi = -\frac{\Omega r \cos\theta}{v_{SW}} B_{R,0}\left(\frac{r_0}{r}\right)^2 \tag{2.23}$$

These equations describe an Archimedean spiral (see Fig. 2.6). They predict that the magnetic field should be approximately radial close to the Sun and more tangential at large heliocentric distances. They also suggest that solar wind with lower speeds will form tighter magnetic field spirals. Comparisons between these equations and the in situ measured magnetic field show good agreement, particularly in low latitude solar wind (Forsyth et al., 1995).

2.3.3 Chew-Goldberger-Low Invariants

Owing to the low collisionality of solar wind plasma, different temperatures (i.e. pressures) are often measured parallel and perpendicular to the local magnetic field. The simplification of a scalar pressure in the ideal MHD equations then breaks down and it becomes necessary to consider separate pressures parallel and perpendicular to $\mathbf{B}$. In this scenario it is possible to derive two closure equations called the double-adiabatic or Chew-Goldberger-Low (CGL) invariants (Chew et al., 1956). The CGL invariants are:

$$\frac{d}{dt}\left(\frac{p_\parallel B^2}{n^3}\right) = 0 \tag{2.24}$$

and

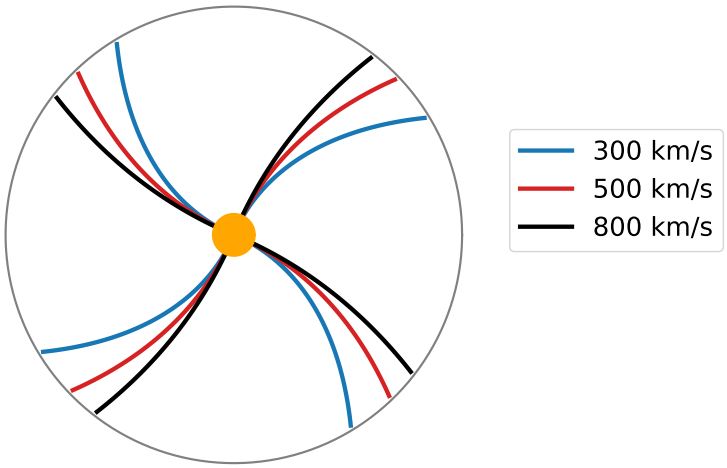


Figure 2.6: Schematic showing the theoretical shape of the interplanetary magnetic field for three solar wind speeds. This figure is based on the Parker spiral equations (Eqs. 2.22 and 2.23). The outer grey circle represents 0.5 au. The Sun's radius has been enlarged by a factor of 10 to make it clearer.

$$\frac{d}{dt}\left(\frac{p_\perp}{nB}\right) = 0. \tag{2.25}$$

These equations close the ideal MHD equations with separate perpendicular and parallel pressures, which is more representative of solar wind observations. It should be noted that in the derivation of Eqs. 2.24 and 2.25 it is assumed that the plasma varies much more slowly than the timescale of particle gyration.

Using the ideal gas equation ($P = nk_BT$), it is possible to re-write the CGL invariants in terms of the plasma temperature:

$$T_\parallel \propto \left(\frac{n}{B}\right)^2 \tag{2.26}$$

$$T_\perp \propto B. \tag{2.27}$$

These equations can then be used to predict how the plasma temperatures will evolve as the solar wind expands. For example, with a purely radial magnetic field ($B \propto r^{-2}$), as expected close to the Sun, and a constant radial solar wind velocity ($n \propto r^{-2}$), the temperatures scale as:

$$T_{\parallel} = constant \tag{2.28}$$

$$T_{\perp} \propto r^{-2}. \tag{2.29}$$

Interestingly, in situ measurements of the solar wind typically deviate from CGL predictions, with $T_{\parallel}$ decreasing faster and $T_{\perp}$ decreasing more slowly than expected. This suggests that an adiabatic description of solar wind expansion is not accurate and additional heating or cooling mechanisms are needed (see Sects. 2.4.7 and 5.10).

2.4 Solar Wind Observations

Since the first solar wind measurements were taken in the 1960s (e.g. Gringauz et al., 1960; Neugebauer and Snyder, 1962) many other missions, including Helios (Marsch et al., 1982*b*,*a*), WIND (Ogilvie et al., 1995), and Ulysses (Balogh et al., 1992; Bame et al., 1992), have observed the solar wind. These missions have been key to developing our knowledge of the solar wind and how it evolves. Here an outline of our current understanding of the solar wind is given.

2.4.1 Velocity Distribution Functions

In space physics, it is common to focus on 3D velocity distribution functions (VDFs) rather than full six-dimensional phase space distributions. The treatment of plasma VDFs is slightly different to gases for which it is common to fit a Maxwellian distribution. This difference arises because space plasmas are not regulated by collisions, but instead by Coulomb interactions and plasma instabilities. This often results in space plasmas having different temperatures parallel ($T_{\parallel}$) and perpendicular ($T_{\perp}$) to the background magnetic field (Marsch et al., 1981). These temperatures represent the spread of particle velocities in the VDF. To account for this when fitting, a bi-Maxwellian distribution can be used for each particle species of mass m:

$$f(\mathbf{v}) = \frac{n}{T_{\perp} T_{\parallel}^{1/2}} \left(\frac{m}{2\pi k_B}\right)^{3/2} \exp\left(-\frac{m}{2k_B}\left[\frac{(\mathbf{v}_{\perp} - \mathbf{v}_{\perp,0})^2}{T_{\perp}} - \frac{(v_{\parallel} - v_{\parallel,0})^2}{T_{\parallel}}\right]\right). \tag{2.30}$$

From this fit the particle number density (n), bulk velocity parallel ($v_{\parallel,0}$) and perpendicular ($\mathbf{v}_{\perp,0}$) to the magnetic field, and temperatures can be found. In practice, VDFs in the solar wind are rarely perfectly described by a Maxwellian (or bi-Maxwellian) and often exhibit more non-equilibrium features such as large differential velocities and additional populations. Fitting Maxwellians to these distributions is therefore an effective tool, but addressing the VDFs themselves is also essential (e.g. see Chapter 4).

2.4.1.1 Ion Velocity Distribution Functions

Solar wind ion VDFs usually contain both proton and $\alpha-$particle populations, reflecting the composition of the corona. In fact, there is often a proton core, proton beam and an $\alpha-$particle population (Hundhausen et al., 1967; Feldman et al., 1973). This $\alpha-$particle population can sometimes also be subdivided into a core and beam (Asbridge et al., 1974; Feldman et al., 1974). The proton core contains the majority of protons ($\sim 90\%$ by number density) and is therefore the most important ion population for solar wind dynamics. The proton beam, on the other hand, is smaller and often travels faster than the core (Hundhausen et al., 1967; Marsch et al., 1982*b*). The exact origins of the proton beam are still unknown. The velocity vector describing the difference in proton core and beam velocities is always aligned (anti-)parallel to the local magnetic field (Hundhausen et al., 1967) and the magnitude of this vector is typically $\sim v_A$ (i.e. the local Alfvén speed, see Sect. 2.1.2.4; Marsch et al., 1982*b*). There are times when the proton core is faster than the beam due to Alfvénic fluctuations, but the explanation of these is covered in Chapter 3. The $\alpha-$particle population is also field-aligned and faster than the proton core (Hirshberg et al., 1974; Asbridge et al., 1976). The drift between the proton core and $\alpha-$particles is often $\sim v_A$ as well (Marsch et al., 1982*a*). If the data resolution is high enough, it is possible to fit Eq. 2.30 to each individual particle population.

Fig. 2.7 shows a selection of Helios-measured proton VDFs in the plane containing the local magnetic field. The colours show the relative number density of ions in each plot (red is largest, blue is smallest). Approximately circular contours indicate isotropic temperatures (i.e. $T_\perp = T_\parallel$) and elliptical contours indicate anisotropic temperatures (i.e. $T_\perp \neq T_\parallel$). Panels A and D show examples of isotropic proton core populations with no clear beam population. The remaining panels show proton cores with various temperature anisotropies and field-aligned populations. Each field-aligned population is likely a proton beam. The evidence for these field-aligned populations is a bulge in the

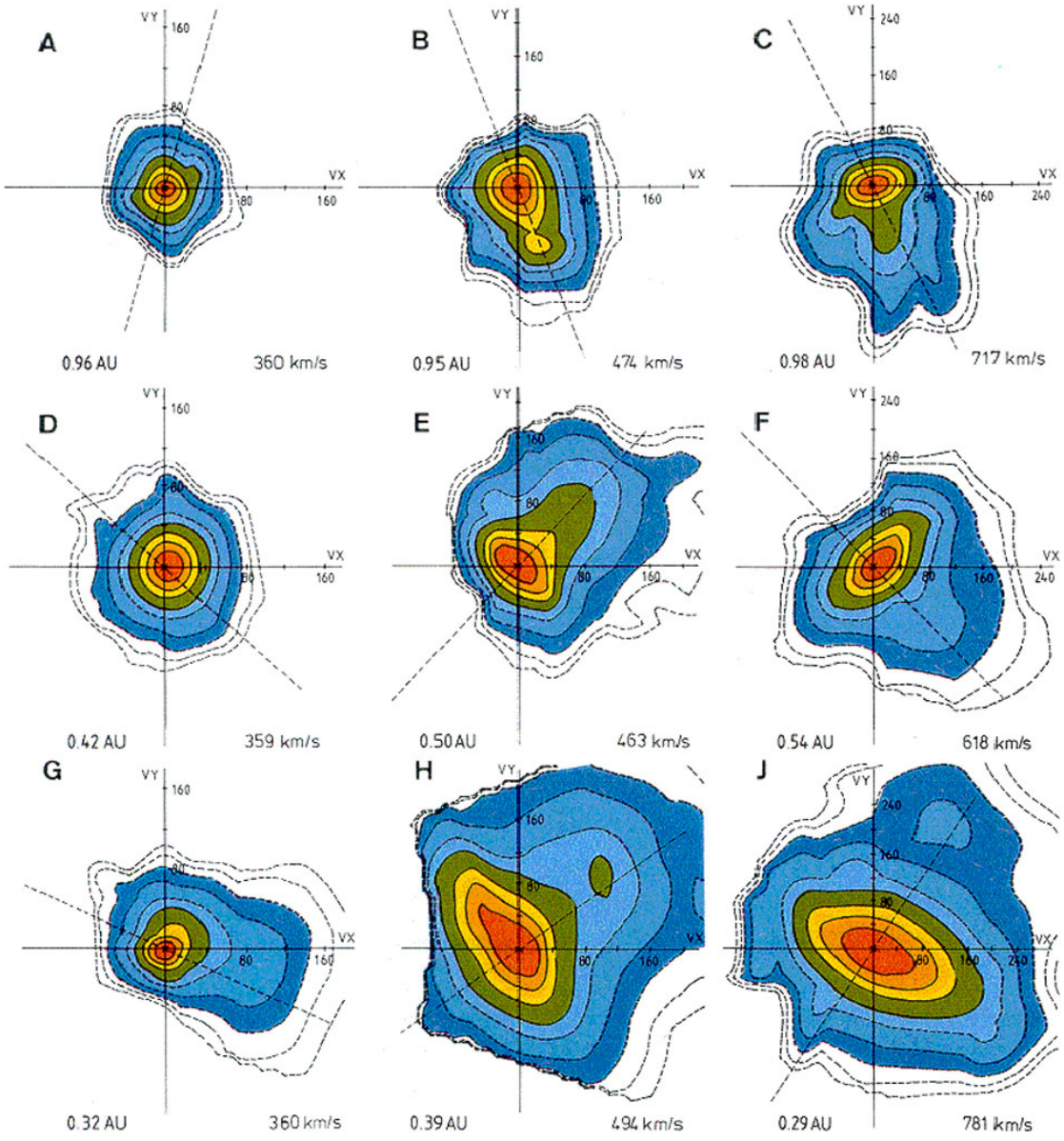


Figure 2.7: Example proton velocity distribution functions measured by the Helios spacecraft. For each distribution, the heliocentric distance and solar wind speed is labelled at the bottom. The colour gradient goes from red (the largest density) to blue (smallest density). The straight dashed black line shows the local magnetic field orientation. *Figure credit: Marsch (2012). ©Springer Science Business Media B.V. (2010). Reproduced with permission. Figure is not included in any open access license of this thesis.*

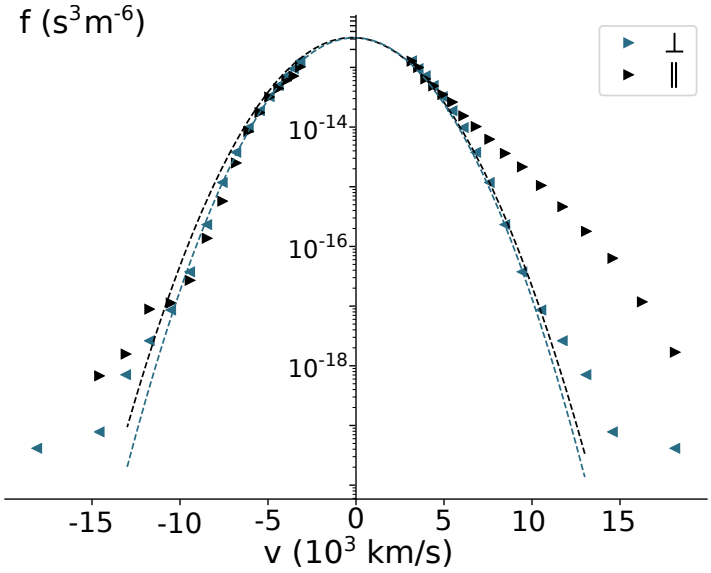


Figure 2.8: Example cuts through an electron VDF measured by Parker Solar Probe in the near-Sun solar wind. The black arrows show the cut through the distribution parallel to the magnetic field and the blue arrows show a cut perpendicular to the magnetic field. The direction of the triangles indicates which instrument on board PSP measured the data: right pointed triangles were measured by SPAN-A and left pointed triangles by SPAN-B (see Sect. 3.2 for more details on the instruments on board PSP). The dashed blue and black lines show the Maxwellian fit to the electron core for the perpendicular and parallel cuts, respectively. *Figure credit: Berčič et al. (2020). ©AAS. Reproduced with permission.*

---

contours on one side of the core which is roughly centred on the magnetic field (dashed line). More information on determining and fitting field-aligned populations is given in Chapter 3.

2.4.1.2 Electron Velocity Distribution Functions

Electron VDFs, in a similar way to ion VDFs, typically have three main populations (e.g. see Pilipp et al., 1987, and references therein). The electron core constitutes the bulk of the electrons and is reasonably well described by a Maxwellian or bi-Maxwellian distribution (e.g. Pierrard et al., 2016). As electrons in the solar wind are more collisional than ions, the electron core tends to have a lower temperature anisotropy than the proton core (Montgomery et al., 1968). The second electron population is called the halo and has no clear counterpart in ion VDFs. The halo consists of the electrons which are faster than the core electrons and can also display a temperature anisotropy (Feldman et al.,

1975). The final electron population is the strahl, which is similar to the proton beam in the sense that it is faster than the electron core population and field-aligned (e.g. Feldman et al., 1978*b*). The strahl electrons are collimated along the magnetic field and have little interaction with the surrounding plasma as they leave the Sun. This means the strahl temperature could be a good proxy for the solar wind source temperature (Jockers, 1970; Lemaire and Scherer, 1970, 1971; Maksimovic et al., 1997; Berčič et al., 2020).

Fig. 2.8 shows 1D cuts through an electron VDF measured in the solar wind. The cut perpendicular to the magnetic field (blue points) is symmetrical. The parallel cut (black points), however, has a high velocity population on the right hand side. This is the field-aligned electron strahl population. The electron halo can be seen where the data deviate from the Maxwellian electron core fits (dashed lines) at $\pm 15 \times 10^3$ km/s.

2.4.1.3 Deriving Macroscopic Quantities

Aside from fitting analytical functions to VDFs, it is also possible to extract bulk parameters by taking higher order moments of the distribution function. By taking the zeroth, first, second and third order moments, it is possible to obtain the particle number density, bulk velocity, pressure tensor and heat flux tensor, respectively:

$$n = \int f(\mathbf{v}) d^3v \tag{2.31}$$

$$\mathbf{u} = \frac{1}{n} \int \mathbf{v} f(\mathbf{v}) d^3v \tag{2.32}$$

$$\mathbf{P} = m \int (\mathbf{v} - \mathbf{u})(\mathbf{v} - \mathbf{u}) f(\mathbf{v}) d^3v \tag{2.33}$$

$$\mathbf{Q} = m \int (\mathbf{v} - \mathbf{u})(\mathbf{v} - \mathbf{u})(\mathbf{v} - \mathbf{u}) f(\mathbf{v}) d^3v. \tag{2.34}$$

2.4.2 Composition

Using data from velocity distribution functions makes it possible to understand the composition of the solar wind. For example, it is known that the solar wind consists predominantly of protons and electrons, but also contains smaller fractions of heavier ions. The second most abundant ion after hydrogen (protons) is ionised helium ($\alpha-$particles), which

is often quantified using the $\alpha-$particle abundance ($A_\alpha = n_\alpha/n_p$). A_α is typically between 3-6% in the solar wind (Ogilvie and Wilkerson, 1969; Robbins et al., 1970; Neugebauer, 1981; Alterman et al., 2021), but it varies over the solar cycle and for different solar wind speeds. For example, during solar minimum A_α is approximately 1-2% in solar wind with speeds < 400 km/s and approximately 4-5% for wind with speeds > 600 km/s (Bame et al., 1977; Feldman et al., 1978*a*; Hirshberg et al., 1972; Kasper et al., 2007, 2012). At solar maximum, however, this dependence on wind speed no longer holds and $A_\alpha \sim$ 4-5% for all wind speeds (Kasper et al., 2007, 2012). The cause of this variation in A_α over the solar cycle and for different wind speeds is still debated, but could be due to the solar wind source regions and/or acceleration processes (see Sect. 5.9 for a more detailed discussion).

Aside from $\alpha-$particles, there are other heavier ions in the solar wind plasma. These include carbon and oxygen. As these heavier ions only contribute small fractions to the plasma, they have limited influence on the solar wind dynamics, but can be useful tracers of solar wind source regions (Bochsler, 2007). In this thesis, only protons and $\alpha-$particles are considered as Parker Solar Probe does not have a heavy ion instrument.

2.4.3 Alfvén Waves in the Solar Wind

The magnetic field in the solar wind fluctuates on a variety of timescales. In order to describe the power associated with each frequency, magnetic field power spectra are used (see Fig. 2.9). The magnetic field fluctuations in the solar wind transfer energy from the largest scales (injection range) to the smallest scales (dissipation range), where the fluctuations can then dissipate and heat the plasma. Between the injection and dissipation ranges is the inertial range. In the inertial range the cascade of energy from larger to smaller scales causes the magnetic field fluctuations to follow a power law dependence. This power law is often used to distinguish between different types of solar wind and source regions (e.g. Chen et al., 2021). In this thesis, the power law dependence is used for this reason and further details of solar wind turbulence are left to other literature.

Solar wind observations show that the inertial range is filled with fluctuations that are consistent with Alfvén waves (Belcher and Davis, 1971). These fluctuations are associated with highly correlated magnetic field and velocity vectors, which is expected for Alfvén waves (see Sect. 2.1.2.4). The magnetic field fluctuations caused by Alfvén waves in the solar wind are of the same order as the field magnitude (non-linear Alfvén waves), which

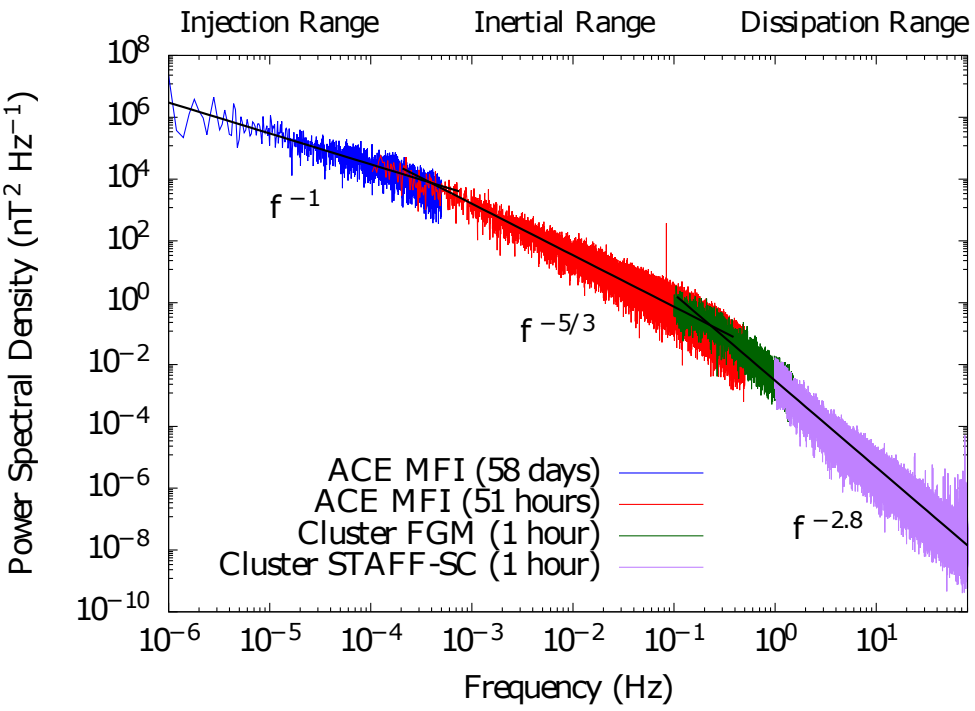


Figure 2.9: Power spectral density of magnetic field fluctuations measured by various spacecraft (shown by different colour lines) in the solar wind. For each range of fluctuations, power laws have been fitted (shown in black) and labelled on the figure. *Figure adapted from Verscharen et al. (2019).*

---

can lead to local reversals in the magnetic field polarity (called switchbacks, see Chapter 4; e.g. Bale et al., 2019). Interestingly, the broad spectrum of Alfvén waves observed in the solar wind displays a similar property to individual Alfvén waves: the plasma remains incompressible (i.e. n and $|\mathbf{B}|$ remain constant). This results in the magnetic field vector being confined to the surface of a sphere (i.e spherically polarised waves) with radius $|\mathbf{B}|$ and centre (0, 0) nT. The presence of Alfvén waves in the solar wind causes the magnetic field vector to fluctuate with the magnitude of that vector remaining constant to within $\sim 15\%$ over several hours.

Alfvén waves also have a direct influence on the solar wind velocity. For example, Matteini et al. (2014) argued that the increase in solar wind speed for increasing angles between the magnetic field and radial direction was a direct result of anti-sunward Alfvénic fluctuations. Further work has since shown that the proton core velocity (which is approximately equal to the solar wind bulk velocity) depends heavily on the magnetic field orientation, whereas the $\alpha-$particle velocity remains constant (Matteini et al., 2015*b*).

This behaviour is shown in the left panel of Fig. 2.10, using the normal components of the velocity and magnetic field normalised to the local Alfvén speed and magnetic field magnitude, respectively. The x-axis is effectively a measure of the angle of the local magnetic field from the 'background' field.

These velocity changes are consistent with a sphere in velocity space analogous to the magnetic field sphere (see right panel of Fig. 2.10). In this case, the proton core velocity changes due to the presence of Alfvénic fluctuations but remains confined to the surface of a sphere (which is a circle in the 2D plane of Fig. 2.10) with radius $\sim v_A$ centred on $\sim$ (0, 850) km/s. The $\alpha-$particles are located at the centre of this sphere and do not exhibit significant velocity changes. This suggests that Alfvénic fluctuations, to first order, cause a rigid velocity space rotation about the centre of the sphere (Matteini et al., 2015*b*). As the proton core velocity (and therefore the solar wind bulk velocity) is lower than the pivot of this rotation, its velocity is enhanced. The $\alpha-$particles, however, remain at approximately the same velocity as they are found very close to the pivot point (Matteini et al., 2015*b*). Fig. 2.11 summarises this picture and shows how the velocity of the proton core (yellow), $\alpha-$particles (blue) and bulk solar wind speed (black) change as the magnetic field vector rotates.

The exact centre and radius of this velocity circle are still unknown. The centre is typically $\sim v_A$ faster than the proton core along the local magnetic field direction however, this is not always the case. It is currently unclear whether the centre of the sphere depends on the theoretical local Alfvén speed or the local phase speed (which is an empirical estimation of the local Alfvén speed). These two quantities are often similar in the young solar wind, but they can deviate significantly from one another further from the Sun (e.g. Matteini et al., 2014). For further discussion, see Sect. 4.3.3.

2.4.4 Categorisation

In an attempt to further understand the solar wind, it is often classified into different modes. Historically, the solar wind was split purely on its bulk velocity into slow (< 400 km/s) and fast (> 600 km/s) wind. This classification, although simple, has proved useful in many studies and has contributed to a better understanding of the solar wind. For example, the fast wind is known to be hotter, have a larger ion temperature anisotropy, lower density, and exhibit less variability than the slow solar wind (e.g. Marsch et al., 1982*b*). The fast wind has also been found to have a higher correlation between magnetic

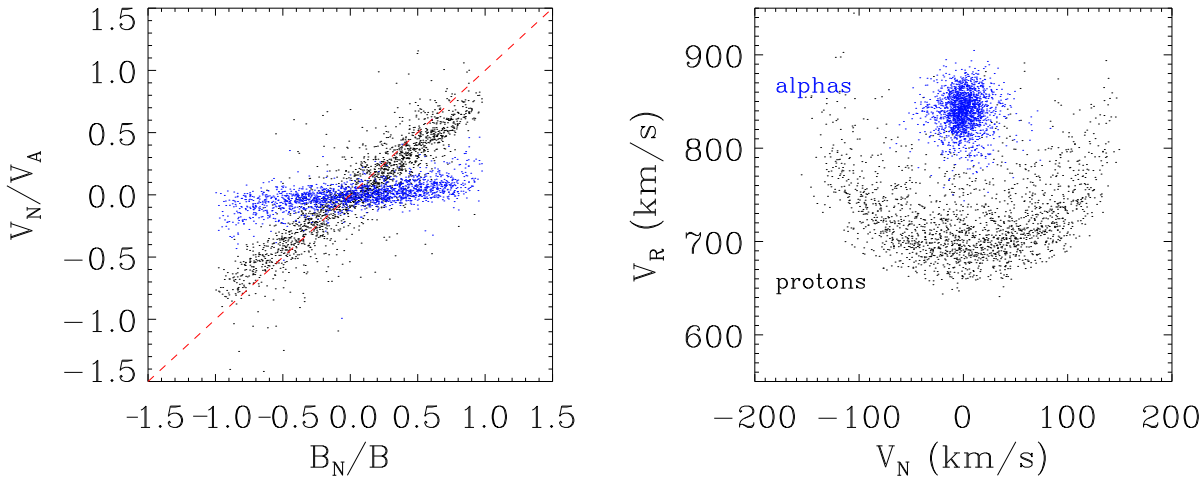


Figure 2.10: (left) Scatter plot of the normal components of the velocity and magnetic field for protons (black) and $\alpha-$particles (blue) normalised by the local Alfvén speed and the total magnetic field magnitude, respectively. The red dashed line shows the gradient which corresponds to the local Alfvén speed. (right) Scatter plot of the radial and normal velocity components for protons and $\alpha-$particles. The data used to make this figure were measured by the Helios spacecraft during a fast solar wind stream. *Figure credit: Matteini et al. (2015b). ©AAS. Reproduced with permission.*

---

field and velocity fluctuations (i.e. it is more Alfvénic). These fluctuations are larger than in slow wind resulting in more power within the power spectra (see Sect. 2.4.3 for an explanation of power spectra). During solar minimum, fast wind is typically found at higher latitudes, whereas slow wind is located towards the solar equator. However, the picture is more muddled at solar maximum (see Fig. 2.12). Fast solar wind is known to come from coronal hole regions (e.g. Krieger et al., 1973; Nolte et al., 1976; Sheeley et al., 1976; Cranmer, 2009), but the origin of slow solar wind is less clear. It is possible that the greater variability seen in the slow wind is due to multiple source regions each releasing slow wind with different characteristics. There is currently a range of candidates for slow wind source regions (see e.g. Abbo et al., 2016) including: coronal hole boundaries (Wang and Sheeley, 1994; Neugebauer et al., 1998), the streamer belt (e.g. Wang et al., 2000), the S-web (Antiochos et al., 2011), active regions (Neugebauer et al., 2002; Harra et al., 2008), or the quiet Sun (Viall and Borovsky, 2020). It is possible that the difficulties in associating slow solar wind to a particular source region is driven by the inappropriate classification based purely on bulk velocity. Therefore, a more refined categorisation may

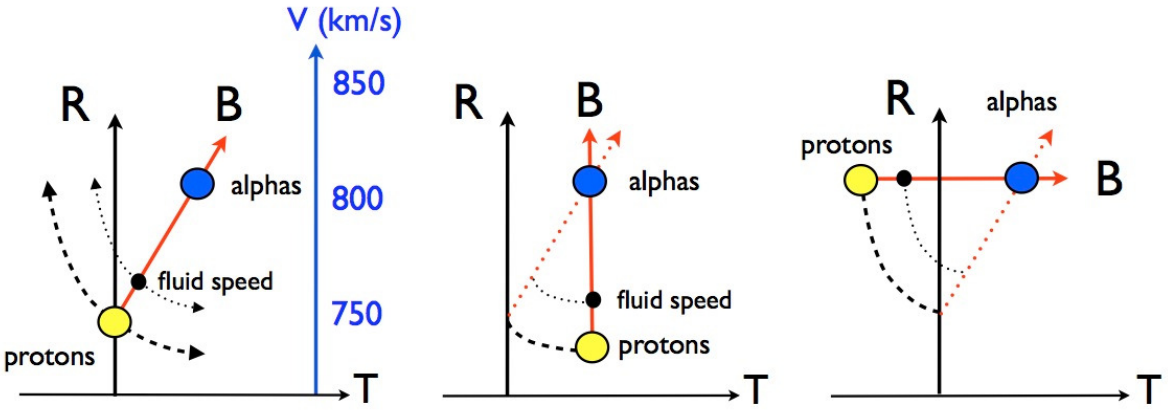


Figure 2.11: Schematic showing the motion of the proton core and the $\alpha-$particles under Alfvénic fluctuations. The proton core (yellow circle) is confined to the perimeter of a circle (black dashed line) centred on the local Alfvén/phase speed. In three dimensions this corresponds to the surface of a sphere, but only two dimensions are shown here for clarity. The $\alpha-$particles (blue circle) travel at the local Alfvén/phase speed and therefore do not experience a rotation. The red arrows show the magnetic field orientation in each case. The total fluid speed is shown by the black circle. *Figure credit: Matteini et al. (2015b). ©AAS. Reproduced with permission.*

---

help.

There have been many attempts to improve the way in which solar wind is split. Zhao et al. (2009) suggested that solar wind should be classified based on its elemental composition. The idea behind this is that the composition of solar wind is frozen-in at the source and not altered by processes and in situ interactions. One impracticality with this classification method is that not all spacecraft have composition instruments on board, meaning that not all studies could utilise this categorisation. Other studies have tried classifying the solar wind using entropy, Alfvén speed and the proton temperature (Xu and Borovsky, 2015), or by applying machine learning techniques (Camporeale et al., 2017; Li et al., 2020). Given the large amounts of data in space physics, machine learning does offer a scalable method for classifying the solar wind. However, machine learning methods can also be less interpretable. This thesis uses a simpler classification suggested by D'Amicis and Bruno (2015), which separates the slow wind based on its Alfvénicity.

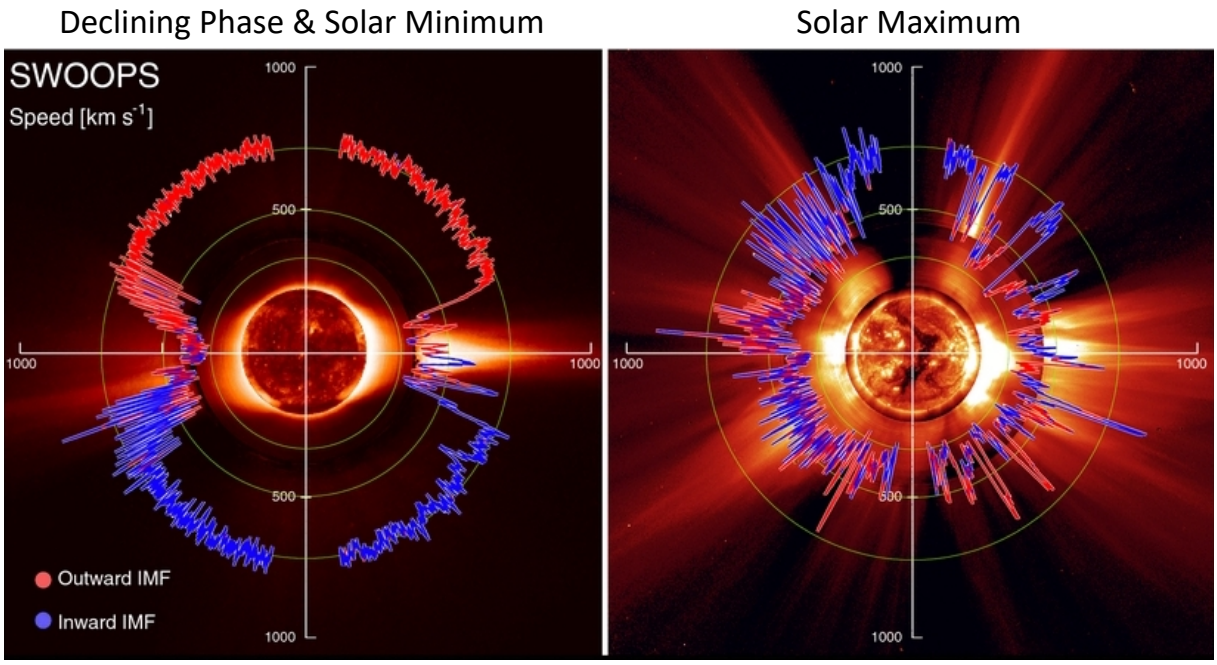


Figure 2.12: Summary of the solar wind observed by the Ulysses spacecraft during a polar orbit at solar minimum (left) and solar maximum (right). Red shows anti-sunward magnetic field and blue shows sunward magnetic field. The distance of the lines from the centre indicates the solar wind speed. *Figure credit: McComas et al. (2003). ©AGU. Reproduced with permission.*

2.4.5 Slow Alfvénic Solar Wind

Whilst the fast solar wind is always highly Alfvénic, the slow wind is not as well organised. The slow wind can have both low and high Alfvénicity (D'Amicis and Bruno, 2015), suggesting a more bimodal picture than fast wind. The earliest measurements of a highly Alfvénic slow wind stream were made during the 1970s by the Helios mission (Marsch et al., 1981). However, it was not until much later on that Alfvénicity was used as a way to subdivide the slow wind. D'Amicis and Bruno (2015) suggested that splitting the slow solar wind into an Alfvénic and a non-Alfvénic component may improve understanding of slow solar wind origins.

The slow Alfvénic wind displays similar properties to fast solar wind (e.g. Perrone et al., 2020). For example, both slow Alfvénic and fast wind have a large differential velocity between the protons and $\alpha-$particles (Berger et al., 2011; Alterman et al., 2018; Stansby et al., 2020*a*). It is possible that the shared characteristics of high Alfvénicity and large $\alpha-$proton drift velocities indicates commonality in the source regions of fast

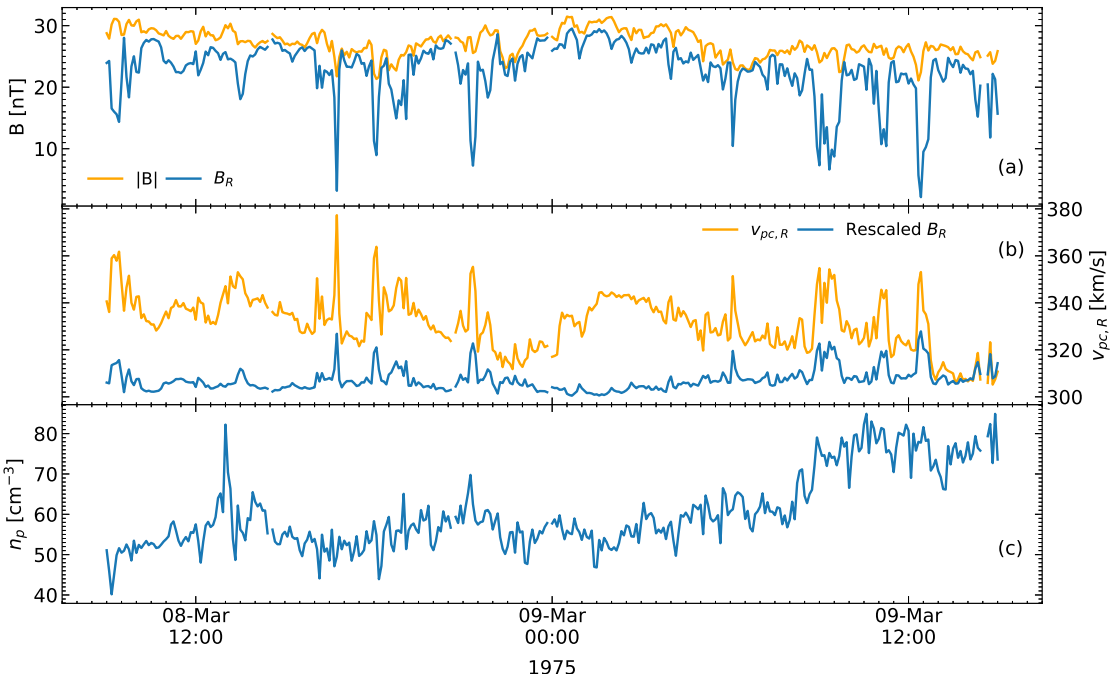


Figure 2.13: Time series of a slow Alfvénic solar wind stream measured by the Helios mission in 1975. The panels show: (a) the magnetic field magnitude and radial component, (b) the proton core radial velocity and the re-scaled radial component of the magnetic field, and (c) the proton number density. B_R has been re-scaled to show the correlation between v_R and B_R.

---

and slow Alfvénic wind. In fact, it has been suggested that slow Alfvénic solar wind may come from the boundaries of coronal holes (D'Amicis and Bruno, 2015; Stakhiv et al., 2015, 2016). In this case, the difference in the bulk speed between slow Alfvénic and fast wind may be due to the expansion of individual flux tubes as the solar wind travels out into the heliosphere (Levine et al., 1977; Wang and Sheeley, 1990; Wang et al., 1997). Fig. 2.13 shows an example slow Alfvénic solar wind stream measured by the Helios mission.

The non-Alfvénic slow wind, on the other hand, is distinct from fast solar wind. It often displays variable mass fluxes (Stansby et al., 2019*a*) which could indicate a less stable source region such as transients in the streamer belt (Einaudi et al., 1999; D'Amicis and Bruno, 2015; Stansby et al., 2019*a*), or active regions (Neugebauer et al., 2002; Harra et al., 2008; D'Amicis and Bruno, 2015). The relative amount of each type of solar wind likely varies throughout the solar cycle, along with the associated source regions. For example, during solar minimum when there are very few active regions, it is unlikely that active regions contribute a significant fraction of the solar wind (Stansby et al., 2021).

The picture of Alfvénic and non-Alfvénic wind can become less clear with increasing heliocentric distance. This is because the solar wind evolves and interacts as it expands into the heliosphere. A consequence of this is that it can be more difficult to distinguish the different types of solar wind at 1 au.

Overall, the idea of Alfvénic and non-Alfvénic slow wind offers a good avenue to further understand the origin of the solar wind. As this categorisation is relatively new, more studies are needed to truly characterise these types of wind (see Chapter 5 for a study on slow Alfvénic wind with PSP data). The currently active solar wind missions outlined in Sect. 2.6 provide a great opportunity for such studies.

2.4.6 Proton Temperature-Velocity Relationships

The solar wind has long been known to exhibit a positive correlation between proton temperature and velocity when averaged over timescales of a few hours and multiple streams (Burlaga and Ogilvie, 1970). However, the cause of this temperature-velocity ($T_p - v$) relationship remains unclear. The $T_p - v$ relationship is not particularly sensitive to the solar cycle (Burlaga and Ogilvie, 1973; Lopez and Freeman, 1986) but it does have distinct behaviours for solar wind with speeds above and below 500 km/s (Lopez and Freeman, 1986). This difference between slow and fast wind could be an indication of varying processes within the young solar wind. The $T_p - v$ relation does not remain constant with heliocentric distance, but instead changes as the solar wind expands (Elliott et al., 2012). In fact, Perrone et al. (2019*b*) showed using Helios data that the $T_p - v$ relationship evolves with heliocentric distance within the same stream of plasma. This change for a single stream could be a direct result of the expansion of flux tubes (Perrone et al., 2019*b*).

The reason a $T_p - v$ relationship exists within the solar wind is actively debated. For example, Matthaeus et al. (2006) has suggested that under specific conditions solar wind turbulence could lead to the observed relationship between temperature and velocity. On the other hand, Démoulin (2009) argues against turbulence as the driver and suggests instead that the processes governing heating and acceleration in the young solar wind are responsible. Démoulin (2009) notes that the observed $T_p - v$ relationship could be caused by numerous heating mechanisms, and therefore cannot be used solely to infer the exact heating/acceleration mechanisms occurring close to the Sun.

2.4.7 Radial Plasma Evolution

Another key observation about the solar wind is that it evolves with heliocentric distance, meaning that the solar wind measured at the Earth is very different from the solar wind that left the Sun. The scaling of key parameters is discussed below.

In a solar wind that expands outwards with a constant, purely-radial velocity, the number density is expected to fall as r^{-2}. In situ observations of the solar wind frequently show good agreement with this prediction (Hellinger et al., 2011, 2013; Perrone et al., 2019*a*) and small differences can be explained by acceleration or deceleration of the solar wind through interactions with other streams (Hellinger et al., 2011).

Comparing the behaviour of $|\mathbf{B}|$ to predictions is slightly more complex as the magnetic field consists of components that scale differently with heliocentric distance. The magnitude of a purely radial magnetic field, for example, should scale as r^{-2}, whereas a purely tangential (or normal) magnetic field should scale as r^{-1}. In the solar wind, $\mathbf{B}$ consists of radial, tangential and normal components (see Parker spiral in Sect. 2.3.2) and it is the relative size of these components that determines the scaling. Close to the Sun $\mathbf{B}$ is approximately radial and should scale as r^{-2}, but at Earth $\mathbf{B}$ has radial and tangential components that are roughly equal in magnitude and so should scale closer to $r^{-1.5}$. Using Helios measurements between 0.3 and 1 au, it has been shown that $|\mathbf{B}| \sim r^{-1.6}$ (Hellinger et al., 2011, 2013).

Finally, the behaviour of the parallel and perpendicular temperatures can be considered. A rough prediction of temperature scalings can be made by assuming that the solar wind expands radially as an adiabatic gas with a single temperature ($T \sim r^{-4/3}$, e.g. Baumjohann and Treumann, 1997). However, this fails to capture that, due to low collisionality, the solar wind exhibits different temperatures perpendicular and parallel to the magnetic field. Instead, the CGL adiabatic invariants (Eqs. 2.26 and 2.27) can be used to predict the temperature evolution. There have been numerous studies that have shown that solar wind observations differ from the predicted behaviour of an adiabatic expansion (Marsch et al., 1982*b*; Hellinger et al., 2011, 2013). In fact, $T_\parallel$ is often found to decay faster with heliocentric distance than predicted while $T_\perp$ decays more slowly (Marsch et al., 1982*b*; Hellinger et al., 2011, 2013). This suggests that there is a cooling mechanism acting on $T_\parallel$ and a heating mechanism for $T_\perp$ (see Sect. 5.10).

2.5 Instrumentation

In order to take reliable measurements of the solar wind many different instruments are used. In this section the operational principles behind electrostatic analysers and fluxgate magnetometers are explained. A further instrument, called a Faraday cup, is extensively detailed in Chapter 3. The following explanations are based on the work by Verscharen et al. (2019).

2.5.1 Electrostatic Analysers

Electrostatic analysers (ESA) are used to measure the distribution of particles within the solar wind. These instruments have been used on many spacecraft previously (e.g. Lin et al., 1995; Halekas et al., 2015; Kasper et al., 2016) and often differ in design based on the science requirements. However, the basic operational principles of all ESAs are the same.

Fig. 2.14 shows the cross section of a basic top hat electrostatic analyser. The instrument consists of an aperture where particles can enter, a set of curved plates (often called collimator plates), and a detector for measuring particle counts. A DC voltage is applied to the collimator plates which creates an electric field between them. This electric field deflects incoming particles so that only the ones reaching the detector have a specific energy-to-charge ratio. By changing the voltage applied to the plates the required energy-to-charge ratio to reach the detector can be adjusted. This allows the instrument to measure particle counts for many energy-to-charge ratios. For each voltage the energy-to-charge ratio required to reach the detector is not a single value. Instead there is a small range of ratios which is determined by the separation between the two collimator plates. ESAs measure the counts of incoming particles for a combination of energy-to-charge ratios, elevation angles and azimuthal angles. This allows a 3D particle distribution function to be reconstructed from the data. One drawback of this ESA design is that it is not possible to accurately distinguish between different particle species in the detector counts. Therefore, ESAs can be equipped with a time-of-flight measurement to differentiate particles. The plasma data used in Chapters 5 and 6 were measured by an ESA.

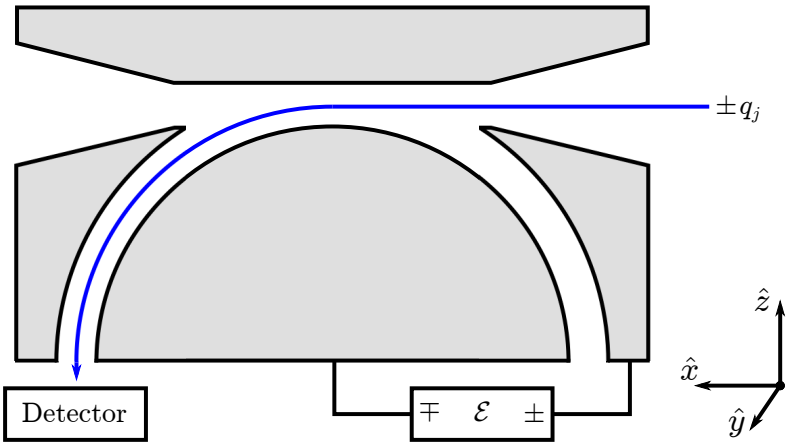


Figure 2.14: Cross section of a top hat electrostatic analyser. The instrument has three main parts: the aperture, the curved collimator plates, and the detector. Particles enter the instrument through the aperture before getting deflected by electric fields between the two collimator plates. If particles have a specific energy-to-charge ratio (that depends on the electric field and the collimator plates' radius of curvature) they will reach the detector and be measured. *Figure credit: Verscharen et al. (2019).*

2.5.2 Fluxgate Magnetometers

Fluxgate magnetometers are commonly used to measure magnetic fields in the solar wind. Typically, they are useful for lower frequency measurements (<10 Hz) and search coil magnetometers (not discussed here) are used for higher cadence measurements. Fluxgate magnetometers have been used on many spacecraft to date (e.g. Lepping et al., 1995; Balogh et al., 1997; Bale et al., 2016).

Fluxgate magnetometers consist of a ferromagnetic core with two coils (drive and sense) wrapped around it (see Fig. 2.15). The ferromagnetic core responds to magnetic field by becoming magnetised itself. If the magnetic field applied to the core is large enough, the core's magnetisation saturates and further increases in the external field will not increase the magnetic field of the core. This saturation underpins how these magnetometers work.

A periodic drive current is applied to create a magnetic field. In the absence of a solar wind magnetic field ($\mathbf{B}_{ext} = \mathbf{0}$) all parts of the core (green and blue areas) saturate and unsaturate at the same time (as the drive magnetic field is uniform throughout the core). As the core is symmetrical, this results in no net change in magnetic flux. Therefore, no current is induced in the sense coil. However, if a solar wind magnetic field is present

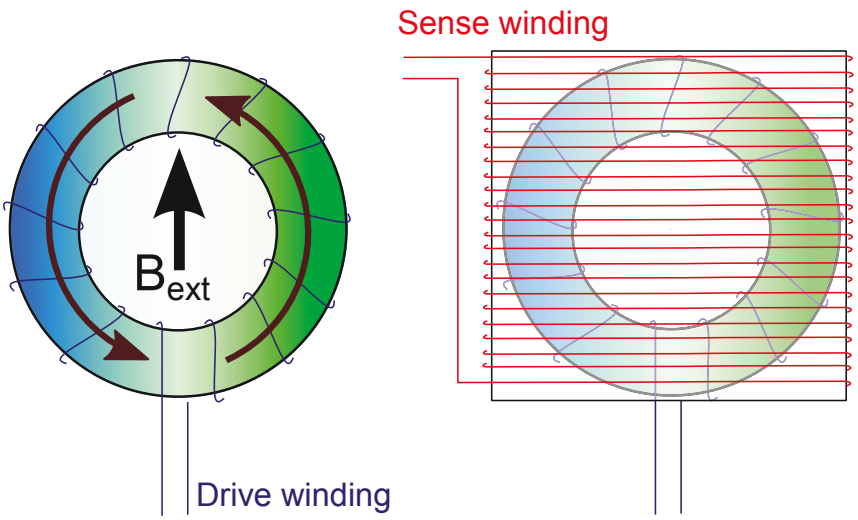


Figure 2.15: Diagram showing the design of a fluxgate magnetometer. There are two coils around the ferromagnetic core, a drive winding and a sense winding. *Figure credit: Mistry (2017). Used under a Creative Commons Attribution Non-Commercial No Derivatives licence.*

($\mathbf{B}_{ext} \neq \mathbf{0}$) the magnetic field experienced by the core is not uniform. To make the following description easier it is assumed that the solar wind magnetic field is in the plane of the core ring (as shown in Fig. 2.15). In approximately half of the core the drive and solar wind magnetic fields act in the same direction, increasing the local field experienced by the core. Equally in the other half of the core the drive and solar wind fields oppose each other, leading to a local reduction in the magnetic field felt by the core. This asymmetry introduced by the solar wind magnetic field results in the two halves of the core saturating and unsaturating asynchronously. The lack of uniformity in the core magnetisation leads to non-zero changes in the magnetic flux. As a result a current is induced in the sense winding. This current signature can then be used to determine the solar wind magnetic field. Each core ring (Fig. 2.15) is sensitive to one direction. Therefore, three orthogonal rings are used to measure a three-dimensional magnetic field vector.

2.6 Current Space Missions

Two new spacecraft have been launched with the purpose of improving our understanding of the inner heliosphere. These spacecraft, called Parker Solar Probe (Fox et al., 2016) and

Solar Orbiter (Müller et al., 2013), have complementary mission objectives and provide vital data for studies of the solar wind. It is currently a particularly active phase of space science research, making it an exciting time to work in the field. The main details of each spacecraft are outlined here.

2.6.1 Parker Solar Probe

2.6.1.1 Mission Overview

The Parker Solar Probe (PSP) mission was launched in August 2018 with the aim of measuring the near-Sun solar wind (see Fig. 2.16). Since then, it has measured data closer to the Sun than any previous spacecraft. The overall goal of PSP is to take in situ measurements within 10 solar radii of the Sun. This will be achieved using a series of Venus gravity assists throughout the mission to gradually reduce PSP's perihelion distance. To date, PSP has completed 13 perihelion passes (often called solar encounters) of its planned 24 passes (see Fig. 2.17).

2.6.1.2 Instruments

The instruments on board PSP are split into four instrument suites: Solar Wind Electrons Alphas and Protons (SWEAP; Kasper et al., 2016), Wide-field Imager for Solar Probe (WISPR; Vourlidas et al., 2016), Electromagnetic Fields Investigations (FIELDS; Bale et al., 2016), and Integrated Science Investigation of the Sun (IS⊙IS; McComas et al., 2016). These suites contain a collection of individual instruments for measuring various aspects of in situ solar wind and for making remote sensing observations. The main instrument suites used in this thesis are FIELDS and SWEAP. The FIELDS data are detailed below and the SWEAP data are left to the relevant chapters (see Chapter 3 and Chapter 5).

2.6.1.3 FIELDS Data

The FIELDS instrument suite is designed to collect data that will be valuable for studies of magnetic and electric fields, plasma waves, and solar radio emissions. The suite has a variety of detectors to measure these data including five voltage probes, two fluxgate magnetometers (see Sect. 2.5.2), and one search coil magnetometer. Four of the voltage probes stick out behind the heat shield, while the fifth is located on the spacecraft boom.



Figure 2.16: (left) Image of Parker Solar Probe inside the rocket before its launch in August 2018. *Image credit: NASA/Johns Hopkins APL/Ed Whitman, Whitman (2018).* (right) Image of Solar Orbiter before its launch in February 2020. *Figure reproduced with permission from ESA. Copyright: ESA - S. Corvaja, ESA (2020).*

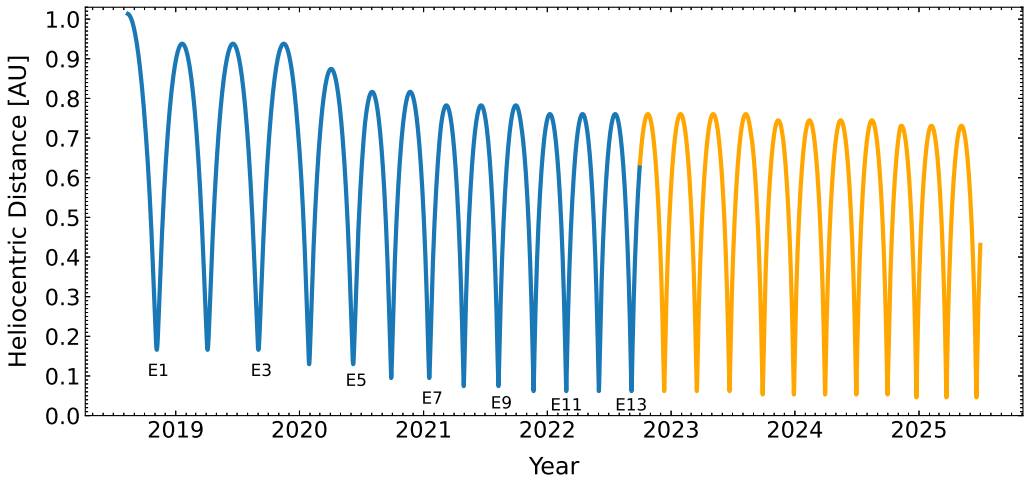


Figure 2.17: Time series of Parker Solar Probe's heliocentric distance during the planned mission phase. The blue data show the progress of Parker Solar Probe to date, and the orange data show its future trajectory. The odd numbered encounters to date have been labelled.

This configuration allows the plasma electric field in two directions and the fluctuations in a third direction to be measured. All of the magnetometers on board PSP are located on the boom to reduce the influence of other electronics on the magnetic field data. To further reduce the impact of the spacecraft on magnetic field measurements the two fluxgate magnetometers are separated on the boom. This allows the magnetic field from the spacecraft to be characterised and removed by comparing the data from both detectors.

In this thesis, the level 2 magnetic field data from the fluxgate magnetometers are predominantly used. The data are often down-sampled from their original cadence (2.3-292.9 samples/sec) to 1 Hz, reducing computation requirements for this analysis. The method for down-sampling is as follows. A series of evenly spaced timestamps (at 1Hz resolution) is created for the full time period that is to be down-sampled. The values for each timestamp are then populated by calculating the mean of the data within $\pm$ 0.5 seconds of the timestamp. These reduced cadence data are appropriate for this thesis as higher frequency fluctuations are rarely considered. In Chapter 4, the electric field measurements are used briefly. Throughout this thesis, electron number density (n_e), which is calculated from quasi-thermal noise measurements, is often used.

2.6.2 Solar Orbiter

Solar Orbiter is a joint mission between the European Space Agency and NASA (see Fig. 2.16). It was launched on February 10, 2020 and has a 7 year mission phase with an additional 3 years in the extended mission phase. Solar Orbiter, unlike PSP, is not designed to get as close to the Sun as possible. Instead, Solar Orbiter will leave the ecliptic plane to take measurements of the solar poles. Its closest approach to the Sun will be 0.28 au, but the spacecraft will reach a latitude of 25° in the nominal phase and $\sim$ 35° in the extended phase. Solar Orbiter has 4 in situ instruments and 6 remote sensing instruments on board (Müller et al., 2013, 2020). The descriptions of these instruments are left to the relevant literature (Müller et al., 2013, 2020, and references therein).

Chapter 3

Fitting Solar Probe Cup Data

Parts of this chapter have been published in Woolley et al. (2020).

3.1 Introduction

Solar Probe Cup (SPC; Case et al. 2020) is a Faraday cup on board the Parker Solar Probe mission (Fox et al., 2016). It is part of the SWEAP instrument suite (Kasper et al., 2016) which is designed to comprehensively measure the solar wind environment around the spacecraft. The data from these plasma instruments provide a novel opportunity for studying the near-Sun solar wind, but in order to fully utilise the data, it is important to understand any constraints and limitations.

In this chapter, the main focus is the operational principles of SPC. The other instruments are left to their respective literature. Sect. 3.2 begins by explaining the instrument suite that SPC is part of. Sect. 3.3 explains how the SPC instrument measures an ion velocity distribution function and Sect. 3.4 describes how these raw data are processed. Sect. 3.5 describes how the one-dimensional SPC measurements relate to three-dimensional ion distributions, before Sect. 3.6 discusses how the parameters of the proton core population can be extracted from the data. Important instrument limitations are highlighted in Sect. 3.7, before a comparison of the moments and fits of the data is shown in Sect. 3.8. Finally, Sect. 3.9 shows an overview of data from Parker Solar Probe's first solar encounter. The methods outlined in this chapter are crucial for the study presented in Chapter 4.

3.2 The SWEAP Instrument Suite

The Solar Wind Electrons, Alphas and Protons (SWEAP) instrument suite (Kasper et al., 2016) on board Parker Solar Probe is comprised of a variety of plasma instruments designed to measure the solar wind in situ (see Fig. 3.1). There are three electrostatic analysers (see Sect. 2.5.1; Whittlesey et al., 2020) - two for electrons and one for ions - and a Faraday cup which measures both electrons and ions. The electron electrostatic analysers are on both the ram (SPAN-A) and anti-ram (SPAN-B) sides of the spacecraft, whereas the ion electrostatic analyser is only on the ram side (SPAN-A). These electrostatic analysers have a wide field-of-view (FOV), but are located behind the spacecraft heat shield, and therefore cannot measure ions and electrons travelling radially with respect to the spacecraft. As such, SPC, which extends out from behind the heat shield, is used for measuring particles that are obscured from SPAN-A and SPAN-B. Whilst SPC provides an opportunity to measure solar wind obscured from the electrostatic analyser FOV, there is a trade off. This is because Faraday cups only measure one-dimensional particle distribution function whereas electrostatic analysers can measure three-dimensional distributions.

SPC protrudes from behind the spacecraft heat shield and measures the solar wind that is flowing radially with respect to the spacecraft. SPC has a 60° field-of-view that allows it to complement the measurements made by the other plasma instruments. This 60° field-of-view was chosen to fully capture the ion distribution for both radial and non-radial flows. The extent to which the solar wind flow can deviate from radial while the ion distribution function remains fully captured depends on the plasma temperature. In Sect. 4.3, there is potential evidence for the instrument not fully capturing the ion distribution function. However, it is currently unclear whether this is an instrumental or physical effect. The design of SPC is similar to other Faraday cups that have been used previously to make solar wind measurements (e.g. Bridge et al., 1977; Ogilvie et al., 1995). However, the materials used to make SPC are more resilient to the hostile near-Sun environment. SPC measures a one-dimensional velocity distribution function (referred to as a reduced distribution function, RDF) along the radial direction towards the Sun for both ions and electrons.

In this thesis, the fitting procedure for the SPC ion data is outlined. Data from the other SWEAP instruments are used in later chapters, but the fitting procedures for these

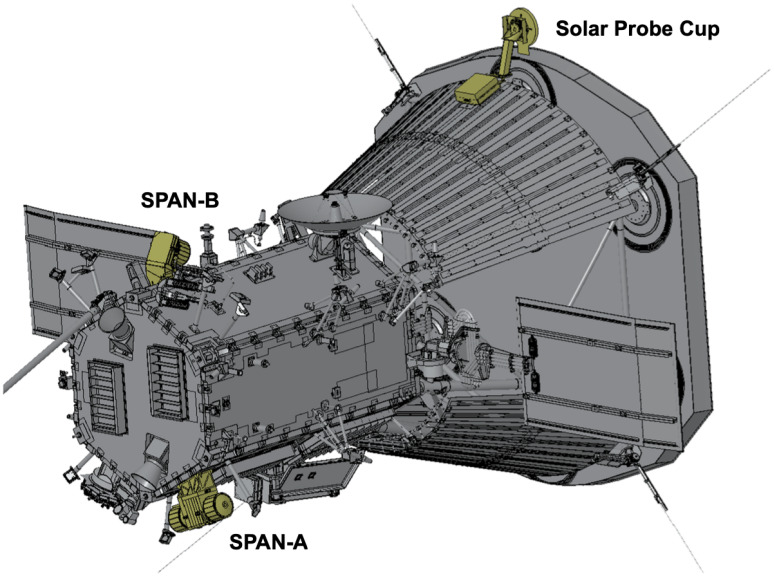


Figure 3.1: Diagram showing locations of SWEAP instruments on board Parker Solar Probe. The ram side of the spacecraft points downwards and the anti-ram side points upwards. The heat shield is on the right and is directed towards the Sun. Solar Probe Cup points out from behind the heat shield to measure the incoming solar wind. *Figure adapted from Kasper et al. (2016).*

---

are left to the relevant publications.

3.3 Solar Probe Cup: Design and Operation

SPC measures ion distributions by splitting the incoming solar wind ions into 'slices' based on their energy-to-charge ratio (E/q) and counting the number of ions in each slice. SPC is only sensitive to the kinetic energy of the ions along the axis of the sensor which is the Sun-spacecraft line (radial) for PSP encounters. SPC, therefore, measures a 'cut' along the radial direction. This cut can be thought of as equivalent to measuring a three-dimensional velocity distribution and integrating over the two non-radial directions. In order to filter the incoming ions, a series of voltage grids is used (see Fig. 3.2). A high voltage modulator grid (HVMG) is located between two ground grids. When a voltage is applied to the HVMG two electric fields acting in opposite directions are created. The first electric field filters the incoming ions based on their E/q. Any ions that are not filtered out by this first electric field then get accelerated back to their original velocity

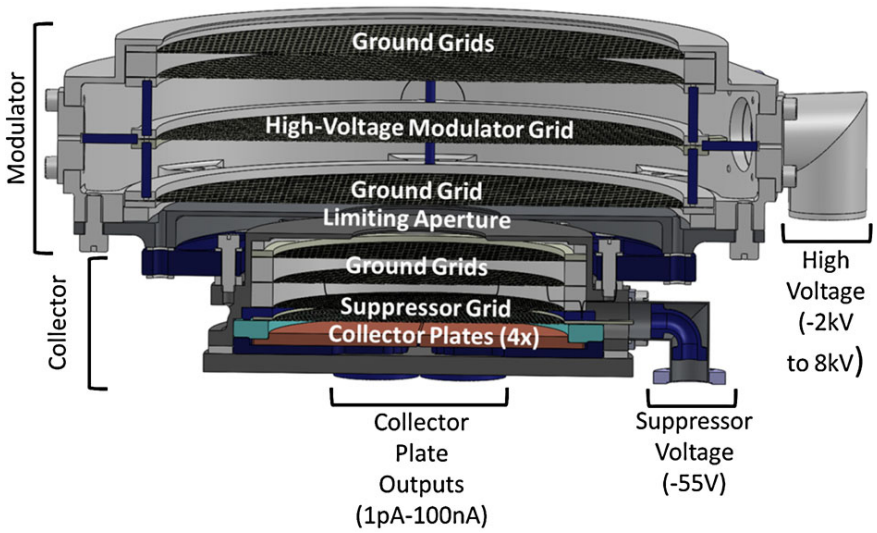


Figure 3.2: Cross sectional diagram of the Solar Probe Cup sensor. The instrument is split into a modulator unit that filters the incoming solar wind and a collector unit that records the number of particles. The solar wind enters the instrument from the top and passes through the modulator before reaching the collector plates. *Figure reproduced from Kasper et al. (2016).*

---

by the second electric field. These ions can then travel through the aperture and impact the circular collection plate. This circular collection plate is split into four equally sized detectors which record a current when ions collide with them. The ratios of the currents from the detectors can be used to estimate the flow angle of the solar wind into the sensor.

Electrons can be emitted from the collector plate due to the collisions of incoming solar wind particles and due to photoelectric emission caused by radiation. If this emission is not counteracted in some way, a charge imbalance can be created on the collector plates and the data quality can be negatively impacted. A suppression grid is therefore located above the detector. This suppression grid creates an electric field which repels these secondary electrons and stops them escaping from the plates. The suppression grid is 99% effective at preventing secondary electrons, with the remaining 1% of secondary electrons accounted for by pre-processing the data (Kasper et al., 2016; Case et al., 2020).

SPC builds up a one-dimensional ion distribution by gradually increasing the voltages applied to the HVMG and measuring the alternating current for every voltage 'window'. Each voltage window is defined by a lower (V_{Low}) and a higher (V_{high}) voltage, between which the HVMG oscillates sinusoidally. For a particular window, only ions with E/q between V_{Low} and V_{high} contribute to the alternating current. After a full scan through

the voltage windows, the current and voltage measurements can be converted into a velocity distribution function as outlined in Sect. 3.4.

SPC has two different operational modes: peak tracking and full scan. The full scan mode covers a wider range of voltage windows, whereas the peak tracking mode focuses only on the peak of the RDF. The ion full scan mode is used to identify the peak before peak tracking is used to provide higher resolution. In this work, the ion peak tracking mode data are solely used as this has a higher cadence and resolution than the ion full scan mode.

3.4 Processing Reduced Distribution Functions

As with most instruments, the raw SPC data are pre-processed by the instrument team before being released to the community. This is because pre-processing requires detailed knowledge of the instrument and can therefore only be done by the relevant team. Once the data are released, they are split into different levels depending on how much processing has been done. Despite the plasma bulk parameters available in the level 3 files, the focus of this chapter is on the one-dimensional distribution functions that can be reconstructed from the level 2 files. This reconstruction is motivated by a desire to investigate the fitting by the instrument team and to address the underlying distribution functions. The data in the level 2 files contain variables for this reconstruction. These variables include the upper and lower bounds of each voltage window and the differential charge flux density, D. The differential charge flux density is the amount of charge from ions with $V_{low} \leq \frac{E}{q} \leq V_{high}$ passing through a unit area aligned along the SPC look direction ($\hat{z}$) per second.

The level 3 data files contain parameters that would typically be derived from ion distribution functions (i.e. temperature, density and velocity). These include moments of the whole SPC-measured RDFs and fits to the proton core population. These bulk parameters are very good for providing an overview of the data. However, without a good understanding of the caveats and limitations of these data, it is hard to draw conclusions. Moreover, to fully understand the microphysics it is important to be able to address the RDFs themselves. Therefore, the level 2 data products are converted to RDFs for this work and a proton core fitting procedure is applied (see Sect. 3.6). The process for converting level 2 data into RDFs is applied directly from the steps outlined in Case et al. (2020):

1. First, the average velocity of an ion in a given voltage window ($\overline{v_Z}$) was calculated using:

$$\overline{v_Z} = \sqrt{\frac{2}{\pi}\frac{2eV_{high}}{m_p}}\mathrm{E}\left(\frac{V_{low}}{V_{high}}\right) \tag{3.1}$$

where E() is the elliptical integral of the second kind.

2. Next, the width of the voltage window was converted into velocity units using:

$$\Delta v = \sqrt{\frac{2e(V_{high}+V_{low})}{m_p} - 2\overline{v_z}^2} \tag{3.2}$$

3. Finally, the RDF was calculated using:

$$F(\overline{v_z}) \simeq \frac{1}{10^{11}}\frac{D}{e\overline{v_z}\Delta v}. \tag{3.3}$$

During encounter phases of the mission, the orientation of SPC is directly along the Sun-spacecraft line, therefore $\overline{v_z} = v_R$. It should be noted that this v_R represents the radial velocity of individual ion species rather than the bulk solar wind speed (denoted u).

Fig. 3.3 shows an example RDF measured close to perihelion during PSP's first solar encounter and reconstructed using the method outlined above. The majority of the protons are travelling at speeds below 550 km/s indicating that this distribution was measured in a slow solar wind interval. There is a peak at around 300 km/s associated with the proton core population, and a bump at around 450 km/s which could be a proton beam. The high velocity tail ($>$ 600 km/s) is predominantly α-particles, which due to their E/q get shifted by a factor of $\sqrt{2}$. This measurement was made during SPC's peak tracking mode.

There are uncertainties associated with each SPC measurement. These arise from multiple factors including the orientation of the SPC sensor not being perfectly aligned along the Sun-spacecraft line, mechanical offsets of the instrumentation, and uncertainties in the voltages applied to filter particles. A further uncertainty arises due to the non-zero time required to make a measurement of the particle flux for each voltage window. During the measurement, the magnetic field orientation can change which has the effect of smearing the distribution function.

For each measurement provided in the level 2 data files there is an associated uncertainty. However, propagating these uncertainties through the RDF reconstruction

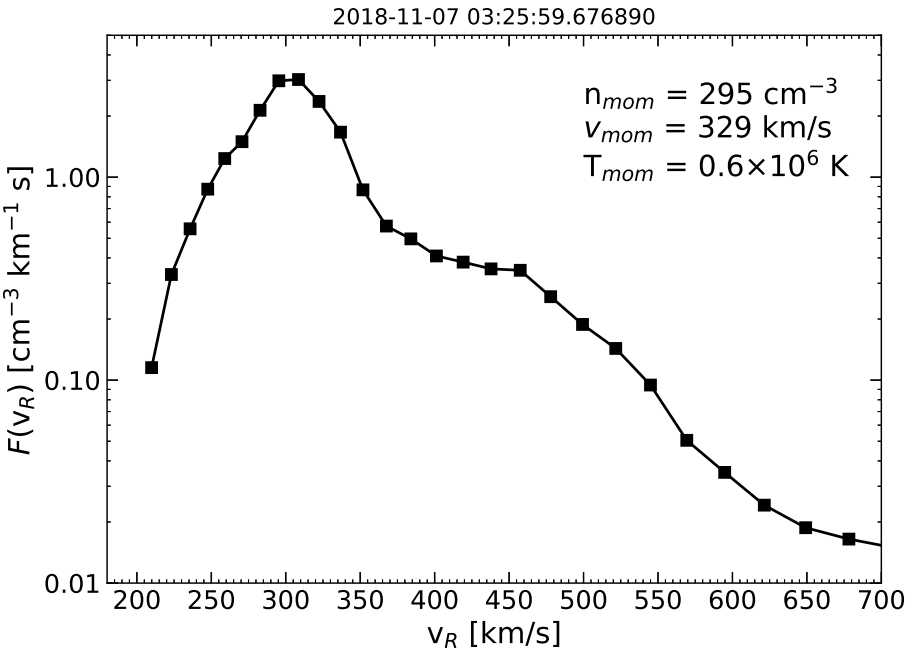


Figure 3.3: Example reduced distribution function measured at 03:25:59.676890 on November 7, 2018 during PSP's first solar encounter. The peak at $\simeq$ 300 km/s is associated with the proton core population. There is also a bump at $\simeq$ 450 km/s which is likely a proton beam. The plasma parameters calculated by taking moments of this RDF (see Sect. 3.8) are shown in the top right.

---

procedure outlined above results in very large uncertainties, which are not realistic. To get appropriately sized uncertainties for the RDFs, a similar approach to that used by the instrument team (which is more complex than the approach used here and requires specific knowledge about the instrument response) is required.

The uncertainties in the flux measurements could be estimated without a full treatment of the errors by considering the instrument noise. A value for the instrument noise could be calculated by comparing many RDFs and determining at which distribution function value the RDFs saturate at. This was not done here, but could be a future project for SPC studies.

3.5 Radial Cuts through Ion Distribution Functions

From Fig. 3.3 it appears as if it would be straightforward to identify ion populations in the RDF. However, there are some issues that arise because SPC is effectively reducing the three-dimensional solar wind ion distribution to a one-dimensional distribution. SPC does this by making a radial 'cut' through the three-dimensional distribution. It is worth investigating how different ion distribution functions would behave in the SPC data. For this discussion, the situation is simplified to a 1D cut through a 2D distribution in the R-T plane (by assuming gyrotropy). This makes the distributions easier to visualise but the same arguments can be extended to three dimensions.

Here the most general case of a plasma with temperature anisotropy in the proton core and beam populations (i.e. $T_\perp > T_\parallel$), and a differential velocity between the proton core, proton beam and $\alpha-$particle populations is considered. The α-particles are chosen to be isotropic here as typically α-particles have an anisotropy closer to 1 than protons do (e.g. Stansby et al., 2019*b*). Fig. 3.4 shows how the SPC-measured RDFs of this plasma would change due to the presence of Alfvénic fluctuations (see Sect. 2.4.3). For each of the four cases in Fig. 3.4, the left panel shows the ion distribution function in the R-T plane and the right panel shows the expected RDF measured by SPC. In the top left a black arrow shows the local magnetic field orientation. The vertical direction corresponds to the radial direction in RTN coordinates and therefore the direction of SPC's cut through the distributions. The left panels in each plot were created by rotating the background distribution (panel a) around the Alfvén speed in the proton core frame. The right panels were created by plotting Maxwellian distributions based on the parameters of each population under the rotation (i.e. v_R, n and T_R, which was calculated using Eq. 3.4). This is equivalent to integrating bi-Maxwellian distributions over v_T.

Panel (a) shows the ion distribution function expected for a radially aligned background magnetic field (vertically up the page). The proton core (red) is the slowest population ($\simeq$ 300 km/s) and the proton beam (blue) is the fastest population ($\simeq$ 500 km/s). The $\alpha-$particles (green) travel at intermediate speeds but are shifted by a factor of $\sqrt{2}$ in velocity when measured by SPC due to their E/q.

Panels (b), (c) and (d) show situations where the magnetic field has rotated relative to the background radial field in panel (a) due to Alfvénic fluctuations. As explained in Sect. 2.4.3, this causes a rigid velocity space rotation of the ion populations. In this

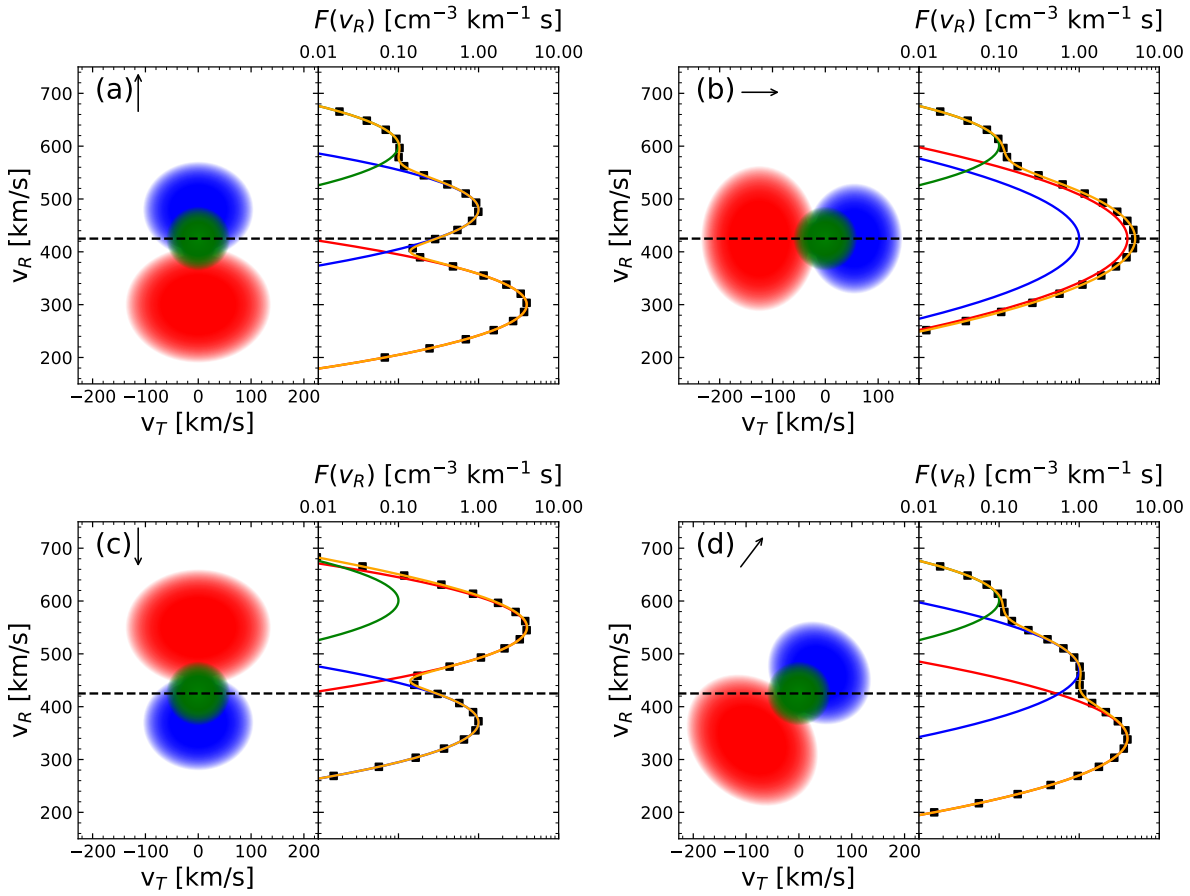


Figure 3.4: Schematic showing how changes in the local magnetic field orientation would affect the reduced distribution function measured by SPC for an anti-sunward radially aligned background field. Each subplot is split into two parts: the left side shows the distribution of the proton core (red), proton beam (blue) and $\alpha-$particles (green) in the velocity R-T plane, and the right side shows how SPC would measure this distribution. The black dashed line shows the point about which the velocity-space rotation happens (see Sect. 2.4.3). On the right hand side, the orange line shows the sum of the distributions and the black scatter points show the reduced distribution function that SPC might measure using discrete velocity intervals. The black arrow in each plot shows the orientation of the local magnetic field. The $\alpha-$particles' bulk velocity is shifted by a factor of $\sqrt{2}$ (due to their E/q) when measured by SPC, and therefore the $\alpha-$particles appear at faster velocities than is shown by the ellipses. Panel (a) shows the background orientation with the proton beam travelling faster than the $\alpha-$particles and the proton core. Panels (b) and (c) show the situation when the local magnetic field has rotated by 90° and 180°, respectively. Panel (d) shows the case where the magnetic field has rotated by less than 90° from the background orientation. In each case, the width of the ellipse is related to the temperature (i.e. wider ellipse corresponds to a higher temperature). The parameters used for each population are shown in Tab. 3.1.

	Proton Core	Proton Beam	$\alpha - particles$
v_R [km/s]	300	480	425
$T_\parallel$ [$\times 10^6$K]	0.15	0.15	0.59
$T_\perp$ [$\times 10^6$K]	0.30	0.30	0.59
n [%]	78	19	3

Table 3.1: The parameters used to make Fig. 3.4. The total ion number density is 446 cm^{-3} and the Alfvén speed is 125 km/s. These values were chosen as they are a reflection of typical properties that are observed in the solar wind. The only parameters that deviate substantially from solar wind observations are the α-particle temperatures. These were chosen to be lower than typical values to make the dynamics of the proton core and beam more obvious in Fig. 3.4.

---

example, the centre of this rotation is the mean velocity of the $\alpha-$particle population; therefore the $\alpha-$particle population remains in the same location for the four scenarios. The proton core and proton beam populations move, however, leading to different RDFs.

In panel (b), the magnetic field has rotated 90° from its background orientation. Under this configuration, SPC measures the distribution perpendicular to the local magnetic field. Due to the temperature anisotropy of the plasma, the width of the individual populations in the RDF is larger than when SPC measures (anti-)parallel to the magnetic field (panels a and c). Also, the proton core obscures the proton beam which leads to a slightly larger total count in the main peak as the beam also contributes to the peak velocity bins.

In panel (c), the magnetic field has rotated 180° from its original orientation, meaning that SPC is once again measuring the distribution along the magnetic field (anti-parallel). Here, assuming the underlying population distributions have not changed, SPC should measure a similar distribution to panel (a) but with the proton core and proton beam at different velocities.

In panel (d), the magnetic field has rotated from the background to an intermediate angle where the proton core and beam are beginning to overlap. This can widen the peak of $F(v_R)$ and make it difficult to distinguish the separate core and beam populations. This is actually the most common situation in the solar wind, meaning that it can be difficult to distinguish each ion population regularly. However, due to the proton core being much larger than any other population, it is possible to get reasonable fits to the proton core population at most times. It is also worth noting that any temperatures derived from these intermediate angles do not correspond to either parallel or perpendicular temperatures

with respect to the background magnetic field. Care must then be taken when interpreting these temperatures. In general, the radial temperatures measured by SPC are related to the perpendicular and parallel temperatures by (Kasper et al., 2002; Huang et al., 2020):

$$T_R = T_\parallel \cos^2 \theta_{BR} + T_\perp \sin^2 \theta_{BR}, \tag{3.4}$$

where θ_{BR} is the angle between the magnetic field and the radial direction.

3.6 Fitting the Reduced Distribution Functions

Using the ideas presented in the previous section, individual populations in the RDFs can be fit. The easiest population to fit is the proton core which is, by definition, associated with the peak in the RDF. To fit the proton core, the following procedure was used:

1. The peak data point of the RDF, F_{max}, was found.

2. F_{max} and 3 points on either side of it were selected for fitting. Three points either side were used because, from visual inspection, this was appropriate to capture the main peak without washing out the finer structure of the distribution.

3. A Maxwellian distribution of the following form was fitted to the seven data points:

$$F_{pc}(v_R) = \frac{n_{pc}}{\sqrt{\pi} w_R} \cdot \exp\left(\frac{(v_R - v_{pc,R})^2}{w_R^2}\right) \tag{3.5}$$

   with thermal speed:

$$w_R^2 = \frac{2k_B T_{pc,R}}{m_p}. \tag{3.6}$$

   It should be noted that a subscript pc refers to the proton core and a subscript R is used as a reminder that directionally dependent quantities (i.e. temperature and thermal speed) are measured along the radial direction with SPC.

4. The proton core parameters (density, radial velocity and radial temperature) were obtained from this fit. The tangential and normal velocities were calculated using the radial velocity and the flow angles of the solar wind into SPC. The total density of the RDF (n_{mom}) was also calculated by taking moments (see Sect. 3.8).

5. The proton core fits were then filtered to remove any cases where the fitting was poor. Two criteria were used to determine this:

(a) Only fits where $n_{pc} < n_{mom}$ were kept. This ensured that the proton core density was smaller than the total RDF density. Filtering data using this condition works well when all or the majority of the proton core population is captured in the RDF. However, this filtering could be inappropriate if only a section of the core was captured and the rest was inferred by extrapolating the core fit. Visual inspection showed no indication that the core was poorly captured in any of the RDFs.

(b) Only fits where the sum of the residuals was lower than a threshold were kept. The threshold for the residuals was set based on the individual streams of interest. For the work presented in Chapter 4, the residuals threshold was 0.05, which was manually chosen to ensure fits were adequately representative of the underlying distributions.

6. In some cases, large proton beam populations, comparable in size to the proton core, had to be dealt with. These large beams were particularly problematic because they often got captured by the proton core fits, leading to an over-estimation of the proton core. The large proton beams were dealt with as follows:

   (a) First, the number of data points above $0.5F_{max}$ were counted. If this number was high, it suggested a particularly large proton beam (or a naturally wide proton core which was visually checked for each case).

   (b) For θ_{BR} angles of 0°-60° or 120°-180°, the proton core and beam should be reasonably distinct populations in the SPC distributions (see Sect. 3.5). Therefore, RDFs with more than 8 data points above $0.5F_{max}$ were manually checked. This visual inspection was easier than using an algorithm to identify whether distributions were consistent with a single core Maxwellian or a core and beam population. The main objective of this was to look for the presence of a beam, which typically manifests as a bump in an otherwise smooth Maxwellian distribution. This inspection can lead to subjectivity, but for the interval considered in this thesis, very few distributions were manually checked. Those which appeared to have large beams were discarded.

   (c) For θ_{BR} angles between 60° and 120°, the core and beam begin to overlap meaning that the core obstructs the beam (see panel b, Fig. 3.4). As a result, at these angles it is still possible to get a reasonable estimate of the proton

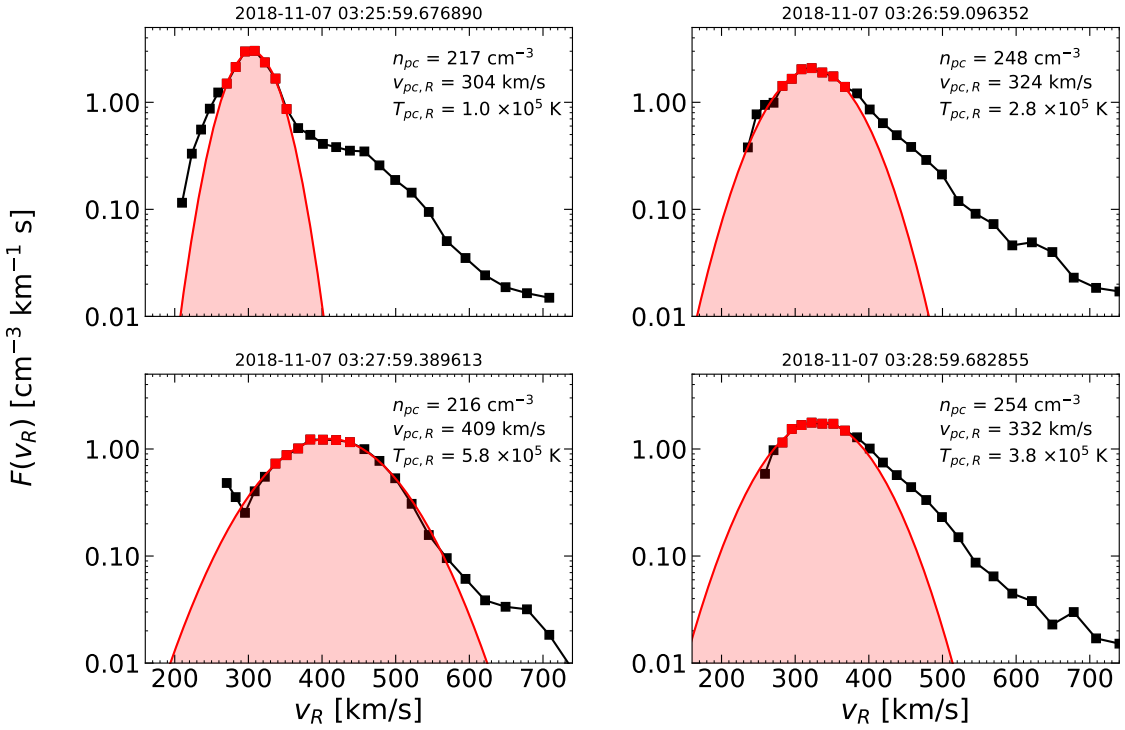


Figure 3.5: Example proton core fits to reduced distribution functions measured at various times by PSP. The red data show the 7 points used to fit a Maxwellian to the core population. The parameters of the core fits are shown in the top right of each panel.

---

core in the presence of a large proton beam. All proton core fits were kept for θ_{BR} angles in this range.

7. Finally, the distributions in each interval of interest were manually checked to remove any remaining bad fits. This was feasible as the intervals investigated were small. Complete automation of SPC fitting could lead to errors if not checked and, therefore, care must be taken in interpreting the data.

Fig. 3.5 shows four RDFs measured by SPC at different times. The proton core fits capture the changes in the distributions well, showing that this method of fitting is robust, provided visual inspection of the fitting is done. It is worth noting that the lowest velocity bins are often not well captured, but that this does not poorly impact the core fitting.

During some time intervals, it was also possible to fit the proton beam and the $\alpha-$particle population. This was only feasible when each population was well separated

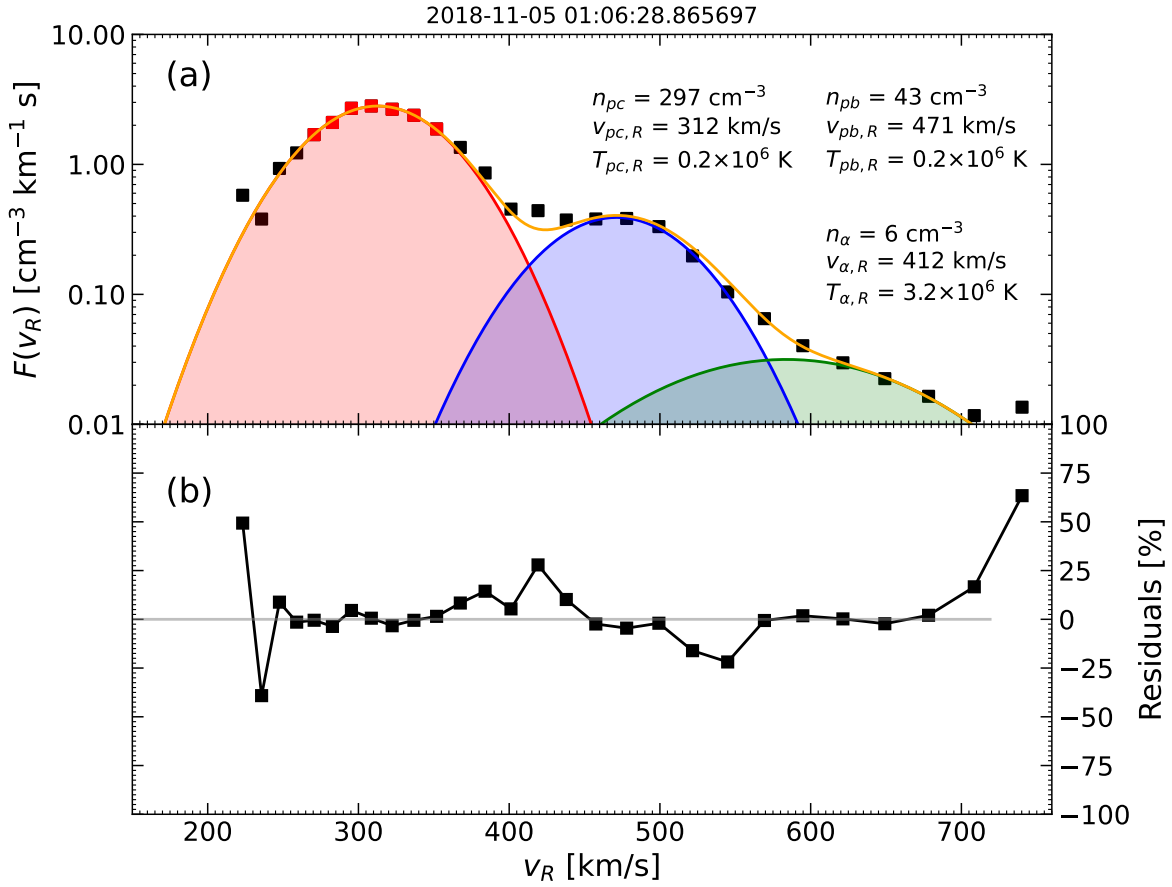


Figure 3.6: Panel (a): Reduced distribution function measured by Solar Probe Cup on November 5, 2018 at 01:06:28.865697. The proton core (red), proton beam (blue) and $\alpha-$particle (green) fits are shown. The orange line shows the sum of the fits. Panel (b) shows the fit residuals as a percentage of the fit values. Only the lowest velocity and highest velocity points are not well fit. The lowest velocity points are likely bad measurements whereas the high velocity points could be an $\alpha-$particle beam. During this time, the magnetic field was orientated approximately radially. The proton beam streams ahead of the proton core by approximately the local Alfvén speed. The α-particles are velocity-shifted in the RDF by a factor of $\sqrt{2}$ due to their E/q. This means they appear to stream faster than the beam, at about 580 km/s, in the RDF. In fact, when this shift is accounted for the α-particles have a velocity of 412 km/s, which is slower than the proton beam. The fit parameters of the proton core (subscript pc), proton beam (subscript pb) and $\alpha-$particles (subscript α) are shown in panel (a). *Figure credit: Woolley et al. (2020). ©Oxford University Press. Reproduced with permission.*

and the measured counts were high. An example is shown in Fig. 3.6 with fits to all three populations. In order to fit the proton beam and the α-particles, the proton core was fit first and removed from the data. Maxwellian distributions were then fit to the remaining data. As such, fitting the proton beam and the α-particles does not affect the proton core fits. These fits to the three populations are not used for analysis in this thesis. Therefore, the method of fitting the proton core and then removing it was used to aid in tuning the proton beam and $\alpha-$particle fitting algorithms. However, if this data was to be used for a study, a combined three-population fit would be more accurate.

3.7 Instrument Limitations

As with all instruments, SPC has some limitations. In order to use the SPC data appropriately, it is important to consider these limitations and when they apply.

As SPC measures a radial distribution function, when extracting direction-dependent quantities (e.g. temperature) care must be taken. The proton core temperature from the SPC RDFs is always the radial temperature along the Sun-spacecraft line, but depending on the magnetic field when the distribution function is measured, this can correspond to different cuts with respect to the magnetic field (see Fig. 3.4). If the magnetic field is parallel or anti-parallel to the radial direction (panels a and c) then the SPC radial temperature corresponds to the temperature parallel to the magnetic field (i.e. $T_{\parallel}$). If, however, the magnetic field is perpendicular to the radial direction (panel b) the SPC radial temperature corresponds to the temperature perpendicular to the magnetic field. On occasions when the magnetic field is neither parallel nor perpendicular to the radial direction (panel d), the SPC radial temperature is a combination of $T_{\perp}$ and $T_{\parallel}$. This is a key point to note in general, but especially for studies involving changing magnetic field orientations such as switchbacks (see Chapter 4).

Another related limitation is that because the distributions that SPC measures are one-dimensional, it is impossible to measure the temperature anisotropy of the plasma simultaneously. One solution to this is to assume that the anisotropy does not vary significantly over a given timescale and then statistically compare temperatures when the magnetic field is parallel and perpendicular to the radial in an interval (Huang et al., 2020). However, this is not suitable for smaller scale studies.

The final limitation worth mentioning here is that SPC is designed to measure solar

wind that flows radially towards the spacecraft rather than solar wind with large relative tangential speed to the spacecraft. As the mission progresses and PSP gets closer to the Sun, its tangential velocity increases. This in turn increases the angle at which the solar wind flows into the SPC sensor and will eventually mean that SPC will be less able to measure solar wind during the later encounters. As a result, in the later encounters, the SPAN instruments will be much more important than SPC (see Kasper et al. (2016) for more details).

3.8 Comparing Moments and Fits of the Proton Core

As mentioned in Sect. 2.4.1, there are two ways to extract bulk parameters from ion velocity distribution functions: by taking moments of the whole distribution or by fitting the individual populations. These two methods can lead to different results, and it is important to understand why. Fig. 3.7 shows a time series comparing the parameters from fitting and moments. It should be noted that no filtering on the proton core fits has been applied here. This is to show how the fitting procedure works in general. The panels show: (a) radial velocity, (b) tangential velocity, (c) normal velocity, (d) density, and (e) temperature.

The radial velocity (panel a) is predominantly greater for the moments than the proton core fits. This is because when fitting the proton core, the higher velocity part of the RDF is often not included in the fitting. The moments however, do include this higher velocity part, which increases the average velocity of the RDF above the proton core velocity. There are, however, times when the radial velocity from the fits is greater than that of the moments. These times occur when PSP measures highly Alfvénic structures called switchbacks (see Chapter 4). As these switchbacks are Alfvénic, they cause a velocity-space rotation in the ion distribution function, which can lead to a faster proton core than proton beam (e.g. see panel (c) in Fig. 3.4). In these cases, the moments include a lower velocity contribution from the beam which reduces the average velocity of the RDF below that of the proton core.

The tangential and normal fit and moment velocities appear to be more consistent with each other than the radial velocities do. However, this is not the case. The size of the y-scale relative to the magnitude of the tangential and normal components means that the differences between the fits and moments are not as clear as with the radial

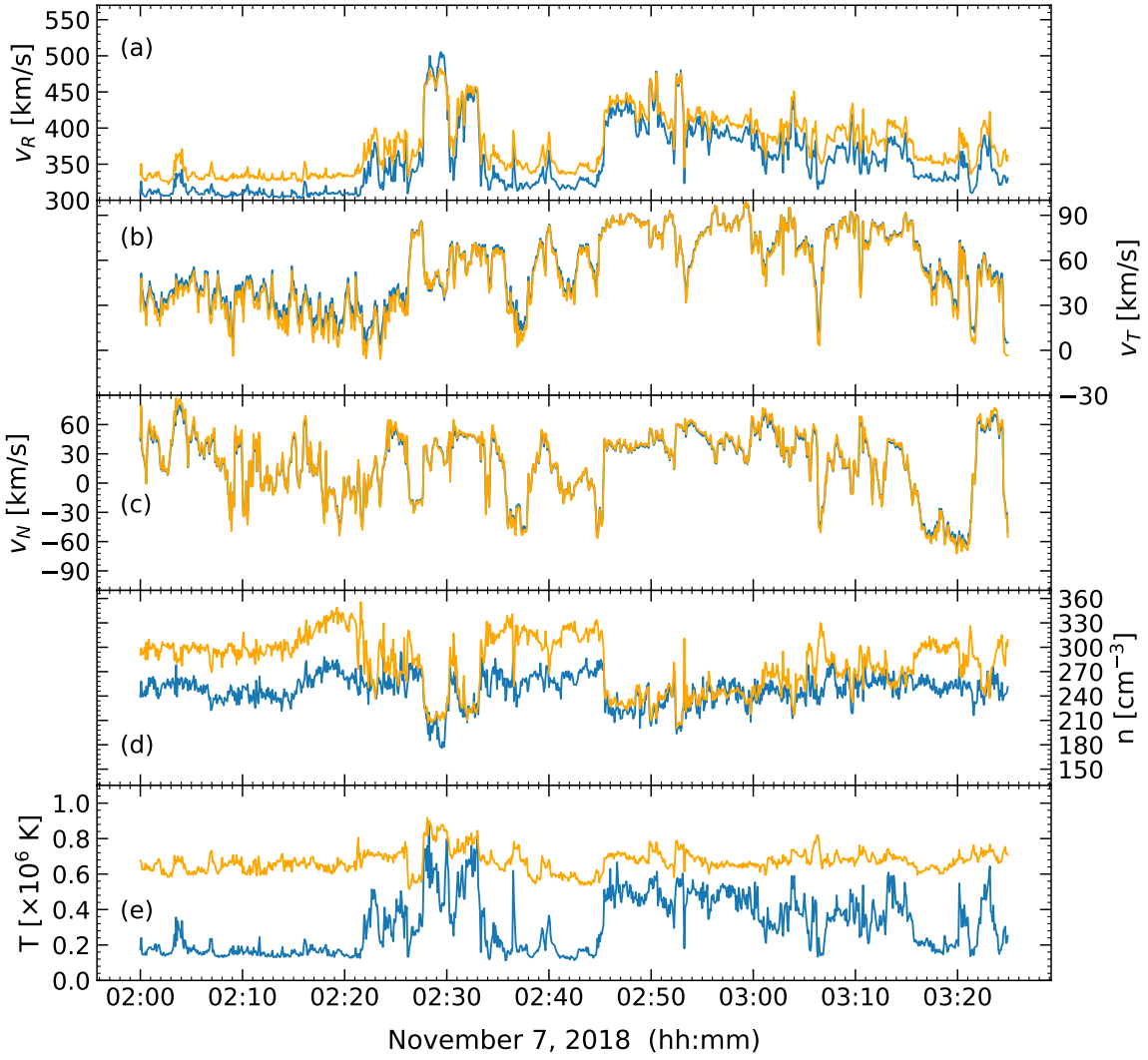


Figure 3.7: Time series comparing parameters calculated using moments (orange) and fits to the proton core (blue) in the SPC RDFs. The panels show: (a) radial velocity, (b) tangential velocity, (c) normal velocity, (d) density, and (e) temperature. The data were taken over a 1.5 hour interval on Nov 7, 2018 during PSP's first solar encounter.

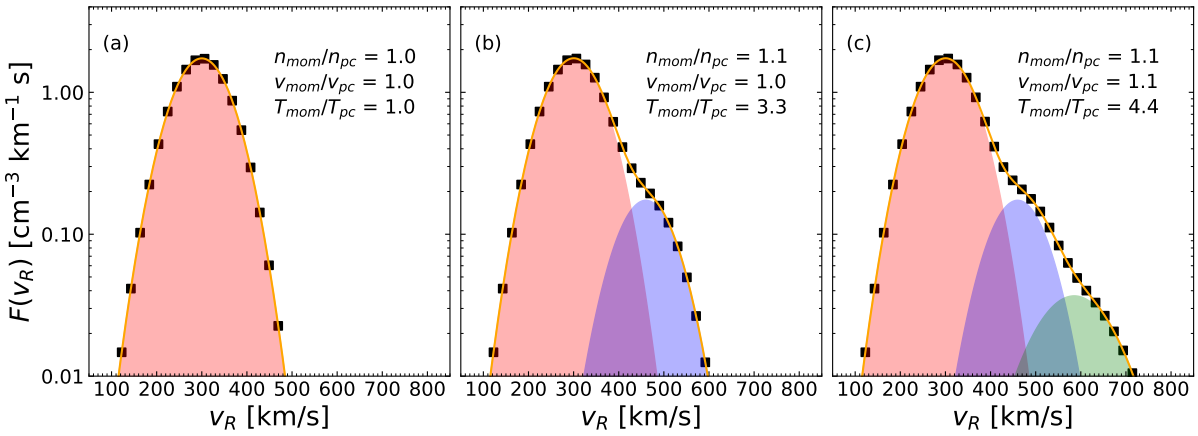


Figure 3.8: Example reduced distribution functions showing how moments are influenced by additional populations. The panels show RDFs consisting of: (a) a single proton core population, (b) a proton core and proton beam population, and (c) a proton core, proton beam and $\alpha-$particle population. The proton core (red) has $n_{pc} = 250$ cm^{-3}, $v_{pc} = 300$ km/s, and $T_{pc} = 0.2 \times 10^6$ K. The proton beam has the same temperature as the core but a faster velocity ($v_{pb} = 460$ km/s) and 10% of the core density. The $\alpha-$particles have a density of 3% of the core, a temperature that is twice that of the core, and a velocity of 585 km/s. The values given in the top right of each panel show the ratio of moments of the whole distribution to the proton core fit parameters. These values are along the radial but the subscript R has been dropped for brevity in this figure.

---

velocity. In fact, the tangential and normal velocities for each method differ by the same proportion as the radial velocities do.

For the majority of the data, the density of the moments is higher than the fits. This makes physical sense because the proton core is a subset of the whole distribution and should therefore have a lower density. There are, however, times when the density of the proton core fits is higher than the moments. This could happen in cases where the proton core has been over estimated, hence the need for filtering of the proton fits before drawing any conclusions. Another situation where the proton core fit density may be larger than the moments is if the proton core is not well captured by SPC. This could happen if the proton core was particularly slow, but no evidence for poorly captured proton cores was seen during visual inspection of the RDFs for this interval.

The temperature of the moments is consistently higher than that of the fits. At around 02:10, the temperature calculated from the moments is ~ 4 times higher than that of the proton core fit. The reason for this is explained using Fig. 3.8. The panels

show three different theoretical RDFs that have been constructed using typical values for the November 7, 2018 interval. Panel (a) shows a single proton core population, panel (b) shows a proton core and a proton beam, and panel (c) shows a proton core, proton beam and $\alpha-$particle population. For each panel, the plasma properties were calculated using moments and compared to the proton core parameters. The ratios of these quantities (shown in the top right of each plot) highlight that T_{mom} is extremely sensitive to additional populations, whereas n_{mom} and v_{mom} are less strongly influenced by proton beams and $\alpha-$particles. For example, in panel (c) T_{mom} is 4.4 times higher than the proton core temperature, which is a direct result of the additional populations.

The sensitivity of T_{mom} to additional ion populations also explains why the ratios of T_{mom}/T_{pc} and n_{mom}/n_{pc} follow each other closely in Fig. 3.7. When $n_{mom}/n_{pc} \simeq 1$ this implies that the distribution contains a large proton core population and very small beam and $\alpha-$particle populations. In this case, $T_{mom}/T_{pc} \simeq 1$ as shown in panel (a) of Fig. 3.8. In contrast, when $n_{mom}/n_{pc} > 1$, it implies that there are non-negligible beam and/or $\alpha-$particle populations. As T_{mom} is particularly sensitive to additional populations, this increases T_{mom}/T_{pc} (see panel (c) in Fig. 3.8).

Due to the large discrepancies between T_{mom} and T_{pc}, taking temperature moments of distribution functions must be done with care. Temperature moments can be particularly useful if computational resources are limited, as taking moments is much less computationally intensive than fitting distribution functions. This makes moments good for getting an overview of the solar wind, before analysing intervals in more depth using fits. It is worth stressing that n_{mom} and v_{mom} are much less sensitive to extra ion populations and are often good approximations to the proton core parameters, provided the proton beam is not too large.

3.9 PSP Encounter 1 Overview

Using the FIELDS magnetic field data and the SPC moments outlined in this section, an overview of PSP's first solar encounter is shown. This is a particularly interesting encounter because it was the first spacecraft to take data at heliocentric distances less than 0.29 au.

Fig. 3.9 shows data from this first encounter. Throughout the 11 day period, the magnetic field magnitude (panel a) was heavily dependent on heliocentric distance (panel

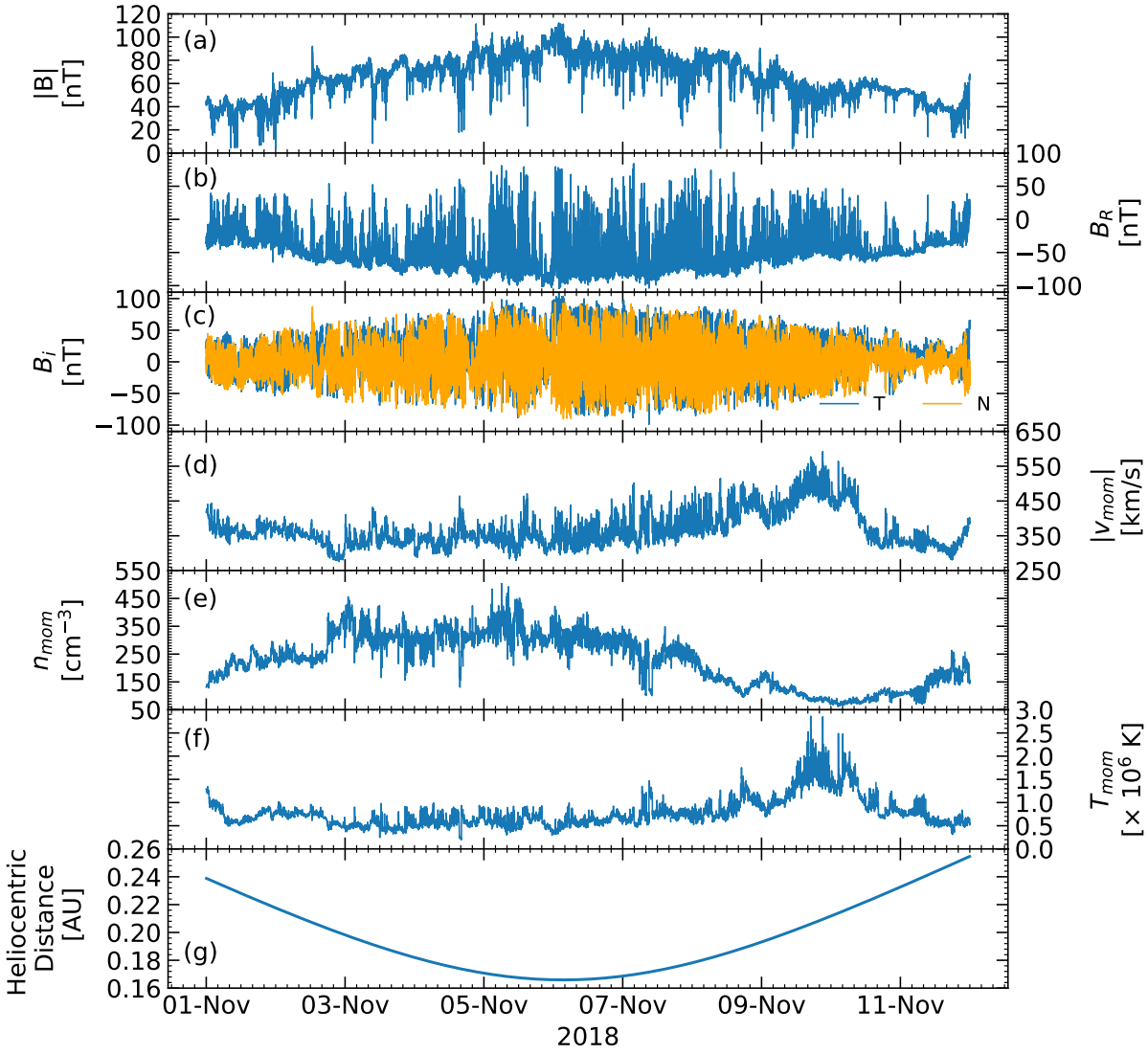


Figure 3.9: Time series of Parker Solar Probe's first solar encounter during November 2018. The panels show: (a) the magnetic field magnitude, (b) the radial component of the magnetic field, (c) the tangential and normal components of the magnetic field, (d) the ion velocity, (e) the ion density, (f) the ion temperature, and (g) the heliocentric distance of Parker Solar Probe.

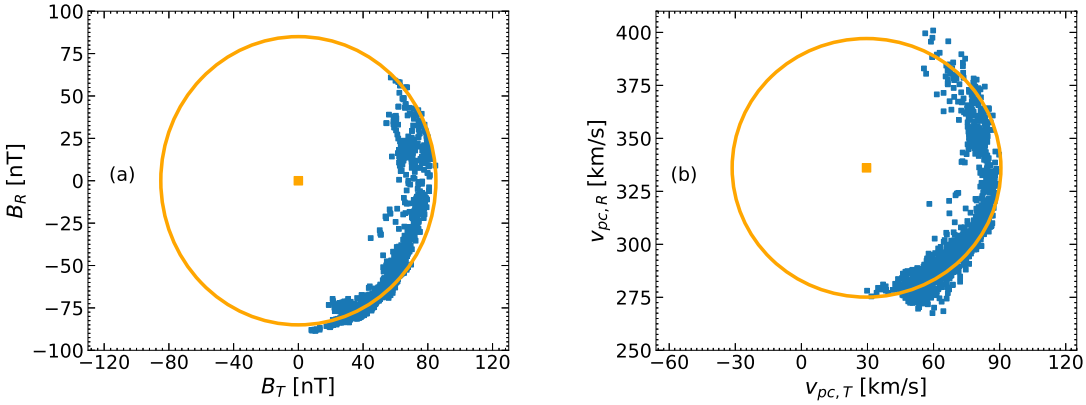


Figure 3.10: Plots showing the behaviour of the magnetic field (panel a) and proton core velocity (panel b) in the T-R plane under Alfvénic fluctuations. The data are from an interval during PSP's first solar encounter (2018, November 5 06:55:05-07:19:30). The circles show the 2D projection of the 3D spheres that both the magnetic field and velocity vectors lie on. The centre of the magnetic field circle is (0,0) nT and the centre of the velocity circle is (30, 335) km/s. The radius of the magnetic field circle is $|\mathbf{B}|$. The radius of the velocity circle is approximately the local phase speed (61 km/s). *Figure credit: Woolley et al. (2020). ©Oxford University Press. Reproduced with permission.*

---

g), with $|\mathbf{B}|$ reaching $\sim$ 100 nT at perihelion. Panel (b) shows that the radial component of the magnetic field had a baseline that was approximately equal to -$|\mathbf{B}|$ with discrete 'spikes' away from this baseline. These features are called magnetic field switchbacks and addressed in Chapter 4. From the SPC measurements, it is clear that the wind measured by PSP is slow (panel d). This is consistent with expectations when measuring solar wind at low latitudes during solar minimum. There is also a high correlation between fluctuations in the magnetic field and velocity components (not shown here) which indicates the high Alfvénicity of this solar wind. Finally, panels (e) and (f) show the density and temperature, respectively. Between November, 9 and November, 11 there is a solar wind stream with higher temperature and lower density than the rest of the encounter. This could be related to the small equatorial coronal hole that was present during this time (Bale et al., 2019). In fact, it is likely that a lot of the wind in this encounter originated in or close to the boundary of this coronal hole (Bale et al., 2019).

It is also possible to use the SPC fitted data to see the behaviour of the proton core in Alfvénic solar wind. As mentioned previously (see Sect. 2.4.3), under Alfvénic fluctuations the magnetic field vector and the proton core velocity vector are confined to the surface

of a sphere in their respective 3D spaces. Fig. 3.10 shows a 2D projection of this sphere in the T-R plane for the magnetic field (panel a) and the proton core velocity (panel b). Both the magnetic field and the proton core velocity lie on the perimeter of the circle (as shown previously with Ulysses data in Fig. 2.10). The radius of the magnetic field circle is $|\mathbf{B}|$ and the radius of the proton core velocity circle $\sim v_{phase}$ (61 km/s). During this time, the local Alfvén speed (97 km/s) is approximately 50% larger than the phase speed. This further confirms the ideas discussed in Sects. 2.4.3 and 3.5.

3.10 Conclusions

In this chapter, an overview of the Solar Probe Cup instrument was given. The measurements used to build up a 1D ion distribution function were explained, and the process for converting level 2 SPC data into reduced distribution functions was shown. The fitting method used to extract bulk parameters from the SPC data was detailed. The limitations of SPC were discussed, with a particular emphasis on the fact that SPC measures 1D radial cuts through the 3D solar wind ion distribution. For the majority of data, these radial cuts are neither parallel nor perpendicular to the magnetic field. Therefore, it is not possible to recover direction-dependent quantities (e.g. $T_\perp$ and $T_\parallel$) without assuming a relationship between these quantities and the magnetic field orientation (e.g. Eq. 3.4). Moreover, care must be taken when comparing direction-dependent quantities under arbitrary magnetic field configurations. A comparison between SPC moments and fits was made, focusing on the advantages and disadvantages of each method. In particular, temperatures calculated using moments are very sensitive to additional ion populations. Finally, the SPC data were used to show an overview of PSP's first solar encounter and confirm results shown previously with Alfvénic wind measured by Ulysses. The data and methods explained in this chapter are vital for the study in Chapter 4.

Chapter 4

The Proton Core Population Inside Slow Solar Wind Switchbacks

Parts of this chapter have been published in Woolley et al. (2020).

4.1 Introduction

Switchbacks are discrete structures corresponding to rotations of the magnetic field away from its background orientation. These rotations can reverse the local magnetic field polarity within a solar wind stream so that it is opposite to the large scale polarity associated with that stream. Magnetic field switchbacks are not a consequence of the spacecraft passing over source regions with opposite polarities, but are instead associated with folds in the local magnetic field within a single polarity source region (Balogh et al., 1999). Switchbacks are thought to be related to the heating and acceleration mechanisms in the near-Sun solar wind, and are therefore a particularly active area of research within the community. However, despite measurements of switchbacks from both Ulysses (Balogh et al., 1999; Neugebauer and Goldstein, 2013) and Helios (Horbury et al., 2018), these structures remain poorly understood. This is a direct result of two issues surrounding the Ulysses and Helios data. Firstly, the duration of switchbacks, which is of the order of seconds to a few minutes (Dudok de Wit et al., 2020), is comparable to the cadence of plasma data from these spacecraft. This means that ion VDFs measured completely within switchbacks are rare. Secondly, the switchbacks measured at large heliocentric distances appear very different from those closer to the Sun, indicating that they evolve

as the solar wind expands. This means that to get a clear picture of switchbacks, they need to be measured much closer to the Sun. Fortunately, the instruments on board Parker Solar Probe address both of these issues by measuring high cadence plasma data within 0.3 au. In this chapter, the SPC data are used to understand the proton core behaviour within switchbacks.

In Sect. 4.2 the current state of switchback knowledge is outlined, including the questions addressed here. A case study switchback is analysed in detail in Sect. 4.3 and other switchbacks measured by PSP are presented in Sect. 4.4. In Sect. 4.5 the results are discussed in relation to switchback origins, before Sect. 4.6 discusses how the work presented here fits with a subsequent study. The chapter ends with a discussion of the conclusions and the remaining questions surrounding switchbacks.

4.2 Switchback Background

Switchbacks are Alfvénic structures with constant $|\mathbf{B}|$, meaning that fluctuations in the magnetic field are highly correlated with fluctuations in the plasma velocity (see Fig. 4.1). In switchbacks the magnetic field fluctuations are $\sim |\mathbf{B}|$ and have an upper limit of $2|\mathbf{B}|$ which corresponds to a full 180° reversal of the magnetic field orientation with constant $|\mathbf{B}|$. According to Eq. 2.14, which describes the relationship between magnetic field and velocity fluctuations for an Alfvénic plasma, these magnetic field fluctuations correspond to velocity fluctuations $\sim v_A$ and with an upper limit of $2v_A$. Observational data agree with both the order of velocity fluctuations in switchbacks (Matteini et al., 2014) and the upper limit of $2v_A$ (Kasper et al., 2019). It is worth noting that, due to the correlations between the magnetic field and velocity fluctuations, the velocity fluctuations associated with switchbacks always lead to an enhanced solar wind speed above the background (Matteini et al., 2014).

Switchbacks were first discovered in the fast solar wind data from Ulysses (Balogh et al., 1999; Neugebauer and Goldstein, 2013) and Helios (Horbury et al., 2018) beyond 0.3 au, but have since been measured by Parker Solar Probe in slow near-Sun solar wind (Bale et al., 2019; Kasper et al., 2019). There are striking differences between the switchbacks measured close to the Sun and those measured outside 0.3 au, which suggests that these structures evolve and change as the solar wind expands. The switchbacks seen by PSP occur ubiquitously and have durations from seconds to tens of minutes, but exhibit no

specific timescale (Dudok de Wit et al., 2020). They are grouped into larger-scale 'patches' (Horbury et al., 2020) with timescales of ∼10 hrs that are separated by 'quiet periods' with timescales ∼1 hr (see Fig. 4.2). However, data from larger heliocentric distances show no such patch structure or ubiquity, indicating that both switchbacks and patches undergo significant evolution as the solar wind expands.

Currently, switchbacks are one of the most popular areas in solar wind research meaning that there have been numerous studies addressing the PSP-measured switchbacks. McManus et al. (2020) investigated the behaviour of cross helicity during solar wind intervals with significant switchback activity. Cross helicity measures the balance of outward and inward propagating waves with respect to the bulk solar wind frame. It can be defined in such a way that, regardless of the background magnetic field, a positive cross helicity corresponds to an abundance of outward propagating waves compared to inward propagating waves. McManus et al. (2020) found that the cross helicity signature reverses sign within switchbacks, further supporting the suggestion of Balogh et al. (1999) that switchbacks are folds in the local magnetic field rather than polarity reversals of the overall magnetic field. Laker et al. (2021*a*) statistically studied the shape of switchbacks by considering the angle at which PSP cut through them and the spatial extent of switchbacks in the in situ data. They found that switchbacks were consistent with high aspect ratio structures (i.e. long and thin) with typical scale sizes of $\sim 10^4$ km in further support of the evidence presented by Horbury et al. (2020). The scale size of switchbacks is considerably larger than typical kinetic scales such as ion and electron gyration radii. Finally, Dudok de Wit et al. (2020) used a statistical analysis of the duration of switchbacks to shown that they have no characteristic time. One area that has yet to be investigated, however, is the behaviour of the proton core population inside magnetic switchbacks. This is the focus of this chapter.

The behaviour of the proton core population is particularly interesting because it allows an investigation into how the largest ion population changes between the background solar wind and the switchbacks. This can help to characterise the properties of switchbacks and relate in situ data to switchback theories. In this chapter, the SPC-measured RDFs are used to characterise the proton core population and address the following questions:

1. Is the plasma inside a switchback distinctly different from the background plasma?

2. Do switchbacks obey a temperature-velocity relationship?

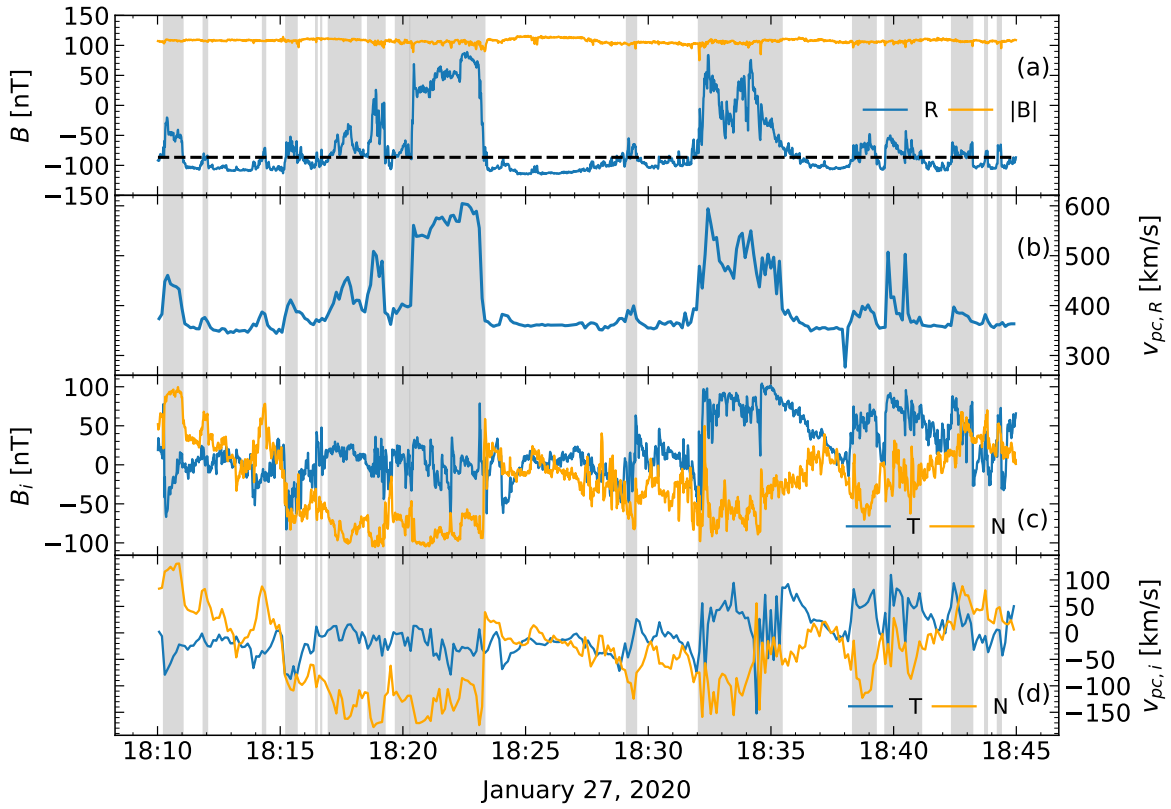


Figure 4.1: Time series showing magnetic field switchbacks measured by Parker Solar Probe. The panels show: (a) the magnetic field radial component and magnitude, (b) the proton core radial velocity, (c) the magnetic field tangential and normal components, and (d) the proton core tangential and normal velocity. The black dashed line shows the threshold for identifying switchbacks (a 30° deflection from the background magnetic field orientation calculated on a timescale of several hours) and the grey shaded regions show the switchbacks in this interval. The radial magnetic field and proton core velocity components are highly correlated, indicating the Alfvénicity of switchbacks.

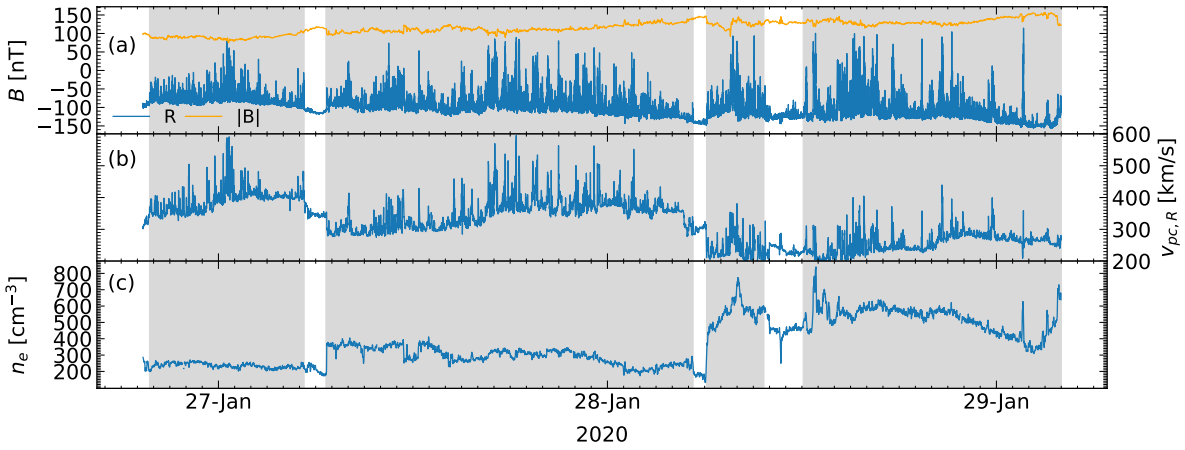


Figure 4.2: Time series showing switchback patches in the solar wind during Parker Solar Probe's fourth solar encounter. The panels show: (a) the magnetic field radial component and magnitude, (b) the proton core radial velocity, and (c) the electron number density. The grey shaded regions show the patches and the unshaded regions show the quiet periods that separate patches.

---

3. What is the dominant energy that switchbacks carry?

This chapter starts with an in-depth analysis of a case study switchback before the analysis is extended to additional switchbacks found in the first two PSP encounters.

4.3 Case Study Switchback

4.3.1 Selecting the Case Study

In Sect. 3.5 it was shown that, in general, the 1D 'cuts' SPC makes through a 3D ion VDF correspond to different temperature measurements. However, in the case of radial and anti-radial magnetic field the SPC temperature measurements both correspond to temperatures parallel to the local magnetic field. It is, therefore, only possible to meaningfully compare temperatures measured when the magnetic field is radial to temperatures measured when the magnetic field is anti-radial. Fortunately, the background magnetic field measured by PSP during encounter 1 was approximately radially sunward, allowing the SPC data to be exploited by identifying a switchback that underwent a full 180° reversal in the magnetic field. These full-reversal switchbacks were rarely seen in the data, but it was possible to identify a case study switchback.

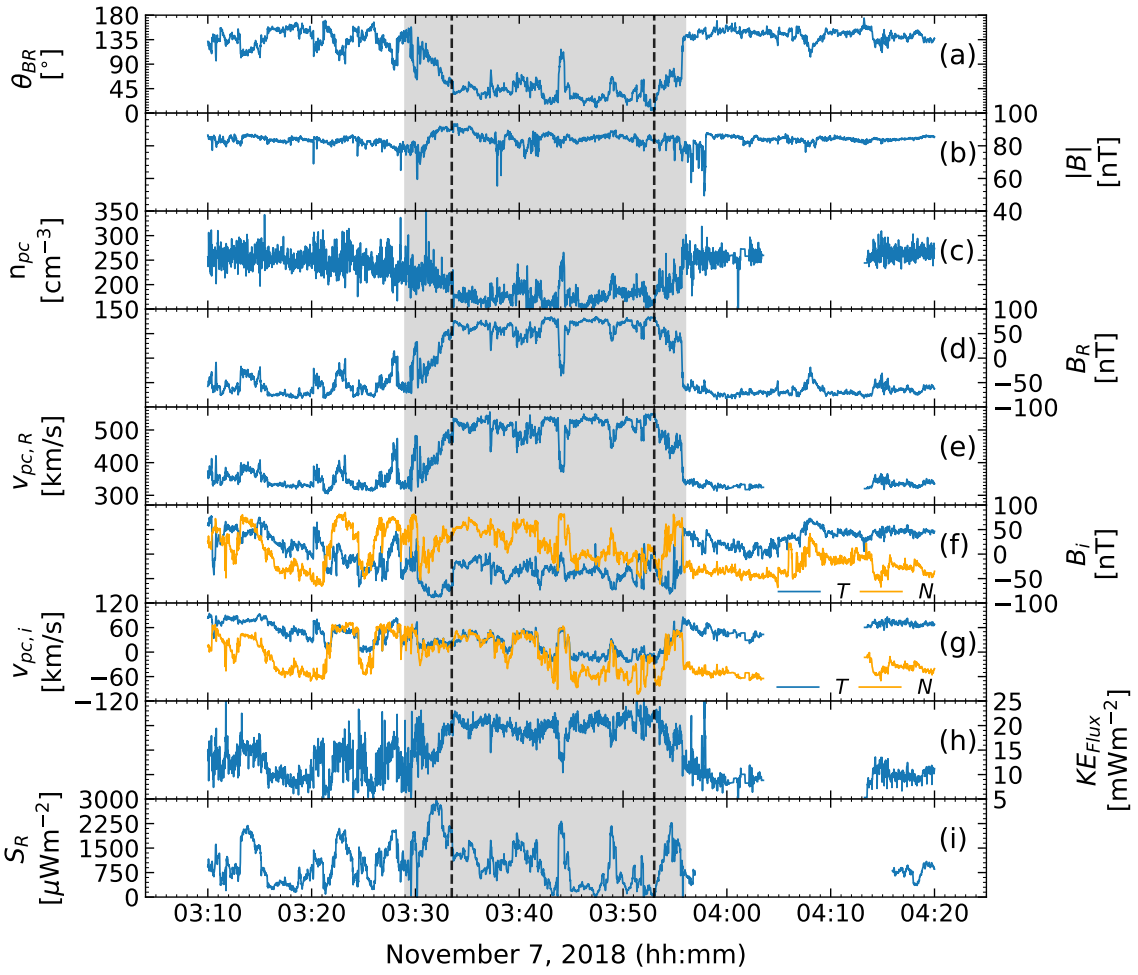


Figure 4.3: Time series of a magnetic field switchback (shaded grey) identified on November 7, 2018. The panels show: (a) magnetic field cone angle, (b) magnetic field magnitude, (c) proton core number density, (d) radial component of the magnetic field (e) radial component of the proton core velocity, (f) the tangential and normal components of the magnetic field, (g) the tangential and normal components of the proton core velocity, (h) the radial kinetic energy flux, and (i) the radial Poynting flux. The black dashed vertical lines show the region inside the switchbacks where the magnetic field was reasonably stable and approximately a full-reversal from the background field. *Figure credit: Woolley et al. (2020). ©Oxford University Press. Reproduced with permission.*

A full-reversal switchback that occurred on November 7, 2018 was manually identified. This switchback, which had a duration of ∼25 mins, was measured when PSP was 37.6 R_S from the Sun. Fig. 4.3 shows a time series of the case study switchback and background solar wind either side of it (Note: There is a plasma data gap of approximately 10 mins after the switchback). Panel (a) shows the magnetic field cone angle rotate from near 180° in the background plasma to ∼0° in the switchback. This demonstrates that this switchback undergoes a full-reversal in the magnetic field orientation and is appropriate for analysing with SPC data. Panel (b) shows the magnetic field magnitude remains approximately constant throughout the interval which is typical of switchbacks. Panel (c) shows that the proton core density drops inside the switchback. There is currently insufficient evidence to determine whether this density drop is caused by a reduction in the distribution within the instrument FOV, or whether switchbacks have lower density than the surrounding plasma. However, the high correlation between density (panel c) and the magnetic field cone angle (panel a) suggests that it could be the former. If the former is true this effect should not change the distribution shape, only reduce the total amount of ions measured. Inside the switchback, the radial component of the magnetic field (panel d) has undergone a full-reversal from approximately -70nT to 70nT. During this time, the radial component of the proton core velocity (panel e) has increased from ∼ 350 km/s to > 500 km/s. By comparing the profiles in panels (d) and (e), it is very clear that the fluctuations in the radial magnetic field and proton core velocity components are well correlated. This is due to the high Alfvénicity of the switchback. Similar highly correlated fluctuations are also evident when comparing the tangential and normal components of the magnetic field and proton core velocity (panels f and g). Panels (h) and (i) show the radial kinetic energy and radial Poynting flux respectively. These quantities are discussed in Sect. 4.3.4.

4.3.2 Proton Core Temperature

Using the switchback case study, the behaviour of the proton core temperature can now be investigated. For the interval shown in Fig. 4.3, the SPC-measured proton core temperature (referred to as temperature for the rest of this section for brevity and denoted $T_{pc,R}$) is plotted against the magnetic field cone angle (panel b in Fig. 4.4). The temperature profile does not monotonically increase or decrease as a function of θ_{BR}, but peaks at intermediate angles close to $\theta_{BR} = 90°$. The temperature falls off either side of this peak

and has comparable values when $\theta_{BR} = 0°$ and $\theta_{BR} = 180°$. This behaviour is interesting for two reasons.

Firstly, the peak of the temperature profile occurs when the local magnetic field is approximately perpendicular to the radial direction. As discussed in Sect. 3.5, under these conditions SPC measures the perpendicular temperature of the plasma. This could indicate that $T_{pc,\perp} > T_{pc,\parallel}$ during this interval, which is commonly seen in the solar wind. However, no firm conclusions can be drawn as $T_{pc,\perp}$ and $T_{pc,\parallel}$ cannot be measured at the same time with SPC.

Secondly, it is interesting that the temperature is comparable when $\theta_{BR} = 0°$ and $\theta_{BR} = 180°$. At both of these angles, the SPC temperature corresponds to the parallel temperature. More specifically, when $\theta_{BR} = 180°$ SPC measures $T_{pc,\parallel}$ in the background solar wind and when $\theta_{BR} = 0°$ SPC measures $T_{pc,\parallel}$ inside the switchback. These temperatures are therefore directly comparable. The data here suggest that $T_{pc,\parallel}$ is the same inside and outside full-reversal switchbacks, indicating that speed enhancements within switchbacks may not follow a typical temperature-velocity relationship.

These observations are consistent with a rigid velocity space rotation of an ion VDF with temperature anisotropy ($T_{pc,\perp}/T_{pc,\parallel}$) of $\simeq 6$. The expected $T_{pc,R}$ profile of such an ion VDF is shown as the black solid line (Eq. 3.4). From Fig. 4.4 it can be seen that the data follow this expected profile well, however, there are some deviations. For example, there seems to be a small systematic deviation for $\theta_{BR} < 60°$. It is currently unclear what causes this deviation. It could be an instrumental issue or a physical mechanism.

In general, the SPC temperature profile for this switchback is consistent with the expected profile of a rigidly rotating anisotropic plasma VDF, despite the small deviation in Fig. 4.4. This suggests that the temperature changes seen by SPC throughout the switchback are due to different geometrical cuts through the VDF, rather than a change in the underlying plasma conditions. This result can be further supported by looking at the RDFs throughout the switchback.

4.3.3 Reduced Distribution Functions

Fig. 4.5 shows the SPC-measured RDFs for various magnetic field cone angles throughout the case study switchback (the magnetic field cone angle is the angle between the local magnetic field and the radial direction). The red shaded regions show the proton core fits and the green shaded region shows the α-particles, which could only be reasonably

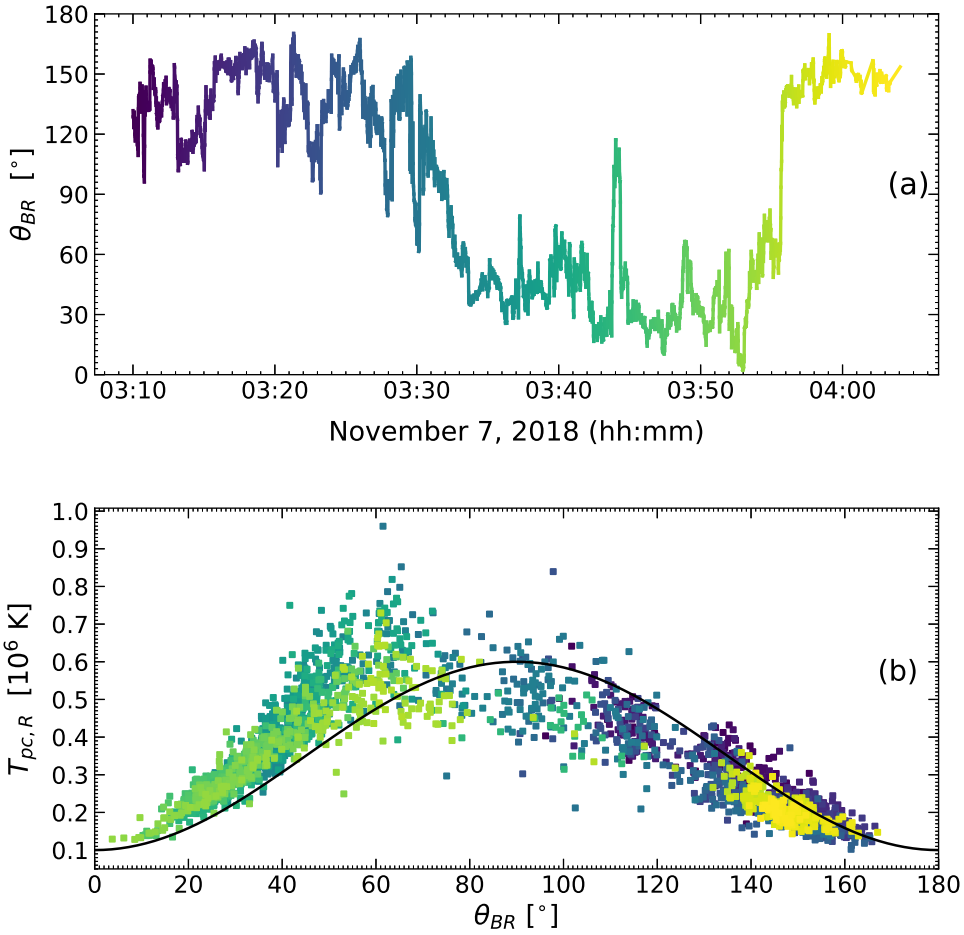


Figure 4.4: Panel (a) shows a time series of magnetic field cone angle for the interval in Fig. 4.3 and panel (b) shows the SPC-measured temperature against magnetic field cone angle. The colours of each point indicate the time through the interval; purple corresponds to the earliest times and yellow corresponds to the latest. The black line in panel (b) shows Eq. 3.4 with $T_{pc,\perp} = 0.6{\times}10^6$ K and $T_{pc,\parallel} = 0.1{\times}10^6$ K. This is the expected profile for a rigid velocity-space rotation of a plasma VDF. *Figure credit: Woolley et al. (2020). ©Oxford University Press. Reproduced with permission.*

separated from the proton beam, and therefore fit, for perpendicular magnetic field angles (see discussion in Sect. 3.5).

Panel (a) shows the background plasma before the switchback. During this time, the magnetic field is almost completely anti-radial (i.e. radially aligned in the sunward direction) with $\theta_{BR} = 167°$. The proton core population has a radial velocity of $\simeq 300$ km/s and there could be a proton beam with $v_R \simeq 460$ km/s, although this has not been fit for reasons explained in Sect. 3.6.

In panel (b), the RDF corresponds to an ion distribution function measured inside the switchback when the magnetic field is perpendicular to the radial ($\theta_{BR} = 90°$). The proton core distribution is much wider than in panel (a), indicating that it has a larger temperature. This temperature corresponds to the proton core perpendicular temperature as the magnetic field is at 90° to the radial. The whole RDF is nicely fit with a proton core and an α-particle population because, due to the rotation of ion species under Alfvénic fluctuation explained in Sect. 3.5, the proton core obscures the smaller proton beam from being measured. As mentioned in Sect. 3.4, the α-particles have been shifted by a factor of $\sqrt{2}$ in velocity and are actually travelling at around 425 km/s.

Panel (c) shows the RDF inside the switchback, when the magnetic field has undergone a full rotation from the background field ($\theta_{BR} = 2°$). The distribution looks very similar to that in panel (a) except that the proton core is found at a higher velocity, as expected based on the motion of ion populations under Alfvénic fluctuations (see Sect. 2.4.3 and 3.5). To compare the distributions in panel (a) and panel (c), the RDF from panel (a) was rigidly rotated in velocity space and over plotted on the RDF from panel (c) as shown in panel (d). The shapes of the two distributions are remarkably similar to each other, indicating that the plasma inside the switchback is not distinctly different and is consistent with a rigid velocity space rotation of the background plasma distribution. This further supports the results shown in Sect. 4.3.2. It is worth noting that while the shapes of the distributions are similar, the RDF from the background plasma has higher particle counts than the switchback RDF for the velocity bins associated with the proton core (i.e. orange line is above the black line for $v_R > 450$ km/s). The difference in counts between the two distributions is larger than the measurement errors, indicating that the density change is significant. This density change could be a result of a smaller fraction of the distribution being within the instrument FOV, or a signature that switchbacks are less dense than the surrounding solar wind. Due to the density change dominating the

difference between the two distributions, it is not possible to conclude whether the shapes of the RDFs are statistically the same. As such, it is concluded that they are markedly similar, but equality is not claimed.

An estimate of the point in velocity space (in the proton core reference frame) about which the distribution function rotated was calculated from the motion of the RDFs. By considering the proton core velocity in the two extreme cases (i.e. radial and anti-radial cases), this rotation speed was estimated to be 115 km/s. The velocity and magnetic field fluctuations were used to get an empirical estimation of the local Alfvén speed using Eq. 2.14 (see Fig. 4.6). This speed, often referred to as the local phase speed, can deviate from the theoretical local Alfvén speed for reasons that are currently unknown. In this case, the local phase speed (110 km/s) was comparable to the rotation speed estimated previously (115 km/s) and the local Alfvén speed (110 km/s) calculated using Eq. 2.15. This suggests that the centre of rotation is close to both the local Alfvén speed and the local phase speed. This, however, is not always true as the local phase speed and local Alfvén speed deviate from each other by greater amounts as the solar wind expands into the heliosphere (e.g. Matteini et al., 2014).

4.3.4 Poynting Flux and Kinetic Energy Flux

The proton core data can also be used to characterise the energy dynamics within switchbacks. Here the kinetic energy flux and Poynting flux are considered. The discussion is limited to the radial fluxes to consider the amount of energy transferred per unit time through a radially aligned unit area (i.e. the power switchbacks transport radially away from the Sun). For the kinetic energy, the radial kinetic energy flux is approximately equal to the kinetic energy flux as v_R is the dominant velocity component. For the Poynting flux, however, this is not the case as the tangential and normal components can have significant energy.

Panels (h) and (i) in Fig. 4.3 show the radial kinetic energy flux and the radial Poynting flux, respectively. Inside the switchback, the kinetic energy flux increases because the velocity of the proton core increases. In fact, the kinetic energy flux profile is similar to the proton core radial velocity and, because the solar wind is Alfvénic in this interval, the radial magnetic field profiles. The radial Poynting flux is low in the background plasma, although its profile follows the magnetic field angle closely. As the magnetic field begins to rotate at the start of the switchback, the radial Poynting flux increases,

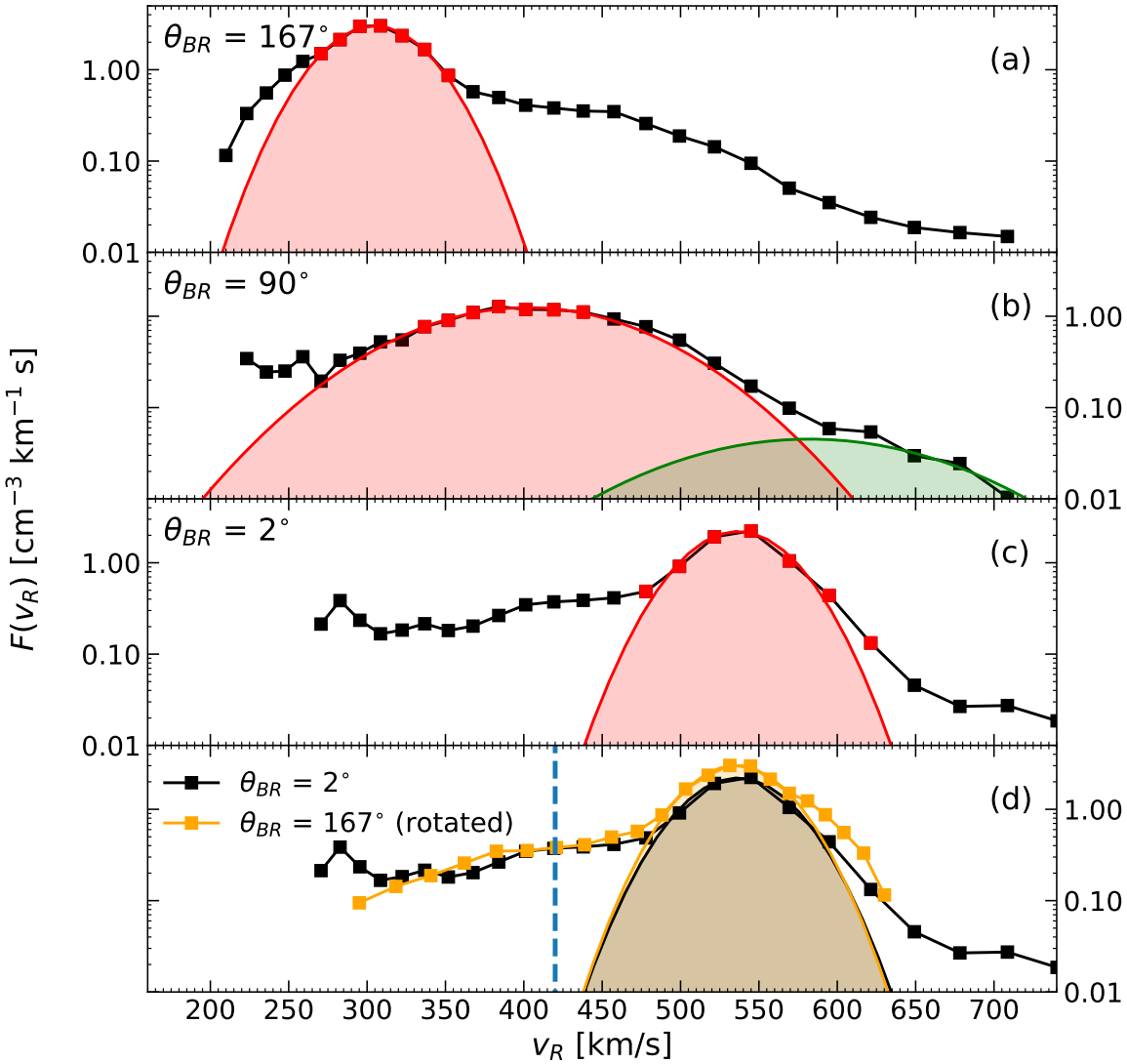


Figure 4.5: Reduced distribution functions throughout the case study switchback on November 7, 2018. Panels (a) – (c) show the RDFs measured by SPC for (near) anti-parallel, perpendicular and parallel magnetic fields, respectively. The proton core (red) and $\alpha-$particle (green) fits are shown. The red points show the data used for fitting the proton core population. Panel (d) shows the distribution of panel (a) rotated about the local phase speed in the proton core frame (orange) and the distribution from panel (c) (black). The local phase speed in the proton core frame is shown by the dashed blue vertical line. *Figure credit: Woolley et al. (2020). ©Oxford University Press. Reproduced with permission.*

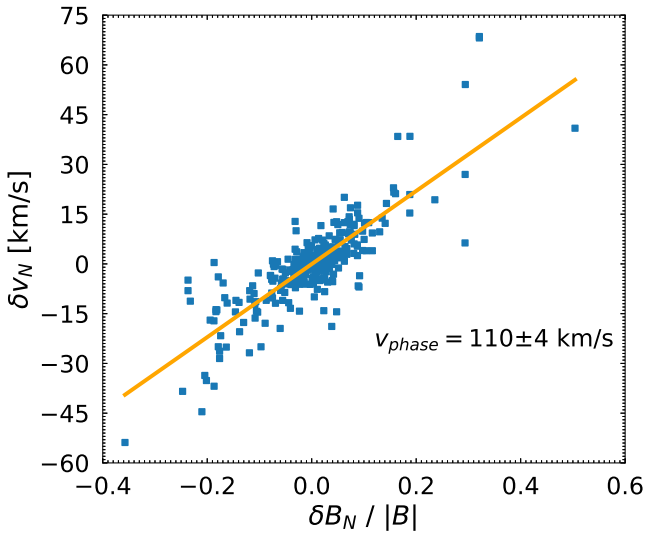


Figure 4.6: Scatter plot of the normal components of the velocity fluctuations and normalised magnetic field fluctuations. The gradient of the fitted line (orange) provides an empirical estimate for the local Alfvén speed (called the local phase speed) based on Eq. 2.14.

---

reaching a maximum when the magnetic field is perpendicular to the radial direction. As the magnetic field continues to rotate, the radial Poynting flux drops and returns approximately to its background level inside the switchback. At the end of the switchback, as the magnetic field returns to its background orientation, the same behaviour is seen (i.e. the Poynting flux peaks at intermediate angles but returns to a low value in the background plasma). This behaviour directly agrees with the functional form presented in Mozer et al. (2020).

Throughout the whole interval, the kinetic energy flux is larger than the radial Poynting flux although the ratio of these quantities varies. Before the switchback, in the background solar wind the kinetic energy flux is ∼20 times larger than the Poynting flux. When $\theta_{BR} \simeq 90°$, the kinetic energy flux is only ∼5 times larger, as the Poynting flux reaches its maximum value here. Inside the switchback, when $\theta_{BR} = 0°$ the Poynting flux has a similar value to the background field, yet the kinetic energy flux is enhanced relative to the background. Therefore, the kinetic energy flux is ∼40 times larger than the Poynting flux inside the switchback. This shows that the kinetic energy flux always dominates over the Poynting flux in this switchback and could indicate that kinetic energy is more important than electromagnetic energy for the energy dynamics of switchbacks.

It is possible to get a general expression for the ratio of the radial kinetic energy flux to

radial Poynting flux using observations. As the electric field is dominated by the motional electric field (i.e. $\mathbf{E} \simeq -\mathbf{v} \times \mathbf{B}$) the radial Poynting flux can be written as:

$$S_R = \frac{1}{\mu_0}\left(-v_N B_R B_N - v_T B_R B_T + v_R(B_N^2 + B_T^2)\right). \tag{4.1}$$

Because $v_R >> v_T, v_N$, the third term dominates the expression for S_R and the ratio of Poynting flux to kinetic energy flux can be expressed as:

$$\Gamma = \frac{S_r}{KE_{flux}} \sim \frac{\frac{1}{\mu_0} v_R B_\perp^2}{\frac{1}{2}\rho v_R^3} \sim \frac{2}{v_R^2}\frac{B_\perp^2}{\mu_0 \rho}. \tag{4.2}$$

where $B_\perp^2 = B_T^2 + B_N^2 = (B\sin\theta_{BR})^2$.

This ratio can then be applied to the case of fluctuations with constant $|\mathbf{B}|$. Under these fluctuations, Γ is expected to reach a maximum value at $\theta_{BR} = 90°$ because this is the point where increases in v_R are counteracted by increases in $B_\perp$. For $\theta_{BR} < 90°$, v_R continues to increase but $B_\perp$ starts to decrease. Therefore, using the fact that $B_\perp = B$ by definition when $\theta_{BR} = 90°$, the maximum ratio, Γ_{max}, can be written as:

$$\Gamma_{max} \sim 2\left(\frac{v_A}{v_R}\right)^2\Bigg|_{\theta_{BR}=90°}, \tag{4.3}$$

where v_A is the Alfvén speed.

This ratio can then be used to estimate the upper limit for the Poynting flux carried by a switchback. For the case study switchback, $\Gamma_{max} \sim 1/5$. Eq. 4.3 can also be used to predict what ratios will be seen at different heliocentric distances. For example, as PSP approaches the Alfvén radius this ratio will approach ~ 1 as $v_R \to v_A$. This will result in similar amounts of electromagnetic and kinetic energy carried radially outwards by the switchbacks. However, it is not clear whether switchbacks with $\geq 90°$ rotations exist closer to the Sun as $\delta\mathbf{B}/|\mathbf{B}|$ reduces for decreasing heliocentric distance.

4.4 Other Switchbacks in Parker Solar Probe Data

The results from Sect. 4.3 show that the case study switchback had a similar proton core parallel temperature to the background solar wind. However, this is not necessarily true for all full-reversal switchbacks. To check whether the results can be generalised more of these switchbacks were analysed. Full-reversal switchbacks were manually identified in PSP's first and second solar encounters. As full-reversal switchbacks are rarely seen in

the data, the criteria for selecting appropriate switchbacks were relaxed. Any switchback with $>$ 8 data points with $\theta_{BR} < 30$ degrees was chosen. Note that the background magnetic field corresponded to $\theta_{BR} \simeq 180°$ during encounter 1 and 2, therefore $\theta_{BR} \simeq 30°$ corresponds to a $\simeq 150°$ rotation from the background magnetic field. Eq. 3.4 was used to fit the data for $\theta_{BR} < 30$ degrees and $\theta_{BR} >$150 degrees, providing estimates of the parallel temperature inside and outside the switchback, respectively. It was only possible to fit 4 additional switchbacks this way, as very few switchbacks reached $\theta_{BR} < 30$ degrees (i.e. it is uncommon for switchbacks to deviate by $\sim 150°$ from the background magnetic field). The statistics of full-reversal switchbacks are, therefore, limited.

Tab. 4.1 shows the results of this fitting for each switchback including the case study. The temperatures inside switchbacks and in the background solar wind are consistent with each other within error. This suggests that $T_{pc,\parallel}$ inside full-reversal switchbacks is not sufficiently enhanced above the background plasma. Using the predicted fast solar wind $T_{pc,\parallel} - v$ relationship at $35R_S$ from (Perrone et al., 2019*b*), it was possible to estimate the expected $T_{pc,\parallel}$ inside switchbacks based on the velocity increase from the background. In each case, this predicted $T_{pc,\parallel}$ was significantly larger than the observed $T_{pc,\parallel}$ within the switchbacks. This could suggest that full-reversal switchbacks do not follow typical $T_p - v$ relationships, or that fast and slow Alfvénic wind have very different $T_p - v$ relationships, and applying a fast wind $T_p - v$ relationship to slow Alfvénic wind is not appropriate. From these results, it is possible to conclude that full-reversal switchbacks have a similar $T_{pc,\parallel}$ to the background solar wind. However, it is not possible to draw conclusions about switchbacks that do not undergo full-reversals. For this, SPAN plasma data must be used (see Sect. 4.6 for a discussion on the results from a subsequent study using SPAN data).

4.5 Switchback Origins

The evidence presented here suggests that the proton core parallel temperature is the same inside and outside full-reversal switchbacks. This was further supported by the behaviour of the RDFs within a case study switchback. These results suggest that the plasma inside full-reversal switchbacks, and potentially all switchbacks, is consistent, to first order, with a rigid velocity-space rotation of the background plasma (i.e. the switchbacks rotate the background plasma distributions but do not significantly change the shape of them). In light of these results, a discussion about switchback origin theories is given below.

Switchback Time Interval	Background $T_{\parallel}$ [$\times 10^6$K]	Switchback $T_{\parallel}$ [$\times 10^6$K]	Predicted Switchback $T_{\parallel}$ [$\times 10^6$K]
1st Nov 18 01:00 - 02:30	0.165 ± 0.031	0.198 ± 0.038	0.262
5th Nov 18 13:45 - 14:20	0.106 ± 0.020	0.076 ± 0.014	0.279
7th Nov 18 03:10 - 04:05	0.111 ± 0.021	0.128 ± 0.024	0.284
31st Mar 19 10:24 - 10:40	0.087 ± 0.017	0.104 ± 0.020	0.216
1st Apr 19 09:50 - 10:46	0.119 ± 0.023	0.173 ± 0.033	0.214

Table 4.1: Proton core parallel temperatures inside and outside five switchbacks (including the case study) measured by Parker Solar Probe. The temperatures inside the switchbacks are within error of the temperatures in the background solar wind, and deviate considerably from the predicted temperatures based on the suggested fast solar wind $T_{pc,\parallel} - v$ relationship in (Perrone et al., 2019*b*). The temperatures are quoted with a 19% error (Case et al., 2020).

There are currently two broad types of theory that describe how switchbacks may be formed: those that involve magnetic reconnection (e.g. Zank et al., 2020; Sterling and Moore, 2020; Drake et al., 2021) and those that involve Alfvénic turbulence (e.g. Squire et al., 2020; Mallet et al., 2021). Reconnection-based theories involve an impulsive magnetic reconnection event which releases either a flux rope (Drake et al., 2021) or Alfvén waves (e.g. Karpen et al., 2017; Roberts et al., 2018; Sterling and Moore, 2020) into the solar wind. In the case of a flux rope, it has been suggested that the flux rope could decay as the solar wind expands, leading to the structures measured in situ by PSP (Drake et al., 2021). For Alfvén waves released into the solar wind by reconnection, however, it has been suggested that they could steepen into larger Alfvén waves before being measured as switchbacks by spacecraft (Sterling and Moore, 2020). Turbulence based theories involve Alfvénic fluctuations within the solar atmosphere. These theories do not require a particular mechanism for the existence of these fluctuations, but argue that the expansion of the solar wind would cause small fluctuations to grow into the switchbacks seen by spacecraft (Squire et al., 2020; Mallet et al., 2021).

The results presented in this chapter do not necessarily rule out any of the theories described above, but they do provide important constraints. For example, to be consistent with the evidence in this chapter, the switchback models must be able to replicate similar plasma conditions inside and outside full-reversal switchbacks.

It is worth noting here that the term 'switchback' is used broadly within the community for most magnetic field deflections away from the background field. It is possible that

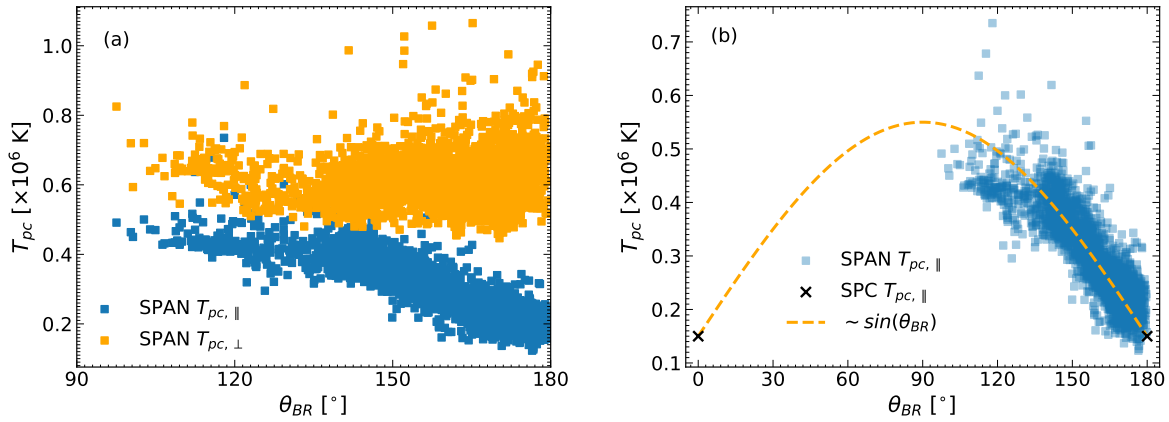


Figure 4.7: Scatter plots showing: (a) the proton core parallel (blue) and perpendicular (orange) temperatures measured by SPAN during a 6-hour interval discussed in Woodham et al. (2021), and (b) the proton core parallel temperature measured by SPAN (blue) and the expected SPC proton core parallel temperatures for a full-reversal switchback (black). The orange dashed line in panel (b) shows a sinusoidal profile of $T_{pc,\parallel}$ which is consistent with both the SPC and SPAN measurements.

---

there are different types of switchbacks with different origins (e.g. Tenerani et al., 2021). This means that further work is needed to determine whether switchbacks can be formed by multiple mechanisms and, if so, which mechanism is most dominant.

4.6 Temperature Profiles for Switchbacks

As mentioned throughout this chapter, this study was limited to full or near-full-reversal switchbacks due to the measurement capabilities of the SPC instrument. However, since the work presented here was published, SPAN data have become available, allowing an analysis of intermediate switchbacks too. In fact, a subsequent study by Woodham et al. (2021) used SPAN data to show that the proton core parallel temperature increases inside switchbacks, while the perpendicular temperature remains constant. Fig. 4.7 (panel a) shows a summary of these findings for the 6-hour interval (with a background magnetic field corresponding to $\theta_{BR} = 180°$) discussed in Woodham et al. (2021). The results of Woodham et al. (2021), therefore, appear contradictory to the results presented in Sect. 4.3 and 4.4. However, both studies can be reconciled by considering the measurements of each instrument and possible functional forms of the $T_{pc,\parallel} - \theta_{BR}$ relationship.

Both SPC and SPAN are limited in the data they can take due to a combination of their design, their position of the spacecraft, the orbital trajectory of PSP, and the plasma dynamics within the solar wind. For example, SPC can only measure $T_{pc,\parallel}$ when $\theta_{BR} = 0°$ or 180°, as discussed in Sect. 3.5. On the other hand, SPAN can only take reliable measurements when the proton core population is within the instrument field of view. For the interval discussed in Woodham et al. (2021), this corresponds to $90° \leq \theta_{BR} \leq 180°$. Fig. 4.7 (panel b) shows the same SPAN $T_{pc,\parallel}$ data as panel (a) and the expected $T_{pc,\parallel}$ measurements from SPC for a full-reversal switchback (based on the behaviour shown in Sect. 4.3). It should be noted that the SPC data are 'expected' because there was no full-reversal switchback within this interval. From Fig. 4.7, it is clear that the SPC measurement of $T_{pc,\parallel}$ inside a switchback (i.e. $\theta_{BR} = 0°$) is not within the range of angles that SPAN can measure. The results of this chapter and Woodham et al. (2021), therefore, do not contradict each other, and can in fact be reconciled if $T_{pc,\parallel} \sim sin(\theta_{BR})$. It is possible that within a patch of switchbacks, there is a non-monotonic $T_{pc,\parallel} - v$ relationship (e.g. $T_{pc,\parallel} \sim sin(\theta_{BR})$) which is distinct from $T_p - v$ relationships observed on larger scales (e.g. Burlaga and Ogilvie, 1970; Lopez and Freeman, 1986). However, it remains unclear whether $T_{pc,\parallel}$ has this functional form or what underlying physical mechanism would be responsible for this sinusoidal dependence.

4.7 Conclusions

In this chapter, SPC-measured ion distribution functions were used to investigate the behaviour of the proton core population within magnetic field switchbacks. A single case study switchback from PSP's first solar encounter was identified. The magnetic field within this switchback had undergone a full reversal from its background orientation. Therefore, it was possible to compare SPC-measured temperatures inside and outside the switchback. RDFs at various times were analysed to determine the differences between the switchback and background plasma. The relative sizes of the kinetic energy and Poynting flux carried by the switchback were calculated. The key results from the case study switchback were validated using additional full-reversal switchbacks. Finally, possible switchback origins and ways to reconcile the work here with a subsequent study were discussed.

The results presented in this chapter indicate that the plasma within switchbacks is

consistent with a velocity space rotation of the background solar wind plasma. This rotation occurs around a pivot velocity that is approximately v_A faster than the proton core population. This finding is consistent with the behaviour of ion species previously reported (Matteini et al., 2014, 2015*b*) and outlined in Sect. 2.4.3. Interestingly, whilst this rotation increases the velocity of the proton core, it does not significantly alter the shape of the RDF. The RDF measured within the case study switchback is not distinctly different from the RDF in the background solar wind, once the velocity space rotation has been accounted for.

A direct consequence of comparable RDFs within the switchback and the background solar wind is that $T_{pc,\parallel}$ is also very similar within the two plasmas. This result was further confirmed by four additional full-reversal switchbacks. The similarity between $T_{pc,\parallel}$ in these switchbacks and the surrounding solar wind indicates that full-reversal switchbacks do not exhibit a clear $T_{pc,\parallel} - v$ relationship. As the solar wind $T_p - v$ relationship is thought to be related to how the near-Sun solar wind is heated (see Sect. 2.4.6), this could be an indication that switchback plasma is not subject to the same heating processes as larger scale solar wind streams. Unfortunately, only full-reversal switchbacks were studied here because of SPC's limitations (Sect. 3.7). Therefore, no direct conclusions can be drawn for intermediate switchbacks. However, based on the discussion in Sect. 4.6 it is possible that switchbacks display a non-monotonic $T_{pc,\parallel} - v$ relationship within a given patch which is separate from larger scale $T_p - v$ relationships reported previously (e.g. Burlaga and Ogilvie, 1970; Lopez and Freeman, 1986).

Finally, it was shown that throughout the case study switchback the radial kinetic energy flux was at least 5 times larger than the radial Poynting flux. This suggests that the kinetic energy flux is much more dominant than the Poynting flux in switchbacks measured during PSP's first solar encounter. From Eq. 4.2, it was clear that the intermediate velocity switchbacks carry the largest amount of radial Poynting flux outwards, while the fastest (and slowest) carry negligible amounts. This makes it highly unlikely that the switchback dynamics are governed by this electromagnetic energy. It was, however, reasoned that as the Alfvén speed increases and the solar wind radial velocity decreases with decreasing heliocentric distance, the radial Poynting flux could dominate over the kinetic energy flux at smaller heliocentric distances.

The work in this chapter addressed some of the questions surrounding switchbacks, but there are still many that remain. For example, it is not clear if the results from this

chapter and the study by Woodham et al. (2021) reconcile with each other (see Sect. 4.6 for a discussion). However, a detailed study on $T_{pc,\parallel}$ inside switchbacks measured during later Parker Solar Probe encounters could help to resolve this question. Switchback research would also benefit from studies connecting theoretical models to in situ measured data. This connection should become easier to address as data from smaller heliocentric distances become available. Finally, studies on the larger scale patch and quiet period structure could complement investigations into switchback origins. The following two chapters of this thesis focus on the switchback patches and quiet periods.

Chapter 5

Characterising Slow Alfvénic Solar Wind inside Patches at 0.13au

Parts of this chapter have been previously published in Woolley et al. (2021).

5.1 Introduction

Patches, as mentioned in Sect. 4.2, are large scale groupings of individual switchbacks. They have typical timescales of hours to days, and are separated by solar wind intervals with very few, if any, switchbacks (Horbury et al., 2020). The discovery of patches in the PSP data was particularly striking as this larger scale structure had not been seen by previous spacecraft, indicating that the patch structure observed in the near-Sun solar wind evolves with increasing heliocentric distance. Patches are an important phenomenon to study because they could not only contribute to the understanding of individual switchbacks, but could also be related to distinct solar wind source regions. Given that most studies to date have focused on individual switchbacks, this chapter aims to characterise the plasma in patches and use this characterisation to better understand their origins. The fact that PSP had the same orbital trajectory during encounter 4 and 5 is exploited and provides a unique opportunity to identify two patches measured at the same heliocentric distance and latitude.

After outlining the relevant background in Sect. 5.2, the data used for this study are described (Sect. 5.3). Sect. 5.4 provides an overview of PSP's fourth and fifth solar encounters before Sect. 5.5 explains how two patches were identified for this work.

The plasma properties of the patches are compared in Sect. 5.6 and used to justify a potential source region for the patches in Sect. 5.7. Sect. 5.8 and Sect. 5.9 discuss the properties of switchbacks and $\alpha-$particle abundance during the patches, respectively. Sect. 5.10 compares the patch plasma to similar solar wind studied at 0.3 au with the Helios spacecraft.

5.2 Patch Background

Despite being measured in all PSP encounters to date, not much is known about switchback patches. This is, in part, due to the fact that most studies have focused on individual switchbacks (e.g. Woolley et al., 2020; Dudok de Wit et al., 2020), rather than this larger scale patch structure. Since then, however, some notable patch studies have been conducted. For example, Woodham et al. (2021) showed that $T_{pc,\parallel}$ in patches tends to be enhanced above the background, whereas $T_{pc,\perp}$ remains relatively constant. It has also been suggested that switchback patches could be related to solar granulation and supergranulation scales (Fargette et al., 2021), although the full extent of this relationship remains unknown.

As patches are heavily linked to switchbacks, it is important to study both structures in order to build a complete description of the physics. Studies of the larger scale patch structure can provide insights into the solar source regions associated with switchbacks, allowing a more focused approach to modelling these phenomena. Following on from Chapter 4, which focused on individual switchbacks, this chapter, addresses two patches measured at the same heliocentric distance and latitude. A comparison of the patch properties is used to make one of the first attempts at associating patches to a solar source region. The following questions are addressed:

1. How similar are the properties within two patches when spatial evolution effects are reduced?

2. What is a possible solar source of switchback patches?

3. Is the wind inside patches consistent with any previously observed solar wind?

5.3 Data

In this study, data from the FIELDS (Bale et al., 2016) and SWEAP (Kasper et al., 2016) instrument suites are used. The FIELDS data were outlined previously in Sect. 2.6.1.3, so the discussion is limited to the SWEAP SPAN data here. It is worth noting that in this study, the data analysed were measured during PSP's fourth and fifth perihelia. Therefore, due to the large tangential velocity of the spacecraft during this time, the data from SPC are unreliable as the ion distributions are often outside the instrument's FOV (see Sect. 3.7). Instead the 3D ion distribution functions measured by the electrostatic analyser (see Sect. 2.5.1) on the ram side of the spacecraft are used.

In order to extract meaningful parameters from the 3D ion distribution functions, a two population bi-Maxwellian was fit to the data. This fitting was done by Michael McManus. The concept behind this fitting is similar to that for the SPC data (see Sect. 3.6), but it includes a secondary proton population and additional dimensions. Details of this fitting procedure can be found in Finley et al. (2021). However, it should be noted that this is only one way of extracting bulk parameters from the distributions and other authors have tried different approaches (e.g. Stansby et al., 2018; Woodham et al., 2021). From the 3D ion distribution functions, it was possible to extract: density, velocity, and temperatures perpendicular and parallel to the magnetic field for both the proton core and proton beam.

As with the SPC data outlined in Chapter 3, care must be taken when working with the SPAN data. The highly Alfvénic nature of the near-Sun solar wind can result in the proton core and beam moving outside the instrument field-of-view. This is a direct result of the motion of ion species under Alfvénic fluctuations and can make the fits unreliable. In this work, the focus is on the proton core population as this is more stable within the SPAN FOV. As the SPAN-ion sensor has an $\alpha-$particle channel, it is also possible to fit the $\alpha-$particle population using a similar procedure, after removing the proton contamination. The SPAN proton and $\alpha-$particle fits used in this study were provided by Michael McManus.

Fig. 5.1 shows an example 3D ion velocity distribution function measured by SPAN in the instrument frame. The top panel shows the $v_x - v_y$ plane and the bottom panel shows the $v_x - v_z$ plane. The proton core population is within the instrument FOV during this time and has been fitted with a bi-Maxwellian (dotted contours).

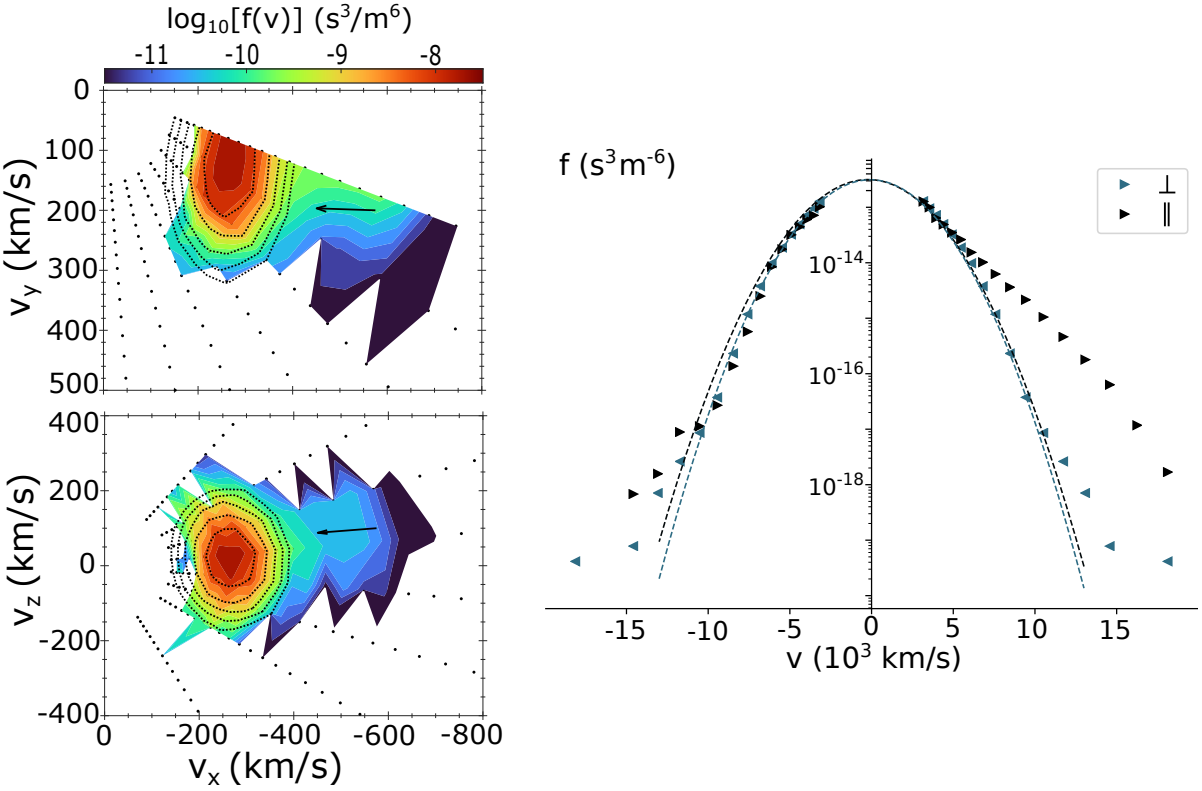


Figure 5.1: (left) 3D ion VDF measured by SPAN in the instrument frame. The black arrow indicates the average magnetic field orientation at this time. The dotted contours show the fit to the proton core population. *Figure credit: Woodham et al. (2021). ©ESO. Reproduced with permission.* (right) Example cuts through an electron VDF measured by Parker Solar Probe in the near-Sun solar wind. The black arrows show the cut through the distribution parallel to the magnetic field and the blue arrows show a cut perpendicular to the magnetic field. The direction of the triangles indicates which instrument on board PSP measured the data: right pointed triangles were measured by SPAN-A and left pointed triangles by SPAN-B (see Sect. 3.2 for more details on the instruments on board PSP). The dashed blue and black lines show the Maxwellian fit to the electron core for the perpendicular and parallel cuts, respectively. *Figure credit: Berčič et al. (2020). ©AAS. Reproduced with permission.*

In addition to ions, electrons can provide useful information about the solar wind too. Here the electron strahl parallel temperature, which was obtained by fitting a 1D Maxwellian to the electron strahl population in the magnetic field aligned solar wind rest frame, is used. The magnetic field aligned solar wind rest frame was found using magnetic field measurements from the MAG instrument and velocity moments from SPAN-ions. The full details of this fitting procedure are outlined in Berčič et al. (2020). The electron fits used in this study were provided by Laura Berčič. Fig. 5.1 shows cuts through a 3D electron VDF measured by SPAN.

5.4 Encounter 4 and 5 Overview

Before analysing and investigating individual patches in encounter 4 and 5, it is worth looking at the data for these intervals. Fig. 5.2 shows an overview of the PSP measurements during encounter 4 (left) and encounter 5 (right). During this time PSP reached a closest approach of approximately 0.13 au (panel g) and sampled wind within 4° of the equatorial plane (panel f). The orbital trajectory of PSP during these two encounters was the same, apart from a shift in longitude.

Panel (a) shows the magnetic field magnitude which peaks at roughly 150nT in both encounters and falls off either side of perihelion. In the first half of both encounters, $|\mathbf{B}|$ falls off approximately as r^{-2} (orange dashed line), which is expected for a radial magnetic field. However, $|\mathbf{B}|$ deviates more substantially from this theoretical prediction in the second half of both encounters. This is likely because PSP is embedded in the streamer belt close to the HCS, where the behaviour of $\mathbf{B}$ is more complex. Panel (b) shows that the behaviour of B_R changes from being full of switchbacks that are grouped into patch structure, to fewer smaller switchbacks that are not so well defined by patches close to the HCS. This suggests that patches are a feature of solar wind away from the HCS, but may not be present in the streamer belt wind. The distinct change in plasma conditions between the two halves of the encounter can also be seen in the suppression of the proton core radial velocity (panel c), the reduction in the proton core temperature anisotropy (panel d), and the increase in electron density (panel e) after perihelion. These parameter changes are consistent with the current picture of streamer belt solar wind.

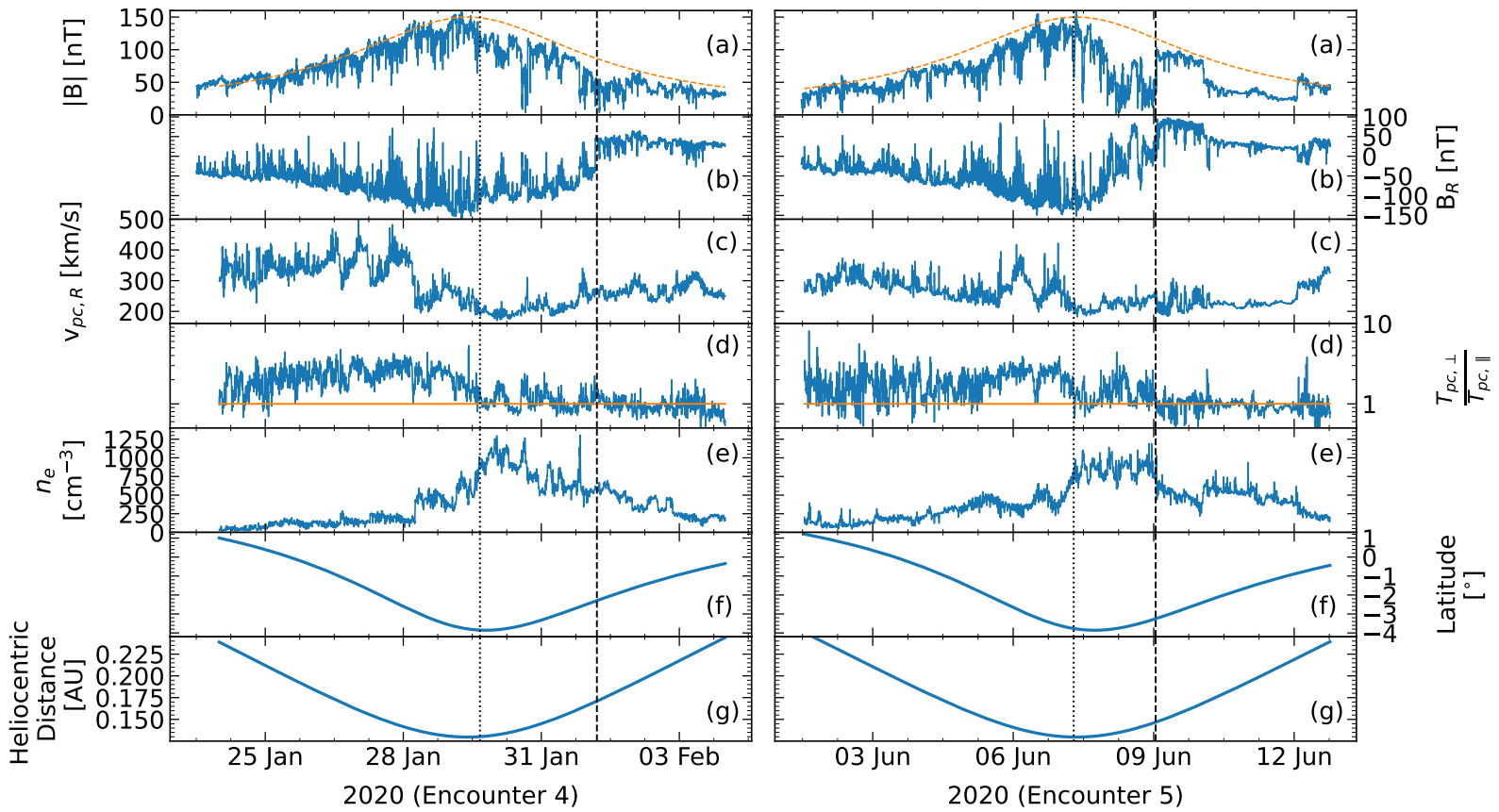


Figure 5.2: Time series of encounter 4 (left) and encounter 5 (right) data from Parker Solar Probe. The panels show: (a) the magnetic field magnitude, (b) the radial component of the magnetic field, (c) the proton core radial velocity, (d) the proton core temperature anisotropy, (e) the electron number density, (f) PSP's latitude, and (g) PSP's heliocentric distance. The black dotted vertical lines indicate when PSP enters the streamer belt. The black dashed lines indicate when PSP crossed the HCS. The orange dashed line in panel (a) shows the expected $|\mathbf{B}|$ profile for a radially expanding solar wind (r^{-2}), and the solid orange line in panel (d) shows where the temperature anisotropy is unity.

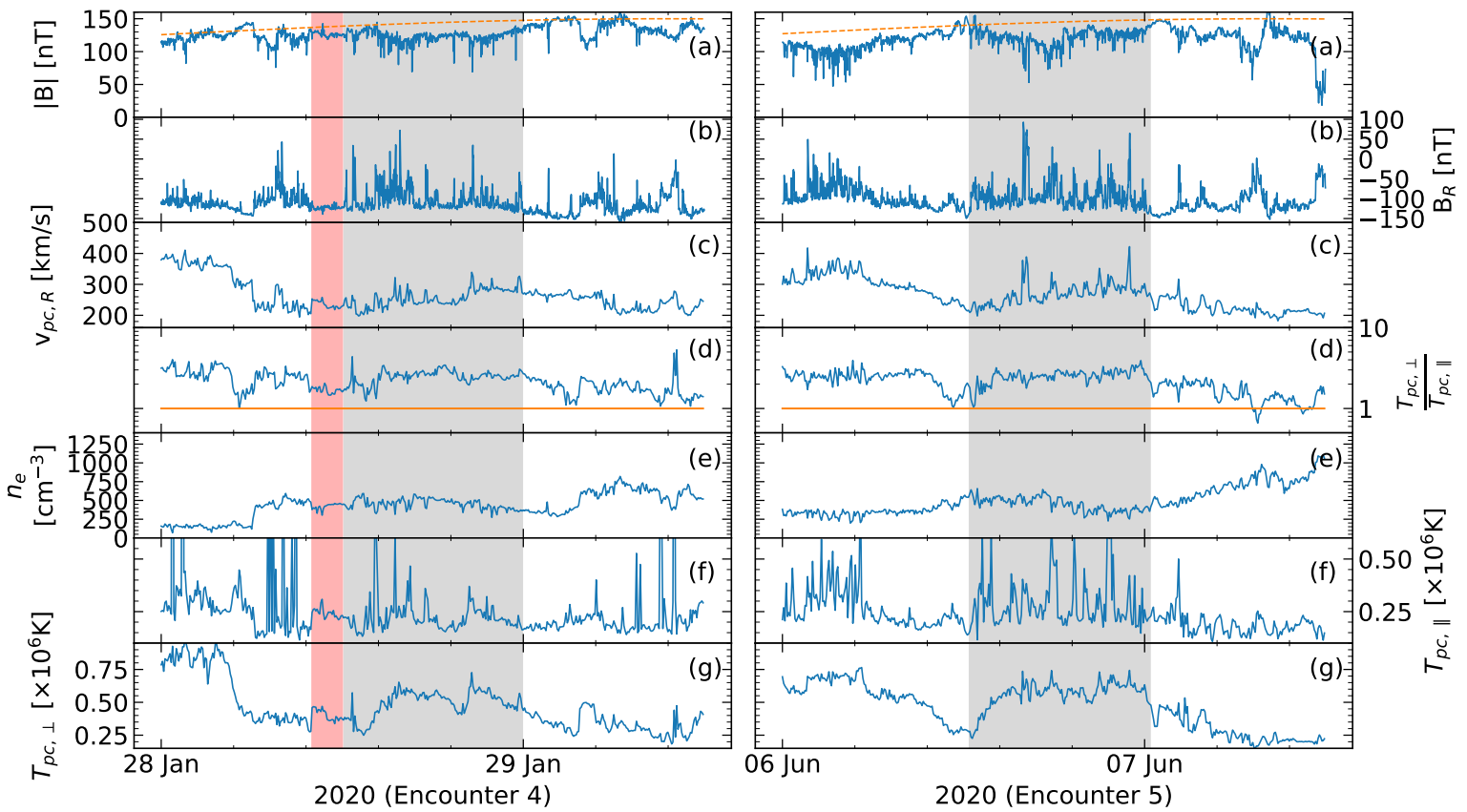


Figure 5.3: Time series of the two chosen patches (shaded grey) and the quiet period (shaded red). The panels show: (a) the magnetic field magnitude, (b) the radial component of the magnetic field, (c) the proton core radial velocity, (d) the proton core temperature anisotropy, (e) the electron number density, (f) the proton core parallel temperature, and (g) the proton core perpendicular temperature. The orange dashed line in panel (a) shows the expected $|\mathbf{B}|$ profile for a radially expanding solar wind (r^{-2}), and the solid orange line in panel (d) shows where the temperature anisotropy is unity. *Figure credit: Woolley et al. (2021). ©Oxford University Press. Reproduced with permission.*

5.5 Identification of Patches

Now that the key features of encounter 4 and 5 have been discussed, the patches can be analysed. The first step towards understanding patches and the solar wind properties within them is to be able to identify them. Because patches are a new discovery with the PSP data, there is currently no consensus for identifying them or the quiet periods that often separate them. It is difficult to automate the identification of patches as there is no single parameter that consistently signifies a change in the solar wind. Often a manual approach is the most appropriate for identifying these solar wind structures. Here the PSP encounter 4 and 5 data were visually inspected to find a pair of patches to compare.

The main objective when identifying patches for this study was to be able to reduce spatial evolution. To do this, two patches were identified at the same heliocentric distance (0.13 au) and the same latitude (-3.5°), although it was not possible for the patches to also have the same longitude. The justification for prioritising the same latitude and radius over the same longitude is that previous studies have shown that solar wind properties are heavily dependent on latitude (e.g. Laker et al., 2021*b*) and heliocentric distance (e.g. Hellinger et al., 2011, 2013). The dependence on latitude is particularly important during solar minimum as the heliospheric current sheet is flat, and small changes in latitude can result in spacecraft measuring different structures (Laker et al., 2021*b*).

The chosen patches were the clearest example of two patches measured at the same heliocentric distance and latitude throughout the fourth and fifth encounters. A quiet period that was measured just before the encounter 4 patch was also identified. This quiet period is used as a comparison interval to the patches during this study. Fig. 5.3 shows the two patches (shaded grey) and the quiet period (shaded red) used for comparison. The patches (quiet periods) are most clearly shown in the magnetic field radial component (panel b) by the presence (absence) of switchbacks. Both patches have a rising velocity profile throughout (panel c) and a proton core temperature anisotropy above 1 (panel d). The electron number density (panel e) remains roughly constant in the patches. The proton core parallel (panel f) and perpendicular (panel g) temperatures appear to vary with the radial magnetic field and the radial velocity, respectively. The quiet period is approximately 2 hrs long whereas the patches are approximately 12 hrs long. This timescale difference is typical of the PSP data as quiet periods tend to be much shorter in duration than patches.

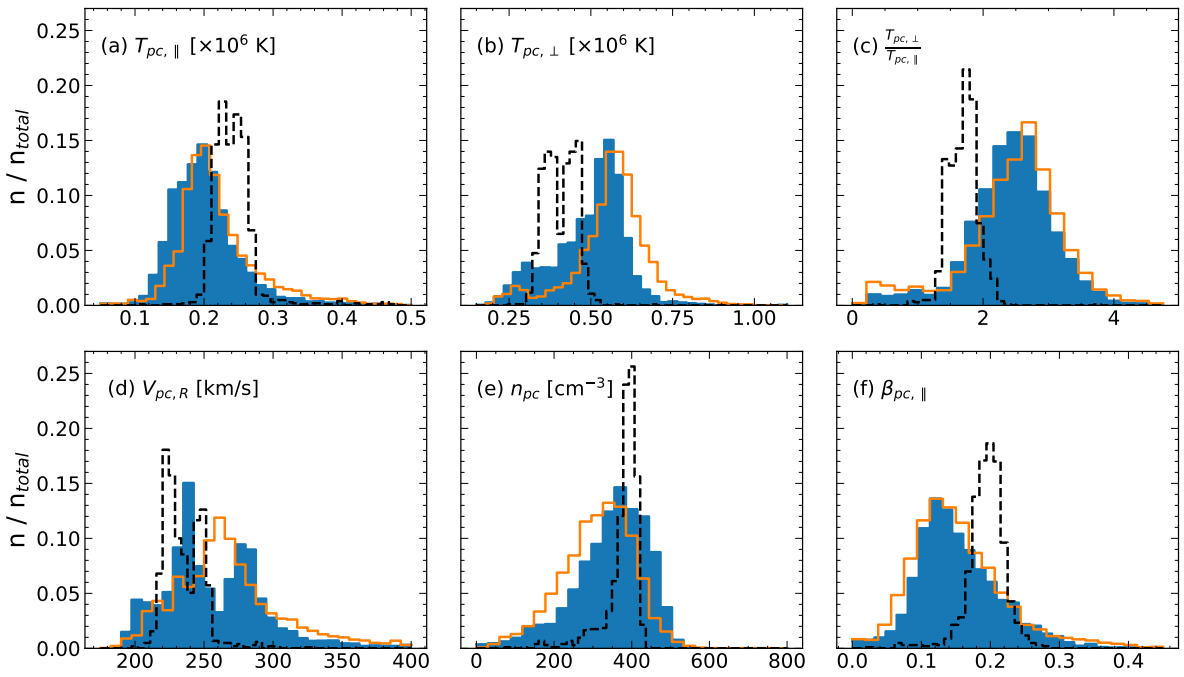


Figure 5.4: Distributions of proton core plasma properties within the encounter 4 patch (blue), encounter 5 patch (orange) and the quiet period (black). The panels show: (a) parallel temperature, (b) perpendicular temperature, (c) temperature anisotropy, (d) radial velocity, (e) density, and (f) plasma parallel β. Each distribution is normalised by the total number of counts. *Figure credit: Woolley et al. (2021). ©Oxford University Press. Reproduced with permission.*

5.6 Plasma Properties of the Patches

As these patches were measured at the same heliocentric distance and latitude, the data provide a very rare opportunity for studying the plasma properties without significant influences from spatial evolution of the plasma. Fig. 5.4 shows the distributions of key plasma parameters for the encounter 4 patch (blue), encounter 5 patch (orange) and the quiet period (black).

The first thing to note is that, in general, the distributions of the patch plasma parameters are much more similar to each other than they are to the quiet period plasma parameters. Both patches have proton core parallel temperatures (panel a) that peak around 0.2×10^6 K, perpendicular temperatures (panel b) that peak around 0.6 ×10^6 K, and anisotropies ~ 3 (panel c). The proton core densities (panel e) and plasma $\beta_{\parallel}$ (panel f) peak at 360 cm^{-3} and 0.15, respectively.

Interestingly, the proton core radial velocity distributions (panel d) of the patches

show different behaviour. The encounter 5 patch has a distribution peaked at about 260 km/s whereas the encounter 4 patch has a double peaked distribution at about 240 km/s and 270 km/s. This difference is caused by the varying velocity profiles within each patch. The encounter 5 patch has a smooth velocity increase throughout, while the encounter 4 patch displays a more discontinuous increase. This is likely caused by the internal dynamics of the patch region which are not considered in detail here. These velocity differences may also explain the slight temperature discrepancies between the two patches. For example, the E5 patch is $\sim 5\%$ faster on average and displays slightly hotter temperatures (predominantly $T_{pc,\perp}$ rather than $T_{pc,\parallel}$) than the E4 patch. This is consistent with typical $T_p - v$ relationships in the solar wind (Burlaga and Ogilvie, 1970; Lopez and Freeman, 1986) and suggests that the $T_p - v$ relationship may be stronger for $T_{pc,\perp}$ than $T_{pc,\parallel}$. A similar result for fast solar wind has been shown previously by Perrone et al. (2019*b*). It is worth noting that a $T_p - v$ relationship between different patches does not contradict the discussion on switchback temperature profiles in Chapter 4. The focus in Chapter 4 was on individual structures within a given solar wind patch, whereas the discussion here compares two different larger scale patches. It is possible that there is both a $T_p - v$ relationship on larger scales between different solar wind streams and a non-monotonic $T_p - v$ relationship for switchbacks within a given stream.

The quiet period has a higher proton core parallel temperature and a lower proton core perpendicular temperature than the patches. This leads to an overall lower anisotropy ~ 1.75. It also has a reduced velocity (~ 220 km/s) and a higher plasma $\beta_{\parallel}$, while the proton core density is similar to and more stable than that of the patches. These results suggest that the plasma inside patches is distinct to the plasma inside quiet periods (see Chapter 6 for a more in-depth study of quiet period properties).

Fig. 5.5 shows distributions of the $\alpha-$particle data from the encounter 5 patch. The $\alpha-$particle data for the encounter 4 patch and quiet period are not shown here because the counts in SPAN were particularly low, and hence the fits were unreliable. The encounter 5 data were visually inspected to ensure the counts were significant and the fits were representative of the distributions.

The encounter 5 $\alpha-$particles, have a parallel temperature $\sim 4.5 \times 10^6$ K (panel a) and a perpendicular temperature $\sim 3.5 \times 10^6$ K (panel b), leading to a temperature anisotropy < 1 (panel c). This is in direct contrast to the proton core which has a temperature anisotropy > 1. $\alpha-$particles may have opposite anisotropy for a couple of

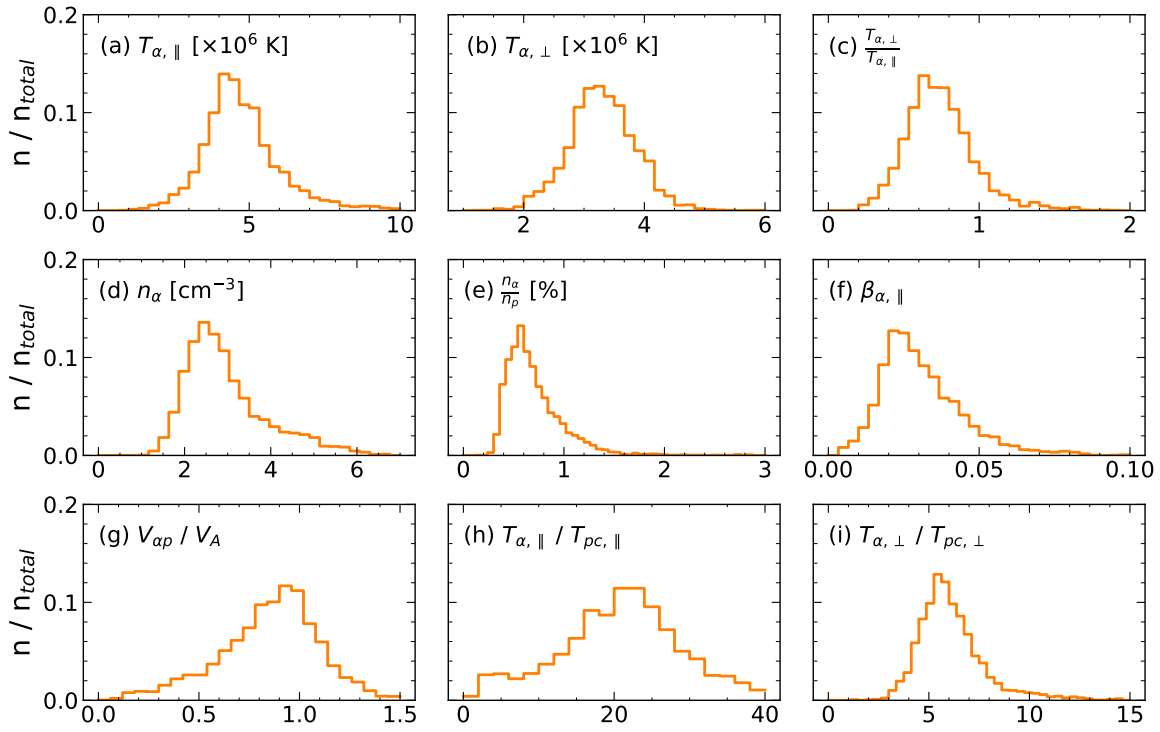


Figure 5.5: Distributions of $\alpha-$particle properties within the encounter 5 patch. The panels show: (a) parallel temperature, (b) perpendicular temperature, (c) temperature anisotropy, (d) density, (e) abundance, (f) plasma parallel β, (g) normalised $\alpha-$proton drift speed, (h) $\alpha-$proton parallel temperature ratio, and (i) $\alpha-$proton perpendicular temperature ratio. Each distribution is normalised by the total number of counts. *Figure credit: Woolley et al. (2021). ©Oxford University Press. Reproduced with permission.*

---

reasons. Firstly, $\alpha-$particles and protons may be subject to different heating mechanisms. However, it is unclear which heating mechanism could produce solar wind with $T_{p,\perp}/T_{p,\parallel} > 1$ and $T_{\alpha,\perp}/T_{\alpha,\parallel} < 1$ close to the Sun. On the other hand, $\alpha-$particles may initially have an anisotropy greater than 1. This anisotropy could then be reduced by plasma instabilities as the solar wind evolves (Maruca et al., 2012). The evolution of the patch solar wind is discussed in more detail in Sect. 5.10.

The density of $\alpha-$particles is around 3 cm^{-3} leading to an abundance ~ 0.6 %. This is low compared to what is observed at 1 au (Ogilvie and Wilkerson, 1969; Robbins et al., 1970; Neugebauer, 1981; Alterman et al., 2021), and is discussed further in Sect. 5.9. Panel (g) shows that whilst the drift speed between the $\alpha-$particles and the proton core peaks at v_A, it can be more or less than the local Alfvén speed. Finally, panels (h) and (i) show $\alpha-$particle to proton core parallel and perpendicular temperature ratios. The

$\alpha-$particles are typically ~ 20 times hotter than the proton core parallel to and ~ 6 times hotter than the proton core perpendicular to the local magnetic field. These ratios are consistent with previous results reported by Stansby et al. (2020*a*). The large $\alpha-$proton temperature ratios could be direct evidence of preferential ion heating in the solar wind by instabilities (e.g. Gary et al., 2000) or close to the Sun by some mechanism (e.g. Chandran, 2010).

The plasma conditions presented above suggest that the two case study patches are associated with slow Alfvénic solar wind. Not only does the solar wind in these intervals have a low bulk speed and a high correlation between the magnetic field and velocity fluctuations, it also exhibits proton temperature anisotropy, large $\alpha-$proton differential speeds and high $\alpha-$proton temperature ratios. These properties have been previously reported for slow Alfvénic wind in the Helios data (Stansby et al., 2020*a*). Given that the patch solar wind studied here is consistent with slow Alfvénic wind, the potential source of this wind can be investigated.

5.7 Determining the Source Region

5.7.1 Electron Strahl Parallel Temperature

As the electron strahl population undergoes little interaction as it leaves the Sun, the electron strahl parallel temperature ($T_{strahl,\parallel}$) is thought to be a good estimate of the source temperature in the corona (Berčič et al., 2020). Therefore, by considering $T_{strahl,\parallel}$ in each interval it is possible to obtain an approximate source region temperature. Fig. 5.6 shows the distributions of the electron strahl parallel temperature for the two patches and the quiet period. The distributions are similar and all peak around 1.1×10^6 K. This similarity is not simply due to the $T_e - v$ relationship for electrons, as for a given solar wind speed the strahl temperature can vary by $\sim 25\%$ (Berčič et al., 2020). Therefore, Fig. 5.6 indicates that the solar wind in all three intervals originates from regions on the Sun with similar temperatures. However, this does not necessarily mean that the solar wind originates in the same source region.

There is currently no clear consensus on the electron temperatures within different solar source regions. Previous work by Berčič et al. (2020) using early PSP data suggests that a crude categorisation of electron strahl temperatures can distinguish between coronal

features on the Sun. Berčič et al. (2020) separated the electron strahl temperatures into low ($< 0.87 \times 10^6$ K), intermediate (0.87×10^6 - 0.99×10^6 K) and high ($> 0.99 \times 10^6$ K) values. Based on this categorisation, the low temperature values correspond to the centres of large coronal holes, whereas intermediate and high temperatures correspond to the boundary regions of small coronal holes. For the solar wind intervals discussed in this chapter, the strahl temperatures (Fig. 5.6) appear larger than those of solar wind from the centre of a coronal hole in PSP's first solar encounter (Berčič et al., 2020). In fact, based on the data discussed in Berčič et al. (2020), Fig. 5.6 suggests the solar wind in the patches and quiet period is consistent with coronal hole boundary regions (i.e. $T_{strahl,\parallel} > 0.99 \times 10^6$ K). However, this conclusion is not definitive as there are discrepancies between coronal hole temperature estimates. For example, David et al. (1998) found that the electron temperature within coronal holes could not be larger than 10^6 K whereas, Ko et al. (1997) found that the electron temperature could reach 1.5×10^6 K. Discrepancies in electron strahl temperature mainly originate from determining the exact origin of the electron population that is being measured. This is particularly difficult close to the intersection of two source regions (i.e. at the boundary of coronal hole and quiet Sun regions). Further work is need to fully relate in situ $T_{strahl,\parallel}$ data to solar source regions.

For this work, it is only possible to conclude that the solar wind in the three intervals originated in source regions with a similar temperature. The remainder of this section presents evidence for the source region of the patches (the origins of quiet periods are left for Chapter 6).

5.7.2 Potential Field Source Surface Mapping

It is possible to predict which source region on the Sun the plasma originated from. To do this a combination of ballistic mapping and a Potential Field Source Surface (PFSS) model (Altschuler and Newkirk, 1969; Schatten et al., 1969) is used.

Ballistic mapping determines the location on the source surface - the distance from the Sun where all magnetic field lines are assumed to be radial - where the plasma was released. This mapping effectively follows the Parker spiral back towards the Sun to account for the rotation of the Sun during the plasma transit time. The simplest way to do ballistic mapping is to assume that the solar wind travels away from the Sun with a constant, purely radial velocity (v_R). Under this assumption, the source surface longitude can be determined using:

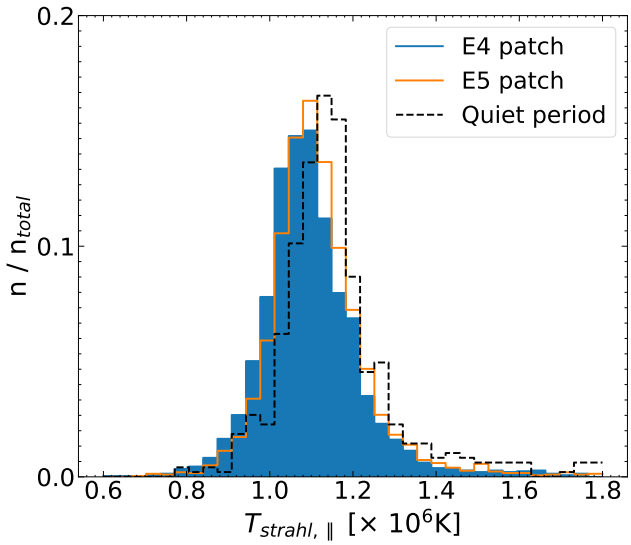


Figure 5.6: Distributions of the electron strahl parallel temperature for the encounter 4 patch (blue), encounter 5 patch (orange) and the quiet period (black). The distributions are normalised by the total number of counts. *Figure credit: Woolley et al. (2021). ©Oxford University Press. Reproduced with permission.*

$$Lon_{SS} = Lon_{PSP} + \frac{R_{PSP} - R_{SS}}{v_R}\Omega, \tag{5.1}$$

where Ω is the rotation rate of the Sun and R_{SS} is typically taken to be $2.5R_S$. As the solar wind is assumed to have a purely radial velocity in this mapping, the source surface latitude is taken to be the latitude at which the solar wind was measured.

Using these source surface coordinates, the PFSS model can then be applied. The PFSS model assumes that the solar corona is current free (i.e. $\bigtriangledown \times \mathbf{B} = 0$) and therefore the magnetic field can be written as a scalar potential (i.e. $\mathbf{B} = -\bigtriangledown \phi_B$). Whilst the assumption of a current-free corona is not an accurate description of the solar atmosphere, it is sufficient for uses when mapping to large scale solar features. Applying Gauss' law to the scalar potential gives Laplace's equation:

$$\bigtriangledown^2 \phi_B = 0, \tag{5.2}$$

which can be solved to trace the magnetic field lines from the source surface back to the solar surface. In order to solve this equation, the model requires a Global Oscillation Network Group (GONG; Harvey et al. (1996)) magnetogram as the input.

PFSS mapping has been used in a variety of other studies (e.g. Badman et al., 2020; Laker et al., 2021*b*; O'Kane et al., 2021) and can be implemented with the python pfsspy package (Stansby et al., 2020*b*). It is worth noting that PFSS models are not perfect as they assume a current-free corona and always map to open magnetic field lines. Therefore, PFSS mapping should not be used solely to justify a given source region, but as complementary evidence to support other analysis.

When the PFSS model was applied to the two patches considered here, it was found that they both originated close to the boundary of the southern polar coronal hole (see Fig. 5.7). The connectivity of this model was consistent with the magnetic field polarity observed by PSP through these intervals. However, as PSP was close to the HCS during this time, further evidence is needed to rule out streamer belt contributions.

5.7.3 Magnetic Field Power Spectral Density

It may be possible to distinguish various solar wind source regions based on the magnetic field power spectral density (PSD). Previous work by Chen et al. (2021) showed that the inertial range scaling on the inbound and outbound section of encounter 4 were different. Chen et al. (2021) argued that this difference was due to the proximity of PSP to the HCS in the second half of the encounter. It was shown that the solar wind measured near to the HCS had an inertial range scaling of $f^{-5/3}$ whereas, the solar wind measured away from the HCS has an inertial range scaling of $f^{-3/2}$ (Chen et al., 2020, 2021).

Fig. 5.8 shows the PSD of magnetic field fluctuations for the two patches. The inertial range scaling of both patches is consistent with $f^{-3/2}$ rather than $f^{-5/3}$. This indicates that the solar wind in patches is not consistent with wind close to the HCS (i.e. streamer belt wind). Instead, the patch wind is consistent with solar wind from another source which is likely to be a polar coronal hole during solar minimum.

5.7.4 Similarity to Fast Solar Wind

The plasma properties presented in Sect. 5.6 show similarities to the fast solar wind which is already known to come from coronal holes (Krieger et al., 1973; Nolte et al., 1976; Sheeley et al., 1976; Neugebauer et al., 1998). For example, fast solar wind typically displays high $\alpha-$proton drifts (Berger et al., 2011; Alterman et al., 2018), anisotropic proton temperatures (Marsch et al., 1982*b*) and larger $\alpha-$proton temperature ratios (Marsch

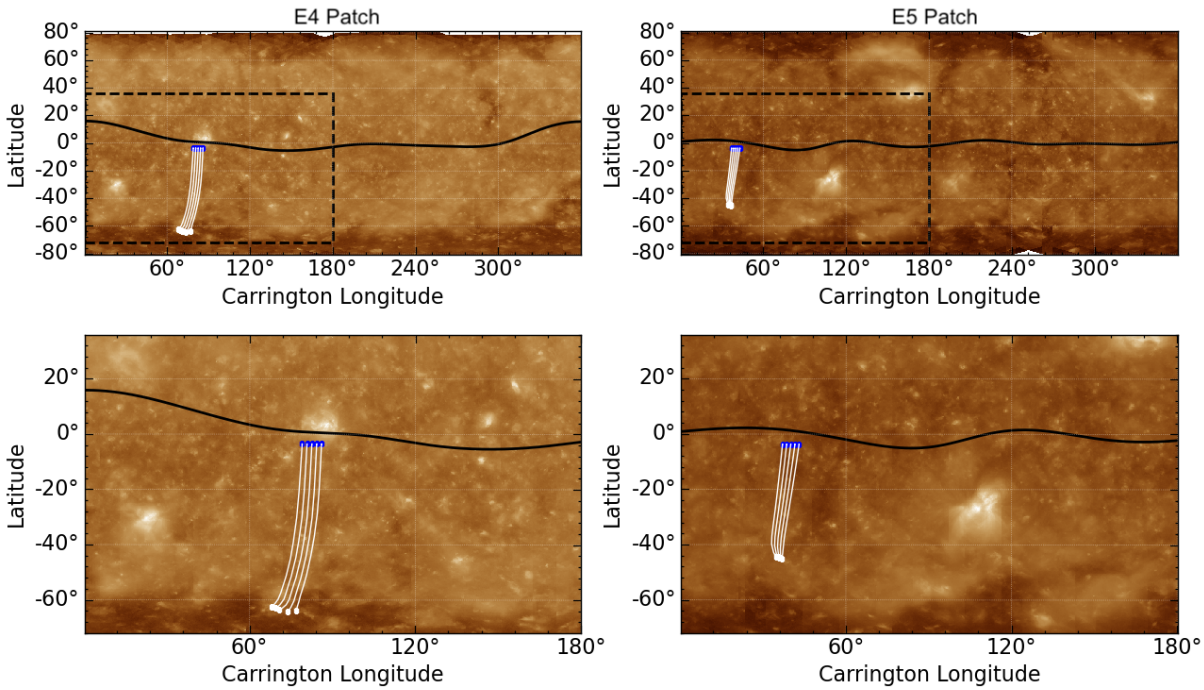


Figure 5.7: Potential Field Source Surface (PFSS) mappings for the encounter 4 (left) and encounter 5 (right) patches. The top row shows the whole solar surface and the bottom row shows a close up of the region of interest (indicated with a dashed box in the top row). The blue points show where PSP measured the solar wind and the white points show where it was magnetically connected to during this time. The black solid line shows the heliospheric current sheet. The solar surface image is made from a combination of 19.3nm AIA images measured over a solar rotation. *Figure credit: Woolley et al. (2021). ©Oxford University Press. Reproduced with permission.*

et al., 1982*a*; Stansby et al., 2020*a*). It is also common for the fast solar wind to display anisotropic $\alpha-$particle temperatures in the opposite sense to protons (i.e. $T_{\alpha,\perp}/T_{\alpha,\parallel} < 1$) (Marsch et al., 1982*b*). All of these characteristics were observed in the patch solar wind studied here and a previous slow Alfvénic wind study (Stansby et al., 2020*a*). Following arguments presented by previous studies (e.g. D'Amicis and Bruno, 2015; Stakhiv et al., 2015, 2016; Stansby et al., 2020*a*), this could indicate that the slow Alfvénic wind associated with patches could also originate in coronal holes or at coronal hole boundaries.

5.7.5 Summary of Possible Source Regions

The three pieces of evidence presented in this section suggest that patch solar wind is associated with coronal hole source regions. The two patches studied here were measured by PSP during solar minimum when no equatorial coronal holes were present. Therefore, it is likely that the solar wind in both patches originated in the southern polar coronal hole as indicated by the PFSS mapping. The fact that both patches likely had the same source region could also explain the striking similarities discussed in Sect. 5.6. Further work with the Solar Orbiter heavy ion data could help to confirm the source regions of patches.

5.8 Switchback Statistics in Patches

Additionally, it is worth looking at the properties of switchbacks in these patches. For the purpose of this work, switchbacks were identified based on how the local magnetic field changed with respect to a 5 hr background average. The magnetic field cone angle - the angle between the magnetic field vector and the radial direction in RTN coordinates - was used to identify switchbacks as any time the cone angle varied by more than 20° from the background. Switchbacks with a duration $<$ 1s (four data points) were then filtered out. It should be noted that there is currently no consensus for identifying switchbacks in the solar wind and so each study differs depending on the requirements of that particular work. In this section, waiting time distributions and deflection-duration correlations are computed. The waiting time distributions describe the distributions of times between consecutive switchbacks and have been discussed comprehensively in Dudok de Wit et al. (2020). These were calculated by finding the time difference between the end of one switchback and the start of the next switchback. These time differences were grouped into discrete

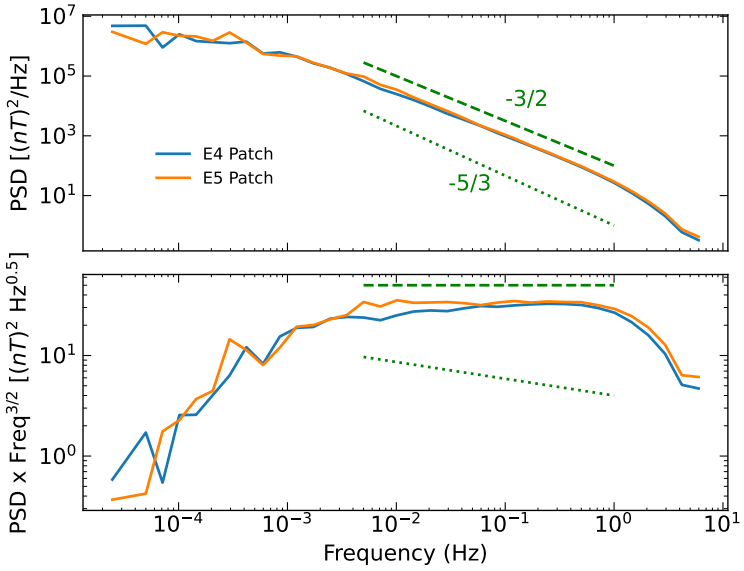


Figure 5.8: Power spectral density (panel a) and compensated power spectral density (panel b) of the total magnetic field fluctuations during the encounter 4 patch (blue) and encounter 5 patch (orange). The dashed (dotted) green lines show the expected gradient for a $f^{-3/2}$ ($f^{-5/3}$) inertial range spectra. *Figure credit: Woolley et al. (2021). ©Oxford University Press. Reproduced with permission.*

---

bins and the counts for each bin were normalised by the total counts to get a probability distribution. Deflection-duration correlations measure the Pearson correlation coefficient between the maximum angle of deflection and the total duration for each switchback.

Tab. 5.1 shows the properties of the switchbacks identified in each patch. Overall, the statistics for each patch are remarkably similar, and both patches have approximately the same number of switchbacks. For each patch, $\sim$ 16 % of the time PSP measures a switchback and the waiting times between switchbacks have similar power laws. These waiting time statistics are consistent with previous work that analysed switchbacks during the first PSP solar encounter (Dudok de Wit et al., 2020). The statistics presented here also support the observation by Horbury et al. (2020) that the switchbacks with larger deflections last for a longer time than those with smaller deflections.

As a final note, 20° was arbitrarily chosen as the threshold for defining switchbacks. This threshold was varied to see how much impact it had on the results presented above. It was found that the results were not strongly dependent on the switchback threshold apart from the fact that the percentage of the streams that were considered switchbacks

	E4 Patch	E5 Patch
No. of switchbacks	817	851
Switchback % of stream	16.4	15.6
Deflection-duration correlation	0.58	0.69
Waiting time power law	-1.44 ± 0.04	-1.51 ± 0.10

Table 5.1: Statistics of switchbacks identified in the E4 and E5 patches. *Table credit: Woolley et al. (2021). ©Oxford University Press. Reproduced with permission.*

---

increased for a decreasing threshold.

5.9 Low $\alpha-$particle Abundance in E5 Patch

A particularly interesting result shown in Fig. 5.5 is the low $\alpha-$particle abundance (A_α) that peaks at $\sim 0.6\%$. This is much lower than the expected A_α at 1 au during solar minimum (1-2%, Hirshberg et al., 1972; Kasper et al., 2007, 2012). This seemingly inconsistent result can be explained using an argument based on a one-dimensional flux tube.

Kasper et al. (2007) showed that by considering the motion of protons and $\alpha-$particles along a one-dimensional flux tube, the $\alpha-$abundance varies with the $\alpha-$proton drift speed. Specifically, as the drift between the two ion species reduces, the $\alpha-$ particle abundance increases. This effect is a direct result of mass conservation and leads to the $\alpha-$abundance of a given stream increasing with heliocentric distance. This increase occurs because of two reasons. First, the drift between the $\alpha-$particles and the protons is typically a large fraction of the local Alfvén speed. As the Alfvén speed decreases with heliocentric distance, so does the drift between the protons and $\alpha-$particles (the Alfvén speed is expected to decrease as r^{-1} for a radially expanding solar wind with a purely radial magnetic field). Second, the fraction of the local Alfvén speed at which the $\alpha-$particles travel ahead of the protons reduces (Marsch et al., 1982*a*; Neugebauer et al., 1996), meaning that the typical $\alpha-$proton drift decreases faster than the Alfvén speed.

Kasper et al. (2007) derived an equation to estimate how the $\alpha-$particle abundance varies with distance as follows. It was assumed that protons and α-particles flow along a one-dimensional flux tube with a cross-sectional area S. Due to conservation of particles for each species, i, the following equation must hold for both protons and $\alpha-$particles at

all distances along that flux tube, r:

$$S_r v_{i,r} n_{i,r} = constant. \tag{5.3}$$

The number density of each species at a distance r along the flux tube can then be related to the number density at any other point along the flux tube, r_0:

$$n_{i,r} = \frac{S_{r_0}}{S_r} \frac{v_{i,r_0}}{v_{i,r}} n_{i,r_0}. \tag{5.4}$$

Taking the ratio of the number density for $\alpha-$particles and protons gives the following equation:

$$A_r = A_{r_0} \frac{(1 + \Delta v_{r_0}/v_{p,r_0})}{(1 + \Delta v_r/v_{p,r})}, \tag{5.5}$$

where $\Delta v_r = v_{\alpha,r} - v_{p,r}$. Eq. 5.5 then allows predictions to be made about the change in $\alpha-$particle abundance from the measurement distance r_0 to another distance r.

Using typical values for the E5 stream, the $\sim 0.6\%$ $\alpha-$particle abundance measured by PSP at $\sim$0.13 au would correspond to an abundance $\sim 0.9\%$ at 1 au. This is much more comparable to the expected abundance for slow solar wind during solar minimum. However, this $\alpha-$particle abundance is still very low compared to the fast Alfvénic solar wind which is also thought to come from coronal holes. The difference in $\alpha-$particle abundances may be a direct result of processes that govern the release and acceleration of the solar wind close to the Sun.

There are two main competing theories about how the solar wind is released. The first theory suggests that all solar wind is initially confined to closed magnetic field loops. These closed loops can then undergo interchange reconnection (see Fig. 5.9) with nearby open magnetic field lines, releasing their plasma onto the open field lines where it can then be accelerated outwards (Fisk et al., 1999; Fisk and Schwadron, 2001). Interestingly, this process could also explain the formation of switchbacks (see Sect. 4.5). In this scenario, the final solar wind conditions measured in the heliosphere are directly related to the conditions of the closed field plasma (Fisk et al., 1999). There have been numerous studies that support this idea, including Fisk (2003) and Gloeckler et al. (2003) which showed that the final solar wind speed squared was inversely proportional to the temperature of closed-loop plasma. Combining this result with the study of Feldman et al. (1999) that

showed hotter loops tends to be larger, leads to the conclusion that the very slowest solar wind comes from the largest closed field lines. More recently, Rakowski and Laming (2012) showed that not only is gravitational settling too slow to alter the abundance inside closed loops as suggested by Byhring (2011), but that the FIP effect (first ionisation potential effect; Laming (2004)) is more effective at depleting the $\alpha-$particle abundance in the largest loops. Overall, this interchange reconnection theory suggests that slow solar wind has a low $\alpha-$particle abundance because it originates in hot, large closed field regions where the FIP effect has depleted the $\alpha-$particle content.

The second theory does not require interchange reconnection in the solar atmosphere and instead suggests that the plasma flows from its source region along open field lines into the heliosphere. In this picture, the final properties of the solar wind are determined by the amount of expansion that occurs as the solar wind travels outwards. In support of this theory, Levine et al. (1977) found a good relationship between the solar wind velocity measured at 1 au and the expansion of the individual magnetic flux tubes. Furthermore, Cranmer et al. (2007) modelled this situation by only varying the magnetic field and achieved reasonable values for various solar wind parameters. Geiss et al. (1970) suggested that the $\alpha-$particles get dragged out into the heliosphere by dynamical friction from the protons. Therefore, the abundance should be highly correlated to the proton flux. In cases when the proton flux is too low, the abundance could be depleted. However, work by Stansby et al. (2020*a*) shows no obvious relationship between abundance and proton flux for streams of different speeds. This suggests that there could be other mechanisms affecting the $\alpha-$particle content.

The results presented in this chapter cannot distinguish between these two theories, and therefore further work must be done to gain a better understanding of $\alpha-$particle abundance in the solar wind. It has also been suggested that the simple binary picture presented above may not be appropriate (Viall and Borovsky, 2020). Some studies have tried to adapt a more complicated framework to explain solar wind conditions that currently cannot be explained by either of the theories outlined previously (Viall and Borovsky, 2020). There is also growing evidence that both of these mechanisms could work in parallel, with each dominating under specific conditions (Fu et al., 2018).

Finally, it is possible to make a prediction of the solar wind $\alpha-$particle abundance closer in based on the Eq. 5.5. As PSP gets closer to the Sun, the Alfvén speed will increase and the solar wind speed may decrease. There will be a point where $v_{SW} = v_A$

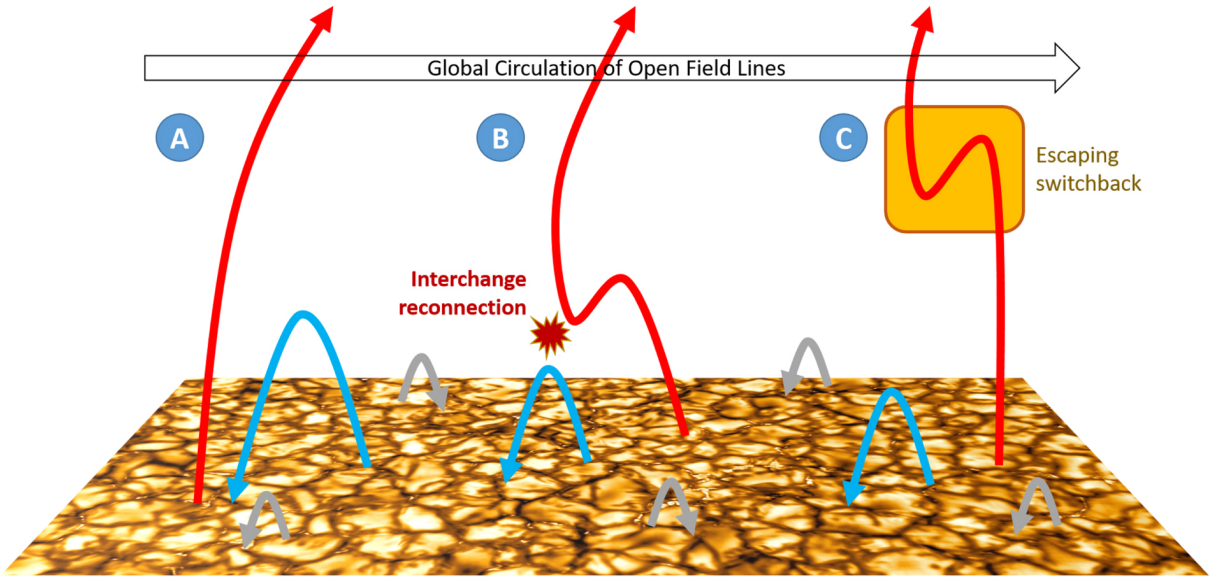


Figure 5.9: Schematic of how a switchback could form via interchange reconnection. The blue and grey arrows show closed magnetic field loops which can reconnect with open magnetic field (red arrows). This reconnection introduces a kink onto the open field line, which can then propagate outwards and form a switchback. *Figure credit: Fisk and Kasper (2020).*

(i.e. the Alfvén critical surface). At this surface, it is reasonable to expect the abundance to be lower than current PSP measurements, and therefore PSP will likely measure slow Alfvénic wind with an abundance $< 0.5\%$.

5.10 Evolution of Slow Alfvénic Solar Wind

Given the plasma properties presented previously in this chapter, the results can be compared to a previous study of slow Alfvénic wind at 0.35au (Stansby et al., 2020*a*). This comparison can help to understand how such wind evolves as it expands outwards from the Sun.

Between these two studies, the proton temperature anisotropy decreases from ~ 3 at 0.13 au to 1-2 at 0.35 au. This indicates that the slow Alfvénic solar wind cools faster perpendicular to the local magnetic field than it does parallel to it. This temperature scaling is consistent with previous observations in fast solar wind using both moments ($T_\perp \propto r^{-0.83}$, $T_\parallel \propto r^{-0.54}$; Hellinger et al., 2011) and fits to the proton core ($T_{pc,\perp} \propto r^{-1.09}$, $T_{pc,\parallel} \propto r^{-0.65}$; Ďurovcová et al., 2019). Interestingly, this is not the case with observations from slow solar wind. In fact, the temperature scaling suggested from the comparison

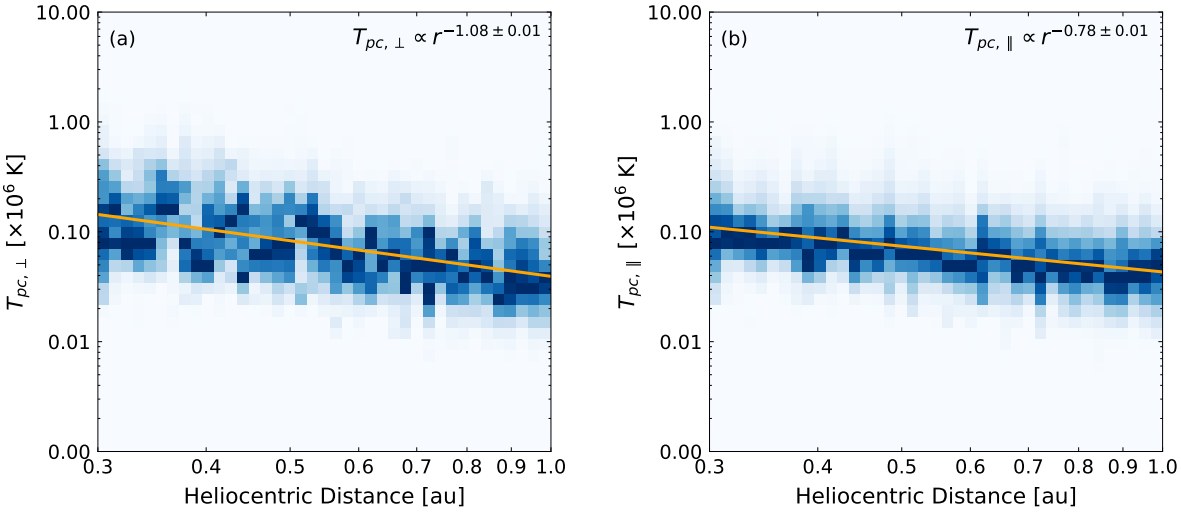


Figure 5.10: Plot of (a) proton core perpendicular temperature and (b) proton core parallel temperature vs heliocentric distance for slow Alfvénic wind measured by the Helios spacecraft. The orange lines show power law fits to these temperature profiles and the radial dependence is given in the top right of each panel. The data used to make these plots are from Stansby et al. (2018).

---

of the study presented in this chapter and the study by Stansby et al. (2020*a*), is only consistent with the scaling of the proton core fits ($T_{pc,\perp} \propto r^{-0.95}$, $T_{pc,\parallel} \propto r^{-0.67}$; Ďurovcová et al., 2019) and not the proton moments ($T_\perp \propto r^{-0.58}$, $T_\parallel \propto r^{-0.59}$; Hellinger et al., 2013) in slow wind. However, none of the above studies separates the solar wind based on Alfvénicity, making a direct comparison more difficult. Fig. 5.10 shows the scaling of the proton core temperatures for slow Alfvénic wind measured by Helios. There is a clear trend showing that the perpendicular temperature has a stronger dependence on heliocentric distance than the parallel temperature. This is consistent with the comparison between the work presented in this chapter and Stansby et al. (2020*a*).

An interesting result to note is that whilst slow Alfvénic and fast solar wind both have steeper $T_{pc,\perp}$ than $T_{pc,\parallel}$ profiles, slow Alfvénic wind reaches isotropy at around 0.35 au, whereas fast solar wind remains anisotropic until larger distances (e.g. Matteini et al., 2007). This indicates either that fast solar wind is more anisotropic in the near-Sun solar wind than slow Alfvénic wind, or that the $T_{pc,\perp}/T_{pc,\parallel}$ scaling of fast wind is weaker than that of slow Alfvénic wind. The former can only be confirmed by measuring data closer to the Sun, which PSP will continue to do throughout its mission phase. The latter, however, can be checked using Fig. 5.10. In fact, Fig. 5.10 shows that the scaling of $T_{pc,\perp}$

in slow Alfvénic wind ($T_{pc,\perp} \propto r^{-1.08}$) is very similar to that in fast wind ($T_{pc,\perp} \propto r^{-1.09}$; Ďurovcová et al., 2019), and that the scaling of $T_{pc,\parallel}$ is stronger in slow Alfvénic wind ($T_{pc,\parallel} \propto r^{-0.78}$) than fast solar wind ($T_{pc,\parallel} \propto r^{-0.65}$; Ďurovcová et al., 2019). This implies that the temperature anisotropy in fast solar wind should fall at a faster rate than the temperature anisotropy in slow Alfvénic wind. In order to be consistent with isotropic slow Alfvénic wind at 0.35 au and anisotropic fast wind at larger heliocentric distances, this implies fast solar wind has a larger temperature anisotropy than slow Alfvénic wind close to the Sun. This larger temperature anisotropy in fast wind could be a direct result of stronger heating mechanisms in the source regions of fast wind. Possible mechanisms leading to a large temperature anisotropy close to the Sun include turbulent dissipation (Verdini et al., 2010), stochastic heating (Chandran, 2010; Bourouaine and Chandran, 2013) and ion-cyclotron resonance (Li et al., 1999).

Whilst the mechanisms mentioned above can explain the preferential perpendicular heating of protons close to the Sun, they do not explain why the proton temperature scalings depart from the adiabatic predictions (i.e CGL predictions from Sect. 2.3.3). It appears that the proton core parallel temperature cools faster than expected with heliocentric distance whereas, the proton core perpendicular temperature cools more slowly. To explain this evolution of the proton core, additional in situ heating and/or cooling mechanisms are needed. Some possible candidates for perpendicular proton heating include in situ stochastic heating (Martinović et al., 2019), cyclotron resonance (Bowen et al., 2021) and turbulent dissipation (Smith et al., 2001). It is also possible that the $\alpha-$proton drift instability (Markovskii et al., 2019) and the firehose instability (Matteini et al., 2006, 2015*a*) regulate the evolution of proton temperatures.

In contrast to the protons, the $\alpha-$particle temperature anisotropy is comparable at both heliocentric distances. This suggests that $T_{\alpha,\perp}$and $T_{\alpha,\parallel}$ cool at comparable rates in slow Alfvénic wind. This is somewhat consistent with observation of $\alpha-$particles in fast wind, which scale by similar amounts ($T_{\alpha,\perp} \propto r^{-1.08}$, $T_{\alpha,\parallel} \propto r^{-1.24}$; Ďurovcová et al., 2019). The anisotropy of $\alpha-$particles is also in the opposite sense to the protons (i.e. $T_{\alpha,\perp}/T_{\alpha,\parallel} < 1$). This could indicate that $\alpha-$particles have $T_{\alpha,\perp}/T_{\alpha,\parallel} > 1$ close to the Sun and evolve much faster than protons. On the other hand, $\alpha-$particles may be subject to different heating mechanisms to protons, specifically ones that do not lead to preferential perpendicular heating. Future solar wind measurements from PSP will help to distinguish these two scenarios.

The equal cooling of $T_{\alpha,\perp}$ and $T_{\alpha,\parallel}$ disagrees with the CGL prediction (Eq. 2.26 and 2.27), and therefore requires heating in the perpendicular direction and/or cooling in the parallel direction. A possible source of $T_{\alpha,\perp}$ heating comes from the reduction in the $\alpha-$proton drift speed (Gary et al., 2000). This drift speed reduces from $\sim$ 90 % of the local Alfvén speed to $\sim$ 50 % between 0.13 and 0.35 au (Stansby et al., 2020*a*; Woolley et al., 2020). This reduction could be driven by drift instabilities that redistribute the drift energy into heating the $\alpha-$particles perpendicular to the magnetic field (e.g. Gary et al., 2000).

5.11 Conclusions

In this chapter SPAN ion and electron data were used to investigate the properties of solar wind within patches. Two patches that were measured at the same latitude and radius were visually identified from encounter 4 and 5 data. The patches were compared to each other and a neighbouring quiet period. This comparison focused on the proton core and $\alpha-$particle properties along with the electron strahl parallel temperature. A possible source of these patches was justified using a potential field source surface mapping, the inertial range scaling of the magnetic field power spectra, and the similarities shown between patch and fast solar wind. Statistics of switchbacks within the patches were given, before the particularly low $\alpha-$particle abundance was discussed. Finally, a comparison between this study and a previous slow Alfvénic wind study was made.

The results in this chapter indicate that the plasma within the two patches was very similar, especially considering the patches were measured in different solar encounters. Overall, the proton core properties were remarkably similar and slight variations in the temperature and velocity were possibly due to the T_p-v relationship (Burlaga and Ogilvie, 1970; Lopez and Freeman, 1986). In contrast, the solar wind properties within the quiet periods were distinct from those in patches. The exact reason for these differences is currently unknown. Further studies, like the one presented in Chapter 6, are required to fully understand patches and quiet periods.

One possible explanation for the differences in quiet periods and patches is that they have different origins. The evidence presented in this chapter suggests that patches are associated with coronal hole source regions. In particular, the two patches in this study were found to be consistent with solar wind from the boundary of the southern polar

coronal hole. Patches could be in situ measurements of coronal hole substructure such as funnels (Tu et al., 2005). However, further work is needed to clarify this connection between in situ and remote measurements.

The solar wind within these patches was slow (< 400 km/s) and displayed a high level of Alfvénicity. Therefore, a comparison between this study and another slow Alfvénic wind study (Stansby et al., 2020*a*) provided one of the first insights into how this type of wind may evolve. $T_{pc,\perp}$ shows a stronger dependence on heliocentric distance than $T_{pc,\parallel}$ in slow Alfvénic wind. This is also seen in fast solar wind. Interestingly, a comparison of temperature scaling in slow Alfvénic and fast wind revealed that the anisotropy of fast wind should decrease faster than the anisotropy of slow Alfvénic wind with heliocentric distance. As fast wind is known to display temperature anisotropy at larger heliocentric distances than slow Alfvénic wind does, these scalings suggest that fast wind must have a larger temperature anisotropy than slow Alfvénic wind close to the Sun.

Finally, the $\alpha-$particle data from the encounter 5 patch showed some interesting results. The $\alpha-$particles were considerably hotter in both the parallel and perpendicular direction compared to protons. This could be a indication of preferential heating mechanisms in the near-Sun solar wind. Furthermore, the $\alpha-$particle temperature anisotropy was less than 1 and in contrast to the proton temperature anisotropy (which is greater than 1). This result suggests that $\alpha-$particles may be subject to different heating mechanisms or evolution than protons. There was also evidence for a remarkably low $\alpha-$particle abundance in the patch, which could be a direct result of how the solar wind is released or heated closer to the Sun.

The low abundance is still not fully understood and it is not clear how slow and fast wind from the same source could have such drastically different abundances. Since the work in this chapter was done, Bale et al. (2021) has investigated patches seen in encounter 6. In this encounter, the patches often have enhanced $\alpha-$particle abundances which appears contradictory to the work presented in this chapter. It is likely that the $\alpha-$particle abundance in patches is dependent on the processes occurring in the solar atmosphere, and can vary greatly inside different structures seen by PSP. The following chapter on quiet periods could complement the results presented here.

Chapter 6

Quiet Periods in Low Latitude Solar Wind

6.1 Introduction

Three of the main structures observed in the near-Sun solar wind by Parker Solar Probe are switchbacks, switchback patches and quiet periods. The previous two chapters have covered switchbacks and patches and therefore this chapter focuses on understanding the quiet periods. Quiet periods typically have timescales ranging from a fraction of an hour to a few hours, and are shorter than the switchback patches but longer than individual switchbacks. Quiet periods have been observed throughout many PSP encounters, but have not been the sole focus of any study to date. In fact, quiet periods have been studied less than both switchbacks and patches, meaning that little is currently known about them. In this chapter, the high resolution plasma and magnetic field data available across multiple PSP encounters are exploited to investigate these structures. The work in this chapter forms the first study purely addressing these quiet periods.

This chapter begins with a discussion of the various structures found in the low latitude solar wind, before two methods used for identifying quiet periods are outlined in Sect. 6.4. Sect. 6.5 discusses whether the quietness can be explained by how the spacecraft samples the fluctuations. In Sect. 6.6 and 6.7 the quiet period properties are analysed and compared to the surrounding solar wind. Sect. 6.8 investigates whether quiet periods have a characteristic scale size before the distributions of quiet periods throughout each encounter are covered (Sect. 6.9). The chapter ends with a discussion on the potential

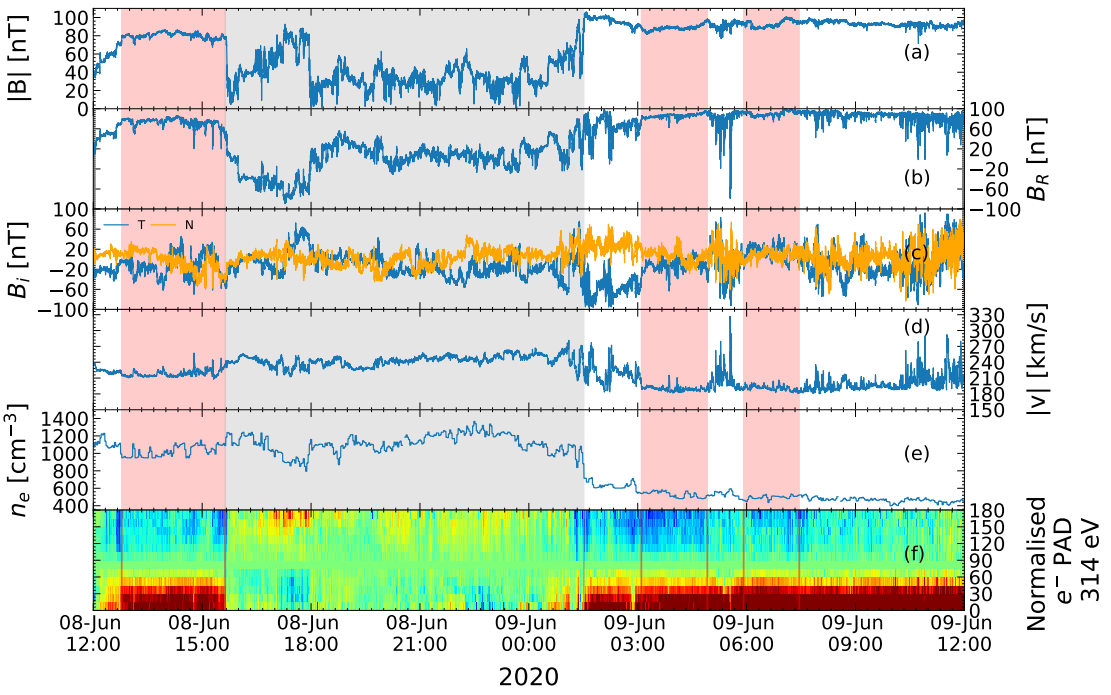


Figure 6.1: Time series of quiet periods (red shaded regions) and a suspected partial current sheet crossing (grey shaded region). The panels show: (a) magnetic field magnitude, (b) the radial component of the magnetic field, (c) the tangential and normal components of the magnetic field, (d) the magnitude of the proton core velocity, (e) the electron number density, and (f) normalised electron pitch angle distribution for electrons with energy of 314eV. The electron PAD is normalised to the 75-90° bin. Blue colours show the lowest counts and red colours show the highest counts.

---

origins of quiet periods (Sect. 6.10) and conclusions (Sect. 6.11) that can be drawn from this work.

6.2 Structures in the Low Latitude Solar Wind

Quiet periods (along with switchbacks and patches) are just a subset of many structures that can be identified in the solar wind based on their magnetic field and/or density profiles. For example, there are periodic density structures (e.g. Viall and Vourlidas, 2015), helmet streamer plasmoids (e.g. Sheeley et al., 1997) and partial HCS crossings (Phan et al., 2021).

Periodic density structures (PDS) are increases in the proton density (of 20%-100% of the background density) that occur on timescales of $\sim$ 90 mins (Kepko et al., 2002;

Kepko and Spence, 2003; Viall and Vourlidas, 2015). They are known to be in pressure balance with their surroundings, meaning that $|\mathbf{B}|$ is reduced within them (Kepko and Spence, 2003). PDS have been observed frequently at 1 au by spacecraft (e.g. Kepko et al., 2002; Kepko and Spence, 2003; Viall et al., 2008) and are thought to drive oscillations in the Earth's magnetosphere (Viall et al., 2009*a*). There is growing evidence that these structures form in the corona and are advected into interplanetary space by the expanding solar wind. For example, they display compositional signatures that are consistent with coronal origins (Viall et al., 2009*b*), and remote sensing observations of similar structures suggest that they form at around $\sim 2.5 R_S$ (Viall et al., 2010; Viall and Vourlidas, 2015). However, the exact formation mechanism of PDS is unknown. It has been suggested that magnetic reconnection could create PDS (Kepko and Spence, 2003; Viall and Vourlidas, 2015), but further work is needed to confirm this.

Helmet streamer plasmoids, which are sometimes referred to as 'blobs', are structures that are thought to originate close to the tips of helmet streamers through some form of magnetic reconnection (Wang et al., 1998; Sheeley et al., 1997, 2007, 2009). They have predominantly been observed in remote sensing images (e.g. Sheeley et al., 1997), but consistent structures have also been observed in in situ data (e.g. Crooker et al., 2004; Suess et al., 2009). Helmet streamer plasmoids are more dense than their surroundings, which is why they appear as brighter features in remote sensing images. There are a variety of possible mechanisms that could release plasma close to helmet streamers (Wang et al., 2000; Rouillard et al., 2010). Therefore, it is likely that there are multiple subcategories of helmet streamer plasmoids. PDS could also be related to magnetic reconnection at the tips of helmet streamers. However, Viall and Vourlidas (2015) argue that helmet streamers are larger scale than PDS and that helmet streamer plasmoids are confined to the plasma sheet, whereas PDS are not.

Partial HCS crossings (see Fig. 6.1) occur when the spacecraft is close to the HCS but does not fully cross it. These can happen when the relative spacecraft motion is aligned along the HCS. Partial HCS crossings occur frequently in the early PSP data. This is because the combination of a relatively flat HCS and the low latitude orbit of PSP results in the spacecraft skimming the HCS. Partial HCS crossings are characterised by increases in the proton density and a reduction in $|\mathbf{B}|$ (Phan et al., 2021).

Quiet periods (as shown in this chapter) are distinct from all of these structures and typically exhibit a stable magnetic field orientation and occur for between a fraction of a

hour and a few hours. In this chapter, the quiet periods are identified and investigated with a focus on three questions:

1. What are the typical properties of quiet periods?
2. Do quiet periods have a characteristic spatial and/or temporal scale?
3. What larger-scale structures and/or solar source regions are quiet periods associated with?

6.3 Data

In this study, plasma (encounters 3-7) and magnetic field (encounters 3-7 and 10) data from PSP are used. These data have already been outlined in previous sections. For information about each data product see Sect. 2.6.1.3 for FIELDS and Sect. 5.3 for SPAN. The only difference between the SPAN data used here and the data used in Chapter 5 is that the fits are only applied to the proton core in this chapter. These data products were provided by Lloyd Woodham as proton core and beam fits by Michael McManus were not available for all encounters of interest. The electron pitch angle distributions (PADs), measured by the SPAN electron electrostatic analysers, are also used in this chapter. These data products show distributions of the electron pitch angle with respect to the local magnetic field orientation, and can help with understanding the magnetic connectivity of the solar wind (see Sect. 6.6). The electron strahl can be identified in these PADs as a peak at either 0° or 180°, depending on the magnetic polarity. The standard way to handle these PADs is to choose an energy bin relative to the strahl electrons and plot the PAD for that specific energy. In this work, 314 eV was an appropriate energy level to capture the strahl signature. From here onward, the counts have been normalised to the 75-90° bin for reference.

6.4 Identifying Quiet Periods

Two different methods were used to identify quiet periods in the data. The first method involved a manual identification by visually inspecting the time series data. Quiet periods were chosen based on the radial magnetic field component and the total variance of the normalised magnetic field components ($\sigma^2 = \sigma_R^2 + \sigma_T^2 + \sigma_N^2$) calculated on a five minute

timescale. For a quiet period to be identified using this method, B_R had to be stable and σ^2 had to be low compared to the surrounding wind. A threshold of $\sigma^2 \sim 0.02$ was used, but this was not a strict criterion. A flexible threshold was required because sometimes a single switchback appeared within an otherwise quiet period. In these cases, short deviations ($\sim$10 mins) of σ^2 above the threshold were accepted. The flexible threshold also allowed the boundaries of quiet periods to be identified more accurately than using a fixed threshold. This is because identification based on a fixed threshold is only accurate up to the resolution of σ^2. In the case of identifying quiet periods, the calculation of σ^2 could be influenced by switchbacks occurring at the end of the five minute calculation period, resulting in a premature identification of the boundary. To avoid this, the boundaries were not always selected as the first time σ^2 was above 0.02, but the time when significant switchbacks were observed in the data. It was only feasible to identify quiet periods with a timescale $\gtrsim$ 1 hr due to the manual nature of this method. Given that each encounter was several days long, looking at timescales below 1 hour would have been extremely time consuming.

The second method involved using an algorithm to determine when σ^2, calculated on a five minute timescale, fell below a chosen threshold. A threshold of 0.02 was found to capture quiet periods well at 0.15 au. This threshold was used and varied according to the weak dependence of σ^2 on heliocentric distance. Using this varying threshold, each five minute interval was classified as quiet or not quiet. A second condition was required for each five minute interval to stop the algorithm selecting quiet periods that were part of some larger scale structure. An appropriate condition for this was limiting the amount that $|\mathbf{B}|$ could vary within the interval. Therefore, the five minute intervals also had to satisfy $\max|\mathbf{B}| - \min|\mathbf{B}| < 9\%|\mathbf{B}|$. This 9% threshold was chosen as it appeared to capture the quiet periods well when visually inspecting the data. The five minute intervals that met both of these conditions were then used to identify the quiet periods by combining consecutive intervals. A requirement that quiet periods had to be formed from at least two consecutive five minute intervals was applied to reduce the chance of the algorithm incorrectly selecting anomalies in the data. As such, the algorithm was sensitive to quiet periods with durations $\geq$ 10 mins.

Tab. 6.1 shows a summary of the number of quiet periods identified per day in each PSP encounter using the manual and automatic methods. To correct for the fact that each encounter has a slightly different duration, the number of quiet periods has

Encounter	Manually Identified per Day	Automatically Identified per Day
3	1.6	11.2
4	3.1	12.8
5	2.7	13.0
6	1.9	12.9
7	2.3	10.9
10	1.0	10.3

Table 6.1: Average number of quiet periods identified per day in each PSP encounter using the manual and automatic methods. This table is discussed in more depth in Sect. 6.9.

---

been divided by the total duration of the encounter. Typically, each encounter has 20-30 manually identified quiet periods and over 100 automatically identified quiet periods. The automatic method captures more quiet periods because (i) it is sensitive to quiet periods with a smaller timescale and (ii) it can split one long quiet period into multiple ones if σ^2 momentarily increases above the 0.02 threshold.

Neither identification method is perfect and each one has its own drawbacks. For example, the manual method could be influenced by selection bias and can only be used for quiet periods with timescales $\gtrsim$ 1 hr. The automatic method, on the other hand, does not always capture quiet periods as expected and can pick up unwanted larger scale structure. Due to these drawbacks, a combination of these methods is used throughout this chapter.

6.5 Does θ_{BV} Control the Quietness?

In the solar wind, the magnetic field fluctuations are not isotropic in each direction and have larger power perpendicular to the field than parallel to it (Coleman, 1968; Belcher and Davis, 1971; Horbury et al., 1995). This means that the fluctuation levels measured by the spacecraft depends on how it samples the solar wind with respect to the magnetic field.

One possibility is that the quiet periods seen in the PSP data could be similar to the surrounding wind (e.g. patches), but measured by the spacecraft in such a way that they appear quiet. To investigate this, the dependence of normalised magnetic field variance (σ^2) on the angle between the magnetic field and the relative solar wind flow at the spacecraft (θ_{BV}) is studied. A θ_{BV} angle of 0 implies $\mathbf{B}$ and $\mathbf{V}_{rel}$ are parallel to each

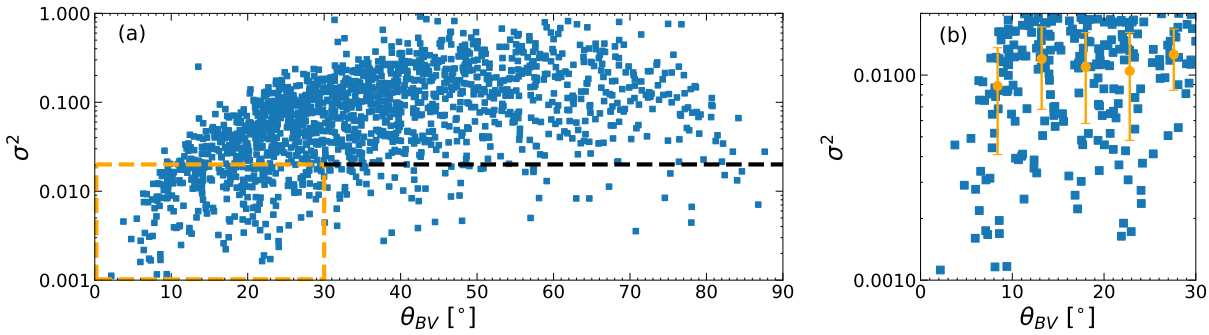


Figure 6.2: Scatter plot of the average normalised magnetic field variance against average θ_{BV} for each 10 minute interval in encounter 7. Panel (a) shows the full domain and panel (b) shows a close up of the orange dashed box in panel (a). The orange points in panel (b) show bin averages and standard deviations calculated only for the data shown within this panel.

---

other (i.e. PSP samples the solar wind along the magnetic field) and $\theta_{BV} = 90°$ implies $\mathbf{B}$ and $\mathbf{V}_{rel}$ are perpendicular to each other (i.e. PSP samples the solar wind perpendicular to the magnetic field).

Fig. 6.2 shows the average σ^2 vs the average θ_{BV} for each 10 minute interval in the encounter 7 data. There is a clear positive correlation between σ^2 and θ_{BV}. However, this does not indicate that a larger θ_{BV} causes a larger σ^2. In fact, the presence of switchbacks, which are large deflections in θ_{BV}, increases both σ^2 and θ_{BV}. It is this underlying cause that leads to the dominant σ^2-θ_{BV} correlation in panel (a) of Fig. 6.2.

In order to determine if there is a relationship between σ^2 and θ_{BV} that is not caused by switchbacks, it is important to consider intervals when switchbacks are not present. In these intervals changes in θ_{BV} are due to changes in the spacecraft velocity and the orientation of the background magnetic field. In fact, the background magnetic field is approximately radial close to the Sun. Therefore, it is typically changes in PSP's velocity that lead to changes of θ_{BV} in the absence of switchbacks. The dashed box in panel (a) of Fig. 6.2 shows the range of values for which it is possible to test the non-switchback σ^2-θ_{BV} correlation during encounter 7. The upper limit of σ^2 in this box is set at 0.02 to exclude switchbacks. This is the same threshold that was used for identifying quiet periods with the automatic method (see Sect. 6.4). The upper limit of θ_{BV} is set by the relative tangential velocity of the spacecraft at perihelion, which gives the largest angle at which a radial magnetic field would be sampled by the spacecraft. It is possible that θ_{BV} is larger than this without the presence of switchbacks (i.e. with a particularly non-radial

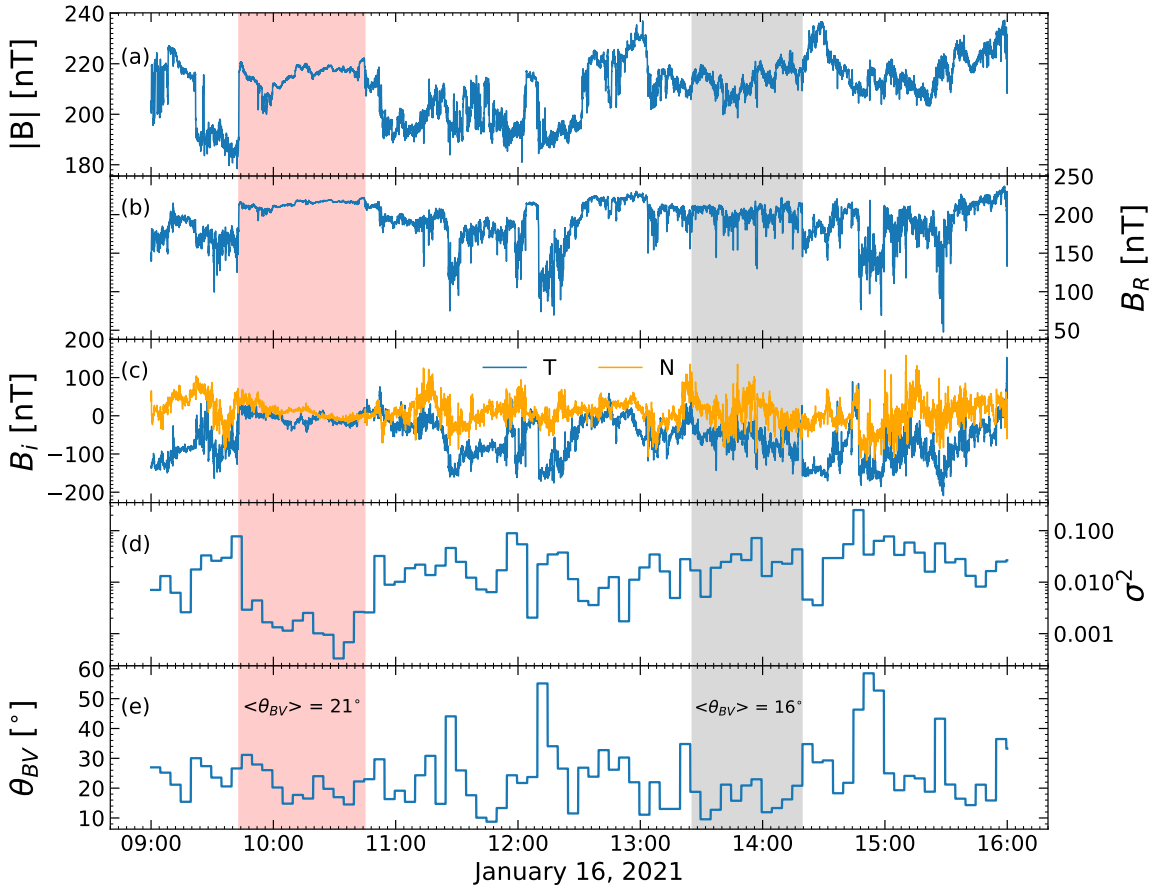


Figure 6.3: Time series of a $\sim$ 7 hr interval of solar wind measured during PSP's seventh solar encounter. A quiet period is shaded in red and a non-quiet region is shaded in grey. The panels show: (a) magnetic field magnitude, (b) radial component of the magnetic field, (c) tangential and normal components of the magnetic field, (d) normalised magnetic field variance, and (e) θ_{BV}. The time format is hh:mm.

background magnetic field), but as the magnetic field is often approximately radial close to the Sun, this is a reasonable estimate for this discussion. Inside the box (panel b), there is no clear relationship between σ^2 and θ_{BV}. Similar σ^2 values are observed for a range of θ_{BV} values. This indicates that in the absence of switchbacks the quietness of an interval is independent of the angle at which the solar wind is sampled.

Further evidence to support these statistics can be found by looking at individual case study quiet periods. Fig. 6.3 shows a ~ 7 hour time series from PSP's encounter 7. The quiet period is highlighted in red and a non-quiet period is highlighted in grey. The quiet period has a consistently low variance ($< 10^{-2}$) and an average θ_{BV} of 21°. On the other hand, the non quiet period has a higher variance than the quiet period ($\sim 2 \times 10^{-2}$), but a lower average θ_{BV} of 16°. This indicates that θ_{BV} does not dominate the quietness and therefore that the underlying fluctuations in these two periods must be different (i.e. the differences are not caused by sampling effects).

It is also possible to consider the changes within a single quiet period. Fig. 6.4 shows a quiet period measured close to perihelion during encounter 7. This was a particularly long event (lasting 5 hours) making it a good case study for looking at θ_{BV} changes within a quiet period. At the beginning of the quiet period $\theta_{BV} \sim 20°$ and $\sigma^2 \sim 10^{-2}$. θ_{BV} then drops suddenly at approximately 09:00 to $< 10°$, but there is no clear corresponding drop in σ^2. In fact, σ^2 tends to gradually decrease throughout the quiet period and is close to its lowest value in the final 30 mins, when θ_{BV} is $\sim 20°$ again. The behaviour of σ^2 and θ_{BV} throughout this quiet period shows no evidence that would indicate θ_{BV} is the dominant controller of σ^2. This further suggests that the quiet periods are quiet not due to a sampling effect, but due to an underlying difference in the level of fluctuations. These results motivate a study to analyse the properties of the quiet periods and link them to possible solar origins.

6.6 Quiet Period Properties

The electron strahl population provides a perfect opportunity to understand whether quiet periods are associated with open or closed magnetic field structures. This is because open and closed field lines are related to different signatures in the electron pitch angle distributions (PADs). Strahl electrons stream away from the Sun along magnetic field lines and the velocity of these electrons is much higher than ions, meaning that they do

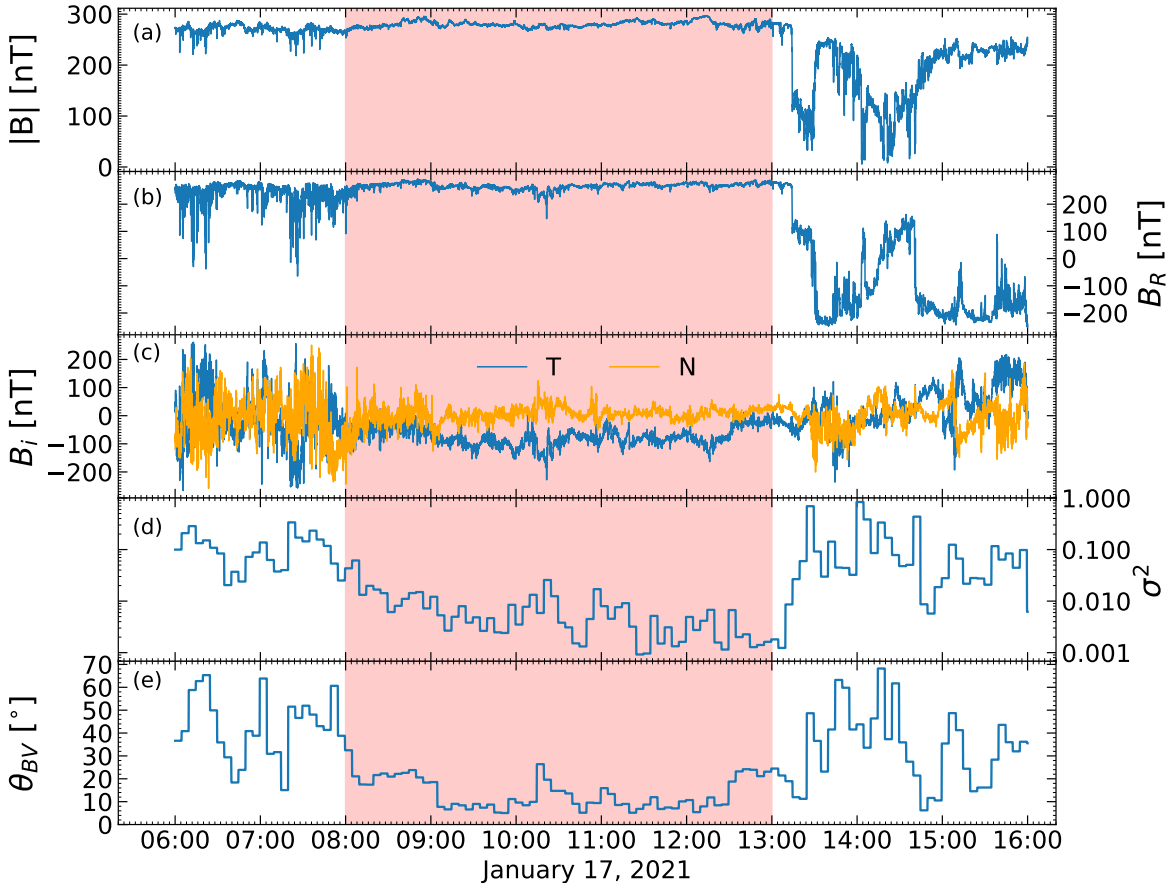


Figure 6.4: Time series of a $\sim$ 5 hr quiet period (shaded red) measured prior to the heliospheric current sheet crossing during PSP's seventh solar encounter. The panels show: (a) magnetic field magnitude, (b) radial component of the magnetic field, (c) tangential and normal components of the magnetic field, (d) total magnetic field variance, and (e) θ_{BV}. The time format is hh:mm.

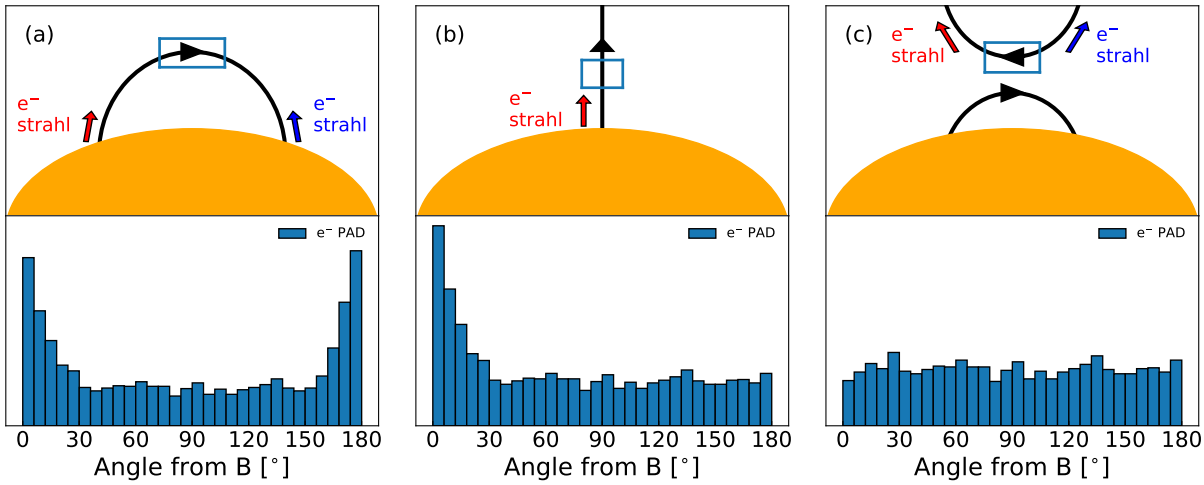


Figure 6.5: Schematic showing how the electron strahl appears in the electron pitch angle distributions. The panels show three different scenarios: (a) a closed magnetic field loop connected at both ends to the Sun, (b) an open magnetic field line connected at one end to the Sun, and (c) a magnetic field structure no longer connected to the Sun. In each case, the histogram shows the expected electron PAD inside the blue boxes. It is important to note that the data used to make the histograms are not in situ data, but were generated for the purpose of explaining the expected behaviour of the electron PAD.

---

not remain with the same bulk solar wind plasma. This leads to three different scenarios which are shown with synthetic data in Fig. 6.5. (a) For magnetic field lines connected at both ends to the Sun, each leg of the closed loop has strahl electrons flowing along it. These strahl electrons are confined to the closed loop which results in a bimodal electron PAD peaking at both 0° and 180° when measured by a spacecraft. (b) For open magnetic field lines, strahl electrons continually flow from the single connected foot point out into the heliosphere. This produces a single peak in the electron PAD at either 0° or 180°, depending on whether the magnetic field polarity is sunward or anti-sunward. (c) Finally, if there is magnetic reconnection in the solar wind, it is possible for parcels of solar wind to be completely disconnected from the Sun. Without a magnetic connection to the Sun the solar wind does not have a continual flow of strahl electrons. The strahl electrons, which were present at the time of reconnection, stream away from the reconnection site faster than the bulk solar wind ions. Therefore, no strahl signature is present when this solar wind parcel is observed by a spacecraft.

Fig. 6.1 shows a timeseries of three quiet periods (red shaded region) identified during PSP's fifth solar encounter. For each quiet period, the magnetic field remains relatively

stable compared to the surrounding solar wind. Panel (f) shows the distribution of electrons for angles from the magnetic field. The red signature at low angles indicates a single electron strahl population is present and that these quiet periods are connected by open magnetic field lines to the Sun. This is in contrast with the neighbouring solar wind interval (shaded grey) which shows no strahl signature, suggesting a structure that is magnetically disconnected from the Sun (scenario c in Fig. 6.5). These types of structures are thought to be partial crossings of the heliospheric current sheet as discussed in Phan et al. (2021). All of the quiet periods identified using the manual and automatic methods have single electron strahl populations, indicating that quiet periods are always associated with open magnetic field lines and are not magnetically disconnected from the Sun.

The magnetic field orientation within quiet periods is consistent with open field lines extending outwards from a rotating Sun (i.e. the Parker spiral). However, the manually identified quiet periods tend to be more radially aligned than the Parker spiral (see panel (c) in Fig. 6.6). This result is also seen in the automatically identified quiet periods (panel a), indicating that this is unlikely to be a selection effect. There are quiet periods that have an average B_T in the opposite sense to the Parker spiral (orange points in panels a and c). This is likely because the Parker spiral is close to the radial direction at small heliocentric distances. Therefore, small deviations of the field from this prediction can reverse the sign of the tangential component.

Finally, it is worth noting that whilst quiet periods may appear to have a radial magnetic field in time series figures, particularly when compared to neighbouring patches, the magnetic field can deviate significantly from a radial orientation. Fig. 6.6 (panels b and d) shows that a large fraction of quiet periods, both identified manually and with an algorithm, have orientations $\gtrsim 10°$ from the radial. It is, therefore, not fitting to describe these quiet periods as purely radial.

6.7 Comparing Quiet Periods to Surrounding Wind

To gain an understanding of the differences between quiet periods and the surrounding solar wind, a comparison of the average properties inside and outside quiet periods is made. For each manually identified quiet period, an interval before and after was selected as surrounding solar wind. There were no strict selection criteria, as that would require

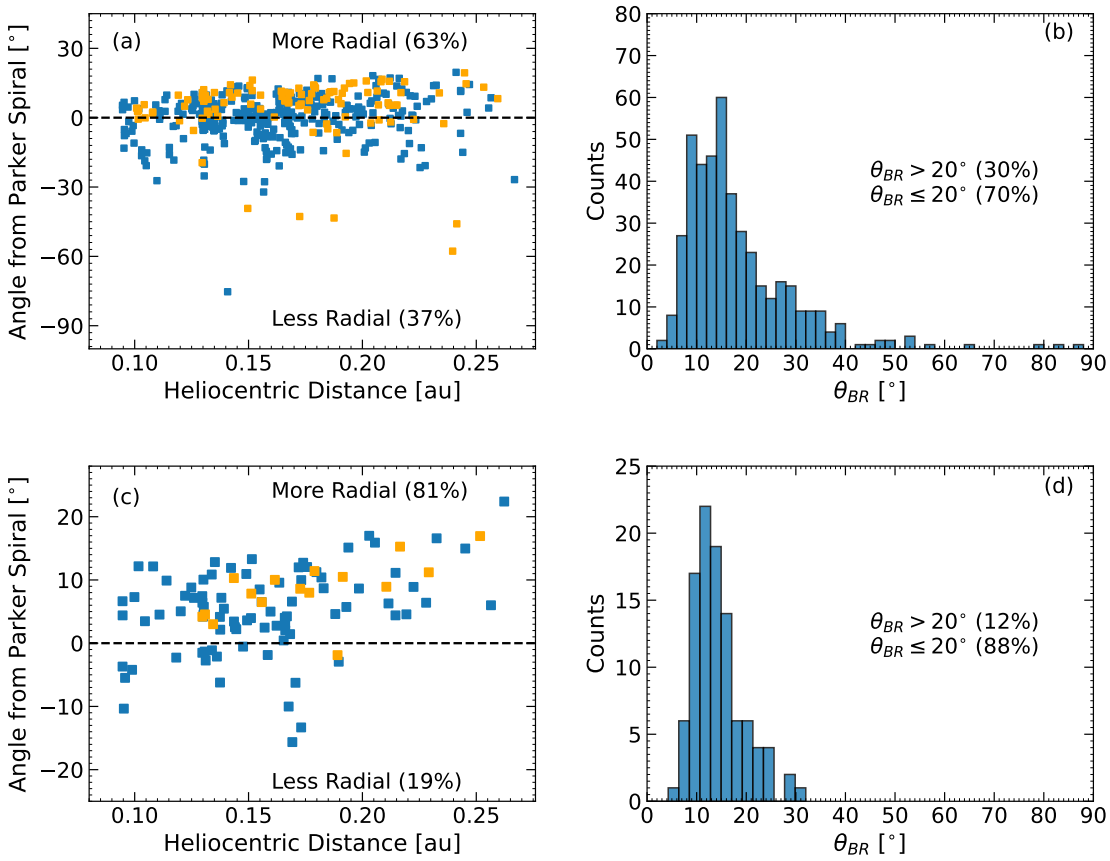


Figure 6.6: Comparison of the magnetic field orientations inside quiet periods identified using the algorithm (top row) and manual selection (bottom row). Panels (a) and (c) show the angle of the magnetic field away from the Parker spiral in the R-T plane for heliocentric distances between 0.08 and 0.275 au. The dashed horizontal line indicates where the magnetic field is aligned with the Parker spiral. Above this line indicates the magnetic field is more radial than the Parker spiral and below indicates when it is less radially aligned. The colours indicate whether the average B_T inside each quiet period has the same orientation as predicted by the Parker spiral: blue indicates the same orientation, orange indicates opposite orientation. Panels (b) and (d) show histograms of the angle between the magnetic field vector and the radial direction.

clear definitions of quiet periods, switchbacks, and patches for which there is currently no consensus. Instead, intervals were chosen that were comparable in timescale to each quiet period and any larger scale structures (e.g. HCS crossings etc.) were avoided. The average properties before and after each quiet period were combined to calculate a background solar wind value for that quiet period. It is important to note that the surrounding wind identified here does not necessarily directly correspond to a patch. This is because the near-Sun solar wind appears more complicated than simply patches separated by quiet periods. Therefore, it is not possible to directly compare the surrounding solar wind here to the patches discussed in Chapter 5.

The top 6 panels in Fig. 6.7 show the ratio of averaged properties inside a quiet period to the averaged properties within the surrounding solar wind (each quiet period corresponds to one data point here). Panels (a) and (b) show that the parallel and perpendicular temperatures inside quiet periods are less than the temperatures in the surrounding solar wind. This result was also seen in a study of patches by Bale et al. (2021). These reduced temperatures could be a direct result of the lower fluctuations in quiet periods, as turbulence is a possible source of solar wind heating (e.g. Smith et al., 2001). A comparison of panels (a) and (b) also shows that $T_{pc,\parallel}$ is more suppressed from the surrounding wind temperature than $T_{pc,\perp}$ is. This is consistent with the findings of Woodham et al. (2021) which showed that $T_{pc,\parallel}$ is enhanced within patches, whereas $T_{pc,\perp}$ remains approximately constant. This behaviour of $T_{pc,\parallel}$ and $T_{pc,\perp}$ results in a temperature anisotropy which is larger in quiet periods than in the surrounding solar wind (panel c). Panel (d) shows that the average electron number density is smaller within quiet periods, whereas the magnetic field magnitude is enhanced (panel e). This could indicate that quiet periods are in some form of pressure balance with their surroundings although future studies with electron pressure are needed to confirm this. Finally, panel (f) shows that the average radial velocity is slightly lower in quiet periods than the surrounding solar wind. This is most likely due to a lack of switchbacks in the quiet periods, as switchbacks enhance the average radial velocity. However, it is worth noting that quiet periods are not always the slowest solar wind in an encounter and other intervals, including patches, can have lower baseline velocities.

The bottom 6 panels in Fig. 6.7 show scatter plots comparing the properties in the quiet periods to the properties in the surrounding solar wind. The quantities have been scaled by their heliocentric dependencies to 0.05 au. Even with this scaling that removes

the heliocentric dependence from each quantity, there is a high correlation between quiet periods and the surrounding wind. This could be a result of similar solar origins or mutual evolution with the surrounding wind.

6.8 Do Quiet Periods Have a Characteristic Scale?

Understanding whether quiet periods have a characteristic scale size in a given direction is important for drawing conclusions about their origins. If quiet periods do have a characteristic length scale and PSP cuts through these structures along the direction of that scale, then there should be a strong dependence between the duration of quiet periods and the relative speed of the solar wind with respect to PSP. This dependence is investigated using the manually identified quiet periods for three scenarios, assuming that a characteristic scale exists.

1. In the first scenario, it is assumed that quiet periods are associated with stable, co-rotating solar wind streams. Under this assumption, the duration of quiet periods should depend heavily on the relative longitudinal speed between PSP and the stream ($v_{\phi,rel}$). To check whether this is the case $v_{\phi,rel}$ was calculated as follows:

$$v_{\phi,rel} = v_{\phi,SW} - v_{\phi,PSP} + v_{rot}, \tag{6.1}$$

   where the final term accounts for the co-rotation of the source region (v_{rot} =14.713°/day). For a stable, co-rotating solar wind stream, the duration is expected to peak when $v_{\phi,rel} = 0$ as the spacecraft would remain in the stream for a long period of time. The duration should then fall off with the inverse of $v_{\phi,rel}$. Panel (a) in Fig. 6.8 shows that there is no significant dependence, on average (orange points), between the duration of quiet periods and the relative longitudinal speed. This suggests that the duration of quiet periods seen by the spacecraft is independent of the longitudinal speed between PSP and a co-rotating source region. This result appears inconsistent with quiet periods being stable, co-rotating solar wind streams with a characteristic scale.

2. As quiet periods appear to be inconsistent with solely longitudinal cuts through stable solar wind streams, it is possible that they are related to structures that get advected over the spacecraft. In this scenario, the relative radial speed ($v_{R,rel}$ =

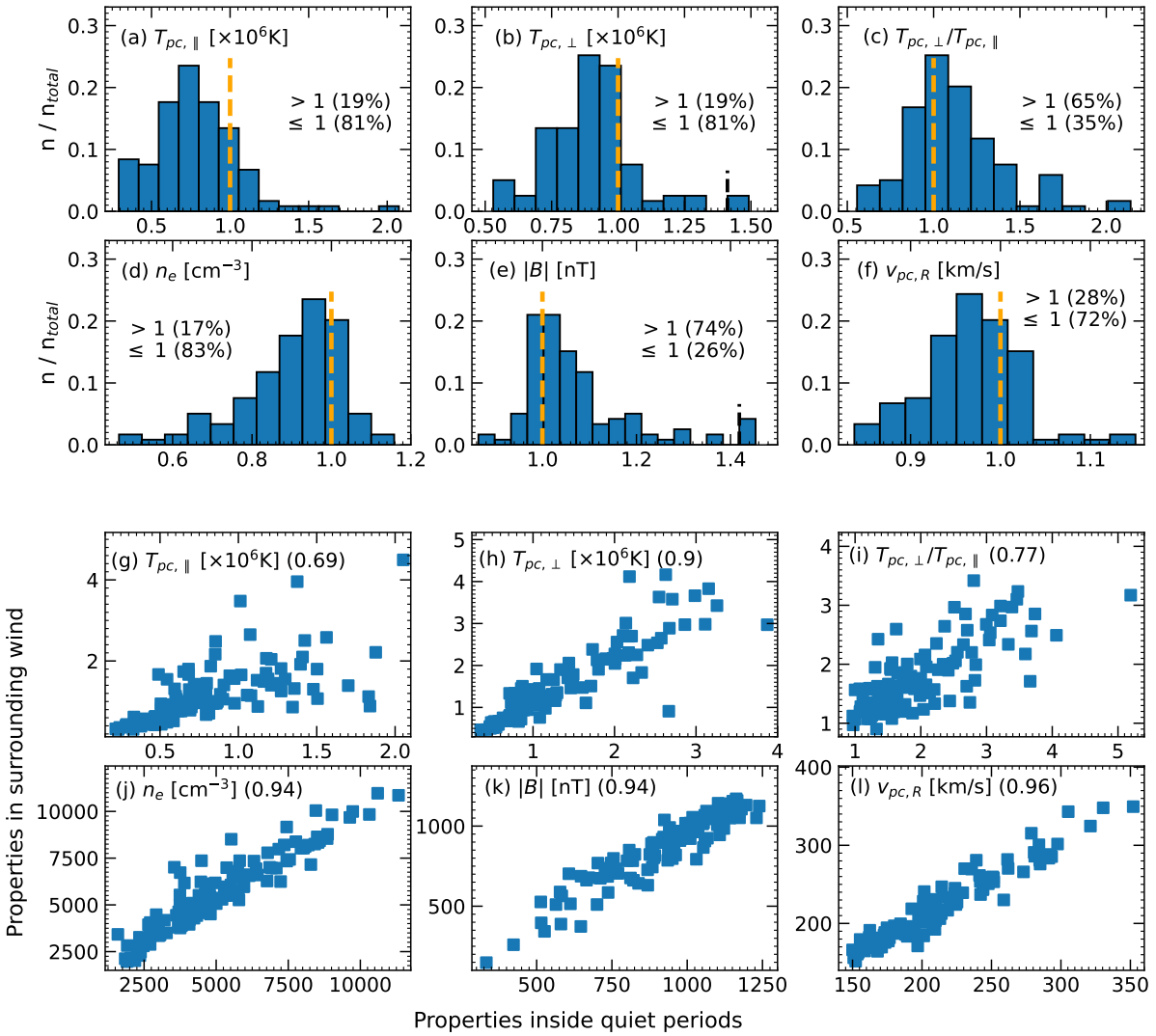


Figure 6.7: (top 6 plots) Histograms of the ratio of various solar wind parameters inside quiet periods to the surrounding solar wind. A ratio is calculated for each individual quiet period using the average properties inside and outside of it. The panels show: (a) the proton core parallel temperature, (b) the proton core perpendicular temperature, (c) the proton core temperature anisotropy, (d) the electron number density, (e) the magnetic field magnitude, and (f) the proton core radial velocity. The dashed orange vertical lines indicate where the ratio is 1. The dashed black lines in panels (b) and (e) indicate where the histogram has been truncated. (bottom 6 plots) Scatter plots of average parameters inside and outside quiet periods. The panels show: (g) the proton core parallel temperature, (h) proton core perpendicular temperature, (i) proton core temperature anisotropy, (j) electron density, (k) magnetic field magnitude, and (l) proton core radial velocity. Each parameter has been scaled by its heliocentric dependence to 0.05 au. The correlations are shown in brackets in each panel. All data in this figure are from manually identified quiet periods.

$v_{R,SW} - v_{R,PSP}$) is important. If quiet periods are associated with structures advected over PSP then their duration would peak for the lowest relative velocities and follow an inverse $v_{R,rel}$ relationship. Panel (b) in Fig. 6.8 shows no clear dependency between quiet period duration and $v_{R,rel}$. This result, in the same way as the discussion for scenario 1, is not consistent with quiet periods being associated with structures purely advected over the spacecraft by the solar wind.

3. Finally, for completeness, the dependence of quiet period duration on the relative latitudinal solar wind speed ($v_{\theta,rel}$) is shown in Fig. 6.8 panel (c). There is once again, no clear relationship between these quantities.

From the above discussion, which is based on the assumption that quiet periods have a characteristic scale, quiet periods do not appear consistent with either spatial structure (latitudinal or longitudinal) that PSP cuts through, or temporal structure that is advected radially over the spacecraft. Therefore, it appears as if the assumption of a quiet period characteristic scale is wrong. From these results, it is possible to conclude that quiet periods, as seen in time series data, have no associated characteristic scale size. This means that either quiet periods intrinsically have no scale size or that they appear to have none in the data. Further analysis of Fig. 6.8 suggests that the latter could be true.

By considering panel (a) it is possible to see that the longest duration quiet periods for each $|v_{\phi,rel}|$ appear to follow an inverse relationship. This is exactly the behaviour that would be expected if quiet periods had a characteristic longitudinal scale size. The fact that only the quiet periods with the longest durations appear consistent with a characteristic longitudinal scale size is interesting. It suggests that if quiet periods do have an intrinsic scale size then PSP does not measure the full longitudinal extent in most cases. In other words, it is possible that quiet periods have an intrinsic characteristic longitudinal scale, which would be seen in the PSP data if PSP cut in and out of these structures longitudinally. However, due to additional effects PSP's cut is not purely longitudinal and so the quiet periods are modulated in the PSP data, making them no longer representative of the underlying characteristic scale. A reason for this possible modulation is given in Sect. 6.10. The black dashed line in panel (a) shows the expected relationship between duration and $|v_{\phi,rel}|$ for a quiet period with a longitudinal scale size of 2°. The majority of quiet periods are constrained by this 2° curve, indicating that the underlying quiet period longitudinal scale size could be ∼2°.

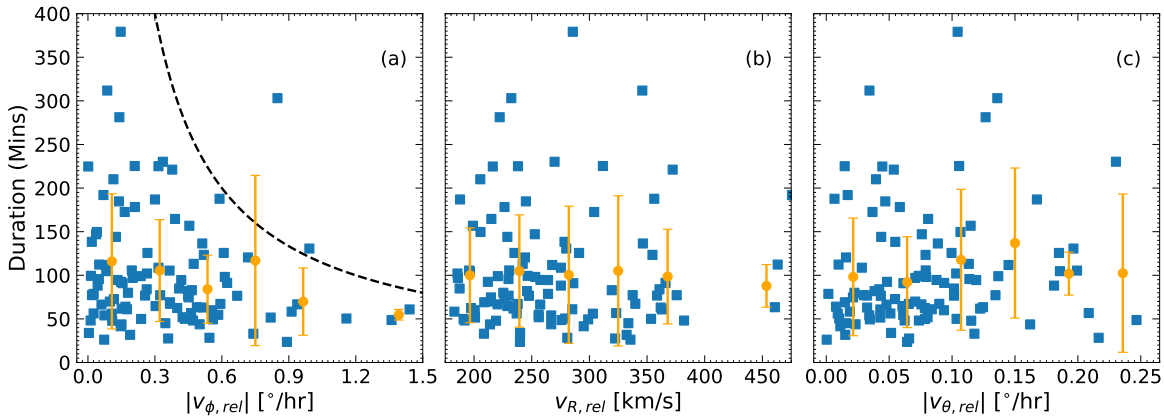


Figure 6.8: Scatter plots of quiet period duration vs the relative speed between PSP and the solar wind in the (a) longitudinal, (b) radial, and (c) latitudinal directions. The orange points show bin averages and the associated standard deviation for each bin. The black dashed line in panel (a) shows the expected duration-velocity profile for a quiet period with a 2° longitudinal scale size. The quiet periods in this figure were identified with the manual method.

6.9 Occurrence of Quiet Periods in each Encounter

Another interesting property of quiet periods is their occurrence within solar encounters. The occurrence rate of quiet periods also varies with the encounter as shown in Tab. 6.1. Unfortunately, due to the lack of a clear definition of what a quiet period is, these values have large errors associated with them. However, it is still worth discussing the trends seen.

The occurrence rate of manually identified quiet periods is smallest for encounters 3 and 10. Interestingly, these are the only two encounters from the six studied here that do not contain a HCS crossing. In contrast, the most quiet periods were found during encounters 4 and 5 where not only was there a HCS crossing, but also the HCS was confined to low latitudes. As PSP has a low latitude orbit the spacecraft was likely in close proximity to the HCS for a considerable amount of time during encounters 4 and 5. This could indicate that quiet periods are associated with the HCS or surrounding solar wind.

A connection between PSP's proximity to the HCS and the appearance of quiet periods in the data could also explain the variation in clustering and temporal distributions of quiet periods between encounters. If there is a connection between proximity and quiet

periods, then when PSP is close to the HCS for a long period it is reasonable to expect an approximately uniform distribution of quiet periods with time. Equally, if the proximity of PSP from the HCS varies massively over an encounter then the quiet periods will display more clustering in time (i.e. they will only appear when PSP is close to the HCS). From a qualitative perspective the quiet periods seem more uniformly distributed in encounters 3 and 4 (during solar minimum) than in the later encounters (during increasing solar activity and therefore with a more inclined HCS). This clustering appears consistent with quiet periods being associated with proximity to the HCS.

In further support of this, Fig. 6.9 shows 4 of the 5 HCS crossings that occurred during encounters 3-7. The HCS crossing from encounter 5 has been excluded (as in Phan et al., 2021) because the time at which the crossing occurred is not clear. All 4 crossings shown in Fig. 6.9 display manually identified quiet periods (shaded red) directly either side of them. The duration of these quiet periods vary between ∼1 hr in the encounter 4 crossing (top left) to ∼5 hrs for the quiet period proceeding the first encounter 7 crossing (bottom left). Fig. 6.9 indicates a strong connection between the HCS and quiet periods. This relationship is explored further in the following section.

6.10 Discussion

The results in Sect. 6.8 suggest that quiet periods may have an intrinsic longitudinal scale size, and that if they do, this scale is rarely seen in the data, The reason for an underlying scale size not appearing in data is likely due to how the spacecraft cuts through the structures. Using the connection between quiet periods and PSP's proximity to the HCS suggested in Sect. 6.9, it may be possible to explain the apparent lack of scale size for most quiet periods.

The argument is as follows. If quiet periods do have a characteristic longitudinal scale size, this will only be seen in the data if PSP cuts through the full longitudinal extent of these structures. Any cuts that do not include the full longitudinal extent will not be representative of the underlying scale. As quiet periods seem to be associated with solar wind close to the HCS, a combination of PSP's orbit and the HCS shape likely affects how PSP cuts through quiet periods. For example, for PSP to measure the full longitude of a quiet period, it would have to skim close to the HCS for a long uninterrupted period of time. Any latitudinal changes in the HCS or PSP could interrupt the measurement of the

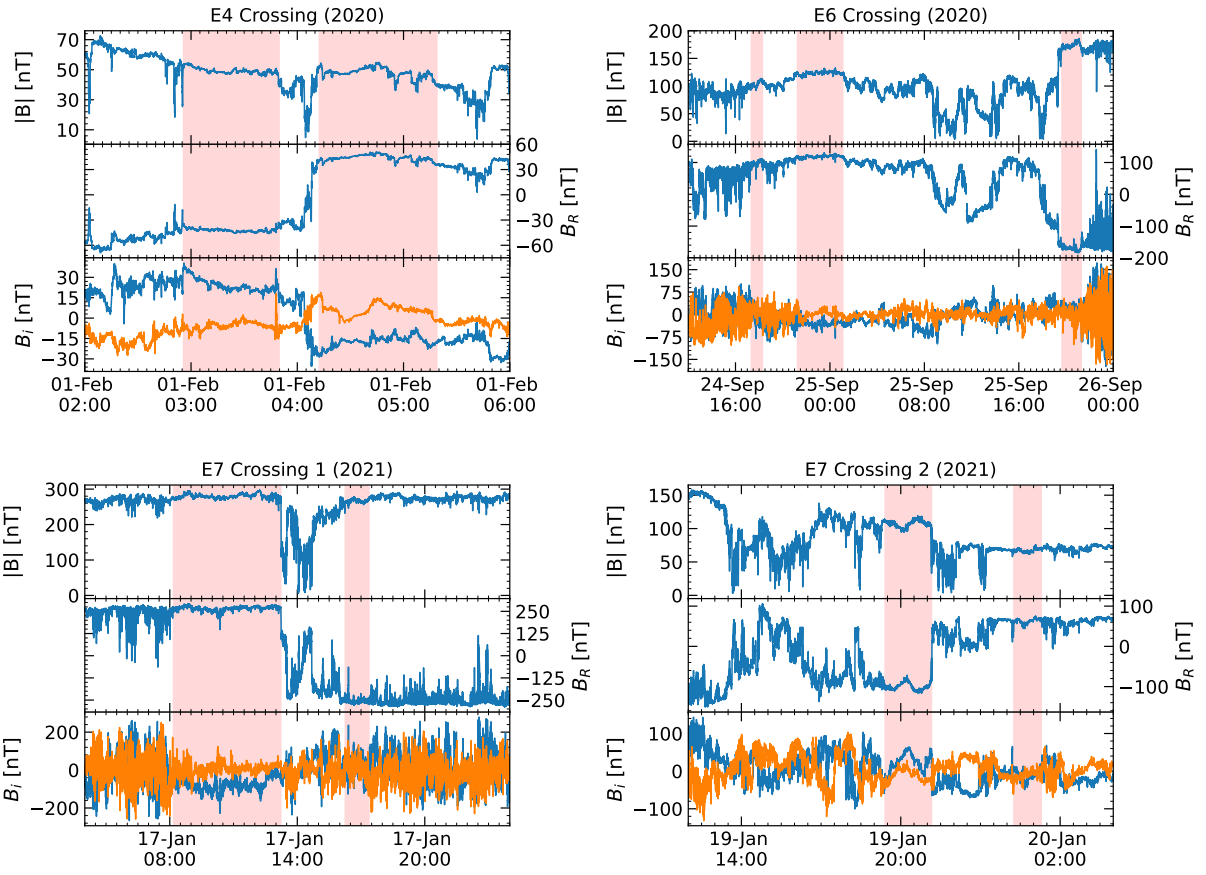


Figure 6.9: Time series of four HCS crossings observed during the early PSP encounters. In each plot the panels show (from top to bottom): the magnetic field magnitude, the magnetic field radial component, and the magnetic field tangential (blue) and normal (orange) components. The red shaded regions show quiet periods that were manually identified. Note that the timescale shown on the x-axis varies significantly between the four crossings.

quiet period and therefore the associated scale size. Given that the region surrounding the HCS is dynamic, it is reasonable to assume such uninterrupted measurements would be rare. Therefore, very few of the quiet periods observed by PSP would involve a full longitudinal cut, resulting in a duration-velocity plot similar to panel (a) in Fig. 6.8.

Based on the argument above, the results presented here are consistent with quiet periods having an intrinsic longitudinal scale size that is often obscured from the data by the interplay between the HCS and PSP's orbit. The proximity of quiet period streams to the HCS also explains why the clustering, distribution and number of quiet periods changes between encounters.

Whilst this theory fits some of the results well, there remain some unsolved questions. For example, it is not clear whether quiet periods are associated with what would be traditionally referred to as streamer belt solar wind or whether quiet periods contain a distinct type of solar wind. It is also unknown where these quiet period streams originate from on the Sun and why they are so highly correlated with the surrounding solar wind. Further work with ion composition measurements, such as those available from Solar Orbiter, would complement the research done here.

6.11 Conclusions

In this chapter, SPAN and FIELDS data were used to analyse quiet periods. This was the first study to focus solely on these structures and aimed to get a better understanding of their properties. Quiet periods were identified using both a manual and an algorithmic approach. Key properties of quiet periods were outlined before the plasma within these structures was compared to the surrounding solar wind. Potential characteristic scales of quiet periods were also investigated. The occurrence of quiet periods through different encounters was detailed, before a discussion about potential quiet period origins was presented.

The results in this chapter show that quiet periods are not simply quiet due to how PSP measured the solar wind with respect to the magnetic field. Instead quiet periods are associated with solar wind that intrinsically has weaker fluctuations. Quiet periods are associated with open magnetic field lines and are typically cooler than their surroundings. This could be a direct results of weaker fluctuations leading to reduced heating of the solar wind. There is a high correlation between the plasma properties inside and outside of

quiet periods which could indicate commonality in either the source or evolution of this solar wind. However, more studies are needed to understand this.

The evidence shown here suggests that quiet periods are associated with solar wind streams close to the HCS. These streams could have a characteristic longitudinal scale ($\sim 2^{\circ}$), but the combination of HCS dynamics and PSP's orbit obscures this characteristic scale from most of the quiet periods. This interpretation explains why quiet periods are often clustered in encounters, are always seen around HCS crossings, and why the number of quiet periods varies between encounters. Unfortunately, the origin of quiet period solar wind is still unknown. However, when ion composition data becomes available for Solar Orbiter there will be more opportunities to understand where this solar wind originates from.

Chapter 7

Conclusions

The Parker Solar Probe mission was the first spacecraft to make in situ measurements of the solar wind below 0.29 au. It achieved this in November 2018, and using a series of Venus gravity assists, has continued to take measurements at increasingly closer heliocentric distances ever since. The early observations from PSP show that the near-Sun solar wind is highly structured and appears qualitatively different from solar wind measurements taken at 1 au. This could be an indication that the solar wind undergoes significant evolution between leaving the Sun and arriving at Earth. To fully understand the solar wind conditions close to the Sun it is therefore important to use in situ data from small heliocentric distances, rather than extrapolating solar wind conditions back from the Earth. In this thesis, the novel PSP data set is exploited to investigate structures present in the near-Sun solar wind. In this chapter, a summary of each piece of work is provided and suggestions for future studies are made.

Chapter 3 focuses on extracting bulk solar wind parameters from the Solar Probe Cup instrument on board PSP. The operational principles behind the Faraday cup are explained and the process for converting raw instrument data into ion velocity distribution functions is given. Due to the design of the SPC instrument, and Faraday cups in general, the measured ion VDFs are one-dimensional 'cuts' through the 'real' three-dimensional ion VDF. Therefore, a one-dimensional Maxwellian distribution is used to fit the proton core population and obtain the core bulk plasma properties (i.e. number density, velocity, and temperature). One downside of measuring a one-dimensional cut of a three-dimensional distribution is that the angle of the cut with respect to the background magnetic field

influences the bulk parameters. This effect is discussed in-depth to ensure correct interpretation of the bulk parameters under different magnetic field orientations. For SPC, the temperature measurements are shown, in general, to be a combination of $T_\perp$ and $T_\parallel$. Only when the local magnetic field is perpendicular or (anti-)parallel to the Sun-spacecraft line does the SPC temperature correspond to $T_\perp$ and $T_\parallel$, respectively. The fitting of this SPC data was particularly important for the first solar encounter as this was the only plasma data available at that time. The SPC data fitted here are used in Chapter 4.

Chapter 4 uses the SPC data from Chapter 3 to investigate magnetic field switchbacks in the first two PSP encounters. These switchbacks are local folds in the magnetic field that appear ubiquitously in the solar wind close to the Sun. Switchbacks have been observed by other spacecraft at larger distances from the Sun (Balogh et al., 1999; Neugebauer and Goldstein, 2013; Horbury et al., 2018). However, the limited cadence of previous data has made studying these structures difficult. The high cadence SPC data provide the first opportunity to study the plasma inside switchbacks.

Chapter 4 focuses on full-reversal switchbacks due to the limitations of the SPC data outlined in Chapter 3. It is shown that the SPC-measured 1D ion VDFs are remarkably similar inside and outside a case study switchback when the rotation of the VDF due to Alfvénic fluctuations is accounted for. This indicates that the differences in the SPC-measured temperature throughout the switchback are due to different geometrical 'cuts' of the 3D ion VDF with respect to the local magnetic field, rather than a change in the underlying distribution. This means that for a full-reversal switchback the proton core parallel temperature is the same inside a switchback as it is within the background plasma. Whilst these findings do not rule out any particular switchback theory, they do provide important constraints for models.

One limitation of this study is that the temperature comparisons are restricted to full-reversal switchbacks only. This issue can be partly resolved by using SPAN data to investigate intermediate switchbacks (Woodham et al., 2021). However, it is still unclear whether the SPAN and SPC results reconcile with each other. Future work could focus on understanding the $T_{pc,\parallel} - \theta_{BR}$ relationship and testing whether it follows a sinusoidal form as suggested in Chapter 4.

Chapter 5 presents one of the first studies aimed at addressing the larger scale grouping of

switchbacks into patches. The work makes use of PSP's fourth and fifth solar encounters, where the orbital trajectory was the same (except for a shift in longitude), to identify two patches measured by PSP at the same heliocentric distance and latitude. These two patches are then compared to each other and a quiet period. The plasma properties within the patches are distinct from the quiet period properties, suggesting that these structures represent two separate modes of solar wind. Moreover, the plasma properties within each patch are remarkably similar for two solar wind intervals measured six months apart. The solar wind in patches is shown to be consistent with slow Alfvénic solar wind from near the boundary of the southern polar coronal hole. A comparison between the slow Alfvénic wind in these patches and the slow Alfvénic wind measured at 0.35 au is shown to understand how this wind may evolve as it expands into the heliosphere.

Another interesting result is the very low $\alpha-$particle abundance observed during the encounter 5 patch. This $\alpha-$particle abundance is particularly low, and in direct contrast to a later study that showed enhancements in the abundance within patches (Bale et al., 2021). The discrepancy between the two studies is an ideal project for future work and could help to better understand the source regions of switchback patches. It is possible that patches have variable properties depending on their solar origin or on the physical mechanisms dominating their release into the solar wind.

Chapter 6 presents the first study solely focused on the quiet periods observed by PSP. This work aims to summarise the properties of these quiet periods and make initial steps towards linking them to a solar source region. In Chapter 6 it is first argued that quiet periods are not simply a result of how the spacecraft samples the solar wind, but are instead distinct solar wind with weaker fluctuations. Using two methods for identifying quiet periods, further properties are explored. It is shown that the solar wind conditions within quiet periods are highly correlated but distinct from the surrounding solar wind properties. Quiet periods are also observed either side of all four clear HCS crossings that occurred during encounters 3-7. The number and clustering of quiet periods is found to vary between each encounter and these results are discussed.

The evidence suggests that quiet periods are related to solar wind near the HCS and that PSP only measures quiet periods when it is within a certain proximity to the HCS. These solar wind features may have an intrinsic longitudinal scale ($\sim 2^{\circ}$) that gets obscured from the data by a combination of PSP's orbital trajectory and the shape of the HCS.

This theory explains why quiet periods are seen either side of HCS crossings and why the distribution and number of quiet periods varies between encounters.

There are still many outstanding questions about quiet periods. Future studies, particularly those utilising both Solar Orbiter and PSP data, should focus on the ion composition within these structures and whether such structures exist at higher latitudes. Both of these research avenues would help to identify where quiet periods originate from and confirm if they are related to solar wind close to the HCS.

Overall, the work in this thesis aims to develop an understanding of the structures seen in the early Parker Solar Probe data. As Parker Solar Probe continues to take measurements closer to the Sun, more of the remaining questions will be answered. The Solar Orbiter mission also provides a great opportunity for multi-spacecraft studies and complements PSP data with composition measurements, which could be vital in understanding the origin of the structures discussed here.

Bibliography

Abbo, L., Ofman, L., Antiochos, S. K., Hansteen, V. H., Harra, L., Ko, Y. K., Lapenta, G., Li, B., Riley, P., Strachan, L., von Steiger, R. and Wang, Y. M. (2016), 'Slow Solar Wind: Observations and Modeling', *Space Sci. Rev.* **201**(1-4), 55–108. DOI/URL: https://doi.org/10.1007/s11214-016-0264-1

Alfvén, H. (1942), 'Existence of Electromagnetic-Hydrodynamic Waves', *Nature* **150**(3805), 405–406. DOI/URL: https://doi.org/10.1038/150405d0

Alterman, B. L., Kasper, J. C., Leamon, R. J. and McIntosh, S. W. (2021), 'Solar Wind Helium Abundance Heralds Solar Cycle Onset', *Sol. Phys.* **296**(4), 67. DOI/URL: https://doi.org/10.1007/s11207-021-01801-9

Alterman, B. L., Kasper, J. C., Stevens, M. L. and Koval, A. (2018), 'A Comparison of Alpha Particle and Proton Beam Differential Flows in Collisionally Young Solar Wind', *ApJ* **864**(2), 112. DOI/URL: https://doi.org/10.3847/1538-4357/aad23f

Altschuler, M. D. and Newkirk, G. (1969), 'Magnetic Fields and the Structure of the Solar Corona. I: Methods of Calculating Coronal Fields', *Sol. Phys.* **9**(1), 131–149. DOI/URL: https://doi.org/10.1007/BF00145734

Antiochos, S. K., Mikić, Z., Titov, V. S., Lionello, R. and Linker, J. A. (2011), 'A Model for the Sources of the Slow Solar Wind', *ApJ* **731**(2), 112. DOI/URL: https://doi.org/10.1088/0004-637X/731/2/112

Asbridge, J. R., Bame, S. J. and Feldman, W. C. (1974), 'Abundance Differences in Solar Wind Double Streams', *Sol. Phys.* **37**(2), 451–467. DOI/URL: https://doi.org/10.1007/BF00152503

Asbridge, J. R., Bame, S. J., Feldman, W. C. and Montgomery, M. D. (1976), 'Helium and hydrogen velocity differences in the solar wind', *J. Geophys. Res.* **81**(16), 2719. DOI/URL: https://doi.org/10.1029/JA081i016p02719

Badman, S. T., Bale, S. D., Martínez Oliveros, J. C., Panasenco, O., Velli, M., Stansby, D., Buitrago-Casas, J. C., Réville, V., Bonnell, J. W., Case, A. W., Dudok de Wit, T., Goetz, K., Harvey, P. R., Kasper, J. C., Korreck, K. E., Larson, D. E., Livi, R., MacDowall, R. J., Malaspina, D. M., Pulupa, M., Stevens, M. L. and Whittlesey, P. L. (2020), 'Magnetic Connectivity of the Ecliptic Plane within 0.5 au: Potential Field

Source Surface Modeling of the First Parker Solar Probe Encounter', *ApJS* **246**(2), 23. DOI/URL: https://doi.org/10.3847/1538-4365/ab4da7

Bale, S. D., Badman, S. T., Bonnell, J. W., Bowen, T. A., Burgess, D., Case, A. W., Cattell, C. A., Chandran, B. D. G., Chaston, C. C., Chen, C. H. K., Drake, J. F., de Wit, T. D., Eastwood, J. P., Ergun, R. E., Farrell, W. M., Fong, C., Goetz, K., Goldstein, M., Goodrich, K. A., Harvey, P. R., Horbury, T. S., Howes, G. G., Kasper, J. C., Kellogg, P. J., Klimchuk, J. A., Korreck, K. E., Krasnoselskikh, V. V., Krucker, S., Laker, R., Larson, D. E., MacDowall, R. J., Maksimovic, M., Malaspina, D. M., Martinez-Oliveros, J., McComas, D. J., Meyer-Vernet, N., Moncuquet, M., Mozer, F. S., Phan, T. D., Pulupa, M., Raouafi, N. E., Salem, C., Stansby, D., Stevens, M., Szabo, A., Velli, M., Woolley, T. and Wygant, J. R. (2019), 'Highly structured slow solar wind emerging from an equatorial coronal hole', *Nature* **576**(7786), 237–242. DOI/URL: https://doi.org/10.1038/s41586-019-1818-7

Bale, S. D., Goetz, K., Harvey, P. R., Turin, P., Bonnell, J. W., Dudok de Wit, T., Ergun, R. E., MacDowall, R. J., Pulupa, M., Andre, M., Bolton, M., Bougeret, J. L., Bowen, T. A., Burgess, D., Cattell, C. A., Chandran, B. D. G., Chaston, C. C., Chen, C. H. K., Choi, M. K., Connerney, J. E., Cranmer, S., Diaz-Aguado, M., Donakowski, W., Drake, J. F., Farrell, W. M., Fergeau, P., Fermin, J., Fischer, J., Fox, N., Glaser, D., Goldstein, M., Gordon, D., Hanson, E., Harris, S. E., Hayes, L. M., Hinze, J. J., Hollweg, J. V., Horbury, T. S., Howard, R. A., Hoxie, V., Jannet, G., Karlsson, M., Kasper, J. C., Kellogg, P. J., Kien, M., Klimchuk, J. A., Krasnoselskikh, V. V., Krucker, S., Lynch, J. J., Maksimovic, M., Malaspina, D. M., Marker, S., Martin, P., Martinez-Oliveros, J., McCauley, J., McComas, D. J., McDonald, T., Meyer-Vernet, N., Moncuquet, M., Monson, S. J., Mozer, F. S., Murphy, S. D., Odom, J., Oliverson, R., Olson, J., Parker, E. N., Pankow, D., Phan, T., Quataert, E., Quinn, T., Ruplin, S. W., Salem, C., Seitz, D., Sheppard, D. A., Siy, A., Stevens, K., Summers, D., Szabo, A., Timofeeva, M., Vaivads, A., Velli, M., Yehle, A., Werthimer, D. and Wygant, J. R. (2016), 'The FIELDS Instrument Suite for Solar Probe Plus. Measuring the Coronal Plasma and Magnetic Field, Plasma Waves and Turbulence, and Radio Signatures of Solar Transients', *Space Sci. Rev.* **204**(1-4), 49–82. DOI/URL: https://doi.org/10.1007/s11214-016-0244-5

Bale, S. D., Horbury, T. S., Velli, M., Desai, M. I., Halekas, J. S., McManus, M. D., Panasenco, O., Badman, S. T., Bowen, T. A., Chandran, B. D. G., Drake, J. F., Kasper, J. C., Laker, R., Mallet, A., Matteini, L., Phan, T. D., Raouafi, N. E., Squire, J., Woodham, L. D. and Woolley, T. (2021), 'A Solar Source of Alfvénic Magnetic Field Switchbacks: In Situ Remnants of Magnetic Funnels on Supergranulation Scales', *ApJ* **923**(2), 174. DOI/URL: https://doi.org/10.3847/1538-4357/ac2d8c

Ballot, J., Roudier, T., Malherbe, J. M. and Frank, Z. (2021), 'Changes in granulation scales over the solar cycle seen with SDO/HMI and Hinode/SOT', *A&A* **652**, A103. DOI/URL: https://doi.org/10.1051/0004-6361/202039436

Balogh, A., Beek, T. J., Forsyth, R. J., Hedgecock, P. C., Marquedant, R. J., Smith, E. J., Southwood, D. J. and Tsurutani, B. T. (1992), 'The magnetic field investigation on the ULYSSES mission - Instrumentation and preliminary scientific results', *A&AS* **92**(2), 221–236. DOI/URL: https://ui.adsabs.harvard.edu/abs/1992A&AS...92..221B

Balogh, A., Dunlop, M. W., Cowley, S. W. H., Southwood, D. J., Thomlinson, J. G., Glassmeier, K. H., Musmann, G., Luhr, H., Buchert, S., Acuna, M. H., Fairfield, D. H., Slavin, J. A., Riedler, W., Schwingenschuh, K. and Kivelson, M. G. (1997), 'The Cluster Magnetic Field Investigation', *Space Sci. Rev.* **79**, 65–91. DOI/URL: https://doi.org/10.1023/A:1004970907748

Balogh, A., Forsyth, R. J., Lucek, E. A., Horbury, T. S. and Smith, E. J. (1999), 'Heliospheric magnetic field polarity inversions at high heliographic latitudes', *Geophys. Res. Lett.* **26**(6), 631–634. DOI/URL: https://doi.org/10.1029/1999GL900061

Bame, S. J., Asbridge, J. R., Feldman, W. C. and Gosling, J. T. (1977), 'Evidence for a structure-free state at high solar wind speeds', *J. Geophys. Res.* **82**(10), 1487. DOI/URL: https://doi.org/10.1029/JA082i010p01487

Bame, S. J., McComas, D. J., Barraclough, B. L., Phillips, J. L., Sofaly, K. J., Chavez, J. C., Goldstein, B. E. and Sakurai, R. K. (1992), 'The ULYSSES solar wind plasma experiment', *A&AS* **92**(2), 237–265. DOI/URL: https://ui.adsabs.harvard.edu/abs/1992A&AS...92..237B

Baumjohann, W. and Treumann, R. A. (1997), *Basic space plasma physics*, Imperial College Press, London.

Belcher, J. W. and Davis, Leverett, J. (1971), 'Large-amplitude Alfvén waves in the interplanetary medium, 2', *J. Geophys. Res.* **76**(16), 3534. DOI/URL: https://doi.org/10.1029/JA076i016p03534

Berger, L., Wimmer-Schweingruber, R. F. and Gloeckler, G. (2011), 'Systematic Measurements of Ion-Proton Differential Streaming in the Solar Wind', *Phys. Rev. Lett.* **106**(15), 151103. DOI/URL: https://doi.org/10.1103/PhysRevLett.106.151103

Berčič, L., Larson, D., Whittlesey, P., Maksimović, M., Badman, S. T., Landi, S., Matteini, L., Bale, S. D., Bonnell, J. W., Case, A. W., Dudok de Wit, T., Goetz, K., Harvey, P. R., Kasper, J. C., Korreck, K. E., Livi, R., MacDowall, R. J., Malaspina, D. M., Pulupa, M. and Stevens, M. L. (2020), 'Coronal Electron Temperature Inferred from the Strahl Electrons in the Inner Heliosphere: Parker Solar Probe and Helios Observations', *ApJ* **892**(2), 88. DOI/URL: https://doi.org/10.3847/1538-4357/ab7b7a

Biermann, L. (1957), 'Solar corpuscular radiation and the interplanetary gas', *The Observatory* **77**, 109–110.

Bochsler, P. (2007), 'Minor ions in the solar wind', *A&ARv* **14**(1), 1–40. DOI/URL:

https://doi.org/10.1007/s00159-006-0002-x

Bourouaine, S. and Chandran, B. D. G. (2013), 'Observational Test of Stochastic Heating in Low-β Fast-solar-wind Streams', *ApJ* **774**(2), 96. DOI/URL: https://doi.org/10.1088/0004-637X/774/2/96

Bowen, T. A., Squire, J., Bale, S. D., Chandran, B., Duan, D., Klein, K. G., Larson, D., Mallet, A., McManus, M. D., Meyrand, R., Verniero, J. L. and Woodham, L. D. (2021), 'The In Situ Signature of Cyclotron Resonant Heating', *arXiv e-prints* p. arXiv:2111.05400. DOI/URL: https://doi.org/10.48550/arXiv.2111.05400

Bridge, H. S., Belcher, J. W., Butler, R. J., Lazarus, A. J., Mavretic, A. M., Sullivan, J. D., Siscoe, G. L. and Vasyliunas, V. M. (1977), 'The Plasma Experiment on the 1977 Voyager Mission', *Space Sci. Rev.* **21**(3), 259–287. DOI/URL: https://doi.org/10.1007/BF00211542

Burlaga, L. F. and Ogilvie, K. W. (1970), 'Heating of the Solar Wind', *ApJ* **159**, 659. DOI/URL: https://doi.org/10.1086/150340

Burlaga, L. F. and Ogilvie, K. W. (1973), 'Solar wind temperature and speed', *J. Geophys. Res.* **78**(13), 2028. DOI/URL: https://doi.org/10.1029/JA078i013p02028

Byhring, H. S. (2011), 'The Helium Abundance in Polar Coronal Holes and the Fast Solar Wind', *ApJ* **738**(2), 172. DOI/URL: https://doi.org/10.1088/0004-637X/738/2/172

Camporeale, E., Carè, A. and Borovsky, J. E. (2017), 'Classification of Solar Wind With Machine Learning', *Journal of Geophysical Research (Space Physics)* **122**(11), 10,910–10,920. DOI/URL: https://doi.org/10.1002/2017JA024383

Carrington, R. C. (1859), 'Description of a Singular Appearance seen in the Sun on September 1, 1859', *MNRAS* **20**, 13–15. DOI/URL: https://doi.org/10.1093/mnras/20.1.13

Case, A. W., Kasper, J. C., Stevens, M. L., Korreck, K. E., Paulson, K., Daigneau, P., Caldwell, D., Freeman, M., Henry, T., Klingensmith, B., Bookbinder, J. A., Robinson, M., Berg, P., Tiu, C., Wright, K. H., J., Reinhart, M. J., Curtis, D., Ludlam, M., Larson, D., Whittlesey, P., Livi, R., Klein, K. G. and Martinović, M. M. (2020), 'The Solar Probe Cup on the Parker Solar Probe', *ApJS* **246**(2), 43. DOI/URL: https://doi.org/10.3847/1538-4365/ab5a7b

Chandran, B. D. G. (2010), 'Alfvén-wave Turbulence and Perpendicular Ion Temperatures in Coronal Holes', *ApJ* **720**(1), 548–554. DOI/URL: https://doi.org/10.1088/0004-637X/720/1/548

Chen, C. H. K., Bale, S. D., Bonnell, J. W., Borovikov, D., Bowen, T. A., Burgess, D., Case, A. W., Chandran, B. D. G., de Wit, T. D., Goetz, K., Harvey, P. R., Kasper, J. C.,

Klein, K. G., Korreck, K. E., Larson, D., Livi, R., MacDowall, R. J., Malaspina, D. M., Mallet, A., McManus, M. D., Moncuquet, M., Pulupa, M., Stevens, M. L. and Whittlesey, P. (2020), 'The Evolution and Role of Solar Wind Turbulence in the Inner Heliosphere', *ApJS* **246**(2), 53. DOI/URL: https://doi.org/10.3847/1538-4365/ab60a3

Chen, C. H. K., Chandran, B. D. G., Woodham, L. D., Jones, S. I., Perez, J. C., Bourouaine, S., Bowen, T. A., Klein, K. G., Moncuquet, M., Kasper, J. C. and Bale, S. D. (2021), 'The near-sun streamer belt solar wind: turbulence and solar wind acceleration', *A&A* **650**, L3. DOI/URL: https://doi.org/10.1051/0004-6361/202039872

Chew, G. F., Goldberger, M. L. and Low, F. E. (1956), 'The Boltzmann Equation and the One-Fluid Hydromagnetic Equations in the Absence of Particle Collisions', *Proceedings of the Royal Society of London Series A* **236**(1204), 112–118. DOI/URL: https://doi.org/10.1098/rspa.1956.0116

Coleman, Paul J., J. (1968), 'Turbulence, Viscosity, and Dissipation in the Solar-Wind Plasma', *ApJ* **153**, 371. DOI/URL: https://doi.org/10.1086/149674

Cranmer, S. R. (2009), 'Coronal Holes', *Living Reviews in Solar Physics* **6**(1), 3. DOI/URL: https://doi.org/10.12942/lrsp-2009-3

Cranmer, S. R., van Ballegooijen, A. A. and Edgar, R. J. (2007), 'Self-consistent Coronal Heating and Solar Wind Acceleration from Anisotropic Magnetohydrodynamic Turbulence', *ApJS* **171**(2), 520–551. DOI/URL: https://doi.org/10.1086/518001

Crooker, N. U., Huang, C. L., Lamassa, S. M., Larson, D. E., Kahler, S. W. and Spence, H. E. (2004), 'Heliospheric plasma sheets', *Journal of Geophysical Research (Space Physics)* **109**(A3), A03107. DOI/URL: https://doi.org/10.1029/2003JA010170

D'Amicis, R. and Bruno, R. (2015), 'On the Origin of Highly Alfvénic Slow Solar Wind', *ApJ* **805**(1), 84. DOI/URL: https://doi.org/10.1088/0004-637X/805/1/84

David, C., Gabriel, A. H., Bely-Dubau, F., Fludra, A., Lemaire, P. and Wilhelm, K. (1998), 'Measurement of the electron temperature gradient in a solar coronal hole', *A&A* **336**, L90–L94. DOI/URL: https://ui.adsabs.harvard.edu/abs/1998A&A...336L..90D

Démoulin, P. (2009), 'Why Do Temperature and Velocity Have Different Relationships in the Solar Wind and in Interplanetary Coronal Mass Ejections?', *Sol. Phys.* **257**(1), 169–184. DOI/URL: https://doi.org/10.1007/s11207-009-9338-5

Drake, J. F., Agapitov, O., Swisdak, M., Badman, S. T., Bale, S. D., Horbury, T. S., Kasper, J. C., MacDowall, R. J., Mozer, F. S., Phan, T. D., Pulupa, M., Szabo, A. and Velli, M. (2021), 'Switchbacks as signatures of magnetic flux ropes generated by interchange reconnection in the corona', *A&A* **650**, A2. DOI/URL: https://doi.org/10.1051/0004-6361/202039432

Dudok de Wit, T., Krasnoselskikh, V. V., Bale, S. D., Bonnell, J. W., Bowen, T. A., Chen, C. H. K., Froment, C., Goetz, K., Harvey, P. R., Jagarlamudi, V. K., Larosa, A., MacDowall, R. J., Malaspina, D. M., Matthaeus, W. H., Pulupa, M., Velli, M. and Whittlesey, P. L. (2020), 'Switchbacks in the Near-Sun Magnetic Field: Long Memory and Impact on the Turbulence Cascade', *ApJS* **246**(2), 39. DOI/URL: https://doi.org/10.3847/1538-4365/ab5853

Einaudi, G., Boncinelli, P., Dahlburg, R. B. and Karpen, J. T. (1999), 'Formation of the slow solar wind in a coronal streamer', *J. Geophys. Res.* **104**(A1), 521–534. DOI/URL: https://doi.org/10.1029/98JA02394

Elliott, H. A., Henney, C. J., McComas, D. J., Smith, C. W. and Vasquez, B. J. (2012), 'Temporal and radial variation of the solar wind temperature-speed relationship', *Journal of Geophysical Research (Space Physics)* **117**(A9), A09102. DOI/URL: https://doi.org/10.1029/2011JA017125

ESA (2020), 'Last glimpse of Solar Orbiter before launch', *[photograph] ESA* . DOI/URL: https://www.esa.int/var/esa/storage/images/esa_multimedia/images/2020/02/last_glimpse_of_solar_orbiter_before_launch/21826084-2-eng-GB/Last_glimpse_of_Solar_Orbiter_before_launch_pillars.jpg

Fargette, N., Lavraud, B., Rouillard, A. P., Réville, V., Dudok De Wit, T., Froment, C., Halekas, J. S., Phan, T. D., Malaspina, D. M., Bale, S. D., Kasper, J. C., Louarn, P., Case, A. W., Korreck, K. E., Larson, D. E., Pulupa, M., Stevens, M. L., Whittlesey, P. L. and Berthomier, M. (2021), 'Characteristic Scales of Magnetic Switchback Patches Near the Sun and Their Possible Association With Solar Supergranulation and Granulation', *ApJ* **919**(2), 96. DOI/URL: https://doi.org/10.3847/1538-4357/ac1112

Feldman, U., Widing, K. G. and Warren, H. P. (1999), 'Morphology of the Quiet Solar Upper Atmosphere in the $4\times10^4 < T_e < 1.4\times10^6$ K Temperature Regime', *ApJ* **522**(2), 1133–1147. DOI/URL: https://doi.org/10.1086/307682

Feldman, W. C., Asbridge, J. R., Bame, S. J. and Gosling, J. T. (1978*a*), 'Long-term variations of selected solar wind properties: Imp 6, 7, and 8 results', *J. Geophys. Res.* **83**(A5), 2177–2189. DOI/URL: https://doi.org/10.1029/JA083iA05p02177

Feldman, W. C., Asbridge, J. R., Bame, S. J., Gosling, J. T. and Lemons, D. S. (1978*b*), 'Characteristic electron variations across simple high-speed solar wind streams', *J. Geophys. Res.* **83**(A11), 5285–5296. DOI/URL: https://doi.org/10.1029/JA083iA11p05285

Feldman, W. C., Asbridge, J. R., Bame, S. J. and Montgomery, M. D. (1973), 'Double ion streams in the solar wind', *J. Geophys. Res.* **78**(13), 2017. DOI/URL: https://doi.org/10.1029/JA078i013p02017

Feldman, W. C., Asbridge, J. R., Bame, S. J. and Montgomery, M. D. (1974), 'Interpen-

etrating solar wind streams.', *Reviews of Geophysics and Space Physics* **12**, 715–723. DOI/URL: https://doi.org/10.1029/RG012i004p00715

Feldman, W. C., Asbridge, J. R., Bame, S. J., Montgomery, M. D. and Gary, S. P. (1975), 'Solar wind electrons', *J. Geophys. Res.* **80**(31), 4181. DOI/URL: https://doi.org/10.1029/JA080i031p04181

Finley, A. J., McManus, M. D., Matt, S. P., Kasper, J. C., Korreck, K. E., Case, A. W., Stevens, M. L., Whittlesey, P., Larson, D., Livi, R., Bale, S. D., Dudok de Wit, T., Goetz, K., Harvey, P. R., MacDowall, R. J., Malaspina, D. M. and Pulupa, M. (2021), 'The contribution of alpha particles to the solar wind angular momentum flux in the inner heliosphere', *A&A* **650**, A17. DOI/URL: https://doi.org/10.1051/0004-6361/202039288

Fisk, L. A. (2003), 'Acceleration of the solar wind as a result of the reconnection of open magnetic flux with coronal loops', *Journal of Geophysical Research (Space Physics)* **108**(A4), 1157. DOI/URL: https://doi.org/10.1029/2002JA009284

Fisk, L. A. and Kasper, J. C. (2020), 'Global Circulation of the Open Magnetic Flux of the Sun', *ApJ* **894**(1), L4. DOI/URL: https://doi.org/10.3847/2041-8213/ab8acd

Fisk, L. A. and Schwadron, N. A. (2001), 'The Behavior of the Open Magnetic Field of the Sun', *ApJ* **560**(1), 425–438. DOI/URL: https://doi.org/10.1086/322503

Fisk, L. A., Schwadron, N. A. and Zurbuchen, T. H. (1999), 'Acceleration of the fast solar wind by the emergence of new magnetic flux', *J. Geophys. Res.* **104**(A9), 19765–19772. DOI/URL: https://doi.org/10.1029/1999JA900256

Forsyth, R. J., Balogh, A., Smith, E. J., Murphy, N. and McComas, D. J. (1995), 'The underlying magnetic field direction in Ulysses observations of the southern polar heliosphere', *Geophys. Res. Lett.* **22**(23), 3321–3324. DOI/URL: https://doi.org/10.1029/95GL02646

Fox, N. J., Velli, M. C., Bale, S. D., Decker, R., Driesman, A., Howard, R. A., Kasper, J. C., Kinnison, J., Kusterer, M., Lario, D., Lockwood, M. K., McComas, D. J., Raouafi, N. E. and Szabo, A. (2016), 'The Solar Probe Plus Mission: Humanity's First Visit to Our Star', *Space Sci. Rev.* **204**(1-4), 7–48. DOI/URL: https://doi.org/10.1007/s11214-015-0211-6

Fu, H., Madjarska, M. S., Li, B., Xia, L. and Huang, Z. (2018), 'Helium abundance and speed difference between helium ions and protons in the solar wind from coronal holes, active regions, and quiet Sun', *MNRAS* **478**(2), 1884–1892. DOI/URL: https://doi.org/10.1093/mnras/sty1211

Gary, S. P., Yin, L., Winske, D. and Reisenfeld, D. B. (2000), 'Electromagnetic alpha/proton instabilities in the solar wind', *Geophys. Res. Lett.* **27**(9), 1355–1358. DOI/URL: https://doi.org/10.1029/2000GL000019

Geiss, J., Hirt, P. and Leutwyler, H. (1970), 'On Acceleration and Motion of Ions in Corona and Solar Wind', *Sol. Phys.* **12**(3), 458–483. DOI/URL: https://doi.org/10.1007/BF00148028

Gloeckler, G., Zurbuchen, T. H. and Geiss, J. (2003), 'Implications of the observed anticorrelation between solar wind speed and coronal electron temperature', *Journal of Geophysical Research (Space Physics)* **108**(A4), 1158. DOI/URL: https://doi.org/10.1029/2002JA009286

Gringauz, K. I., Bezrokikh, V. V., Ozerov, V. D. and Rybchinskii, R. E. (1960), 'A Study of the Interplanetary Ionized Gas, High-Energy Electrons and Corpuscular Radiation from the Sun by Means of the Three-Electrode Trap for Charged Particles on the Second Soviet Cosmic Rocket', *Soviet Physics Doklady* **5**, 361. DOI/URL: https://ui.adsabs.harvard.edu/abs/1960SPhD....5..361G

Hale, G. E. (1908), 'On the Probable Existence of a Magnetic Field in Sun-Spots', *ApJ* **28**, 315. DOI/URL: https://doi.org/10.1086/141602

Halekas, J. S., Taylor, E. R., Dalton, G., Johnson, G., Curtis, D. W., McFadden, J. P., Mitchell, D. L., Lin, R. P. and Jakosky, B. M. (2015), 'The Solar Wind Ion Analyzer for MAVEN', *Space Sci. Rev.* **195**(1-4), 125–151. DOI/URL: https://doi.org/10.1007/s11214-013-0029-z

Halekas, J. S., Whittlesey, P., Larson, D. E., Maksimovic, M., Livi, R., Berthomier, M., Kasper, J. C., Case, A. W., Stevens, M. L., Bale, S. D., MacDowall, R. J. and Pulupa, M. P. (2022), 'The Radial Evolution of the Solar Wind as Organized by Electron Distribution Parameters', *ApJ* **936**(1), 53. DOI/URL: https://doi.org/10.3847/1538-4357/ac85b8

Harra, L. K., Sakao, T., Mandrini, C. H., Hara, H., Imada, S., Young, P. R., van Driel-Gesztelyi, L. and Baker, D. (2008), 'Outflows at the Edges of Active Regions: Contribution to Solar Wind Formation?', *ApJ* **676**(2), L147. DOI/URL: https://doi.org/10.1086/587485

Harvey, J. W., Hill, F., Hubbard, R. P., Kennedy, J. R., Leibacher, J. W., Pintar, J. A., Gilman, P. A., Noyes, R. W., Title, A. M., Toomre, J., Ulrich, R. K., Bhatnagar, A., Kennewell, J. A., Marquette, W., Patron, J., Saa, O. and Yasukawa, E. (1996), 'The Global Oscillation Network Group (GONG) Project', *Science* **272**(5266), 1284–1286. DOI/URL: https://doi.org/10.1126/science.272.5266.1284

Harvey, K. L. (1992), Measurements of Solar Magnetic Fields as an Indicator of Solar Activity Evolution, *in* R. F. Donnelly, ed., 'Solar Electromagnetic Radiation Study for Solar Cycle 22', p. 113. DOI/URL: https://ui.adsabs.harvard.edu/abs/1992sers.conf..113H

Hellinger, P., Matteini, L., Štverák, Š., Trávníček, P. M. and Marsch, E. (2011), 'Heating

and cooling of protons in the fast solar wind between 0.3 and 1 AU: Helios revisited', *Journal of Geophysical Research (Space Physics)* **116**(A9), A09105. DOI/URL: https://doi.org/10.1029/2011JA016674

Hellinger, P., TráVníček, P. M., Štverák, Š., Matteini, L. and Velli, M. (2013), 'Proton thermal energetics in the solar wind: Helios reloaded', *Journal of Geophysical Research (Space Physics)* **118**(4), 1351–1365. DOI/URL: https://doi.org/10.1002/jgra.50107

Henriques, V. (2010), 'High Resolution Granulation', *[photograph] Swedish Vacuum Solar Telescope* . DOI/URL: https://ttt.astro.su.se/isf/gallery/images/2010/gran2_100.png

Hirshberg, J., Asbridge, J. R. and Robbins, D. E. (1972), 'Velocity and flux dependence of the solar-wind helium abundance', *J. Geophys. Res.* **77**(19), 3583. DOI/URL: https://doi.org/10.1029/JA077i019p03583

Hirshberg, J., Asbridge, J. R. and Robbins, D. E. (1974), 'The helium component of solar wind velocity streams', *J. Geophys. Res.* **79**(7), 934. DOI/URL: https://doi.org/10.1029/JA079i007p00934

Horbury, T. S., Balogh, A., Forsyth, R. J. and Smith, E. J. (1995), 'Anisotropy of inertial range turbulence in the polar heliosphere', *Geophys. Res. Lett.* **22**(23), 3405–3408. DOI/URL: https://doi.org/10.1029/95GL03012

Horbury, T. S., Matteini, L. and Stansby, D. (2018), 'Short, large-amplitude speed enhancements in the near-Sunfast solar wind', *MNRAS* **478**(2), 1980–1986. DOI/URL: https://doi.org/10.1093/mnras/sty953

Horbury, T. S., Woolley, T., Laker, R., Matteini, L., Eastwood, J., Bale, S. D., Velli, M., Chandran, B. D. G., Phan, T., Raouafi, N. E., Goetz, K., Harvey, P. R., Pulupa, M., Klein, K. G., Dudok de Wit, T., Kasper, J. C., Korreck, K. E., Case, A. W., Stevens, M. L., Whittlesey, P., Larson, D., MacDowall, R. J., Malaspina, D. M. and Livi, R. (2020), 'Sharp Alfvénic Impulses in the Near-Sun Solar Wind', *ApJS* **246**(2), 45. DOI/URL: https://doi.org/10.3847/1538-4365/ab5b15

Huang, J., Kasper, J. C., Vech, D., Klein, K. G., Stevens, M., Martinović, M. M., Alterman, B. L., Ďurovcová, T., Paulson, K., Maruca, B. A., Qudsi, R. A., Case, A. W., Korreck, K. E., Jian, L. K., Velli, M., Lavraud, B., Hegedus, A., Bert, C. M., Holmes, J., Bale, S. D., Larson, D. E., Livi, R., Whittlesey, P., Pulupa, M., MacDowall, R. J., Malaspina, D. M., Bonnell, J. W., Harvey, P., Goetz, K. and Dudok de Wit, T. (2020), 'Proton Temperature Anisotropy Variations in Inner Heliosphere Estimated with the First Parker Solar Probe Observations', *ApJS* **246**(2), 70. DOI/URL: https://doi.org/10.3847/1538-4365/ab74e0

Hundhausen, A. J., Asbridge, J. R., Bame, S. J., Gilbert, H. E. and Strong, I. B. (1967),

'Vela 3 Satellite Observations of Solar Wind Ions: A Preliminary Report', *J. Geophys. Res.* **72**, 87. DOI/URL: https://doi.org/10.1029/JZ072i001p00087

Jockers, K. (1970), 'Solar Wind Models Based on Exospheric Theory', *A&A* **6**, 219. DOI/URL: https://ui.adsabs.harvard.edu/abs/1970A&A.....6..219J

Karpen, J. T., DeVore, C. R., Antiochos, S. K. and Pariat, E. (2017), 'Reconnection-Driven Coronal-Hole Jets with Gravity and Solar Wind', *ApJ* **834**(1), 62. DOI/URL: https://doi.org/10.3847/1538-4357/834/1/62

Kasper, J. C., Abiad, R., Austin, G., Balat-Pichelin, M., Bale, S. D., Belcher, J. W., Berg, P., Bergner, H., Berthomier, M., Bookbinder, J., Brodu, E., Caldwell, D., Case, A. W., Chandran, B. D. G., Cheimets, P., Cirtain, J. W., Cranmer, S. R., Curtis, D. W., Daigneau, P., Dalton, G., Dasgupta, B., DeTomaso, D., Diaz-Aguado, M., Djordjevic, B., Donaskowski, B., Effinger, M., Florinski, V., Fox, N., Freeman, M., Gallagher, D., Gary, S. P., Gauron, T., Gates, R., Goldstein, M., Golub, L., Gordon, D. A., Gurnee, R., Guth, G., Halekas, J., Hatch, K., Heerikuisen, J., Ho, G., Hu, Q., Johnson, G., Jordan, S. P., Korreck, K. E., Larson, D., Lazarus, A. J., Li, G., Livi, R., Ludlam, M., Maksimovic, M., McFadden, J. P., Marchant, W., Maruca, B. A., McComas, D. J., Messina, L., Mercer, T., Park, S., Peddie, A. M., Pogorelov, N., Reinhart, M. J., Richardson, J. D., Robinson, M., Rosen, I., Skoug, R. M., Slagle, A., Steinberg, J. T., Stevens, M. L., Szabo, A., Taylor, E. R., Tiu, C., Turin, P., Velli, M., Webb, G., Whittlesey, P., Wright, K., Wu, S. T. and Zank, G. (2016), 'Solar Wind Electrons Alphas and Protons (SWEAP) Investigation: Design of the Solar Wind and Coronal Plasma Instrument Suite for Solar Probe Plus', *Space Sci. Rev.* **204**(1-4), 131–186. DOI/URL: https://doi.org/10.1007/s11214-015-0206-3

Kasper, J. C., Bale, S. D., Belcher, J. W., Berthomier, M., Case, A. W., Chandran, B. D. G., Curtis, D. W., Gallagher, D., Gary, S. P., Golub, L., Halekas, J. S., Ho, G. C., Horbury, T. S., Hu, Q., Huang, J., Klein, K. G., Korreck, K. E., Larson, D. E., Livi, R., Maruca, B., Lavraud, B., Louarn, P., Maksimovic, M., Martinovic, M., McGinnis, D., Pogorelov, N. V., Richardson, J. D., Skoug, R. M., Steinberg, J. T., Stevens, M. L., Szabo, A., Velli, M., Whittlesey, P. L., Wright, K. H., Zank, G. P., MacDowall, R. J., McComas, D. J., McNutt, R. L., Pulupa, M., Raouafi, N. E. and Schwadron, N. A. (2019), 'Alfvénic velocity spikes and rotational flows in the near-Sun solar wind', *Nature* **576**(7786), 228–231. DOI/URL: https://doi.org/10.1038/s41586-019-1813-z

Kasper, J. C., Lazarus, A. J. and Gary, S. P. (2002), 'Wind/swe observations of firehose constraint on solar wind proton temperature anisotropy', *Geophysical Research Letters* **29**(17), 20–1–20–4. DOI/URL: https://doi.org/10.1029/2002GL015128

Kasper, J. C., Stevens, M. L., Korreck, K. E., Maruca, B. A., Kiefer, K. K., Schwadron, N. A. and Lepri, S. T. (2012), 'Evolution of the Relationships between Helium Abundance, Minor Ion Charge State, and Solar Wind Speed over the Solar Cycle', *ApJ* **745**(2), 162. DOI/URL: https://doi.org/10.1088/0004-637X/745/2/162

Kasper, J. C., Stevens, M. L., Lazarus, A. J., Steinberg, J. T. and Ogilvie, K. W. (2007), 'Solar Wind Helium Abundance as a Function of Speed and Heliographic Latitude: Variation through a Solar Cycle', *ApJ* **660**(1), 901–910. DOI/URL: https://doi.org/10.1086/510842

Kepko, L. and Spence, H. E. (2003), 'Observations of discrete, global magnetospheric oscillations directly driven by solar wind density variations', *Journal of Geophysical Research (Space Physics)* **108**(A6), 1257. DOI/URL: https://doi.org/10.1029/2002JA009676

Kepko, L., Spence, H. E. and Singer, H. J. (2002), 'ULF waves in the solar wind as direct drivers of magnetospheric pulsations', *Geophys. Res. Lett.* **29**(8), 1197. DOI/URL: https://doi.org/10.1029/2001GL014405

Klimchuk, J. A. (2006), 'On Solving the Coronal Heating Problem', *Sol. Phys.* **234**(1), 41–77. DOI/URL: https://doi.org/10.1007/s11207-006-0055-z

Ko, Y.-K., Fisk, L. A., Geiss, J., Gloeckler, G. and Guhathakurta, M. (1997), 'An Empirical Study of the Electron Temperature and Heavy Ion Velocities in the South Polar Coronal Hole', *Sol. Phys.* **171**(2), 345–361. DOI/URL: https://ui.adsabs.harvard.edu/abs/1997SoPh..171..345K

Krieger, A. S., Timothy, A. F. and Roelof, E. C. (1973), 'A Coronal Hole and Its Identification as the Source of a High Velocity Solar Wind Stream', *Sol. Phys.* **29**(2), 505–525. DOI/URL: https://doi.org/10.1007/BF00150828

Laker, R., Horbury, T. S., Bale, S. D., Matteini, L., Woolley, T., Woodham, L. D., Badman, S. T., Pulupa, M., Kasper, J. C., Stevens, M., Case, A. W. and Korreck, K. E. (2021*a*), 'Statistical analysis of orientation, shape, and size of solar wind switchbacks', *A&A* **650**, A1. DOI/URL: https://doi.org/10.1051/0004-6361/202039354

Laker, R., Horbury, T. S., Bale, S. D., Matteini, L., Woolley, T., Woodham, L. D., Stawarz, J. E., Davies, E. E., Eastwood, J. P., Owens, M. J., O'Brien, H., Evans, V., Angelini, V., Richter, I., Heyner, D., Owen, C. J., Louarn, P. and Fedorov, A. (2021*b*), 'Multi-spacecraft study of the solar wind at solar minimum: Dependence on latitude and transient outflows', *A&A* **652**, A105. DOI/URL: https://doi.org/10.1051/0004-6361/202140679

Laker, R., Horbury, T. S., Matteini, L., Bale, S. D., Stawarz, J. E., Woodham, L. D. and Woolley, T. (2022), 'Switchback deflections beyond the early parker solar probe encounters', *Monthly Notices of the Royal Astronomical Society* . stac2477. DOI/URL: https://doi.org/10.1093/mnras/stac2477

Laming, J. M. (2004), 'A Unified Picture of the First Ionization Potential and Inverse First Ionization Potential Effects', *ApJ* **614**(2), 1063–1072. DOI/URL: https://doi.org/10.1086/423780

Lemaire, J. and Scherer, M. (1970), 'Model of the polar ion-exosphere', *Planet. Space Sci.*

18(1), 103–120. DOI/URL: https://doi.org/10.1016/0032-0633(70)90070-X

Lemaire, J. and Scherer, M. (1971), 'Kinetic models of the solar wind', *J. Geophys. Res.* **76**(31), 7479. DOI/URL: https://doi.org/10.1029/JA076i031p07479

Lepping, R. P., Acũna, M. H., Burlaga, L. F., Farrell, W. M., Slavin, J. A., Schatten, K. H., Mariani, F., Ness, N. F., Neubauer, F. M., Whang, Y. C., Byrnes, J. B., Kennon, R. S., Panetta, P. V., Scheifele, J. and Worley, E. M. (1995), 'The Wind Magnetic Field Investigation', *Space Sci. Rev.* **71**(1-4), 207–229. DOI/URL: https://doi.org/10.1007/BF00751330

Levine, R. H., Altschuler, M. D. and Harvey, J. W. (1977), 'Solar sources of the interplanetary magnetic field and solar wind', *J. Geophys. Res.* **82**(7), 1061. DOI/URL: https://doi.org/10.1029/JA082i007p01061

Li, H., Wang, C., Tu, C. and Xu, F. (2020), 'Machine Learning Approach for Solar Wind Categorization', *Earth and Space Science* **7**(5), e00997. DOI/URL: https://doi.org/10.1029/2019EA000997

Li, X., Habbal, S. R., Hollweg, J. V. and Esser, R. (1999), 'Heating and cooling of protons by turbulence-driven ion cyclotron waves in the fast solar wind', *J. Geophys. Res.* **104**(A2), 2521–2536. DOI/URL: https://doi.org/10.1029/1998JA900126

Lin, R. P., Anderson, K. A., Ashford, S., Carlson, C., Curtis, D., Ergun, R., Larson, D., McFadden, J., McCarthy, M., Parks, G. K., Rème, H., Bosqued, J. M., Coutelier, J., Cotin, F., D'Uston, C., Wenzel, K. P., Sanderson, T. R., Henrion, J., Ronnet, J. C. and Paschmann, G. (1995), 'A Three-Dimensional Plasma and Energetic Particle Investigation for the Wind Spacecraft', *Space Sci. Rev.* **71**(1-4), 125–153. DOI/URL: https://doi.org/10.1007/BF00751328

Lopez, R. E. and Freeman, J. W. (1986), 'Solar wind proton temperature-velocity relationship', *J. Geophys. Res.* **91**(A2), 1701–1705. DOI/URL: https://doi.org/10.1029/JA091iA02p01701

Maksimovic, M., Pierrard, V. and Lemaire, J. F. (1997), 'A kinetic model of the solar wind with Kappa distribution functions in the corona.', *A&A* **324**, 725–734. DOI/URL: https://ui.adsabs.harvard.edu/abs/1997A&A...324..725M

Mallet, A., Squire, J., Chandran, B. D. G., Bowen, T. and Bale, S. D. (2021), 'Evolution of Large-amplitude Alfvén Waves and Generation of Switchbacks in the Expanding Solar Wind', *ApJ* **918**(2), 62. DOI/URL: https://doi.org/10.3847/1538-4357/ac0c12

Markovskii, S. A., Chandran, B. D. G. and Vasquez, B. J. (2019), 'Ion Heating Resulting from the Deceleration of Alpha Particles by a Proton-alpha Drift Instability in a Nonuniform Solar-wind Plasma', *ApJ* **870**(2), 121. DOI/URL: https://doi.org/10.3847/1538-4357/aaf423

Marsch, E. (2012), 'Helios: Evolution of Distribution Functions 0.3-1 AU', *Space Sci. Rev.* **172**(1-4), 23–39. DOI/URL: https://doi.org/10.1007/s11214-010-9734-z

Marsch, E., Rosenbauer, H., Schwenn, R., Muehlhaeuser, K. H. and Denskat, K. U. (1981), 'Pronounced proton core temperature anisotropy, ion differential speed, and simultaneous Alfvén wave activity in slow solar wind at 0.3 AU', *J. Geophys. Res.* **86**(A11), 9199–9203. DOI/URL: https://doi.org/10.1029/JA086iA11p09199

Marsch, E., Rosenbauer, H., Schwenn, R., Muehlhaeuser, K. H. and Neubauer, F. M. (1982*a*), 'Solar wind helium ions: obsevations of the Helios solar probes between 0.3 and 1 AU', *J. Geophys. Res.* **87**(A1), 35–51. DOI/URL: https://doi.org/10.1029/JA087iA01p00035

Marsch, E., Schwenn, R., Rosenbauer, H., Muehlhaeuser, K. H., Pilipp, W. and Neubauer, F. M. (1982*b*), 'Solar wind protons: Three-dimensional velocity distributions and derived plasma parameters measured between 0.3 and 1 AU', *J. Geophys. Res.* **87**(A1), 52–72. DOI/URL: https://doi.org/10.1029/JA087iA01p00052

Martinović, M. M., Klein, K. G. and Bourouaine, S. (2019), 'Radial Evolution of Stochastic Heating in Low-β Solar Wind', *ApJ* **879**(1), 43. DOI/URL: https://doi.org/10.3847/1538-4357/ab23f4

Maruca, B. A., Kasper, J. C. and Gary, S. P. (2012), 'Instability-driven Limits on Helium Temperature Anisotropy in the Solar Wind: Observations and Linear Vlasov Analysis', *ApJ* **748**(2), 137. DOI/URL: https://doi.org/10.1088/0004-637X/748/2/137

Matteini, L., Hellinger, P., Schwartz, S. J. and Landi, S. (2015*a*), 'Fire Hose Instability Driven by Alpha Particle Temperature Anisotropy', *ApJ* **812**(1), 13. DOI/URL: https://doi.org/10.1088/0004-637X/812/1/13

Matteini, L., Horbury, T. S., Neugebauer, M. and Goldstein, B. E. (2014), 'Dependence of solar wind speed on the local magnetic field orientation: Role of Alfvénic fluctuations', *Geophys. Res. Lett.* **41**(2), 259–265. DOI/URL: https://doi.org/10.1002/2013GL058482

Matteini, L., Horbury, T. S., Pantellini, F., Velli, M. and Schwartz, S. J. (2015*b*), 'Ion Kinetic Energy Conservation and Magnetic Field Strength Constancy in Multi-fluid Solar Wind Alfvénic Turbulence', *ApJ* **802**(1), 11. DOI/URL: https://doi.org/10.1088/0004-637X/802/1/11

Matteini, L., Laker, R., Horbury, T., Woodham, L., Bale, S. D., Stawarz, J. E., Woolley, T., Steinvall, K., Jones, G. H., Grant, S. R., Afghan, Q., Galand, M., O'Brien, H., Evans, V., Angelini, V., Maksimovic, M., Chust, T., Khotyaintsev, Y., Krasnoselskikh, V., Kretzschmar, M., Lorfèvre, E., Plettemeier, D., Souček, J., Steller, M., Štverák, Š., Trávníček, P., Vaivads, A., Vecchio, A., Wimmer-Schweingruber, R. F., Ho, G. C., Gómez-Herrero, R., Rodríguez-Pacheco, J., Louarn, P., Fedorov, A., Owen, C. J.,

Bruno, R., Livi, S., Zouganelis, I. and Müller, D. (2021), 'Solar Orbiter's encounter with the tail of comet C/2019 Y4 (ATLAS): Magnetic field draping and cometary pick-up ion waves', *A&A* **656**, A39. DOI/URL: https://doi.org/10.1051/0004-6361/202141229

Matteini, L., Landi, S., Hellinger, P., Pantellini, F., Maksimovic, M., Velli, M., Goldstein, B. E. and Marsch, E. (2007), 'Evolution of the solar wind proton temperature anisotropy from 0.3 to 2.5 AU', *Geophys. Res. Lett.* **34**(20), L20105. DOI/URL: https://doi.org/10.1029/2007GL030920

Matteini, L., Landi, S., Hellinger, P. and Velli, M. (2006), 'Parallel proton fire hose instability in the expanding solar wind: Hybrid simulations', *Journal of Geophysical Research (Space Physics)* **111**(A10), A10101. DOI/URL: https://doi.org/10.1029/2006JA011667

Matthaeus, W. H., Elliott, H. A. and McComas, D. J. (2006), 'Correlation of speed and temperature in the solar wind', *Journal of Geophysical Research (Space Physics)* **111**(A10), A10103. DOI/URL: https://doi.org/10.1029/2006JA011636

McComas, D. J., Alexander, N., Angold, N., Bale, S., Beebe, C., Birdwell, B., Boyle, M., Burgum, J. M., Burnham, J. A., Christian, E. R., Cook, W. R., Cooper, S. A., Cummings, A. C., Davis, A. J., Desai, M. I., Dickinson, J., Dirks, G., Do, D. H., Fox, N., Giacalone, J., Gold, R. E., Gurnee, R. S., Hayes, J. R., Hill, M. E., Kasper, J. C., Kecman, B., Klemic, J., Krimigis, S. M., Labrador, A. W., Layman, R. S., Leske, R. A., Livi, S., Matthaeus, W. H., McNutt, R. L., Mewaldt, R. A., Mitchell, D. G., Nelson, K. S., Parker, C., Rankin, J. S., Roelof, E. C., Schwadron, N. A., Seifert, H., Shuman, S., Stokes, M. R., Stone, E. C., Vandegriff, J. D., Velli, M., von Rosenvinge, T. T., Weidner, S. E., Wiedenbeck, M. E. and Wilson, P. (2016), 'Integrated Science Investigation of the Sun (ISIS): Design of the Energetic Particle Investigation', *Space Sci. Rev.* **204**(1-4), 187–256. DOI/URL: https://doi.org/10.1007/s11214-014-0059-1

McComas, D. J., Elliott, H. A., Schwadron, N. A., Gosling, J. T., Skoug, R. M. and Goldstein, B. E. (2003), 'The three-dimensional solar wind around solar maximum', *Geophys. Res. Lett.* **30**(10), 1517. DOI/URL: https://doi.org/10.1029/2003GL017136

McManus, M. D., Bowen, T. A., Mallet, A., Chen, C. H. K., Chandran, B. D. G., Bale, S. D., Larson, D. E., Dudok de Wit, T., Kasper, J. C., Stevens, M., Whittlesey, P., Livi, R., Korreck, K. E., Goetz, K., Harvey, P. R., Pulupa, M., MacDowall, R. J., Malaspina, D. M., Case, A. W. and Bonnell, J. W. (2020), 'Cross Helicity Reversals in Magnetic Switchbacks', *ApJS* **246**(2), 67. DOI/URL: https://doi.org/10.3847/1538-4365/ab6dce

McManus, M. D., Verniero, J., Bale, S. D., Bowen, T. A., Larson, D. E., Kasper, J. C., Livi, R., Matteini, L., Rahmati, A., Romeo, O., Whittlesey, P. and Woolley, T. (2022), 'Density and Velocity Fluctuations of Alpha Particles in Magnetic Switchbacks', *ApJ*

933(1), 43. DOI/URL: https://doi.org/10.3847/1538-4357/ac6ba3

Meyer-Vernet, N. (2012), *Basics of the Solar Wind*, Cambridge University Press.

Mistry, R. (2017), 'Magnetic reconnection exhausts in the solar wind', *PhD Thesis, Imperial College London, London* . DOI/URL: https://doi.org/10.25560/46008

Montgomery, M. D., Bame, S. J. and Hundhausen, A. J. (1968), 'Solar wind electrons: Vela 4 measurements', *J. Geophys. Res.* **73**(15), 4999. DOI/URL: https://doi.org/10.1029/JA073i015p04999

Morley, S. K. (2020), 'Challenges and Opportunities in Magnetospheric Space Weather Prediction', *Space Weather* **18**(3), e02108. DOI/URL: https://doi.org/10.1029/2018SW002108

Mozer, F. S., Agapitov, O. V., Bale, S. D., Bonnell, J. W., Case, T., Chaston, C. C., Curtis, D. W., Dudok de Wit, T., Goetz, K., Goodrich, K. A., Harvey, P. R., Kasper, J. C., Korreck, K. E., Krasnoselskikh, V., Larson, D. E., Livi, R., MacDowall, R. J., Malaspina, D., Pulupa, M., Stevens, M., Whittlesey, P. L. and Wygant, J. R. (2020), 'Switchbacks in the Solar Magnetic Field: Their Evolution, Their Content, and Their Effects on the Plasma', *ApJS* **246**(2), 68. DOI/URL: https://doi.org/10.3847/1538-4365/ab7196

Müller, D., Marsden, R. G., St. Cyr, O. C. and Gilbert, H. R. (2013), 'Solar Orbiter . Exploring the Sun-Heliosphere Connection', *Sol. Phys.* **285**(1-2), 25–70. DOI/URL: https://doi.org/10.1007/s11207-012-0085-7

Müller, D., St. Cyr, O. C., Zouganelis, I., Gilbert, H. R., Marsden, R., Nieves-Chinchilla, T., Antonucci, E., Auchère, F., Berghmans, D., Horbury, T. S., Howard, R. A., Krucker, S., Maksimovic, M., Owen, C. J., Rochus, P., Rodriguez-Pacheco, J., Romoli, M., Solanki, S. K., Bruno, R., Carlsson, M., Fludra, A., Harra, L., Hassler, D. M., Livi, S., Louarn, P., Peter, H., Schühle, U., Teriaca, L., del Toro Iniesta, J. C., Wimmer-Schweingruber, R. F., Marsch, E., Velli, M., De Groof, A., Walsh, A. and Williams, D. (2020), 'The Solar Orbiter mission. Science overview', *A&A* **642**, A1. DOI/URL: https://doi.org/10.1051/0004-6361/202038467

Neugebauer, M. (1981), 'Observations of Solar-Wind Helium', *Fundamentals Cosmic Phys.* **7**, 131–199. DOI/URL: https://ui.adsabs.harvard.edu/abs/1981FCPh...7..131N

Neugebauer, M., Forsyth, R. J., Galvin, A. B., Harvey, K. L., Hoeksema, J. T., Lazarus, A. J., Lepping, R. P., Linker, J. A., Mikic, Z., Steinberg, J. T., von Steiger, R., Wang, Y. M. and Wimmer-Schweingruber, R. F. (1998), 'Spatial structure of the solar wind and comparisons with solar data and models', *J. Geophys. Res.* **103**(A7), 14587–14600. DOI/URL: https://doi.org/10.1029/98JA00798

Neugebauer, M. and Goldstein, B. E. (2013), Double-proton beams and magnetic switch-

backs in the solar wind, *in* G. P. Zank, J. Borovsky, R. Bruno, J. Cirtain, S. Cranmer, H. Elliott, J. Giacalone, W. Gonzalez, G. Li, E. Marsch, E. Moebius, N. Pogorelov, J. Spann and O. Verkhoglyadova, eds, 'Solar Wind 13', Vol. 1539 of *American Institute of Physics Conference Series*, pp. 46–49. DOI/URL: https://doi.org/10.1063/1.4810986

Neugebauer, M., Goldstein, B. E., Smith, E. J. and Feldman, W. C. (1996), 'Ulysses observations of differential alpha-proton streaming in the solar wind', *J. Geophys. Res.* **101**(A8), 17047–17056. DOI/URL: https://doi.org/10.1029/96JA01406

Neugebauer, M., Liewer, P. C., Smith, E. J., Skoug, R. M. and Zurbuchen, T. H. (2002), 'Sources of the solar wind at solar activity maximum', *Journal of Geophysical Research (Space Physics)* **107**(A12), 1488. DOI/URL: https://doi.org/10.1029/2001JA000306

Neugebauer, M. and Snyder, C. W. (1962), 'Solar Plasma Experiment', *Science* **138**(3545), 1095–1097. DOI/URL: https://doi.org/10.1126/science.138.3545.1095-a

Ng, J. (2020), 'Solar Cycle 25 Is Here. NASA, NOAA Scientists Explain What This Means', *[photograph] NASA* . DOI/URL: https://svs.gsfc.nasa.gov/13714

Nolte, J. T., Krieger, A. S., Timothy, A. F., Gold, R. E., Roelof, E. C., Vaiana, G., Lazarus, A. J., Sullivan, J. D. and McIntosh, P. S. (1976), 'Coronal holes as sources of solar wind.', *Sol. Phys.* **46**(2), 303–322. DOI/URL: https://doi.org/10.1007/BF00149859

Ogilvie, K. W., Chornay, D. J., Fritzenreiter, R. J., Hunsaker, F., Keller, J., Lobell, J., Miller, G., Scudder, J. D., Sittler, E. C., J., Torbert, R. B., Bodet, D., Needell, G., Lazarus, A. J., Steinberg, J. T., Tappan, J. H., Mavretic, A. and Gergin, E. (1995), 'SWE, A Comprehensive Plasma Instrument for the Wind Spacecraft', *Space Sci. Rev.* **71**(1-4), 55–77. DOI/URL: https://doi.org/10.1007/BF00751326

Ogilvie, K. W. and Wilkerson, T. D. (1969), 'Helium Abundance in the Solar Wind', *Sol. Phys.* **8**(2), 435–449. DOI/URL: https://doi.org/10.1007/BF00155391

O'Kane, J., Green, L. M., Davies, E. E., Möstl, C., Hinterreiter, J., Freiherr von Forstner, J. L., Weiss, A. J., Long, D. M. and Amerstorfer, T. (2021), 'Solar origins of a strong stealth CME detected by Solar Orbiter', *A&A* **656**, L6. DOI/URL: https://doi.org/10.1051/0004-6361/202140622

Parker, E. N. (1958), 'Dynamics of the Interplanetary Gas and Magnetic Fields.', *ApJ* **128**, 664. DOI/URL: https://doi.org/10.1086/146579

Perrone, D., D'Amicis, R., De Marco, R., Matteini, L., Stansby, D., Bruno, R. and Horbury, T. S. (2020), 'Highly Alfvénic slow solar wind at 0.3 au during a solar minimum: Helios insights for Parker Solar Probe and Solar Orbiter', *A&A* **633**, A166. DOI/URL:

https://doi.org/10.1051/0004-6361/201937064

Perrone, D., Stansby, D., Horbury, T. S. and Matteini, L. (2019*a*), 'Radial evolution of the solar wind in pure high-speed streams: HELIOS revised observations', *MNRAS* **483**(3), 3730–3737. DOI/URL: https://doi.org/10.1093/mnras/sty3348

Perrone, D., Stansby, D., Horbury, T. S. and Matteini, L. (2019*b*), 'Thermodynamics of pure fast solar wind: radial evolution of the temperature-speed relationship in the inner heliosphere', *MNRAS* **488**(2), 2380–2386. DOI/URL: https://doi.org/10.1093/mnras/stz1877

Petrovay, K. and van Driel-Gesztelyi, L. (1997), 'Making Sense of Sunspot Decay. I. Parabolic Decay Law and Gnevyshev-Waldmeier Relation', *Sol. Phys.* **176**(2), 249–266. DOI/URL: https://doi.org/10.1023/A:1004988123265

Phan, T. D., Lavraud, B., Halekas, J. S., Øieroset, M., Drake, J. F., Eastwood, J. P., Shay, M. A., Pyakurel, P. S., Bale, S. D., Larson, D., Livi, R., Whittlesey, P. L., Rahmati, A., Pulupa, M., McManus, M. D., Verniero, J. L., Bonnell, J. W., Schwadron, N. A., Stevens, M., Case, A. W., Kasper, J. C., MacDowall, R. J., Szabo, P. A., Koval, A., Korreck, K. E., Dudok de Wit, T., Malaspina, D., Goetz, K. and Harvey, P. R. (2021), 'Prevalence of magnetic reconnection in the near-Sun heliospheric current sheet', *A&A* **650**, A13. DOI/URL: https://doi.org/10.1051/0004-6361/202039863

Pierrard, V., Lazar, M., Poedts, S., Štverák, Š., Maksimovic, M. and Trávníček, P. M. (2016), 'The Electron Temperature and Anisotropy in the Solar Wind. Comparison of the Core and Halo Populations', *Sol. Phys.* **291**(7), 2165–2179. DOI/URL: https://doi.org/10.1007/s11207-016-0961-7

Pilipp, W. G., Miggenrieder, H., Montgomery, M. D., Mühlhäuser, K. H., Rosenbauer, H. and Schwenn, R. (1987), 'Characteristics of electron velocity distribution functions in the solar wind derived from the helios plasma experiment', *J. Geophys. Res.* **92**(A2), 1075–1092. DOI/URL: https://doi.org/10.1029/JA092iA02p01075

Rakowski, C. E. and Laming, J. M. (2012), 'On the Origin of the Slow Speed Solar Wind: Helium Abundance Variations', *ApJ* **754**(1), 65. DOI/URL: https://doi.org/10.1088/0004-637X/754/1/65

Raouafi, N. E., Matteini, L., Squire, J., Badman, S. T., Velli, M., Klein, K. G., Chen, C. H. K., Matthaeus, W. H., Szabo, A., Linton, M., Allen, R. C., Szalay, J. R., Bruno, R., Decker, R. B., Akhavan-Tafti, M., Agapitov, O. V., Bale, S. D., Bandyopadhyay, R., Battams, K., Berčič, L., Bourouaine, S., Bowen, T., Cattell, C., Chandran, B. D. G., Chhiber, R., Cohen, C. M. S., D'Amicis, R., Giacalone, J., Hess, P., Howard, R. A., Horbury, T. S., Jagarlamudi, V. K., Joyce, C. J., Kasper, J. C., Kinnison, J., Laker, R., Liewer, P., Malaspina, D. M., Mann, I., McComas, D. J., Niembro-Hernandez, T., Panasenco, O., Pokorný, P., Pusack, A., Pulupa, M., Perez, J. C., Riley, P., Rouillard, A. P., Shi, C., Stenborg, G., Tenerani, A., Verniero, J. L., Viall, N., Vourlidas, A.,

Wood, B. E., Woodham, L. D. and Woolley, T. (2023), 'Parker Solar Probe: Four Years of Discoveries at Solar Cycle Minimum', *arXiv e-prints* p. arXiv:2301.02727.

Robbins, D. E., Hundhausen, A. J. and Bame, S. J. (1970), 'Helium in the solar wind', *J. Geophys. Res.* **75**(7), 1178. DOI/URL: https://doi.org/10.1029/JA075i007p01178

Roberts, M. A., Uritsky, V. M., DeVore, C. R. and Karpen, J. T. (2018), 'Simulated Encounters of the Parker Solar Probe with a Coronal-hole Jet', *ApJ* **866**(1), 14. DOI/URL: https://doi.org/10.3847/1538-4357/aadb41

Rouillard, A. P., Davies, J. A., Lavraud, B., Forsyth, R. J., Savani, N. P., Bewsher, D., Brown, D. S., Sheeley, N. R., Davis, C. J., Harrison, R. A., Howard, R. A., Vourlidas, A., Lockwood, M., Crothers, S. R. and Eyles, C. J. (2010), 'Intermittent release of transients in the slow solar wind: 1. Remote sensing observations', *Journal of Geophysical Research (Space Physics)* **115**(A4), A04103. DOI/URL: https://doi.org/10.1029/2009JA014471

Schatten, K. H., Wilcox, J. M. and Ness, N. F. (1969), 'A model of interplanetary and coronal magnetic fields', *Sol. Phys.* **6**(3), 442–455. DOI/URL: https://doi.org/10.1007/BF00146478

Schove, D. J. (1955), 'The Sunspot Cycle, 649 B.C. to A.D. 2000', *J. Geophys. Res.* **60**(2), 127–146. DOI/URL: https://doi.org/10.1029/JZ060i002p00127

Sheeley, N. R., J., Harvey, J. W. and Feldman, W. C. (1976), 'Coronal holes, solar wind streams, and recurrent geomagnetic disturbances: 1973-1976', *Sol. Phys.* **49**(2), 271–278. DOI/URL: https://doi.org/10.1007/BF00162451

Sheeley, N. R., J., Lee, D. D. H., Casto, K. P., Wang, Y. M. and Rich, N. B. (2009), 'The Structure of Streamer Blobs', *ApJ* **694**(2), 1471–1480. DOI/URL: https://doi.org/10.1088/0004-637X/694/2/1471

Sheeley, N. R., J., Warren, H. P. and Wang, Y. M. (2007), 'A Streamer Ejection with Reconnection Close to the Sun', *ApJ* **671**(1), 926–935. DOI/URL: https://doi.org/10.1086/522940

Sheeley, N. R., Wang, Y. M., Hawley, S. H., Brueckner, G. E., Dere, K. P., Howard, R. A., Koomen, M. J., Korendyke, C. M., Michels, D. J., Paswaters, S. E., Socker, D. G., St. Cyr, O. C., Wang, D., Lamy, P. L., Llebaria, A., Schwenn, R., Simnett, G. M., Plunkett, S. and Biesecker, D. A. (1997), 'Measurements of Flow Speeds in the Corona Between 2 and 30 R_S', *ApJ* **484**(1), 472–478. DOI/URL: https://doi.org/10.1086/304338

Smith, C. W., Matthaeus, W. H., Zank, G. P., Ness, N. F., Oughton, S. and Richardson, J. D. (2001), 'Heating of the low-latitude solar wind by dissipation of turbulent magnetic fluctuations', *J. Geophys. Res.* **106**(A5), 8253–8272. DOI/URL: https://doi.org/10.1029/2000JA000366

Solanki, S. K. (2003), 'Sunspots: An overview', *A&ARv* **11**(2-3), 153–286. DOI/URL: https://doi.org/10.1007/s00159-003-0018-4

Squire, J., Chandran, B. D. G. and Meyrand, R. (2020), 'In-situ Switchback Formation in the Expanding Solar Wind', *ApJ* **891**(1), L2. DOI/URL: https://doi.org/10.3847/2041-8213/ab74e1

Stakhiv, M., Landi, E., Lepri, S. T., Oran, R. and Zurbuchen, T. H. (2015), 'On the Origin of Mid-latitude Fast Wind: Challenging the Two-state Solar Wind Paradigm', *ApJ* **801**(2), 100. DOI/URL: https://doi.org/10.1088/0004-637X/801/2/100

Stakhiv, M., Lepri, S. T., Landi, E., Tracy, P. and Zurbuchen, T. H. (2016), 'On Solar Wind Origin and Acceleration: Measurements from ACE', *ApJ* **829**(2), 117. DOI/URL: https://doi.org/10.3847/0004-637X/829/2/117

Stansby, D., Green, L. M., van Driel-Gesztelyi, L. and Horbury, T. S. (2021), 'Active Region Contributions to the Solar Wind over Multiple Solar Cycles', *Sol. Phys.* **296**(8), 116. DOI/URL: https://doi.org/10.1007/s11207-021-01861-x

Stansby, D., Horbury, T. S. and Matteini, L. (2019*a*), 'Diagnosing solar wind origins using in situ measurements in the inner heliosphere', *MNRAS* **482**(2), 1706–1714. DOI/URL: https://doi.org/10.1093/mnras/sty2814

Stansby, D., Matteini, L., Horbury, T. S., Perrone, D., D'Amicis, R. and Berčič, L. (2020*a*), 'The origin of slow Alfvénic solar wind at solar minimum', *MNRAS* **492**(1), 39–44. DOI/URL: https://doi.org/10.1093/mnras/stz3422

Stansby, D., Perrone, D., Matteini, L., Horbury, T. S. and Salem, C. S. (2019*b*), 'Alpha particle thermodynamics in the inner heliosphere fast solar wind', *A&A* **623**, L2. DOI/URL: https://doi.org/10.1051/0004-6361/201834900

Stansby, D., Salem, C., Matteini, L. and Horbury, T. (2018), 'A New Inner Heliosphere Proton Parameter Dataset from the Helios Mission', *Sol. Phys.* **293**(11), 155. DOI/URL: https://doi.org/10.1007/s11207-018-1377-3

Stansby, D., Yeates, A. and Badman, S. T. (2020*b*), 'pfsspy: A python package for potential field source surface modelling', *Journal of Open Source Software* **5**(54), 2732. DOI/URL: https://doi.org/10.21105/joss.02732

Sterling, A. C. and Moore, R. L. (2020), 'Coronal-jet-producing Minifilament Eruptions as a Possible Source of Parker Solar Probe Switchbacks', *ApJ* **896**(2), L18. DOI/URL: https://doi.org/10.3847/2041-8213/ab96be

Suess, S. T., Ko, Y. K., von Steiger, R. and Moore, R. L. (2009), 'Quiescent current sheets in the solar wind and origins of slow wind', *Journal of Geophysical Research (Space Physics)* **114**(A4), A04103. DOI/URL: https://doi.org/10.1029/2008JA013704

Tenerani, A., Sioulas, N., Matteini, L., Panasenco, O., Shi, C. and Velli, M. (2021),

'Evolution of Switchbacks in the Inner Heliosphere', *ApJ* **919**(2), L31. DOI/URL: https://doi.org/10.3847/2041-8213/ac2606

Tu, C.-Y., Zhou, C., Marsch, E., Xia, L.-D., Zhao, L., Wang, J.-X. and Wilhelm, K. (2005), 'Solar Wind Origin in Coronal Funnels', *Science* **308**(5721), 519–523. DOI/URL: https://doi.org/10.1126/science.1109447

Ďurovcová, T., Šafránková, J. and Němeček, Z. (2019), 'Evolution of Relative Drifts in the Expanding Solar Wind: Helios Observations', *Sol. Phys.* **294**(7), 97. DOI/URL: https://doi.org/10.1007/s11207-019-1490-y

Verdini, A., Velli, M., Matthaeus, W. H., Oughton, S. and Dmitruk, P. (2010), 'A Turbulence-Driven Model for Heating and Acceleration of the Fast Wind in Coronal Holes', *ApJ* **708**(2), L116–L120. DOI/URL: https://doi.org/10.1088/2041-8205/708/2/L116

Verscharen, D., Klein, K. G. and Maruca, B. A. (2019), 'The multi-scale nature of the solar wind', *Living Reviews in Solar Physics* **16**(1), 5. DOI/URL: https://doi.org/10.1007/s41116-019-0021-0

Viall, N. M. and Borovsky, J. E. (2020), 'Nine Outstanding Questions of Solar Wind Physics', *Journal of Geophysical Research (Space Physics)* **125**(7), e26005. DOI/URL: https://doi.org/10.1029/2018JA026005

Viall, N. M., Kepko, L. and Spence, H. E. (2008), 'Inherent length-scales of periodic solar wind number density structures', *Journal of Geophysical Research (Space Physics)* **113**(A7), A07101. DOI/URL: https://doi.org/10.1029/2007JA012881

Viall, N. M., Kepko, L. and Spence, H. E. (2009*a*), 'Relative occurrence rates and connection of discrete frequency oscillations in the solar wind density and dayside magnetosphere', *Journal of Geophysical Research (Space Physics)* **114**(A1), A01201. DOI/URL: https://doi.org/10.1029/2008JA013334

Viall, N. M., Spence, H. E. and Kasper, J. (2009*b*), 'Are periodic solar wind number density structures formed in the solar corona?', *Geophys. Res. Lett.* **36**(23), L23102. DOI/URL: https://doi.org/10.1029/2009GL041191

Viall, N. M., Spence, H. E., Vourlidas, A. and Howard, R. (2010), 'Examining Periodic Solar-Wind Density Structures Observed in the SECCHI Heliospheric Imagers', *Sol. Phys.* **267**(1), 175–202. DOI/URL: https://doi.org/10.1007/s11207-010-9633-1

Viall, N. M. and Vourlidas, A. (2015), 'Periodic Density Structures and the Origin of the Slow Solar Wind', *ApJ* **807**(2), 176. DOI/URL: https://doi.org/10.1088/0004-637X/807/2/176

Vourlidas, A., Howard, R. A., Plunkett, S. P., Korendyke, C. M., Thernisien, A. F. R.,

Wang, D., Rich, N., Carter, M. T., Chua, D. H., Socker, D. G., Linton, M. G., Morrill, J. S., Lynch, S., Thurn, A., Van Duyne, P., Hagood, R., Clifford, G., Grey, P. J., Velli, M., Liewer, P. C., Hall, J. R., DeJong, E. M., Mikic, Z., Rochus, P., Mazy, E., Bothmer, V. and Rodmann, J. (2016), 'The Wide-Field Imager for Solar Probe Plus (WISPR)', *Space Sci. Rev.* **204**(1-4), 83–130. DOI/URL: https://doi.org/10.1007/s11214-014-0114-y

Wang, Y. M. and Sheeley, N. R., J. (1990), 'Solar Wind Speed and Coronal Flux-Tube Expansion', *ApJ* **355**, 726. DOI/URL: https://doi.org/10.1086/168805

Wang, Y. M. and Sheeley, N. R., J. (1994), 'Global evolution of interplanetary sector structure, coronal holes, and solar wind streams during 1976-1993: Stackplot displays based on solar magnetic observations', *J. Geophys. Res.* **99**(A4), 6597–6608. DOI/URL: https://doi.org/10.1029/93JA02105

Wang, Y. M., Sheeley, N. R., J., Phillips, J. L. and Goldstein, B. E. (1997), 'Solar Wind Stream Interactions and the Wind Speed-Expansion Factor Relationship.', *ApJ* **488**(1), L51–L54. DOI/URL: https://doi.org/10.1086/310918

Wang, Y. M., Sheeley, N. R., J., Walters, J. H., Brueckner, G. E., Howard, R. A., Michels, D. J., Lamy, P. L., Schwenn, R. and Simnett, G. M. (1998), 'Origin of Streamer Material in the Outer Corona', *ApJ* **498**(2), L165–L168. DOI/URL: https://doi.org/10.1086/311321

Wang, Y. M., Sheeley, N. R., Socker, D. G., Howard, R. A. and Rich, N. B. (2000), 'The dynamical nature of coronal streamers', *J. Geophys. Res.* **105**(A11), 25133–25142. DOI/URL: https://doi.org/10.1029/2000JA000149

Whitman, E. (2018), 'Prepping to Launch for the Sun', *[photograph] NASA* . DOI/URL: https://www.nasa.gov/sites/default/files/thumbnails/image/fencap2.jpg

Whittlesey, P. L., Larson, D. E., Kasper, J. C., Halekas, J., Abatcha, M., Abiad, R., Berthomier, M., Case, A. W., Chen, J., Curtis, D. W., Dalton, G., Klein, K. G., Korreck, K. E., Livi, R., Ludlam, M., Marckwordt, M., Rahmati, A., Robinson, M., Slagle, A., Stevens, M. L., Tiu, C. and Verniero, J. L. (2020), 'The Solar Probe ANalyzers—Electrons on the Parker Solar Probe', *ApJS* **246**(2), 74. DOI/URL: https://doi.org/10.3847/1538-4365/ab7370

Woodham, L. D., Horbury, T. S., Matteini, L., Woolley, T., Laker, R., Bale, S. D., Nicolaou, G., Stawarz, J. E., Stansby, D., Hietala, H., Larson, D. E., Livi, R., Verniero, J. L., McManus, M., Kasper, J. C., Korreck, K. E., Raouafi, N., Moncuquet, M. and Pulupa, M. P. (2021), 'Enhanced proton parallel temperature inside patches of switchbacks in the inner heliosphere', *A&A* **650**, L1. DOI/URL: https://doi.org/10.1051/0004-6361/202039415

Woolley, T., Matteini, L., Horbury, T. S., Bale, S. D., Woodham, L. D., Laker, R., Alter-

man, B. L., Bonnell, J. W., Case, A. W., Kasper, J. C., Klein, K. G., Martinović, M. M. and Stevens, M. (2020), 'Proton core behaviour inside magnetic field switchbacks', *MNRAS* **498**(4), 5524–5531. DOI/URL: https://doi.org/10.1093/mnras/staa2770

Woolley, T., Matteini, L., McManus, M. D., Berčič, L., Badman, S. T., Woodham, L. D., Horbury, T. S., Bale, S. D., Laker, R., Stawarz, J. E. and Larson, D. E. (2021), 'Plasma properties, switchback patches, and low α-particle abundance in slow Alfvénic coronal hole wind at 0.13 au', *MNRAS* **508**(1), 236–244. DOI/URL: https://doi.org/10.1093/mnras/stab2281

Xu, F. and Borovsky, J. E. (2015), 'A new four-plasma categorization scheme for the solar wind', *Journal of Geophysical Research (Space Physics)* **120**(1), 70–100. DOI/URL: https://doi.org/10.1002/2014JA020412

Zank, G. P., Nakanotani, M., Zhao, L. L., Adhikari, L. and Kasper, J. (2020), 'The Origin of Switchbacks in the Solar Corona: Linear Theory', *ApJ* **903**(1), 1. DOI/URL: https://doi.org/10.3847/1538-4357/abb828

Zhao, L., Zurbuchen, T. H. and Fisk, L. A. (2009), 'Global distribution of the solar wind during solar cycle 23: ACE observations', *Geophys. Res. Lett.* **36**(14), L14104. DOI/URL: https://doi.org/10.1029/2009GL039181

Appendix A

Papers

Below is a list of papers associated with the work done throughout my PhD.

First-Author Papers

- Proton core behaviour inside magnetic field switchbacks (Woolley et al., 2020)
- Plasma properties, switchback patches, and low $\alpha-$particle abundance in slow Alfvénic coronal hole wind at 0.13 au (Woolley et al., 2021)

Co-Author Papers

- Highly Structured Slow Solar Wind Emerging from an Equatorial Coronal Hole (Bale et al., 2019)
- Sharp Alfvénic Impulses in the Near-Sun Solar Wind (Horbury et al., 2020)
- Statistical analysis of orientation, shape, and size of solar wind switchbacks (Laker et al., 2021*a*)
- Enhanced proton parallel temperature inside patches of switchbacks in the inner heliosphere (Woodham et al., 2021)
- Multi-spacecraft study of the solar wind at solar minimum: Dependence on latitude and transient outflows (Laker et al., 2021*b*)
- Solar Orbiter's encounter with the tail of comet C/2019 Y4 (ATLAS): Magnetic field draping and cometary pick-up ion waves (Matteini et al., 2021)
- A Solar Source of Alfvénic Magnetic Field Switchbacks: In Situ Remnants of Magnetic Funnels on Supergranulation Scales (Bale et al., 2021)
- Switchback Deflections Beyond the Early Parker Solar Probe Encounters (Laker et al., 2022)
- Density and Velocity Fluctuations of Alpha Particles in Magnetic Switchbacks (McManus et al., 2022)
- Parker Solar Probe: Four Years of Discoveries at Solar Cycle Minimum (Raouafi et al., 2023)

Appendix B

Symbols

$\mathbf{B}$	Magnetic Field
$\mathbf{E}$	Electric Field
$\mathbf{F}$	Lorentz Force
$\mathbf{j}$	Current Density
$\mathbf{P}$	Pressure Tensor
$\mathbf{Q}$	Heat Flux Tensor
$\mathbf{S}$	Poynting Flux
$\mathbf{u}$	Bulk Solar Wind Speed
$\mathbf{v}$	Velocity
A_α	$\alpha-$particle abundance
D	Differential Charge Flux Density
E	Energy
e	Electron Charge
f	Frequency
$f(\mathbf{r}, \mathbf{v}, t)$	Phase-space Distribution Function
F_v	SPC-measured Distribution Function
G	Gravitational Constant
k_B	Boltzmann Constant
m, M	Mass
n	Number Density
P, P_B	Thermal Pressure, Magnetic Pressure
q	Charge
r_c, R_S	Critical Radius, Solar Radius
t	Time

T, $T_\parallel$, $T_\perp$	Temperature (parallel and perpendicular to magnetic field)
V_{high}	High Voltage Modulator Grid Voltage Upper Bound
V_{low}	High Voltage Modulator Grid Voltage Lower Bound
v_A	Alfvén Speed
v_{phase}	Local Solar Wind Phase Speed
β	Plasma Beta
ϵ_0	Vacuum Permittivity
η	Resistivity
θ	Latitude
θ_{BR}	Magnetic Field Cone Angle
θ_{BV}	Angle Between Magnetic Field and Relative SW-Spacecraft Velocity
μ_0	Vacuum Permeability
ρ	Mass Density
σ^2	Total Magnetic Field Variance
ϕ	Longitude
ω	Thermal Speed
Ω	Solar Rotation Rate

Appendix C

Acronyms

CGL	Chew-Goldberger-Low
ESA	Electrostatic Analyser
FIELDS	Electromagnetic Fields Investigations
FIP	First Ionisation Potential
FOV	Field of View
GONG	Global Oscillation Network Group
HCS	Heliospheric Current Sheet
HVMG	High Voltage Modulator Grid
IS$\circ$IS	Integrated Science Investigation of the Sun
MHD	Magnetohydrodynamics
PAD	Pitch Angle Distribution
PDS	Periodic Density Structures
PFSS	Potential Field Source Surface
PSD	Power Spectral Density
PSP	Parker Solar Probe
RDF	Reduced Distribution Function
RTN	Radial Tangential Normal
SPAN	Solar Probe Analyzers
SPC	Solar Probe Cup
SWEAP	Solar Wind Electrons Alphas and Protons
VDF	Velocity Distribution Function
WISPR	Wide-field Imager for Solar Probe

Appendix D

Software

Throughout this thesis, I have used a variety of software. These are listed below:

- Python - https://www.python.org/
- NumPy - https://numpy.org/
- SciPy - https://scipy.org/
- HelioPy - https://github.com/heliopython/heliopy
- Matplotlib - https://matplotlib.org/
- Pandas - https://pandas.pydata.org/
- pfsspy - https://pfsspy.readthedocs.io/en/stable/index.html
- Astropy - https://www.astropy.org/
- JHelioviewer - https://www.jhelioviewer.org/

Appendix E

Data

The data used throughout this thesis is publicly available from various sources.

- Parker Solar Probe Data - https://cdaweb.gsfc.nasa.gov/index.html
- Parker Solar Probe SPICE Kernels - https://sppgway.jhuapl.edu/ancil_products
- Helios Data - https://helios-data.ssl.berkeley.edu/

There is also good documentation available.

- SWEAP Documentation - http://sweap.cfa.harvard.edu/Data.html
- FIELDS Documentation - https://fields.ssl.berkeley.edu/data/

Appendix F

Permissions

All figures from other sources have been reproduced with permission from the copyright holders.

Figure Number	Publisher / Journal	Citation	Permission Status
2.1	SVST	Henriques (2010)	None Required
2.2	Cambridge	Meyer-Vernet (2012)	Granted
2.3	NASA	Ng (2020)	None Required
2.4	ESA	JHelioviewer	None Required
2.7	Springer	Marsch (2012)	Granted
2.8	IOP AAS	Berčič et al. (2020)	Granted
2.9	Springer	Verscharen et al. (2019)	None Required (CC-BY)
2.10	IOP AAS	Matteini et al. (2015*b*)	Granted
2.11	IOP AAS	Matteini et al. (2015*b*)	Granted
2.12	GRL	McComas et al. (2003)	Granted
2.14	Springer	Verscharen et al. (2019)	None Required (CC-BY)
2.15	ICL	Mistry (2017)	None Required
2.16 (left)	NASA	Whitman (2018)	None Required
2.16 (right)	ESA	ESA (2020)	Granted
3.1	Springer	Kasper et al. (2016)	None Required (CC-BY)
3.2	Springer	Kasper et al. (2016)	None Required (CC-BY)
3.6	MNRAS	Woolley et al. (2020)	None Required
3.10	MNRAS	Woolley et al. (2020)	None Required
4.3	MNRAS	Woolley et al. (2020)	None Required
4.4	MNRAS	Woolley et al. (2020)	None Required

Figure Number	Publisher / Journal	Citation	Permission Status
4.5	MNRAS	Woolley et al. (2020)	None Required
5.1 (left)	A&A	Woodham et al. (2021)	Granted
5.1 (right)	IOP AAS	Berčič et al. (2020)	Granted
5.3	MNRAS	Woolley et al. (2021)	None Required
5.4	MNRAS	Woolley et al. (2021)	None Required
5.5	MNRAS	Woolley et al. (2021)	None Required
5.6	MNRAS	Woolley et al. (2021)	None Required
5.7	MNRAS	Woolley et al. (2021)	None Required
5.8	MNRAS	Woolley et al. (2021)	None Required
5.9	IOP AAS	Fisk and Kasper (2020)	None Required (CC-BY)
Tab. 5.1	MNRAS	Woolley et al. (2021)	None Required